Modular Origami-inspired Kinematic Metamaterials

Yunfang Yang

Magdalen College

A dissertation submitted for the degree of Doctor of Philosophy

in the Department of Engineering Science

at the University of Oxford

Michaelmas Term, 2020

To My Family.

ABSTRACT

Modular Origami-inspired Kinematic Metamaterials

Yunfang Yang, Magdalen College, Oxford

A dissertation submitted for the degree of Doctor of Philosophy at the University of Oxford

This dissertation proposed a kinematic-based construction method for reconfigurable mechanical metamaterials. This was achieved by entrenching kinematic mechanisms with predefined motion paths within the unit cells of the metamaterial and connecting the units according to carefully chosen topology pattern. The developed metamaterials are able to perform complex transformation between different configurations, which brings superior tuneable physical properties. The major findings of this dissertation are in following four areas.

First, this research built a bridge between mechanism networks and mechanical metamaterials. The theories of planar and spatial mechanisms were utilised to analyse and program the behaviour of metamaterials. Various interesting metamaterials were developed, including materials whose expansion ratio, volumetric strain and porosity are programmable; structures with multiple deformation paths due to their built-in kinematic bifurcation; and metamaterials with constant negative Poisson's ratios that can be programmed by the parameters of the building blocks. The kinematic-induced design strategy paves the way for a new class of metamaterials that can perform reliable large deformation along predefined motion paths.

Second, different strategies to construct three dimensional (3D) kinematic metamaterials were investigated. While most current origami metamaterials focus on thin shell planar structures, this thesis endeavoured to explore 3D materials. A tilting unit method was proposed for single layer 3D metamaterial, whereas a spatial mechanism-entrenched design strategy was developed for more general 3D metamaterials. The topology and transformation of the unit cells were obtained using the kinematic analysis so that the tuneability of the material became a built-in feature of these metamaterials.

Third, an application of kinematic metamaterials as frequency selective surfaces has been investigated. The metamaterials were designed to have multi-stable states so that it can be locked mechanically in various configurations corresponding to specific passband. The metamaterials were fabricated and tested in electromagnetics experiments to validate their functionality.

Finally, the fabrication strategies of various kinematic metamaterials were explored. Laser engraving technique was mainly used for planar metamaterials. For 3D metamaterials, a multi-material 3D printing method was investigated for millimetre-scale samples, and a multi-process lamination method was developed for meso-scale paper prototypes. These methods provided rich and useful experience for the development of functional metamaterials in the future.

Keywords: mechanical metamaterial, kinematics, linkage mechanisms, modular origami, shape morphing, reconfigurable metamaterial.

ACKNOWLEDGMENT

I would like to express sincere gratitude towards my friends, family, colleagues, college and a great number of organizations for their ongoing support, help and encouragement.

Firstly, I am extremely grateful for the financial support from the Clarendon Fund Scholarship during my DPhil program. My thanks also to the Magdalen College student support funding and travelling grant, and the support from the Air Force Office of Scientific Research, which enabled the building of prototypes in the thesis.

I gratefully acknowledge the guidance from my supervisor, Prof Zhong You. His academic instructions, lifelong advice and support in career development. I appreciate Prof Chris Stevens, Prof Patrick Grant and Prof Ekaterina Shamonina for their guidance in electromagnetic metamaterials; Prof Yan Chen for her help on academic writing; Prof Katia Bertoldi for her supervision during my half-year visiting at Harvard University. My thanks also go to my collaborators Dr Andrea Vallecchi, whose professional advice have led my work into new exciting applications. For the help on building prototypes and experiments, I would like to thank Peter Walters, Bob Scott, Prof Chris MacMinn, Igor Dyson, Matt Towlson, Paul Pattinson and technicians in the workshop and stores.

I appreciate the companion from my friends and colleagues in the Engineering Department, Magdalen College, and School of engineering and applied science at Harvard deeply. I would particularly like to thank the postdoc in our group, Dr Martin Walker and Dr Xiao Zhang, for their insightful advice on my research and kind help on career development.

Last but not least, I want to thank my parents and my boyfriend Bowen for their deep love, care and unconditional support. Because of them, I never feel alone during the triumph and frustration in the past four years.

CONTENTS

LIST OF FIGURES

LIST OF TABLES

NOMENCLATURE

n	Number of links of a linkage
j	Number of joints of a linkage
f_i	Degree-of-freedom of the i joint
m	Mobility of a linkage
$a_{i(i+1)}$	Length of link $i(i+1)$
$\alpha_{i(i+1)}$	Twist angle between joints i and $i+1$
R_i	Offset of joint i
θ_i	Rotational angle of the linkage i
$\mathbf{T}_{i(i+1)}$	Transformation matrix between coordinate system i and coordinate system $i+1$

Chapter 3

ϕ_i	Angle of the quadrilateral unit cell
θ_i	Rotational variable
a, b, c, d	Edge length of the quadrilateral unit cell
l_{E}	Edge length of the fully expanded star pattern
l_{PS}	Edge length of the star pattern in its packed state
l_i	Diagonal length of the voids in tilted cuboid structures
α_{S}	Angle of the star arm
r	Expansion ratio
w	Inclined edge length of the rhombohedron unit
h	Distance between two parallel surfaces
α	Tilting angle between the inclined edge of the rhombohedron and the longer diagonal line of the bottom

β	Corner angle of the side parallelogram plane
γ	Angle between diagonal line and the side edge
δ	Twist angle between plane P′ and the upper plane of the central unit
η	Intersection angle between two neighbouring edges of the parallelogram
e	Volumetric strain of the tilted cuboid structure
V	Volume of tilted the cuboid structure
S	Surface area of the tilted cuboid structure

Chapter 4

θ_i	Dihedral angle of the kinematic unit
L_i	Dimension of the kinematic metamaterial
L_i^0	Initial dimension of the kinematic metamaterial
a	Dimension of the corner cube and the prisms
l_i	Edge length of the triangular prism
L	Edge length of the representative volume element of the metamaterial
H	height of the representative volume element of the metamaterial
h	Height of the triangular prism
c	Dimension of the chopped corner of the variant metamaterial
m, n, k	Number of kinematic modules in different directions
p	Numbers of columns in y-directions that contain open channels
q	Numbers of columns in x-direction that contain open channels
φ, ψ	Dihedral angles of the Bricard mechanism-based kinematic unit
d_0, d_0, d_2	Diameters of the inscribed circles of pores in the kinematic metamaterial
ε_i	Strain in i- direction
e_i	Engineering strain

ε^{log}	True strain
v_{ij}	Poisson's ratio of the metamaterial
f_i	Void fraction of the metamaterial
$A_{s\text{-}ij}$	Surface area of the solid building blocks in the *xy*, *zx* or *yz* planes
$A_{t\text{-}ij}$	Total surface area of the metamaterial in the *xy*, *zx* or *yz* planes
P	Porosity of the metamaterial
V_0	Volume of a triangular prism building block
V_{RVE}	Volume of a representative volume element

Chapter 5

Π	Total potential energy
U	Elastic strain energy stored in the deformed body
V	Potential energy of the applied load associated with the applied force
I	Area moment of inertia
M	Pure moment on the bending ligament
E	Young's modulus
θ_i	Rotational variable
k_i	Equivalent stiffness of the flexure hinge
b_i	Thickness of the sheet material
t_i	Thickness of the hinge i
t	Thickness of the hinges that are not specified
t_c	Cut width
a_i^0	Original length of the thin ligament
a_i	Length of the hinge

l	Dimension of the unit
l_s	Edge length of the star arm
l_t	Length of the triangle edge which is adjacent to the star
α	One acute angle of the triangle for triangle model; star angle for star model
θ_i'	Local rotational angle
R_i	Radius of the local arc corresponding to θ_i'.
n_i	Number of the identical *i* hinges in a single unit.
e	Strain of the structure
F	Force
σ	Conductivity of the sample
T_{ii}	Transmission coefficients of the FSS prototypes (i = *v* or *h*. *v* refers to vertical polarized plane wave, and *h* refers to horizontal polarized plane wave)
R_{ii}	Reflection coefficients of the FSS prototypes

Chapter 1

Introduction

1.1 Mechanical metamaterial

Material is the fundamental media for people to interact with the world. Recent developments in computational and manufacturing technology enable researchers to create metamaterials with carefully designed structures that lead to novel physical properties (Zadpoor, 2016; Bertoldi et al., 2017). The application of metamaterials ranges from acoustic, electromagnetic and photonic fields such as cloaking (Buckmann et al., 2015), superlens (Pendry, 2000) and super-directive antennas (Radkovskaya et al., 2018). Of particular interest is a family of mechanical metamaterials, which exploit shape-changing behaviour to tune their mechanical properties. These physical properties are superior to those of natural materials, such as high stiff-to-weight ratio (Zheng et al., 2014), low thermal conductivity (Boatti et al., 2017), negative Poisson's ratio (Babaee et al., 2013), advantages in energy absorption (Schaedler et al., 2014), as well as good wave propagation property (Coulais et al., 2017). Usually, the features are primarily defined by their designed microstructures rather than their chemical

composition. The shape-morphing structures can be categorized by various construction methods, such as foam-like auxetic structures, instability-based structures, mechanism-based materials, etc. Among them, origami/kirigami-inspired structure is a popular method that belongs to mechanism-based metamaterials. Origami permits complex folding motion along pre-determined creases, and this process can be analysed using kinematic principles. The reconfiguration of origami arises exclusively from their underlying kinematics, independent of the constituent material, and thus almost all materials can be used to fabricate origami-based metamaterials.

Most origami-inspired metamaterials are case-by-case studies without a systematic approach. Typical origami is a two-dimensional structure, and the fabrication options are limited considering the material thickness. Advanced multi-task applications such as soft robotics and wearable devices would demand three-dimensional metamaterials, which require an in-depth understanding of the spatial structural kinematics. However, hardly any three-dimensional metamaterial has been designed using a kinematics approach despite that kinematic deformation is commonly more precise and achievable.

This thesis tries to propose a kinematic-based strategy to design mechanical metamaterials, which would open up a wide design space for the tunability and programmability of multiple physical properties, leading to new avenues of multi-functional materials research. The geometry variation of kinematic metamaterials can largely influence its acoustic, electromagnetic, wave propagation performance, therefore, exciting engineering applications such as optical devices (Liu et al., 2018), medical implants (Kolken et al., 2018) and soft robotics (Rafsanjani et al., 2018) can be achieved accordingly.

1.2 Modular origami and kinematic mechanisms

In order to modify the origami models with consideration of thickness, we focus on a branch of origami art called modular origami, where one first constructs identical units by multiple pieces of paper, then interlock the units with each other to result in one assembly. The main reason for studying modular origami is that the units can be assembled in a structural mechanism way. Generally speaking, the foldability of rigid origami can be modelled kinematically, if we assume the paper panels as rigid bodies and the creases as revolute joints. For a single vertex origami, the axes of the revolute joints meet at one vertex, and the structure is modelled as a spherical linkage. Correspondingly, modular origami structures with polyhedron bodies can be modelled as spatial linkage mechanisms. By designing the shape and connection arrangement of polyhedron units and analyzing them according to mechanism theories, the modular origami models can be designed to reconfigure into various shapes.

Equivalent to the construction of the linkage mechanism network, we can construct an unlimited extension of the material network by tessellating the modular origami units. Different from other construction methods based on a limited number of known origami/kirigami patterns, this study aims to build the bridge among mechanisms networks, origami structures and mechanical metamaterial using modular origami.

1.3 Scope and aim

The aim of this dissertation is to construct kinematics-induced mechanical metamaterials inspired by modular origami. It has been achieved to analyse metamaterials using the kinematic principles, and the focus of this thesis is to initially construct 2D and 3D metamaterials from the viewpoint of linkage mechanisms and explore their possible applications. Three primary research aims are detailed as follows.

1) Construction of metamaterials using kinematic mechanisms

This research aims to design kinematic metamaterials from the construction of mechanism networks. Planar and spatial mechanisms are adopted to design the kinematic units and the connection arrangements among units. Moreover, tessellating the connected units in space or linking different assemblies together can produce metamaterials that switch from one shape to others.

2) 3D metamaterials with complex transformation

While most to-date origami metamaterials adopted thin shell planar patterns, this research endeavours to explore 3D metamaterial construction. By introducing the structural mechanisms into metamaterial construction, numerous spatial linkages can be adapted to connect origami units. The second part of Chapter 3 demonstrated the transition of planar material to 3D material through tilting the unit cells; Chapter 4 presented models constructed by the Sarrus linkage, planar 4*R* linkage, spherical linkage and the Bricard linkage. Some of the proposed metamaterials have bifurcated motion paths which enable them to transform into multiple configurations. Following this path, a great number of 3D metamaterials are remained to be explored.

3) Electromagnetic functionality of mechanical metamaterials

To date, the construction of metamaterials with a given functionality remains challenging, and many designs rely on luck and intuition. In this research, we propose an application of kinematic metamaterials on frequency selective surfaces (Chapter 5). The proposed kirigami pattern has been designed to be bistable to lock in specific configurations, manufactured for experiments and optimized by numerical analysis. Although a systematic approach of rational design is yet to be examined, the cases shown in the thesis proved that the proposed metamaterials have great potentials in other multi-functional applications.

1.4 Dissertation layout

The thesis structure consists of four chapters as follows. Chapter 2 is a literature review encompassing research in mechanical metamaterial, linkage mechanisms and modular origami structures. The metamaterial background includes the construction methods, applications of mechanical metamaterials in acoustic, electromagnetic and photonic fields, as well as their manufacturing techniques. A further discussion on current origami-inspired mechanical metamaterial is also presented. The mechanism review illustrates the kinematic analysis of rigid origami and introduces several typical overconstrained linkages. Finally, some modular origami structures and tessellation patterns are also demonstrated.

Chapter 3 is devoted to the construction of kinematic metamaterials based on planar mechanisms and reconfigurable tilings. Some modular origami made by prism units can be regarded as a network of planar mechanisms. During the transformation, the shape of the voids will change, and the tiling pattern of origami units is geometrically compatible at any configuration. The first part of Chapter 3 focuses on reconfigurable tilings with quadrilateral voids. The voids are modelled as planar four-bar linkages (4*R* linkage), and the reconfigurability of this linkage network is analysed kinematically. This is followed by a discussion on assemblies consisting of more than two types of units, the orientation variation, duality and expand ratio of the structure. The second part is evolved from the reconfigurable tiling, where the cube units are tilted into rhombohedrons, and the connecting edges are no longer perpendicular to the tilting plane. Consequently, the structure folds into a spatial configuration during the deployment. This derivative metamaterial preserves the planar mechanism network of the first example. A series of reconfigurable structures with various spatial shapes, twists and permeability features are constructed by programming the tilting angle, tilting direction and basic shape of the unit. In addition, a multi-layer three-dimensional

metamaterial is proposed. The volumetric strain has been analysed and shows the metamaterial has a massive deformation ability and programmable porosity.

Chapter 4 focuses on the design of 3D metamaterials based on spatial and planar mechanisms. Cubes and prisms building blocks are connected edge-by-edge to form modular origami assembly. The assembly is transformable under the condition that the connection edges are arranged in particular spatial positions. We link the prisms according to spatial linkage mechanisms such as the Sarrus linkage and the Bricard linkage to form a kinematic unit, then tessellate the unit into a metamaterial. Some kinematic units have multi-mode reconfigurability arises exclusively from their underlying kinematics, leading to transformation into different shapes under various stimuli. Based on this approach, a series of spatial mechanisms induced kinematic metamaterials are developed, including materials with tuneable multi-channel permeability, tuneable porosity and programmable constant negative Poisson's ratio. By changing the connection arrangements, prism shapes and numbers, we can program the output behaviour of the metamaterial.

Chapter 5 is a study of the electromagnetic application of mechanical metamaterials. Planar reconfigurable metamaterials that could deform into different patterns for the purpose of frequency selection are developed. Two types of metamaterials are designed and analysed kinematically. Due to their multistable properties, the structures could transform into specific configurations and maintain the shape after the actuation force is removed. This provides convenient mechanical switching among several passbands. Simplified energy models are built and compared with finite element simulations. The kirigami frequency selective surfaces are fabricated and tested for their electromagnetic responses to validate the application.

Conclusions and discussion on future work are given in Chapter 6, which concludes the dissertation.

Chapter 2

Literature Review

2.1 Mechanical metamaterial

Metamaterials are artificial composites with carefully designed microstructures that lead to unusual physical properties (Kadic et al., 2019). These properties are largely defined by the microarchitecture of the metamaterial, rather than the based material. This concept was initially proposed for electromagnetic applications such as perfect lenses (Pendry, 2000), 'invisibility cloaks' (Schurig et al., 2006), super-directive antennas (Radkovskaya et al., 2018) and wireless power devices (Stevens, 2014). Today the functionality of metamaterials has extended towards many aspects of solids, ranging from optical, acoustic to mechanical properties. Most of these metamaterials have unique structures that designed for a specific goal.

Recent research provokes a new trend on the metamaterial design that incorporates tuneability and programmability. The tuneability is an ability for the material's properties to be tuned through deformation controlled by the embedded actuation or external stimuli. The programmability of a metamaterial requires the behaviour of materials to be adjustable through

the selection of design parameters. A recent branch known as mechanical metamaterial opens up a wide design space for tuneable and programmable material (Bertoldi et al., 2017). They are consisted of tailored structural cells that can buckle, deform or change their shapes and elastic energy in response to mechanical stimuli. Tuning the geometry of metamaterial structures can create novel mechanical properties include negative Poisson's ratio, negative elasticity and negative compressibility (Zadpoor, 2016), cause frequency shifts and loss changes in electromagnetic waves (Nauroze et al., 2018), and induce anisotropy and chirality property for tuneable photonic application (Frenzel et al., 2017; Jiang and Li, 2018). These advances enable an unprecedented level of flexibility of the metamaterial properties, making them ideal for multi-functional and multi-task applications (Zhu et al. 2017).

2.1.1 Construction method

The structural design of unit cells is crucial for the reconfigurability of mechanical metamaterials. Generally speaking, the design of unit cells can be categorized into the following strategies:

1) Foam-like auxetic materials

Many natural materials with a cellular structure, such as honeycomb with planar packing cells or foam-like sponge with a spatial array of polyhedral cells, have high stiff-to-weight ratio, low thermal conductivity or advantages in energy absorption (Gibson, 2005). While the mechanical features of most natural materials span a limited range, it is desirable to design auxetic materials that can avoid the weakness of natural materials and exhibit a chosen set of physical properties. Auxetic cellular solids are the most widely studied mechanical metamaterial (Evans and Alderson, 2000; Yang et al., 2004). In 1987, Lakes discovered the first negative Poisson's ratio polyurethane (PU) foam using re-entrant structures (Lakes 1987). Since then, the study on auxetic materials has held a major interest. The researches mainly focus on designing new

structures using tessellation and deployable mechanisms, and on manufacturing the metamaterial in micro- or nano- scale. For instance, the micro-lattice structures shown in Figure 2.1 are comprised of regular space-filling structures that evolved from the honeycomb and Kevin foam. The porous samples are manufactured by the projection of micro-stereolithography, a layer-by-layer additive micro-manufacturing technology. Micro-lattice materials can be ultra-light, ultra-strong or capable of large-scale deformation (Schaedler et al., 2011; Bauer et al., 2014), and these features are valuable in applications such as robust shock absorbers in automotive fields (Schaedler et al., 2014) fasteners, body armors and aerospace (Valdevit et al., 2011).

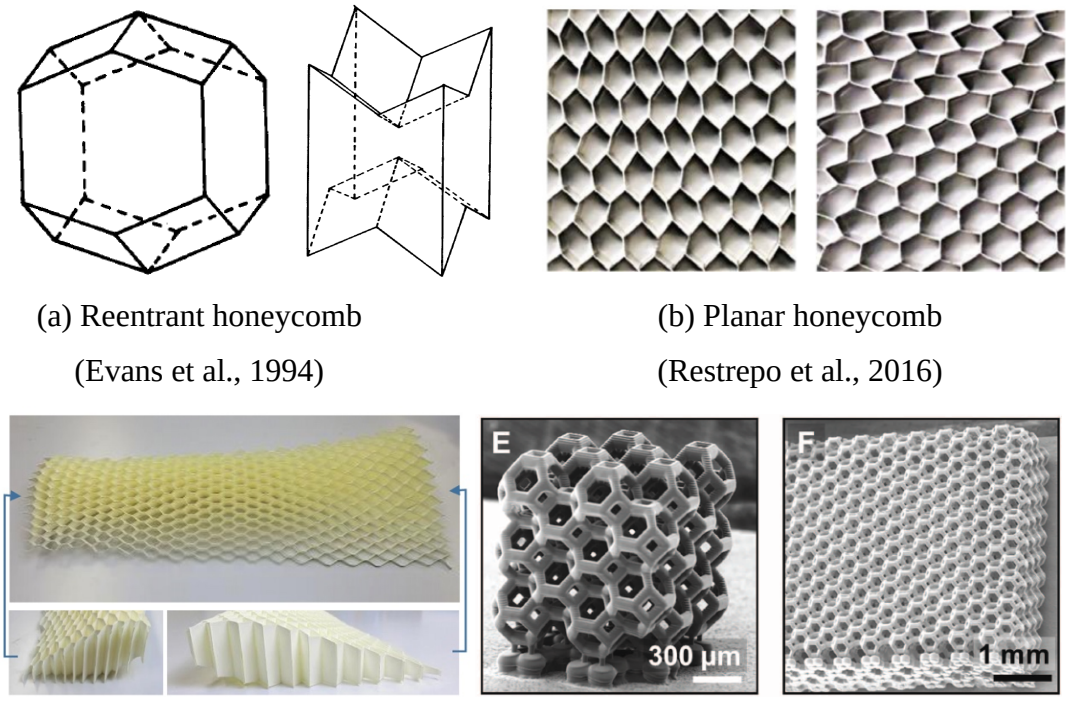

(a) Reentrant honeycomb (Evans et al., 1994)

(b) Planar honeycomb (Restrepo et al., 2016)

(c) 3D honeycomb aircraft wing (Saito et al., 2016)

(d) Micro-lattices of Kevin foam (Zheng et al., 2014)

Figure 2.1 Micro-lattice honeycomb metamaterials.

2) Instability-based metamaterial

Specially designed slender elements can generate large deformations under small external forces, leading to strong geometric nonlinearities. These materials are known as buckling-

induced metamaterials. A typical example of buckling-based metamaterial is an elastomer sheet embedded with circular holes, shown in Figure 2.2 (Mullin et al., 2007; Bertoldi et al., 2010; Zhang et al., 2008). The structure can be regarded as an array of rigid blocks connected by slender ligaments. When applied with uniaxial load, the ligaments tend to buckle, leading to the transformation of rigid blocks, and the holes will shrink correspondingly. The transformation of the rigid blocks follows the rules of hinged square mechanism, while the ligaments deformation follows the mechanical behaviour of beam elements. This transformation is reversible and repeatable. The structures will recover to the initial configuration when external load is removed. The slender ligament design is widely used in mechanical metamaterials, including materials with negative Poisson's ratio (Babaee et al., 2013), negative swelling ratio (Liu et al., 2016), switchable chirality (Kang et al., 2013), meaning the handedness property of the material pattern can be tuned by the deformation. The transformation of buckling induced metamaterials is also applied in photonic metamaterials (Bertoldi and Boyce, 2008) and colour displays (Li et al., 2012).

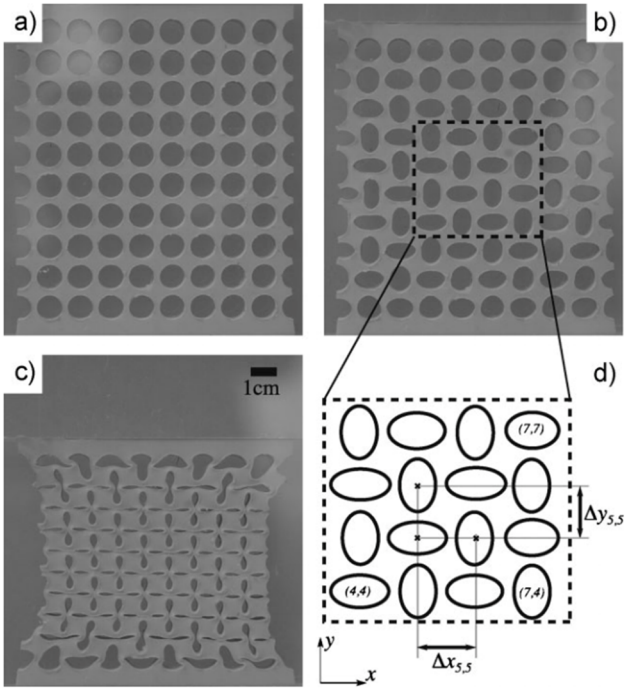

Figure 2.2 A buckling-induced metamaterial with circular holes (Bertoldi et al., 2010).

Another branch of instability-based metamaterials is bistable materials (Figure 2.3). Some elastic structures can perform a rapid, irreversible snap-through behaviour. The phenomenon exists because the geometry of the metamaterial unit cell is designed in such a way that it favours several stable states with lowest elastic energy. The metamaterial tends to lock in its stable states and will not recover to the initial state after unloading (Fargette et al., 2014; Pandey et al., 2014). Because of this energy absorption ability, these designs are widely used in energy-trapping metamaterials (Figure 2.3(a)) (Haghpanah et al., 2016; Shan et al., 2015). Moreover, the bistable unit cells are used to construct 'mechanical logic gate' (Ion et al., 2017). For example, in Figure 2.3(b), the behaviour of the programmable metamaterial is tuned by the combined configuration of its bistable unit cells. Programmable metamaterials can pass the message of external load through deformation or adapt itself to various environmental stimuli.

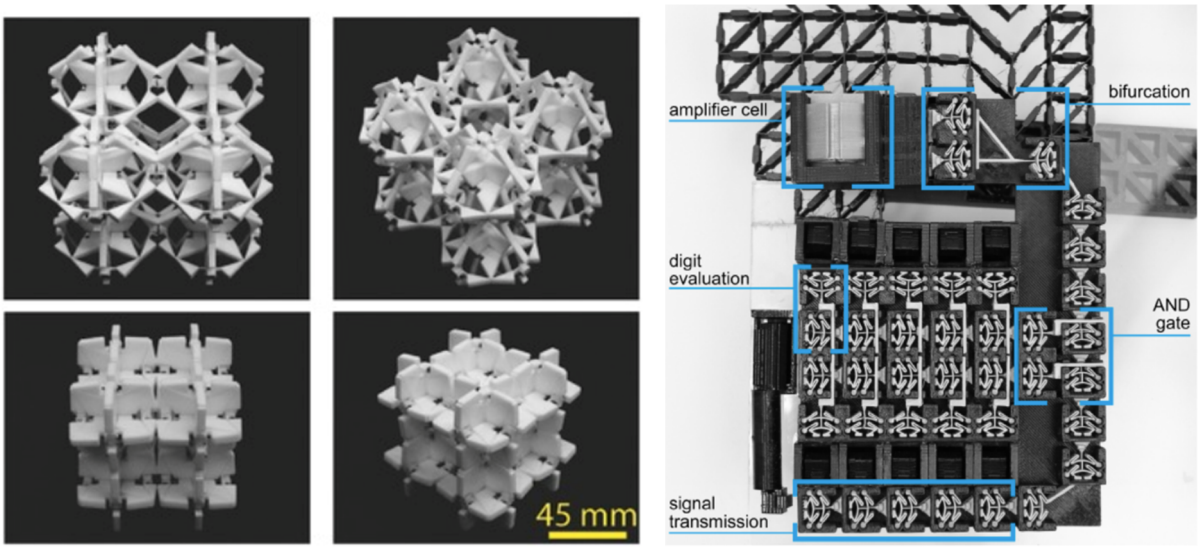

(a) 3D multistable metamaterials (Haghpanah et al., 2016)

(b) Metamaterial door lock (Ion et al., 2017)

Figure 2.3 Multistable architected materials.

The design of mechanical logic gate leads to more advanced architected materials with aperiodic patterns. Most current mechanical metamaterials are constructed in a periodic tessellation; however, more complex metamaterials require aperiodic patterns so that they can

vary their functions in different positions or transform to arbitrary shapes. Figure 2.4(a) shows elastic textures with unit cells in different stiffness (Panetta et al., 2015). With a combinatorial design from shape optimization, the deformation rate for different part of the metamaterial is tuneable upon compression. Therefore, the material can present a smiley face or crying face. Figure 2.4(b) is a 3D textured mechanical metamaterial (Coulais et al., 2016). Researchers designed a series of buckling-induced cubic building blocks that can deform anisotropically.

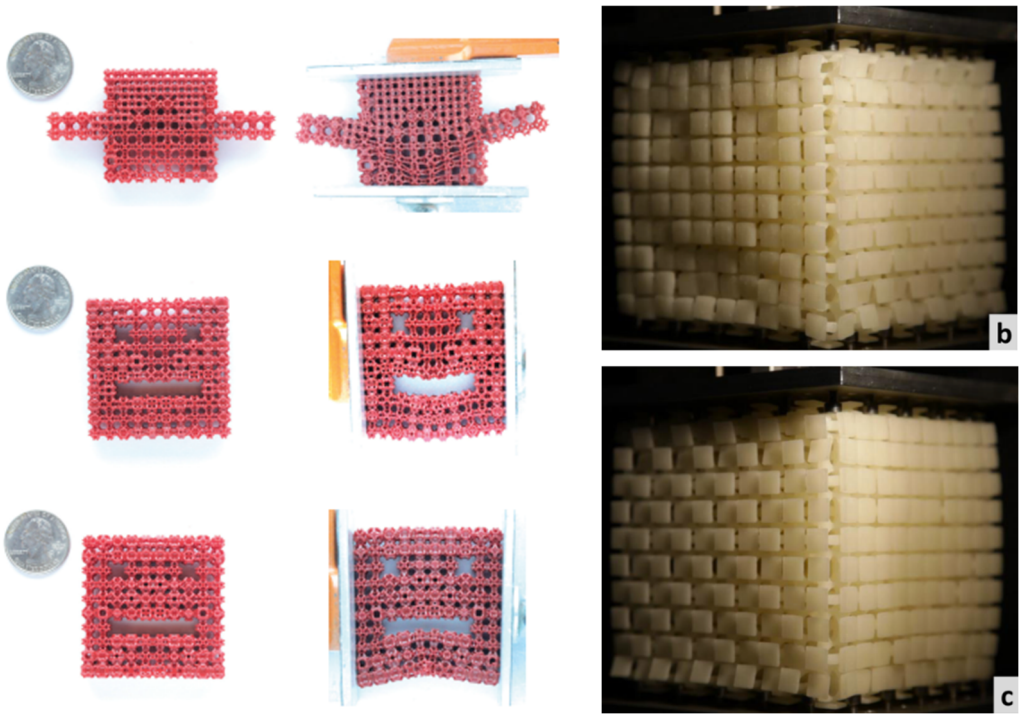

(a) Elastic textures (Panetta et al., 2015)

(b)Voxelated metamaterial (Coulais et al., 2016)

Figure 2.4 Buckling-induced aperiodic metamaterials.

3) Mechanism-based metamaterial

Kinematic mechanisms are assemblies of rigid bodies linked by flexible hinges following a specific arrangement, and they are able to perform predictable zero-energy motion. By designing the geometry of connection position and direction, the mechanism can perform different transformations. It is an efficient tool for the construction and analysis of shape-

morphing metamaterials. A typical example is the hinged square mechanism (Figure 2.5(a)). The rigid square panels are hinged at the corner to form an auxetic planar structure. The parallelogram void between four adjacent squares functions as a planar four-bar linkage. During transformation, the void will be distorted and gradually disappear, and the structure can uniformly contract into a solid panel or expand to a porous grid. This design inspired a large number of mechanical metamaterials (Mullin et al., 2007; Coulais et al., 2015; Overvelde et al., 2012; Tang et al., 2015; Yang and You, 2018). More complex mechanism motions are designed to program the internal microstructure of 3D printed metamaterials (Ion et al., 2016). With embedded interlinked planar linkages, the metamaterial in Figure 2.5(b) can deform in a well-defined way to achieve particular macroscopic movement, such as a door latch or walking robot. A similar aperiodic design named Kinetix can deform into a folding box or a helmet (Ou et al., 2018).

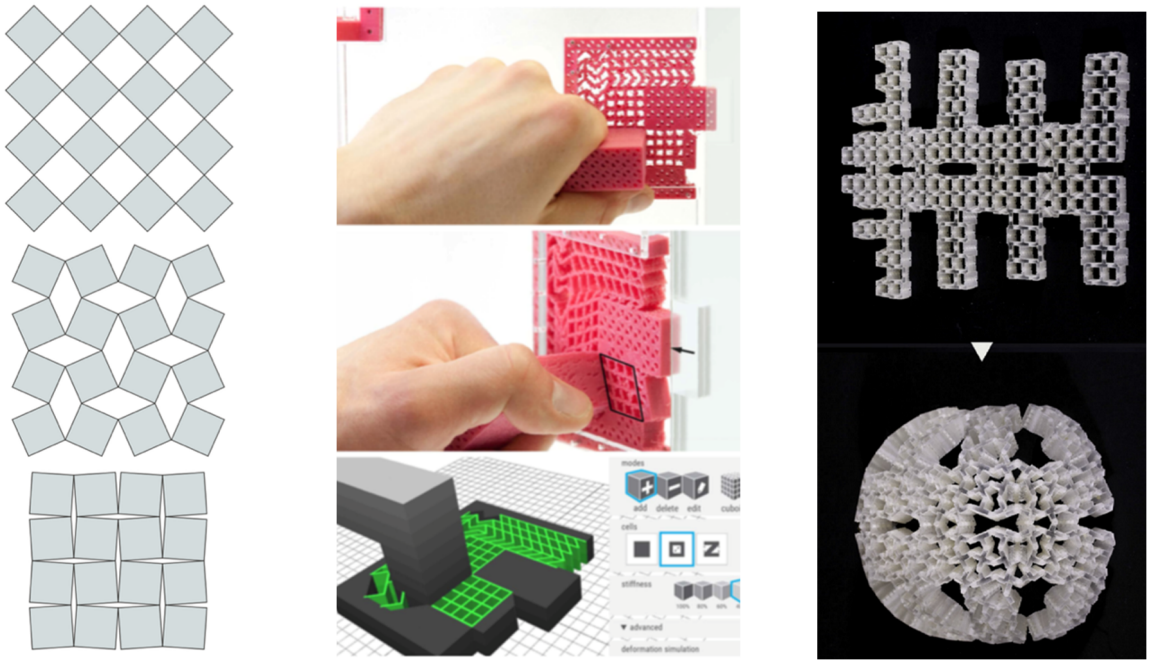

(a) Hinged squares (b) Metamaterial door latch (Ion et al., 2016) (c) Metamaterial helmet (Ou et al., 2018)

Figure 2.5 Hinged square mechanism induced mechanical metamaterials.

An important branch of mechanism-induced metamaterial is origami and kirigami inspired structures (Figure 2.6). In Japanese, ‘ori’ means fold, ‘kiri’ is cut, and ‘kami’ is paper. These paper arts have long been inspiring for engineering applications, such as deployable structure (Miura, 1985), flexible medical stents (Kuribayashi et al., 2006) and expandable solar panels (Badagavi and Chinta, 2017). In recent years, origami, particularly rigid origami that does not cause deformation during the transformation, are utilized for constructing metamaterials, ranging from 2D sheets with pre-defined crease patterns (Tachi and Miura, 2012; Wei et al., 2013) to 3D packing of 2D sheets (Schenk and Guest, 2013) and 3D cellular metamaterials (Overvelde, 2016). The most famous patterns include Miura-ori structure (Lv et al., 2014; Dudte et al., 2016; Silverberg et al., 2014), square twist (Silverberg et al., 2015), waterbomb (Chen et al., 2016) and box-pleat tiling (Hawkes et al., 2010). These patterns can be tuned to fold into different shapes by carefully designing the angle and geometry of the creases. Moreover, people have further studied the bending energy of the creases to produce multi-stable and programmable metamaterials (Coulais et al., 2018).

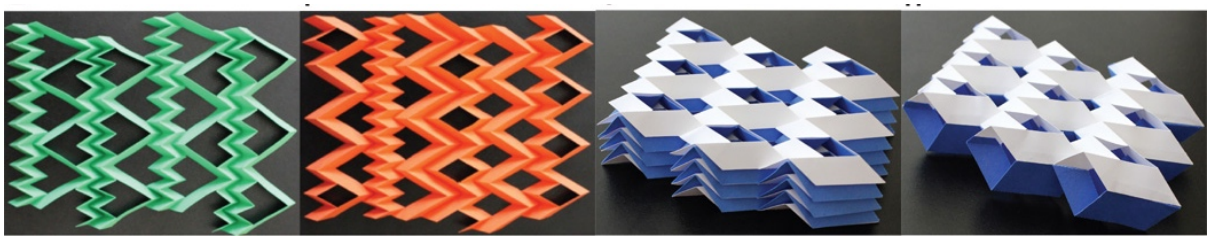

(a) Multi-layer miura-ori metamaterial (Eidini and Paulino, 2015)

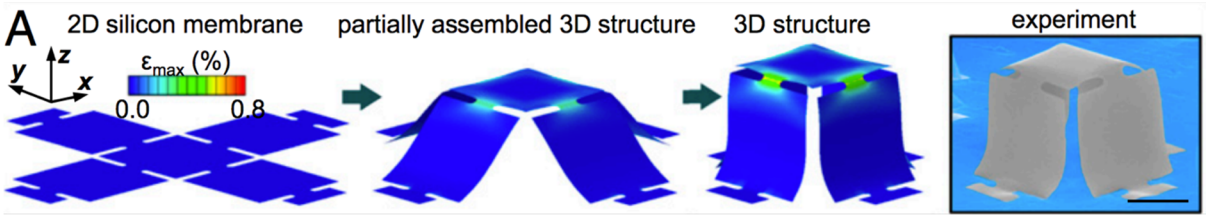

(b) Kirigami nanomembrane (Zhang et al., 2015)

Figure 2.6 Origami and kirigami inspired metamaterials.

The kirigami metamaterials introduce arrays of cuts into the sheet material, which allows extremely large deformation (Gatt et al., 2015). It is widely used in reconfigurable graphene sheets (Blees et al., 2015), nanomembranes (Zhang et al., 2015), flexible electronics (Zhu et al., 2017) and stretchable lithium-ion batteries (Song et al., 2015). By combining origami and kirigami arts, researchers further expand the design space and generate more complex reconfigurable structures (Eidini and Paulino, 2015; Sussman et al., 2015).

A tricky issue in mechanism-based metamaterial is that the perfect mechanism performs zero-energy motion, while in reality, the bending of a thin ligament does not function as a mechanical hinge, and there is an energy cost to realize reconfiguration. To tackle with this issue, some researchers have proposed a compliant rolling-contact architected material (Shaw et al., 2018). The design utilized flexure straps to guide the rolling motions of rigid cams rather than buckle the slender beam to achieve shape morphing, enabling the metamaterial to have large deformation without notably increasing the strain energy of internal stress.

4) Other construction methods

Bio-inspired structural cell is another construction method for mechanical metamaterials. For instance, researchers gain inspiration from glass sponges with regular circular beam structure, which is beneficial for its structural and hydrodynamic performances (Figure 2.7(a)) (Bauer et al., 2014). Materials with similar reinforced beam structures can resist buckling better without compromising stiffness. A drawback of bio-inspired structures is that most researches are case-by-case study, and it is difficult to generalize the construction method.

Mathematicians tried to tackle the problem from pure uniform tessellations in 3D space (Conway et al., 2001). Current works include the Bucklicrystals, which follows the finding that cubic crystal system pattern can generate auxetic behaviour through elastic buckling (Babaee et al., 2013) (Figure 2.7(b)). This study on crystal framework can also be applied in

micro-lattice design (Borcea and Streinu, 2014). Moreover, topological optimization has been used to further analysis and improve the performance of the proposed structures.

Machine learning approach is recently tried in the metamaterial field and is getting popular in the 2D material construction (Wilt et al., 2020). To overcome the challenges of limited number of design and the dependence on designer's prior experiences, researchers have used the GAN (generative adversarial networks) model to generate 2D patterns that can achieve certain configuration or properties (An et al., 2019). The future work for machine learning-based metamaterial lies in solving the problem of small data learning problem and using it in more complex structures.

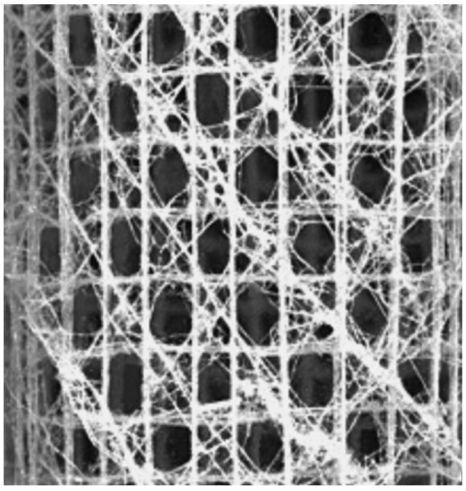

(a) Glass sponge for bio-inspired metamaterials

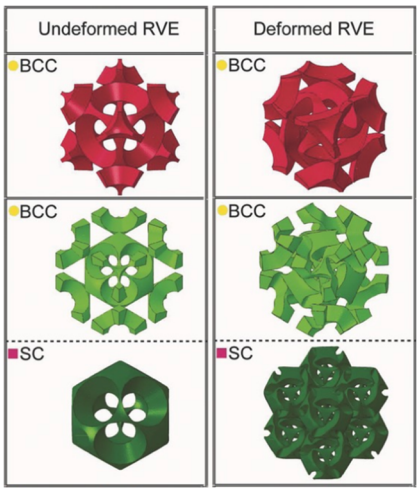

(b) Bucklicrystal from crystal systems (Babaee et al., 2013)

Figure 2.7 Other construction methods.

2.1.2 Rigid origami/kirigami inspired metamaterial

As briefly introduced in the mechanism-based construction method in the previous section, origami and kirigami structures emerge as important inspirations in mechanical metamaterial for their great deformation capacity. As the focus of this thesis is mainly related to rigid origami-inspired kinematic metamaterials, further introduction on this construction method

will be provided in this section. The foldability of rigid origami can be modelled kinematically using linkage mechanisms. The strengths of kinematic construction method include:

1) Compared to instability-based deformation, the kinematic motions of rigid origami structures require little energy to generate, which extends the tuning range of shape morphing and metamaterial stiffness.

2) Origami structures with bifurcation features can be used to construct metamaterials with multiple deformation paths, each with a different final configuration.

3) One can combine different origami cells together using linkage mechanisms to switch the metamaterial from one irregular shape to another, which produces new mechanical features;

4) Because of the scale-free geometric character of origami, the structures can be realized in micro- and nano- scale for reconfigurable microsurgery tools or manufactured in the meter-scale to build transformable architecture material.

Some current researches are illustrated in the following. To date, most origami-inspired mechanical metamaterials use a pattern known as the Miura-ori (Figure 2.8(a)). This is a one degree-of-freedom (DOF) mechanism, and we can stack layers of Miura-ori in a synchronized pattern. One focus of Miura-ori metamaterial is on designing the angles of its crease patterns so as to activate different stiffness, locking and pop-through features. For instance, Silverberg et al. created a pop-through defect on a partially folded Miura-ori by using localized reversed unit cell (Silverberg et al., 2014). In such a case, the compressive stiffness can be tuned by the number and location of such defects. Another focus is on designing Miura-ori tubes as the building blocks and linking them to form cellular solids or cylindrical materials as shown in Figure 2.8(b) (Filipov et al., 2015; Cheung et al., 2014). Tomohiro et al. proposed a series of Miura-ori tube metamaterial and manufactured samples using 3D printing (Cheung et al. 2014). Despite this, the material printed by plastic cannot deploy flexibly as the kinematic model.

Another weakness of Miura-ori packing is that most bistable features and local defect designs are limited to surfaces made from a single sheet. The compatibility of layered Miura-ori prevents the metamaterial from forming local deformation.

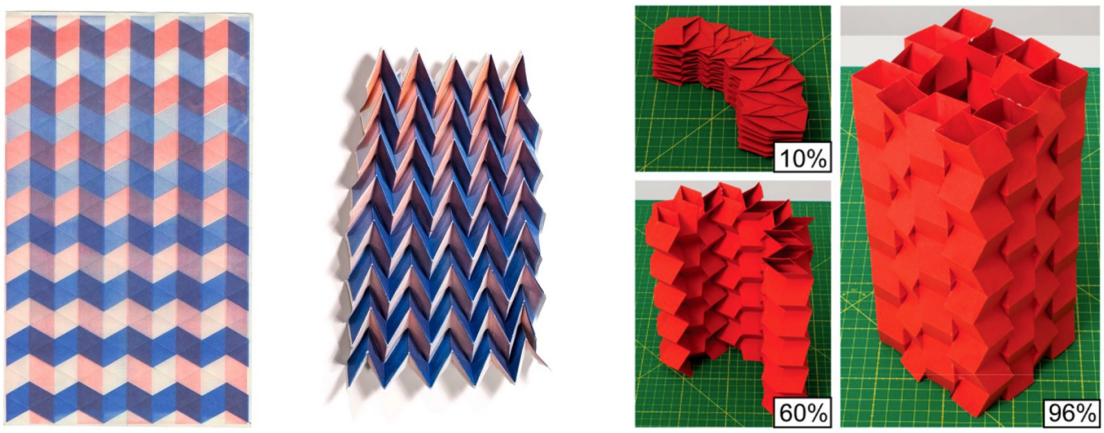

(a) Miura-ori pattern

(b) Cellular assembly of Miura-ori (Filipov et al., 2015)

Figure 2.8 Miura-ori based mechanical metamaterial.

This lack of configuration is made up by another metamaterial study inspired by snapology, a type of modular origami (Overvelde et al., 2016; Overvelde et al., 2017). Snapology uses paper ribbons to create complex extruded polygons and links them together to form one assembly. As shown in Figure 2.9, Johannes et al. presented a series of 3-DOF transformable metamaterial with periodic structures. Firstly, the extruded cubes are used to form origami units; then, the units are connected according to a space-filling tessellation. The metamaterial is fabricated and tested to show its ability of deformation into numerous specific shapes through embedded actuation. One potential application for guiding and radiating acoustic energy along predefined directions is discussed (Babaee et al., 2016).

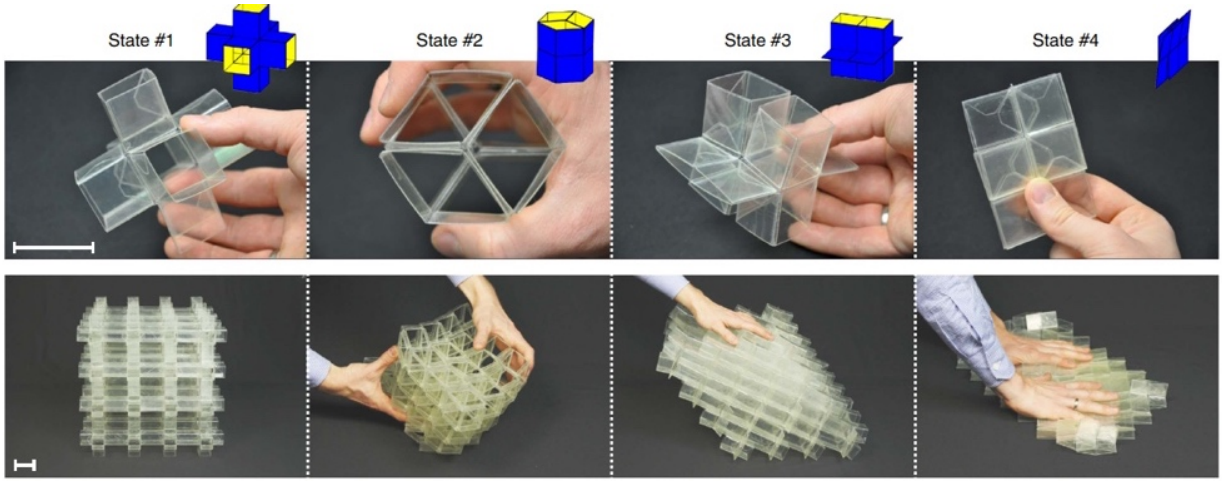

Figure 2.9 Reconfigurable snapology inspired metamaterials (Overvelde et al., 2016).

Kirigami structures also bring about numerous metamaterial designs (Figure 2.10). Most kirigami studies investigate planar patterns made out of a single sheet. For instance, Robin et al. proposed a one-layer shape morphing kirigami metamaterial (Neville et al., 2016), and Tang et al. studied a series of planar kirigami metamaterial with tiling patterns (Tang et al., 2017). A few pieces of research have tried to design 3D kirigami reentrant cells and connect them in a grid pattern: Ruikang et al. and Ahmad et al. presented several kirigami-inspired 3D folding patterns that can transform from single-layer structures (Xie et al., 2015; Rafsanjani and Bertoldi, 2017). Nan et al. suggested a design strategy combining modular origami and kirigami for mechanical metamaterial (Yang and Silverberg, 2017). By varying the module parameters, the metamaterial is able to form various topological shape. The design of aperiodic kirigami pattern becomes increasingly popular due to the demand of designing arbitrary shape and programming the material properties at different positions (Celli et al., 2018; Konaković-Luković et al., 2018). As shown in Figure 2.10(c), by combining different kirigami cells, the metamaterial deforms into an arbitrary 3D shape according to the arrangement of its pattern. This can be an inspiring direction of next-generation programmable smart materials.

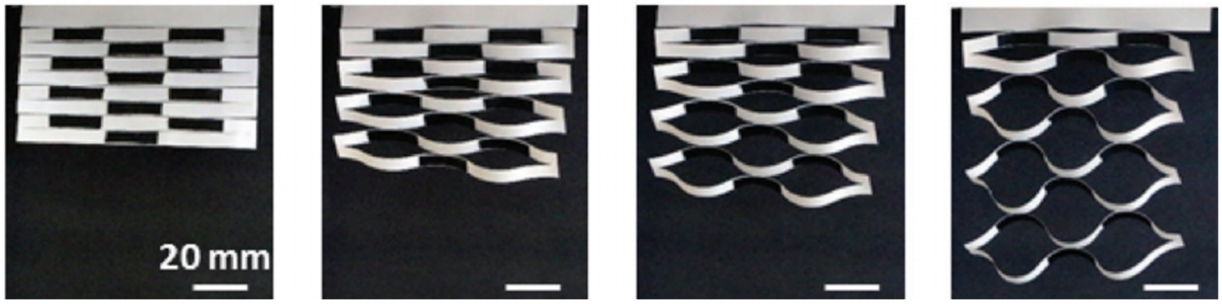

(a) Out of plane deformation of planar kirigami sheet (Tang et al., 2017).

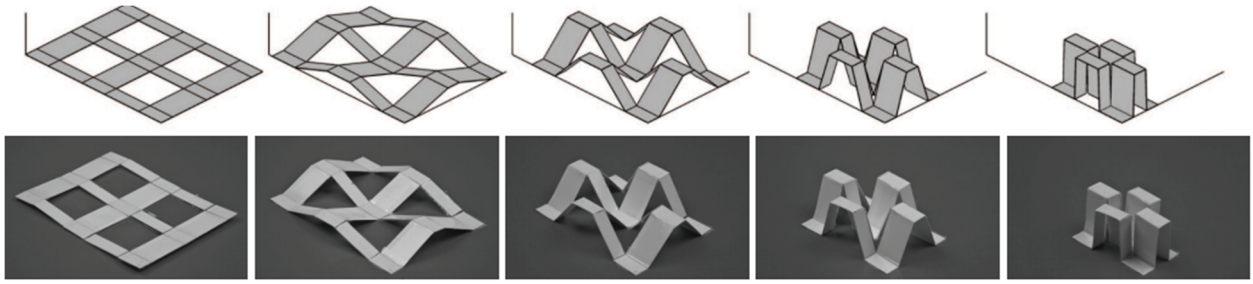

(b) 3D folding of kirigami pattern (Xie et al., 2015).

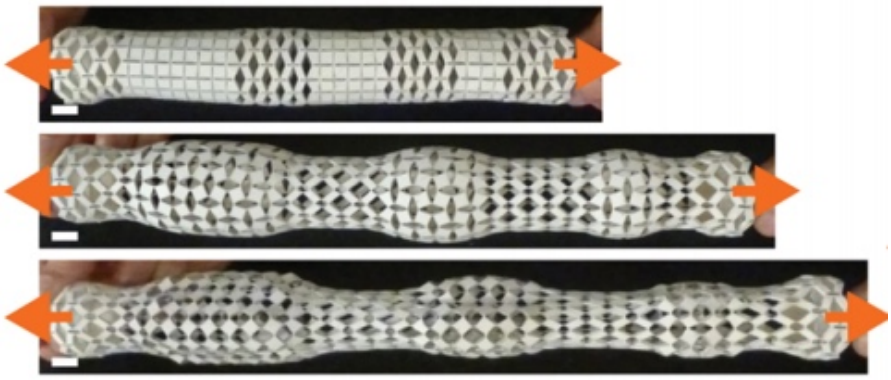

(c) Non-periodic kirigami cut pattern (Celli et al., 2018).

Figure 2.10 Kirigami metamaterials.

In conclusion, to construct rigid origami/kirigami metamaterial in multi-layers with tuneable configurations and programmable mechanical properties, a thorough study on more origami structures, spatial kinematic mechanisms, and tiling patterns for unit arrangement is needed. These will be introduced in the section 2.2-2.4.

2.1.3 Multi-functional metamaterials

The reconfiguration of mechanical metamaterials not only produces novel mechanical properties, but also influences other physical properties. When the dimension of structural cell is much smaller than the wavelength, the metamaterial can be treated as a homogeneous media with effective parameters. This leads to the studies of negative index metamaterials. When the dimension of the unit cell is rather large, other theories should be applied to understand mechanical wave propagation. The geometry of mechanical metamaterial is critical in determining its physical properties, and various multifunctional metamaterials have been developed. Categorized by the length scale, there are acoustic, electromagnetic and photonic metamaterials.

1) Acoustic metamaterial

Acoustic metamaterials are designed to manipulate the propagation of sound waves. Band gaps can be designed and tuned through generating local resonance in a structural cell. Unique tuneable acoustic properties such as cloaking (Cheng et al., 2008; Chen and Chan, 2007) and superlens (Ambati et al., 2007) have been demonstrated building on this concept.

Changing the geometry dynamically to control the bandgaps leads to a number of tuneable acoustic metamaterials (Babaee et al., 2016; Benouhiba et al., 2017). As shown in Figure 2.11(a), the buckling of connection beams changes the stiffness and the natural frequency of the unit cell structure, leading to a shift of resonance frequency (Wang et al., 2014). The acoustic band gap decreases under compression of the material, and further splits and closes due to the rotation mode.

2) Electromagnetic metamaterial

Electromagnetic metamaterials tailor the electric and magnetic response of materials by negative permittivity and permeability. A typical example of tuneable electromagnetic material

is shown in Figure 2.11(b) (Tao et al., 2009). The split Au rings create resonant LC circuits that can generate large local magnetic dipole moments. Placing the split ring in a periodic pattern leads to a large positive magnetic permeability. In this example, the unit cells are attached to a temperature-responsive substrate through cantilever legs. When apply thermal stimuli, the unit cells perform out-of-plane deformation and create a dynamic electric and magnetic response. Mechanical stimuli can also be exploited to tune the electromagnetic metamaterials. In a pre-stretch substrate method, the metallic honeycomb frames can form a wavy surface. During the release of the pre-stretch film, the orientation and geometry shape of the honeycomb will change, which leads to three additional split resonant modes (Lee et al., 2012). The Buckliball with six circular holes and metallic insertion in a sphere unit cell is explored for its electromagnetic performance (Zárate et al., 2016). The axial compression causes structural instability of the buckliball, leading to an increased structural chirality and circular dichroism.

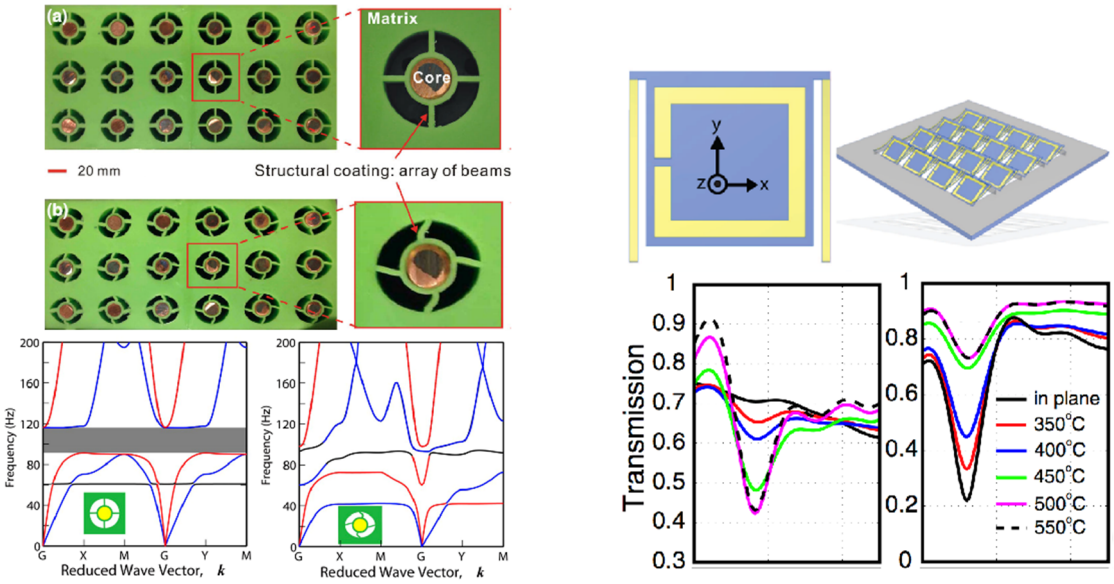

(a)Tuneable acoustic metamaterial (Wang et al., 2014)

(b) Electromagnetic metamaterial (Tao et al., 2009)

Figure 2.11 Tuneable acoustic and electromagnetic metamaterials.

3) Photonic metamaterial

The photonic metamaterial exhibits desired transmission and reflection spectra. The modulation of its chirality can be used for tuning light polarization. For instance, the gold helices structures arranged in a square tiling pattern are capable of blocking circular polarized light while transmitting the others over a broad frequency range (Figure 2.12(a)) (Gansel et al., 2009). Flexible photonic metamaterials can be manufactured by coating nano-gating structures with Au particles immersed colloids on the unit cells (Zhang et al., 2014). To dynamically tune its photonic performance, researchers create spatial variation in temperature to trigger non-uniform deformation at the interface. The reconfigurable unit cells bend according to temperature changes, leading to an increased transmission in higher temperature.

4) Stretchable electronics

Reconfigurable structures provide new methods to enable brittle metal materials with stretchable properties. As shown in Figure 2.12(b), a widely used method is to laminate a film into a pre-stretched soft elastomer (Sun et al., 2006; Cheng et al., 2014). The release of the elastomer creates forces to deform the film into a wavy structure. Another strategy is inspired by origami and kirigami patterns. For instance, the polyethene terephthalate glycol modified (PETG) sheet is cut and folded into 3D solar cells (Lee et al., 2016). With dynamic tuning of the orientation angle according to the incident angle of light, the array of solar cells achieves a 450% increase in energy output. Origami patterns are also used in foldable lithium-ion batteries for their large expansion ratio (Song et al., 2014).

Kirigami patterns are widely used in flexible circuits (Xu et al., 2015, Figure 2.12(c)). Integrated systems incorporating various sensors, antenna, LED, and batteries can be fabricated in a soft skin-like film to attach to the human body (Kim et al., 2011). These types of multifunctional devices provide real-time assessment of individual health. Moreover, the

stretchable electronics can be used to design soft robots. Integrating micro flexible electronics into soft materials can improve the functionality of soft machines (Yoon et al., 2014; Morin et al., 2012 99 100).

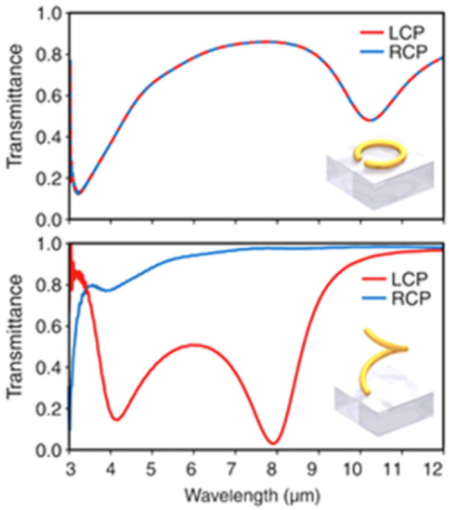

(a) Photonic metamaterial (Gansel et al., 2009)

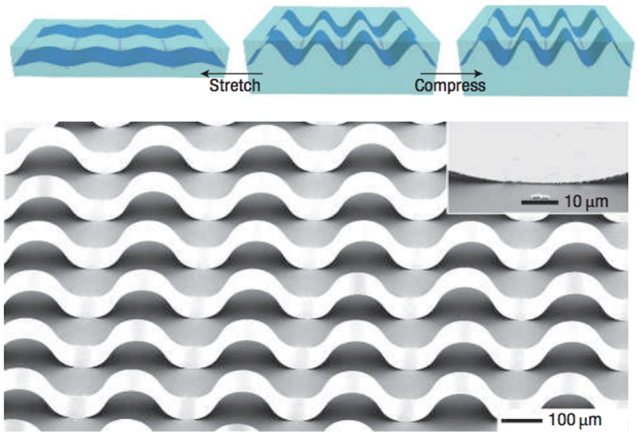

(b) Flexible electronics (Sun et al., 2006)

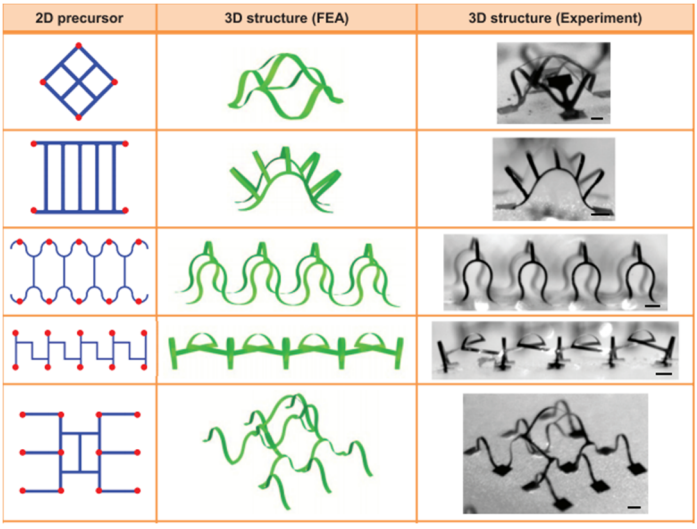

(c) Kirigami-inspired flexible circuit (Xu et al., 2015).

Figure 2.12 Tuneable photonic metamaterials and flexible electronics.

2.1.4 Manufacturing of metamaterials

1) Conventional manufacturing method

The manufacturing method and base material of the metamaterial can influence its mechanic properties dramatically. Traditionally, the auxetic honeycomb foams composed of reentrant

cells with dimensions greater than 1 mm are made by thermo-mechanical processing. The process consists of the compression of original open cell foam into a mould, the heating of the specimen above the softening edge of the foam material, and the cooling of the new structure (Yang et al., 2004). The composition material is usually metal because the honeycomb structure is widely used as sandwich panel cores. Numerous methods for fabricating metal structures using the solid, liquid or vapour phase have been developed. They can be categorized as either a stochastic or a periodic method (Wadley 2002; Wadley et al., 2003). A typical stochastic foaming method is to inject gas into a melt composition. Unlike other metal manufacturing, stochastic foaming is highly dynamic and sensitive to many process parameters. Because the pores generated are in random size and arrangements, this method is not suitable for mechanical metamaterial fabrication. Periodic method has many branches, such as investment casting, sheet crimping process, constructed trusses and metal textiles (Wadley et al., 2003). These manufacturing methods are mostly suitable for truss structures or uniform tiling materials that are packed by layers of metal sheets. The samples are usually used for bearing load or energy absorption, but they are not good at recoverable deformation.

2) Additive manufacturing

Additive manufacturing is a more suitable solution for structures undergoing recoverable deformation. The rapid prototyping technology is widely used for direct manufacturing of centimetre-scale parts, and the layer resolution of a desktop 3D printer can reach 0.1 mm (Castles et al., 2016; Pei et al., 2015). Caroline et al. fabricated a metamaterial inspired by butterfly gyroid using a Stratasys Polyjet 3D printer (Pouya et al., 2016). The principle of Polyjet printer is similar to inkjet printer: photopolymer drops feeds through a nozzle to a building tray. When exposed to UV light, the polymer solidifies and accumulates layer-by-layer according to the pre-sliced geometry pattern of the model. The layering process repeats to manufacture the whole part. The advantage of Polyjet over other 3D printers is that it has

many base material options, including flexible rubber-like materials that are ideal for printing living hinges. As Figure 2.13(a) shows, the metamaterial has complex microarchitecture which is difficult to fabricate by traditional manufacturing method, and the printed model can be compressed repetitively to perform deformation. Recently years, new multi-material Polyjet printers are able to allocate different materials at various positions (Tibbits 2014; Kokkinis et al., 2015; Ge et al., 2016). The Stratasys's Connex series provide multi-material printing with a large variety of material properties, such as different stiffness and colours. The materials share similar base resins, making it possible to bond one material with another. The limit of Polyjet 3D printing includes the scaling of parts: if the structure is too small, e.g., several millimetres or microns, it will be very difficult to remove the support materials, and the assembly is fragile because the scale of the unit cell is comparable to the layer thickness.

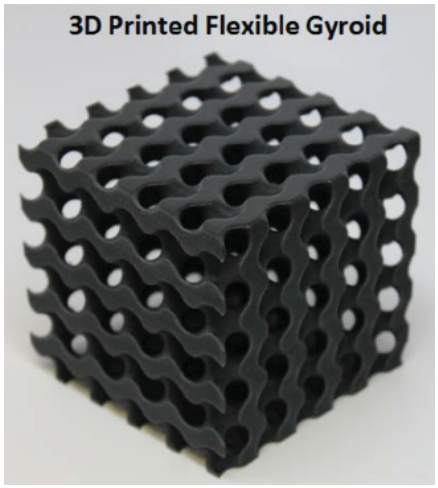

(a) 3D printed polymer gyroid (Pouya et al., 2016)

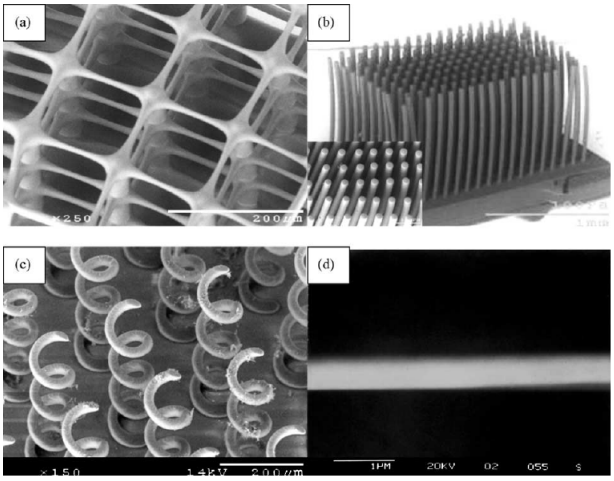

(b) Structures fabricated by PμSL (Sun et al., 2005)

Figure 2.13 Additive manufacturing of metamaterials.

Micro additive manufacturing methods with a higher accuracy such as x-ray lithography, deep UV, LIGA and soft lithography are used to build micro- or nano- structures. A common building process of micro-lattice is as follows: first, making polymer templates using a photo-polymerization process that involves an array of intersecting self-propagating waveguides (or

using direct laser writing (DLW) and two-photon lithography); then, thin-film materials are deposited, and the polymer template is removed by chemical etching (Jang et al., 2013; Maloney et al., 2013). These methods can build high-quality microstructures, but they are rather expensive due to the large quantity of sacrificial material. A new technology called Projection micro-stereolithography(PμSL) combines the high throughput capability of mask lithography with the design flexibility of serial processes (Figure 2.13(b))(Sun et al., 2005). An image corresponding to each layer is projected onto a monomer resin by UV light. This induces a polymerization reaction that transforms the liquid-state resin into a solid layer in the shape of the projected image. The polymerized layer is then lowered into the resin bath, and a new liquid resin layer is formed on top of the polymerized layer to be crosslinked into the identical shape. This process is repeated until the desired number of layers has been fabricated. Xiaoyu et al. introduced the design of projection micro-stereolithography system (PμSL) and showed that this is a straightforward method for micro-scale tetrakaidecahedron construction (Zheng et al., 2012). More varieties of photo-sensitive materials are yet to be developed, and the mechanical properties of the synthesis material are yet to be examined. In conclusion, these achievements pave the way for large scale micro- and nano- manufacturing.

3) Lamination

The proliferation of new technologies surrounding layering manufacturing such as Micro Electro-Mechanical Systems (MEMS), Smart Composite Micro-structures (SCM) and Printable robotics opens exciting opportunities to build origami-inspired mechanisms in a micro-scale. Lamination refers to the creation of mechanisms from primarily planar processes such as cutting and folding, and then laminating flat sheets of various materials together. Daniel et al. introduced the pop-up laminating process in detail (Aukes et al., 2014). Preparation includes definition of the various material additions, removal and lamination operations, and setting rules of physical constraints. A software suite called PopupCAD has been developed

for the design. The manufacturing process is as follows (Figure 2.14(a)): 1) layer cutting and surface preparation; 2) bulk material addition, which may include structural layers and flexible layers together to create kinematic joints; 3) selective material addition and component addition for complex layering design; 4) lamination, where thermoset adhesives are usually adopted; and 5) releasing cutting and scrap removal. Lamination manufacturing can create a variety of mechanical elements, including structural elements, living hinges, rigid connections, and springs. These mechanical elements are especially useful for origami structures that contains a number of flexible creases. Some flexible hinges built by self-folding materials can transform into complex 3D geometries under external stimuli. Flexible hinges also have a significant advantage over rods connected by rotational joints in micro-lattices structures, because the latter is challenging to fabricate in a very small scale. Laminated mechanisms cover a wide range of length scales from 'wood skin' architecture material (WOOD-SKIN, n.d.), self-assembled micro robots (Felton et al., 2013)(Figure 2.14(b)), to active origami by 4D printing (Ge et al., 2014; Zhao et al., 2017). The combination of lamination manufacturing and 3D printing is a promising method for future origami-inspired metamaterial construction.

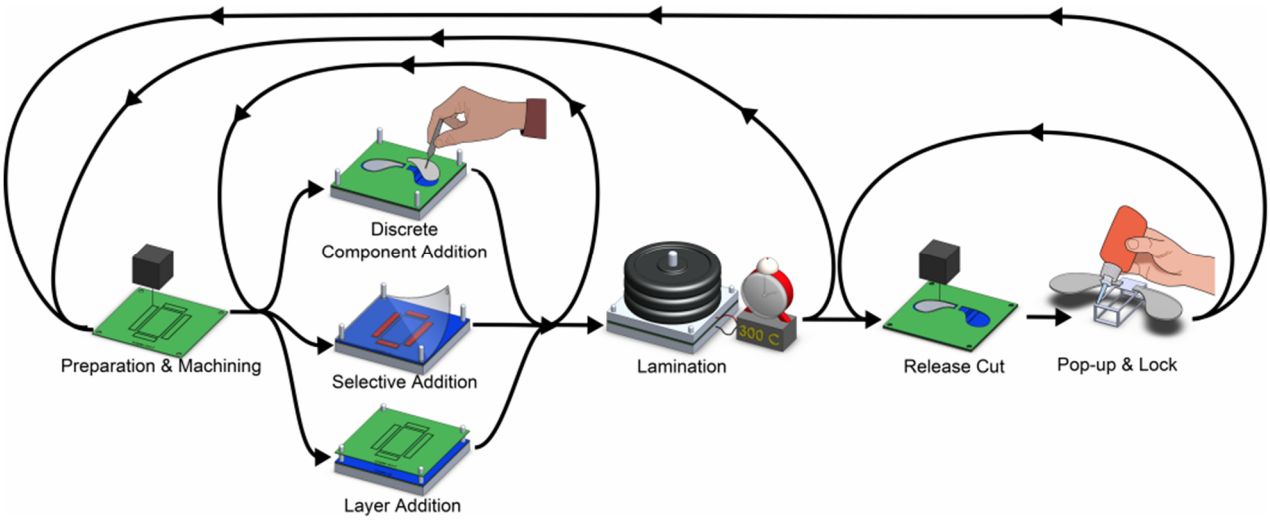

(a) The lamination process of a micro robot.

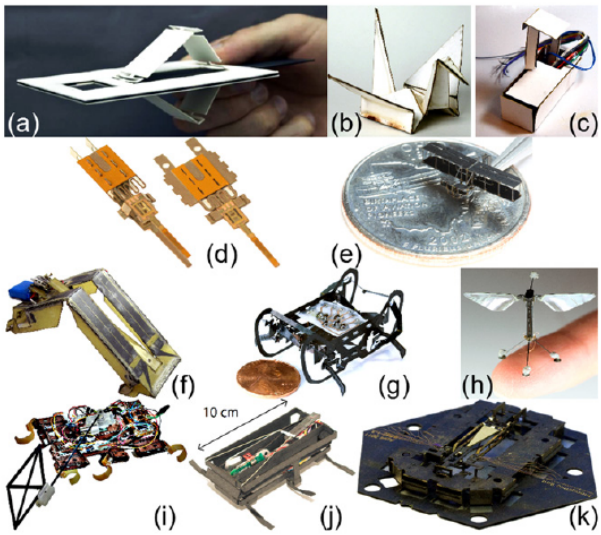

(b) Devices built by lamination.

Figure 2.14 Lamination manufacturing (Aukes et al. 2014).

2.2 Linkages and over-constrained linkages

2.2.1 Rigid origami modelling

Rigid origami is a type of deployable structure that does not cause deformation or creates new creases during the transformation. The transformation of rigid origami can be modelled kinematically by linkage mechanisms. A kinematic linkage refers to an assembly consisting of rigid bodies that are interlinked by lower pair joints, where direct contact between the surfaces of two rigid bodies happens at every point of the connection surface segments (You and Chen, 2011). If we assume the paper panels in a rigid origami as rigid bodies and the creases as revolute joints (*R*), the structure can be treated as a linkage. For a single vertex origami, the axes of the revolute joints meet at the vertex; therefore, the structure can be modelled as a spherical linkage (Figure 2.15). Spherical linkages are spatial mechanisms where the rigid bodies are constrained to rotate about the same fixed point. If the thickness of the origami panel is considered, the axes of revolute joints may not intersect at one point to form a spherical linkage. Under such circumstances, more complex spatial linkages are used to model the transformation. This will be introduced in the thick panel origami section later.

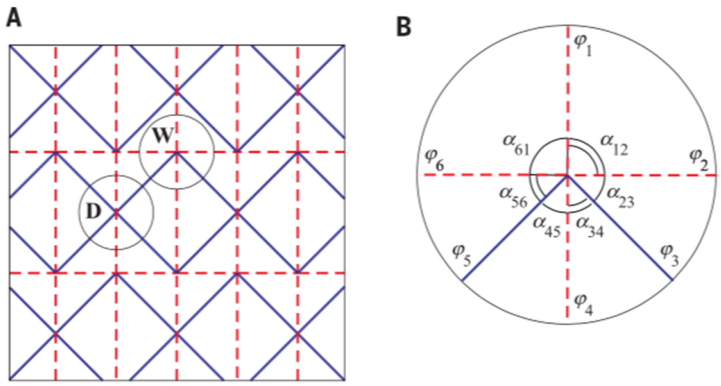

Figure 2.15 Rigid origami modelling of six-crease folding patterns (Chen et al., 2015).

2.2.2 Mobility of linkages

The number of degrees-of-freedom, also known as the mobility of a mechanism, is the number of input forces required to determine the position of all rigid bodies with respect to the ground. Given the number of links *n*, joints *j*, and the degree-of-freedom of each joint $f_i (i = 1, 2, ..., j)$, the mobility *m* can be calculated by the Grubler-Kutzbach mobility criterion (Hunt 1978):

$$m = 6(n - j - 1) + \sum_{i=1}^{j} f_i \tag{2.1}$$

Here we focus on linkages formed by *n* links connected by *n* hinges (also known as revolute joints where $f_i = 1$). Using Eq. (S1), it can be found that

$$m = n - 6 \tag{2.2}$$

In general, *n* must be greater than 6 to enable mobility. If *n* is less or equal to 6, the assembly is either a rigid structure or an overconstrained mechanism, a transformable mechanism where *m*, calculated using Eq. (S1), is less than 1 (You and Chen, 2011). The overconstrained mechanism exists usually under special geometrical conditions. Its motion can be analysed using the matrix method with the Denavit and Hartenberg notation (DH notation) (Beggs 1966). We illustrate the geometric features of two adjacent links in Figure 2.16. $a_{i(i+1)}$ is the length of

link $i(i+1)$, $\alpha_{i(i+1)}$ is the twist angle between joints i and $i+1$, R_i is the offset of joint i, and θ_i is the rotational angle of the linkage i. For a linkage consisting of n links in a loop, the closure equations are

$$\mathbf{T}_{12}\mathbf{T}_{23} \quad \mathbf{T}_{n1} = \mathbf{I}_4 \tag{2.3}$$

where $\mathbf{I}_4$ is the 4×4 unit matrix, and $\mathbf{T}_{i(i+1)}$ (i = 1, 2, …, n. If $i+1 > n$, it is replaced by 1) is the transformation matrix with the following form.

$$\mathbf{T}_{i(i+1)} = \begin{bmatrix} \cos\theta_i & \sin\theta_i & 0 & -a_{i(i+1)} \\ -\cos\alpha_{i(i+1)}\sin\theta_i & \cos\alpha_{i(i+1)}\cos\theta_i & \sin\alpha_{i(i+1)} & -R_i\sin\alpha_{i(i+1)} \\ \sin\alpha_{i(i+1)}\sin\theta_i & -\sin\alpha_{i(i+1)}\cos\theta_i & \cos\alpha_{i(i+1)} & -R_i\cos\alpha_{i(i+1)} \\ 0 & 0 & 0 & 1 \end{bmatrix} \tag{2.4}$$

If one of the kinematic variables θ_i can change freely while the others always fulfil the Eq. (2.3), the linkage has mobility one.

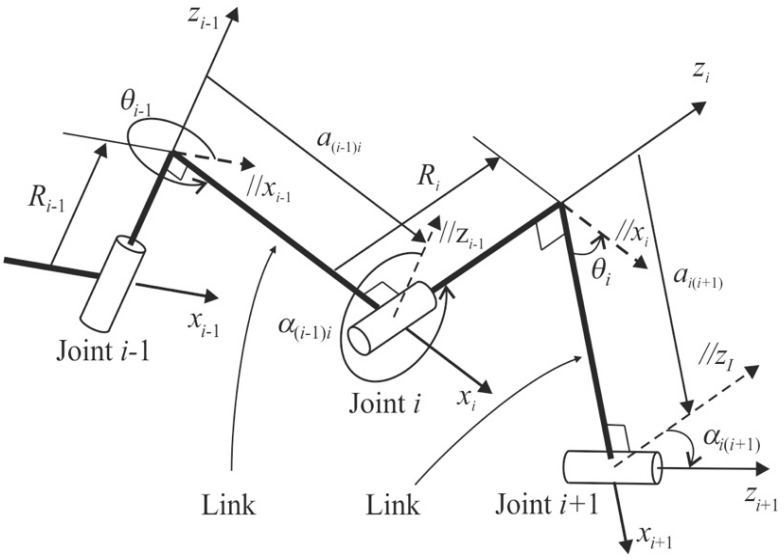

Figure 2.16 Coordinate systems for the links connected by revolute joints.

2.2.3 Overconstrained linkages

1) The Sarrus Linkage

The first published overconstrained mechanism was presented by Pierre Frédéric Sarrus (Sarrus, 1853). It is a six-bar mechanism linked by two sets of parallel hinges, and the direction of the two sets of hinges must be different. As shown in Figure 2.17(a), joints 1, 2, 3 and 4, 5, 6 are parallel to each other while the two sets are not parallel. Joints 3,4 and joints 6,1 are in the same plane. Under these conditions, the Sarrus linkage can perform a rectilinear motion with respect to the base link 3 and 4. Its geometric conditions are as follows:

$$\begin{gathered}\alpha_{12}=\alpha_{23}=\alpha_{45}=\alpha_{56}=0,\ \alpha_{34}=\alpha_{61}\ (\alpha_{34}\neq 0,\pi,2\pi),\\ a_{12}=a_{23}=a_{45}=a_{56}=a,\ a_{34}=a_{61}=0.\end{gathered} \tag{2.5}$$

Two sets of solutions can be obtained using Eq. (2.4), which are

$$\theta_1=-\frac{\theta_5}{2},\ \theta_2=\theta_5,\ \theta_3=\theta_1-\pi,\ \theta_4=\theta_1,\ \theta_6=\theta_3, \tag{2.6}$$

and

$$\theta_1=\frac{\theta_5}{2},\ \theta_2=2\pi-\theta_5,\ \theta_3=\pi-\theta_1,\ \theta_4=\theta_1,\ \theta_6=\pi-\theta_1. \tag{2.7}$$

This indicates that the Sarrus linkage has a bifurcation point when $\theta_2 = \theta_5 = \pi$.

2) The Bennett Linkage

The Bennett linkage is an exception of common 4*R* linkages (Figure 2.17(b)). It is a skewed linkage where the four bars have axes of revolute joints that neither parallel nor concurrent (Bennett 1903). There are three geometric conditions to construct a Bennett linkage:

Two links with the same length and the same twist, i.e.

$$a_{12}=a_{34}=a, a_{23}=a_{41}=b \tag{2.6}$$

$$\alpha_{12}=\alpha_{34}=\alpha, \alpha_{23}=\alpha_{41}=\beta \tag{2.7}$$

Lengths and twists should satisfy the condition

$$\frac{\sin\alpha}{a}=\frac{\sin\beta}{b} \tag{2.8}$$

Offsets are zero, i.e.,

$$R_i=0(i=1,2,3,4) \tag{2.9}$$

Furthermore, the angles should satisfy the following conditions during the motion:

$$\theta_1+\theta_3=2\pi,\theta_2+\theta_4=2\pi$$

$$\tan\frac{\theta_1}{2}\tan\frac{\theta_2}{2}=\frac{\sin\frac{1}{2}(\alpha_{23}+\alpha_{12})}{\sin\frac{1}{2}(\alpha_{23}-\alpha_{12})} \tag{2.10}$$

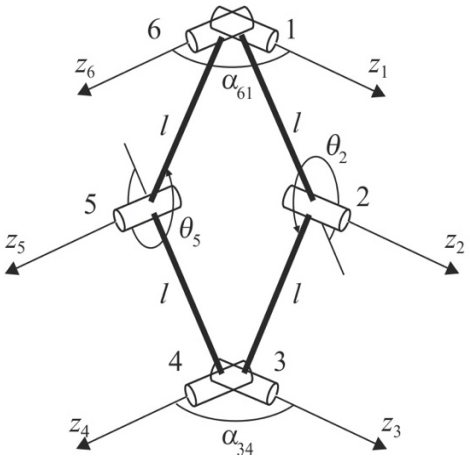

(a) The Sarrus linkage

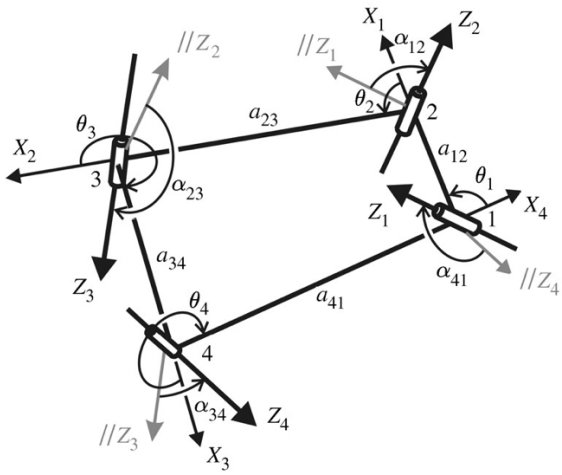

(b) The Bennett linkage

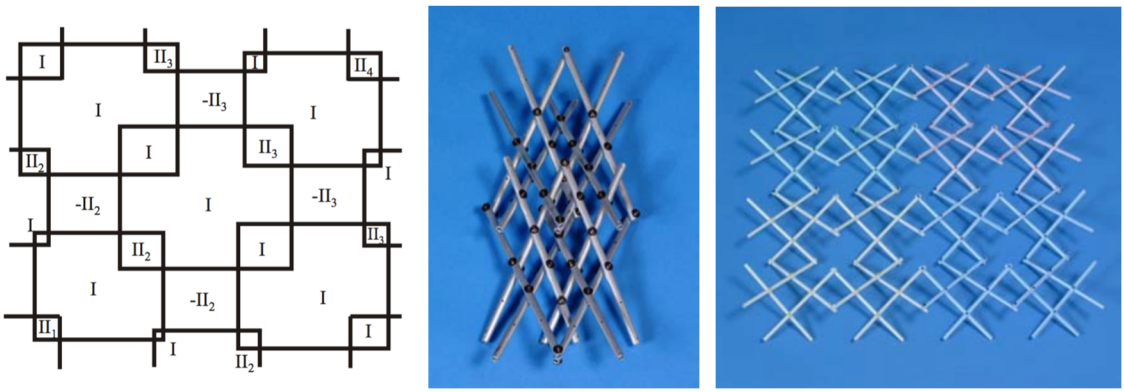

(c) Construction of the Bennett linkage grid (Chen and You, 2005).

Figure 2.17 Overconstrained linkages.

The Bennett linkage is the only spatial 4*R* linkage with a single DOF. Most researches focus on the construction of hybrid mechanisms using the Bennett linkage, and a few studies discussed the possibility for the construction of mechanisms network. Yan et al. presented a geometry method to build a mobile grid using the Bennett linkage as Figure 2.17(c) shows (Chen and You, 2005). The layout pattern is similar to a regular square tiling.

3) The Bricard Linkage

Bricard proposed a series of mobile 6*R* linkages in 1927. It includes six different types: three octahedral cases (Bricard 1897), the line-symmetric case, the plane-symmetric case and the trihedral case (Bricard and Cinématique, 1927). A particular example known as kaleidocycle (or three-fold symmetry type) is a linkage made from identical tetrahedral module. Figure 2.18(a) shows the linkage mechanism and Figure 2.18(b) is an alternative form of the Bricard linkage as a foldable frame (Chen et al., 2005). Each tetrahedron is linked to its neighbouring one along an edge, and the ring can be turned through its centre in a continuous motion. In order to form a close ring, at least six tetrahedrons are required (Schattschneider and Walker, 1977), and the geometrical properties of the six-bar linkage are as follows:

$$\begin{aligned} &a_{12} = a_{23} = a_{34} = a_{45} = a_{56} = a_{61} = h, \\ &\alpha_{12} = \alpha_{34} = \alpha_{56} = \alpha,\ \alpha_{23} = \alpha_{45} = \alpha_{61} = 2\pi - \alpha, \\ &R_i = 0\ \ (i = 1, 2, ..., 6), \end{aligned} \tag{2.11}$$

where h and α are known constants. Substituting Eq. (2.11) into Eq. (2.4) yields

$$\begin{aligned} \theta_1 &= \theta_3 = \theta_5, \\ \theta_2 &= \theta_4 = \theta_6, \end{aligned} \tag{2.12}$$

and

$$\cos^2\alpha + \sin^2\alpha(\cos\theta_1 + \cos\theta_2) + (1 + \cos^2\alpha)\cos\theta_1\cos\theta_2 - 2\cos\alpha\sin\theta_1\sin\theta_2 = 0. \tag{2.13}$$

Another wide-used type is the plane-symmetric Bricard linkage (Figure 2.18(c)); the geometric conditions are as follows:

$$\alpha_{12}+\alpha_{61}=2\pi,\alpha_{23}+\alpha_{56}=2\pi,\alpha_{34}+\alpha_{45}=2\pi,$$
$$a_{12}=a_{61},a_{23}=a_{56},a_{34}=a_{45}, \tag{2.14}$$
$$R_1=R_4=0,R_2=-R_6,R_3=-R_5.$$

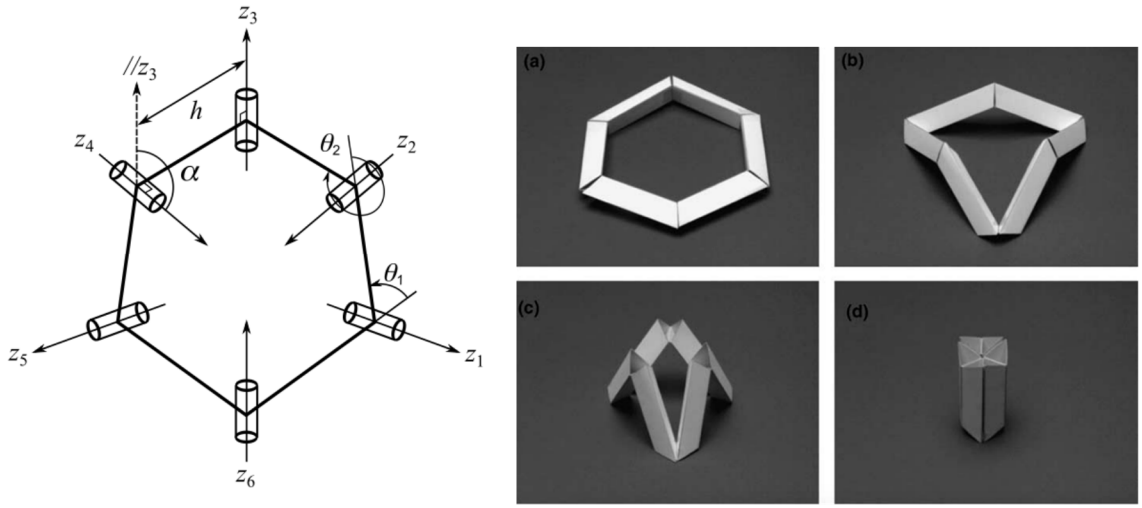

(a) Three-fold symmetry Bricard linkage (b) Alternative form of the Bricard linkage (Chen et al., 2005)

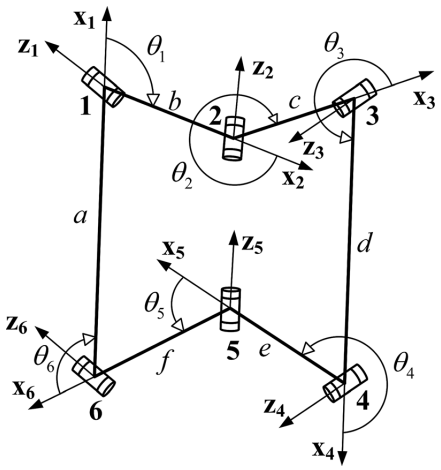

(c)The plane symmetry Bricard linkage (Qi et al., 2017)

Figure 2.18 The Bricard linkages.

2.3 Thick panel origami and modular origami

2.3.1 Thick panel origami

Most origami-inspired engineering applications are based on the thin shell models where the thickness of materials is neglected. In order to apply origami to applications such as roofs, solar

panels and foldable shelters, the models need to be modified with consideration of thickness. Many approaches have been suggested on this (Figure 2.19):

1) Hoberman proposed a hinge shift approach where the hinges are shifted on the top or bottom plane of the panels depending on the folding direction (Hoberman 2010). This strategy can fold the panels without clearance, but the working space of the mechanism is restricted compared to the zero-thickness model, and the strategy is difficult to adopt in comparatively complex assemblies.

2) The tapered material technique proposed by Tachi keeps the hinges on the same plane to preserve the kinematic motion (Tachi 2011). Each panel is trimmed according to the folding dihedral angle to avoid self-intersection during transformation. The drawback of this strategy is that neither can the structure be deployed to its fully flat state nor can it be folded into a void-free compact state.

3) The offset panel method shifts the panels to a distance equal to the material thickness to avoid intersection (Edmondson et al., 2014). Rigid extensions are required for connection between adjacent panels. This design keeps the zero-thickness kinematic motion and achieves a full range of motion, yet the extension parts are vulnerable to break, and the structure cannot achieve the fully flat state.

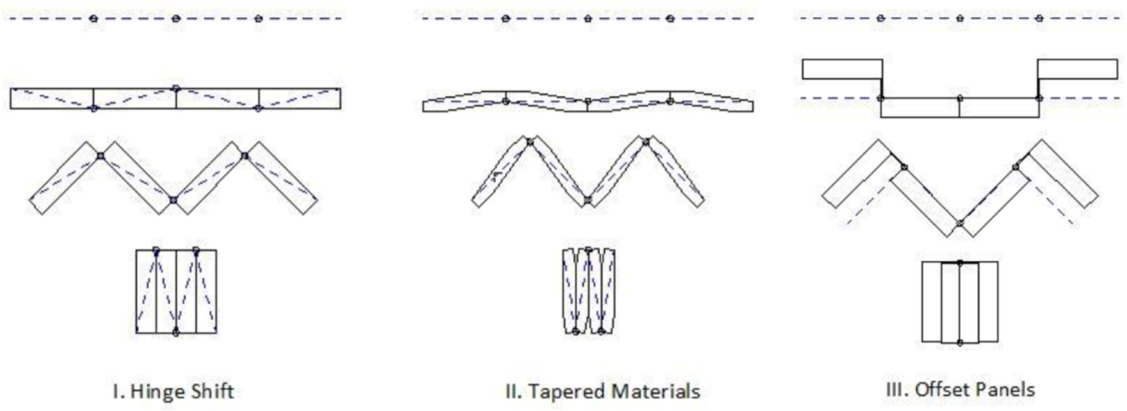

Figure 2.19 Thickness accommodation techniques (Morgan et al., 2016).

These methods provide many inspirations to build thick panel origami models, but they are difficult to be generalized and applied to more complex origami patterns.

Chen proposed a general method using spatial linkages to model each origami vertex (Chen et al., 2015). The spherical linkage around each vertex is replaced by spatial linkages where the revolute joints are placed a distance apart because of the thickness. The foldability conditions are: 1) each loop of the rigid bodies must be a spatial linkage, 2) the assembly of these linkages retains mobility. Typical origami patterns usually have four, five, six creases intersecting at a vertex, so the corresponding mechanisms for thick panel origami are spatial 4*R*, 5*R* and 6*R* linkages. It is possible to design thick panel models based on the zero-thickness pattern using the overconstrained linkages introduced previously.

For instance, for a four-crease origami pattern, the mathematic model can be built as a spherical 4*R* linkage. The thick panel version can be designed by shifting one hinge on the top surface of panels and three on the bottom, as shown in Figure 2.20, a_{12}, a_{23}, a_{34}, a_{41} are distances between fold lines. The shift distance is designed according to the geometry condition of the Bennett linkage, which is the only spatial 4*R* linkage. It can be proved that the relationships among the dihedral angles in zero-thickness spherical linkages are identical to those in the Bennett linkage (Chen et al., 2015). Therefore, the spherical 4*R* and the constructed Bennett linkage are kinematically equivalent. The equivalent spatial 5*R* and 6*R* linkages are constructed for five and six crease rigid origami cases using the same method. The spatial linkage kinematic method for thick panel origami provides the inspiration for constructing metamaterial through mechanism networks. This strategy is adopted in this research.

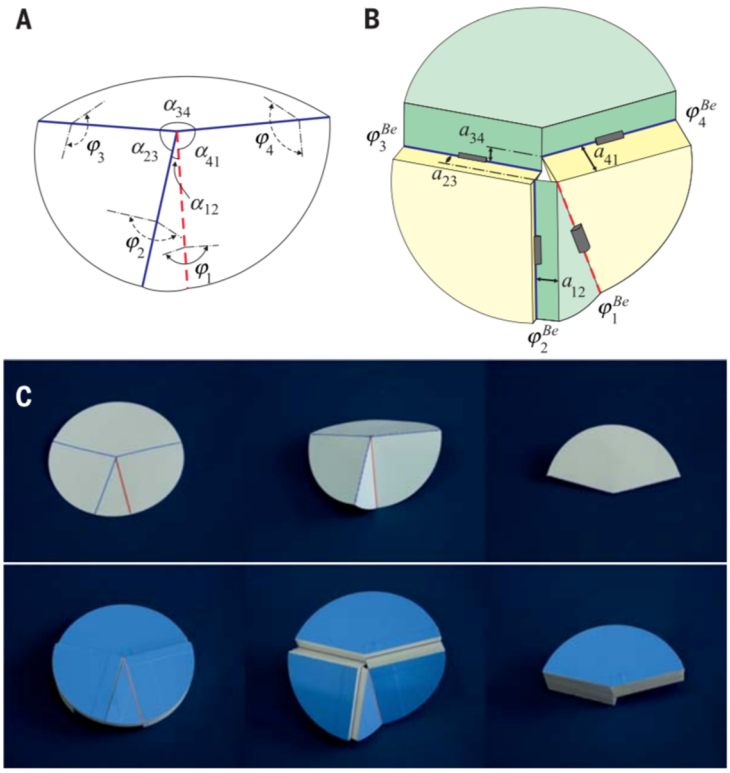

Figure 2.20 Thick panel origami construction using spatial linkages (Chen et al., 2015).

2.3.2 Modular origami

As Figure 2.21 shows, modular origami refers to using a certain number of paper-folded polyhedron units to assemble an integrated structure. Paper-folding polyhedron units have been studied by many artists (Mukerji, 2007; Tarnai et al., 2012; Simon et al., 2012). The basic strategy to construct a unit is to fold one single piece of paper into the shape and tuck extra material into the polyhedron. Other strategy includes the snapology, which uses paper strips to fold and wrap in a two-way weaving method. While folding a single unit is rather simple, combining them in a transformable pattern requires delicate design.

Transformable modular origami can be regarded as a special type of thick panel origami. The paper polyhedron units have a certain thickness, and they are connected in a network that can kinematically transform into different shapes. By designing the shape and connection arrangement of polyhedron units and analysing them according to the kinematic principles, we can program the modular origami models to transform into various shapes.

Figure 2.21 Modular origami models.

2.4 Tilings and space-filling

After discussing the spatial mechanisms for constructing reconfigurable unit cells, we further investigate the way to assemble multiple units in a network without frustration, which is also essential in metamaterial construction. As shown in Figure 2.22, tiling is the most useful tool for designing a regular grid network. Regular tiling refers to filling a plane using regular convex polygonal tiles. There are only three regular tiling patterns, including equilateral triangles, squares, and hexagons (Grünbaum and Shephard 1986). The square tiling pattern is widely used in stretchable metamaterials. Various samples with different cutting strategies, materials and manufacturing methods have been studied (Figure 2.22) (Yang et al., 2016; Tang and Yin, 2017; Tang et al., 2015; Yang et al., 2016), including bistable tessellations (Rafsanjani and Pasini, 2016) and patterns that can transform in multi-steps due to the connection ligament design (Coulais et al., 2018). The Poisson's ratios variation have been studied in some researches (Mitschke et al., 2013). Other semi-regular tilings refer to patterns with regular tiles of more than one shape, and every vertex corner is identically arranged. The tiling patterns can be made transformable by extruding some tiles to form flexible voids; extruding square tiles

will lead to voids that can be modelled by planar 4*R* linkage, and hexagon voids can be represented by 6*R* linkage. The difficulty of designing transformable tilings lies in the control of the multi-DOF mechanism. For instance, a hexagon void modelled as a planar 6*R* mechanism has two DOF and including multiple such mechanisms in a system leads to numerous mobility, which means the transformation will be highly unsynchronized. Special symmetric patterns can be designed to constrain the DOF to synchronize the deformation (Mitschke et al., 2013).

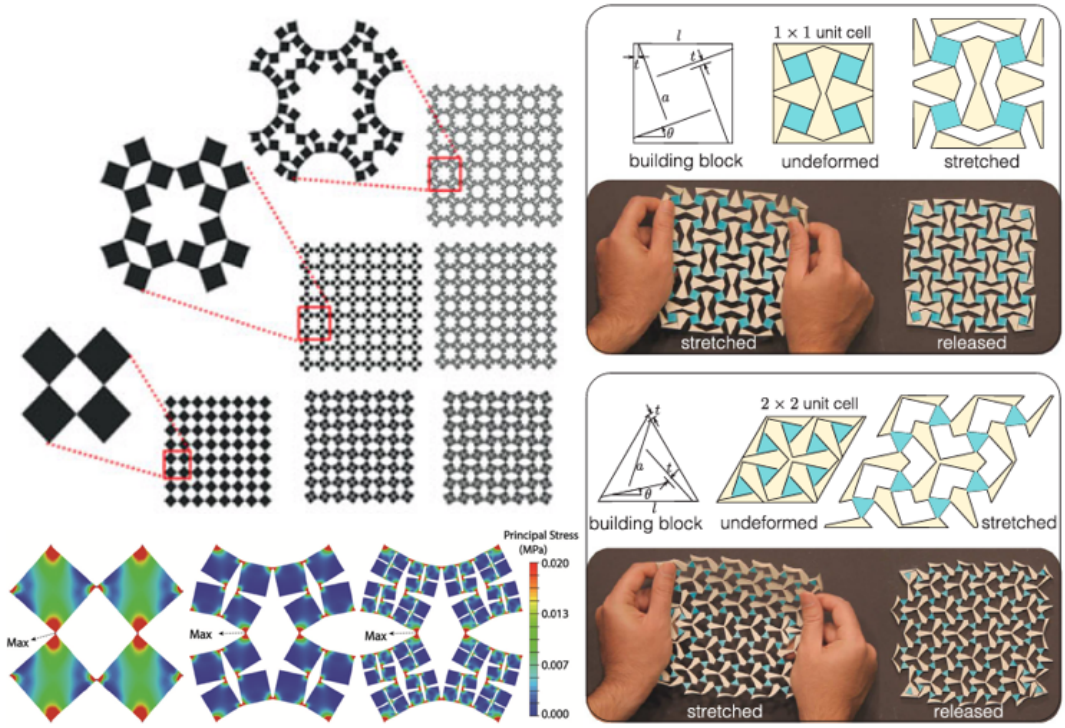

(a) Hierarchical cube tiling (Tang et al., 2015)

(b) Stretchable auxetics (Rafsanjani and Pasini, 2016)

Figure 2.22 Tiling patterns in metamaterials.

2.5 Summary

The research in mechanical metamaterials is bringing about many new applications and possibilities with the rapid development of computational tools, digital fabrication techniques

and theoretical breakthroughs. Rigid origami and kirigami patterns are widely used in the design of metamaterials in recent decades. However, many origami-inspired designs are based on case-by-case pattern and hard to be generalized. The material thickness is rarely considered, leading to the difficulty in realization of theoretical models and the combination of fabrication techniques. Besides, the reconfigurable range of most instability-based metamaterials is still limited.

The demands for future applications include:

1) More complex 3D metamaterials with multiple deformation paths;

2) Spatially textured metamaterials with aperiodic microstructures for arbitrary shape transformation;

3) Metamaterials with more complex energy landscapes such as snap-through behaviour;

4) The rational design of multi-functional metamaterials with a targeted property;

5) Manufacturing multi-material structures using a combinatorial strategy of several manufacturing methods such as 3D printing, laser cutting and two-photon lithography.

Chapter 3

Planar Mechanism Based Kinematic Metamaterial

This chapter is devoted to the construction of kinematic based metamaterials using planar linkage mechanisms. When the connection edges of modular origami units are parallel to each other, the assembly can be modelled as a network of planar linkage mechanisms. In addition, if the building blocks of these modular origami are prisms, the structure can be regarded as a two-dimensional transformable tiling pattern, in which both the polygon units and the voids are seen as tiles. The first part of this chapter focuses on reconfigurable tilings with quadrilateral voids. The quadrilateral voids are modelled as planar four-bar linkages (4*R* linkage), and the reconfigurability of the system is analysed using the principles of mechanisms. This is followed by a discussion on assemblies consisting of more than two geometry types of unit cells, their orientation variation, duality and expansion rate. In the second part of the chapter, the metamaterial with planar mechanisms is further modified to perform three-dimensional transformation. By tilting the prism units into rhombohedrons, a series of kinematic metamaterials with different spatial shapes, twist angles and permeability features are constructed.

3.1 Introduction

Many modular origami models are made by cubes and prism units connected by parallel edges. Some of these structures can present planar transformations. If we see them from the top plane which is normal to their connection edges, the structures can be regarded as transformable tiling patterns with voids inside. During the transformation, the shape of the voids will change, and the tiling pattern is geometrically compatible at any configuration. These voids can be modelled as planar linkage mechanisms. For instance, the cubic modular origami model shown in Figure 3.1(a) is proposed by Ron Resch in 1977 (Resch, 1977). It can transform from a close-packed state to a porous grid. The model can be seen as a planar transformable tiling shown in Figure 3.1(b), which is widely used in mechanical metamaterials. A question of whether there are other similar transformable tilings is naturally raised.

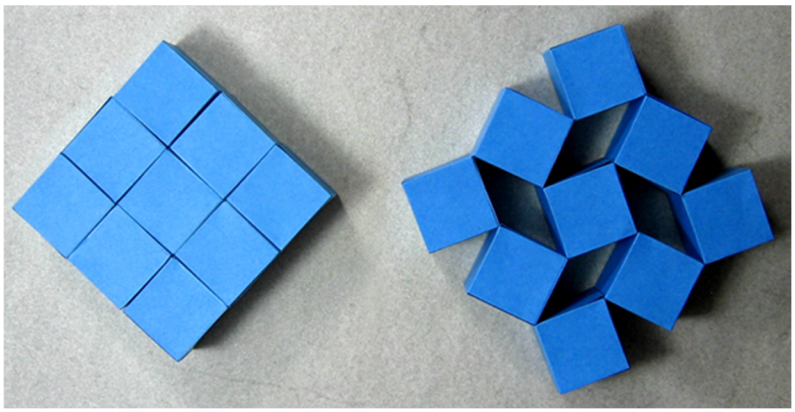

(a) Modular origami model

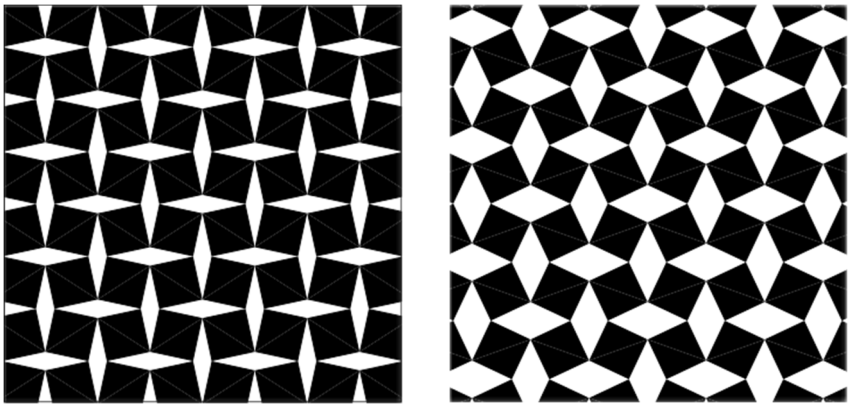

(b) Planar transformable tiling

Figure 3.1 Reconfigurable cube tiling.

To model the transformation, the cubes (or other shaped prisms) are treated as rigid bodies and the voids are seen as planar four-bar linkages (4*R* linkage). Hence, the assembly of nine cubes could be regarded as nine rigid bodies interlinked by four 4*R* linkages. The mobility of the assembly is determined by the topological and geometrical information of the linkage system. This kinematic analysis can be further extended to mobile assemblies composed of arbitrary prisms and rhombohedrons.

3.2 Geometry of reconfigurable quadrilateral tilings

To begin with, the 3D modular origami model is simplified as a 2D pattern where the cubes become squares and the connection edges refer to connection vertices. We can replace the square units by arbitrary quadrilaterals of which the side lengths are *a*, *b*, *c* and *d*. All quadrilaterals in the assembly are identical. To maintain the mobility of the structure, specific geometrical conditions are imposed to the quadrilaterals to form a loop of 4*R* linkages which will be compatible to each other during the transformation.

3.2.1 Arrangement 1

First consider an arrangement of the unit cells shown in Figure 3.2. This pattern is made of three shapes: the rigid quadrilateral unit cell and two quadrilateral voids: one with side lengths *a*, *a*, *c* and *c*, and the other *b*, *b*, *d* and *d* (The tile is drawn in a parallelogram shape to make the structure geometrically compatible at the open state). The angles for the quadrilateral unit cell and voids are marked in Figure 3.2. Note that the two opposite angles of the voids, marked as θ_3 and θ_1, are always identical because of the shape of the voids.

Next, we shall find the conditions under which this tiling is transformable.

Geometrically there are

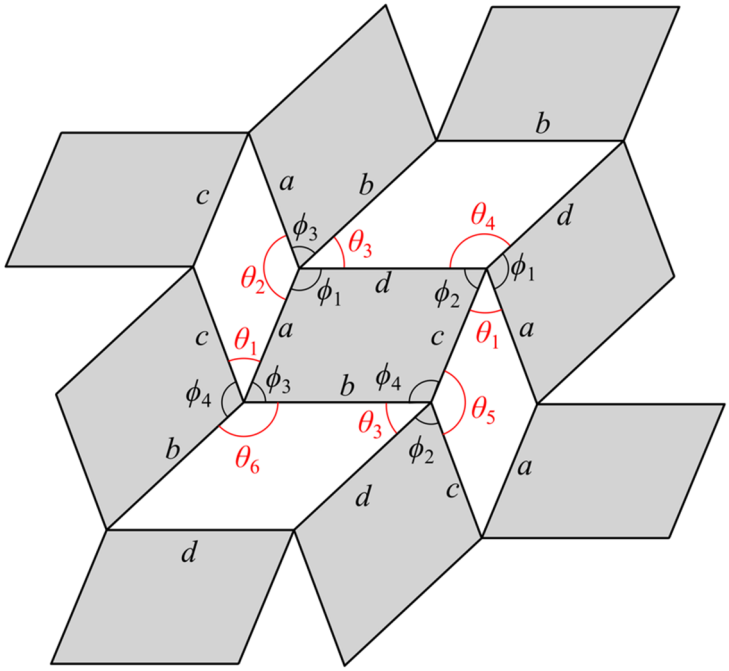

Figure 3.2 An arrangement of the identical quadrilateral unit cells.

$$\begin{aligned} \phi_1+\phi_2+\phi_3+\phi_4 &= 2\pi, \\ 2\theta_1+\theta_2+\theta_5 &= 2\pi, \\ 2\theta_3+\theta_4+\theta_6 &= 2\pi. \end{aligned} \tag{3.1}$$

At each point where quadrilateral unit cells are connected, there must be

$$\begin{aligned} \phi_1+\phi_3+\theta_2+\theta_3 &= 2\pi, \\ \phi_1+\phi_2+\theta_1+\theta_4 &= 2\pi, \\ \phi_2+\phi_4+\theta_3+\theta_5 &= 2\pi, \\ \phi_3+\phi_4+\theta_1+\theta_6 &= 2\pi. \end{aligned} \tag{3.2}$$

Therefore, we have

$$\phi_4 = 2\pi-\phi_1-\phi_2-\phi_3\ , \tag{3.3}$$

$$\theta_1 = \theta_3, \tag{3.4}$$

$$\theta_5 = \phi_1+\phi_3-\theta_3, \tag{3.5}$$

$$\theta_2 = 2\pi-\phi_1-\phi_3-\theta_3, \tag{3.6}$$

$$\theta_6 = \phi_1 + \phi_2 - \theta_3, \tag{3.7}$$

and $$\theta_4 = 2\pi - \phi_1 - \phi_2 - \theta_3. \tag{3.8}$$

The edge lengths are also related by the following relationships.

$$a = \frac{\sin(\phi_1 + \phi_2 + \phi_3)}{\sin\phi_3}\left(\frac{d\sin\phi_1}{\sin(\phi_1 + \phi_2)} - c\right) + \frac{d\sin\phi_2}{\sin(\phi_1 + \phi_2)}, \tag{3.9}$$

$$b = \frac{d\sin\phi_1 - c\sin(\phi_1 + \phi_2)}{\sin\phi_3}, \tag{3.10}$$

$$a\sin\frac{\theta_2}{2} = c\sin\frac{\theta_5}{2}, \tag{3.11}$$

and $$b\sin\frac{\theta_6}{2} = d\sin\frac{\theta_4}{2}. \tag{3.12}$$

The latter two equations are obtained by considering the geometry of the voids. Now substituting Eq. (3.3-10) into Eq. (3.11) and (3.12), there are

$$\sin\frac{\phi_1 + \phi_3 + \theta_3}{2}\sin\frac{\phi_1 + \phi_2 - \theta_3}{2}\left[\begin{array}{l}\dfrac{\sin\phi_1}{\tan\phi_3}\sin(\phi_1 + \phi_2) + \\ \sin\phi_1\cos(\phi_1 + \phi_2) + \sin\phi_2\end{array}\right] =$$

$$\left[\begin{array}{l}\sin\phi_1\sin\dfrac{\phi_1 + \phi_2 - \theta_3}{2} - \\ \sin\phi_3\sin\dfrac{\phi_1 + \phi_2 + \theta_3}{2}\end{array}\right]\left[\begin{array}{l}\sin\dfrac{\phi_1 + \phi_3 - \theta_3}{2} + \\ \sin\dfrac{\phi_1 + \phi_3 + \theta_3}{2}\left(\dfrac{\sin(\phi_1 + \phi_2)}{\tan\phi_3} + \cos(\phi_1 + \phi_2)\right)\end{array}\right] \tag{3.13}$$

If $\phi_1 + \phi_2 = \pi$ and $\phi_1 + \phi_3 = \pi$, both sides of Eq. (3.13) become zero regardless of θ_3. This indicates that under this condition, Eq. (3.13) holds for any θ_3, which means θ_3 is not uniquely determined by ϕ_1, ϕ_2 and ϕ_3. That is to say, this assembly becomes transformable if the quadrilateral unit cells are a parallelogram.

From Eq. (3.4-5) and (3.7), we have $\phi_1 + \phi_3 = \theta_1 + \theta_5$, and $\phi_1 + \phi_2 = \theta_3 + \theta_6$. Hence, $\theta_1 + \theta_5 = \pi$ and $\theta_3 + \theta_6 = \pi$. This indicates that only when the quadrilateral voids are made of

parallelograms, the tiling pattern can be transformable. This conclusion prompts us to consider arrangements with arbitrary tiles and parallelogram voids, which are presented next.

3.2.2 Arrangement 2

Consider now an arrangement with a set of nine quadrilateral unit cells shown in Figure 3.3(a). This is a tiling pattern made of five shapes: the quadrilateral unit cells, two types of rhombic voids with side lengths *a* and *c*, respectively, and two types of parallelogram voids with side lengths *b* and *d*. The voids are classified as different types because their angles could be different.

Now take θ_8 as an input, the following angular relationships can be established geometrically.

$$\phi_4 = 2\pi - \phi_1 - \phi_2 - \phi_3 , \tag{3.14}$$

$$\theta_1 = 2\pi - \phi_1 - \phi_3 - \theta_8 , \tag{3.15}$$

$$\theta_2 = \phi_1 + \phi_3 + \theta_8 - \pi , \tag{3.16}$$

$$\theta_7 = \pi - \theta_8 , \tag{3.17}$$

$$\theta_3 = 3\pi - 2\phi_1 - 2\phi_3 - \theta_8 , \tag{3.18}$$

$$\theta_4 = 2\phi_1 + 2\phi_3 + \theta_8 - 2\pi , \tag{3.19}$$

$$\theta_5 = 2\pi - \phi_1 - \phi_3 - \theta_8 = \theta_1 , \tag{3.20}$$

and

$$\theta_6 = \phi_1 + \phi_3 + \theta_8 - \pi = \theta_2 . \tag{3.21}$$

The quadrilaterals units must not overlap with each other, so the interior angles of the parallelogram voids are only allowed to be between 0 and π. Applying $\theta_i \in [0, \pi] (i = 1 \sim 7)$ to Eq. (3.15-19) yields

$$\begin{gathered} 0 \le \theta_8 \le \pi , \\ \pi - \phi_1 - \phi_3 \le \theta_8 \le 2\pi - \phi_1 - \phi_3 , \\ 2\pi - 2\phi_1 - 2\phi_3 \le \theta_8 \le 3\pi - 2\phi_1 - 2\phi_3 . \end{gathered} \tag{3.22}$$

With further simplification we obtain the range of the quadrilateral angles, which is

$$\frac{\pi}{2} \le \phi_1 + \phi_3 \le \frac{3}{2}\pi \,. \tag{3.23}$$

Were this condition not met, the quadrilateral would overlap during transformation. The parallelogram voids completely close when $\theta_8 = 0$. If the rhombic voids close at the same time, $\theta_1 = 2\pi - \phi_1 - \phi_3 - 0 = \pi$, and thus,

$$\phi_1 + \phi_3 = \pi \,. \tag{3.24}$$

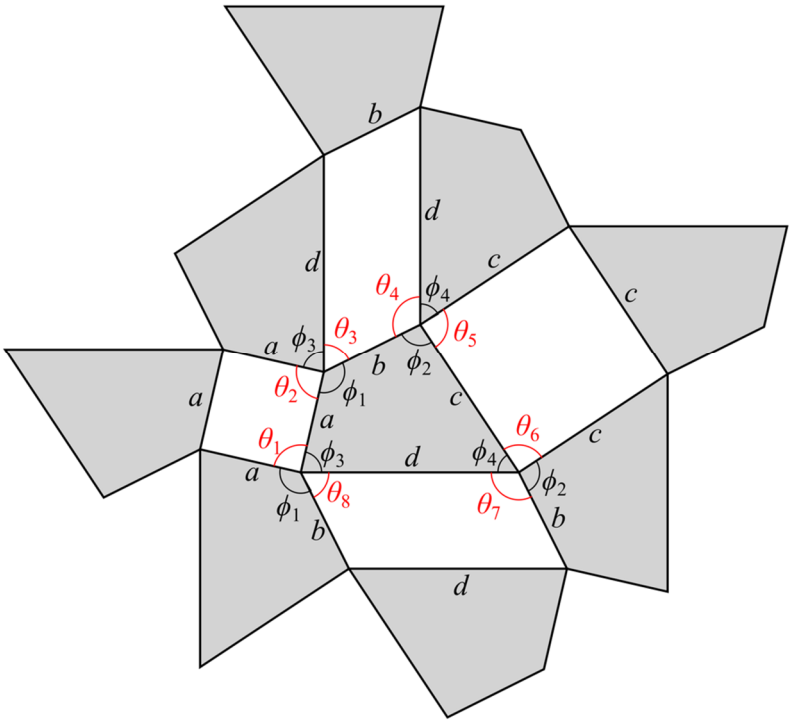

(a) Mathematical model

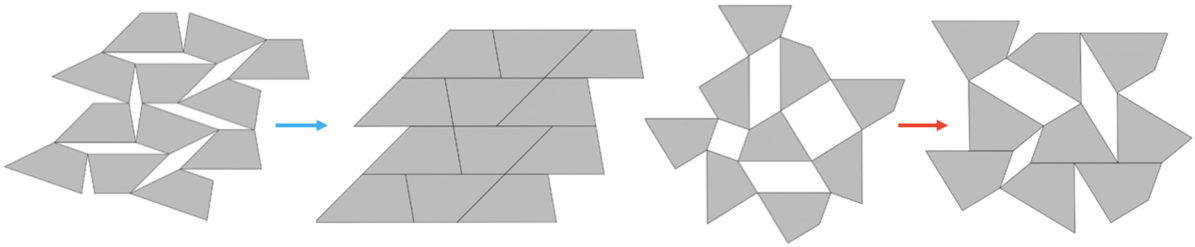

(b) Trapezium assembly (c) Arbitrary quadrilateral unit cells assembly

Figure 3.3 The second arrangement of identical quadrilateral unit cells.

This indicates that the assembly based on this arrangement can only be compactly packed when two opposed edges in the quadrilateral are parallel to each other, i.e., the quadrilateral has to become a trapezium. Figure 3.3(b) shows such a trapezium assembly, whereas a general case consisting of arbitrary quadrilaterals that cannot be close packed is given in Figure 3.3(c).

3.2.3 Arrangement 3

The third arrangement is shown in Figure 3.4(a). The pattern consists of three shapes: a quadrilateral and two parallelograms voids.

Geometrically the angular relationships are

$$\phi_4 = 2\pi - \phi_1 - \phi_2 - \phi_3, \tag{3.25}$$

$$\theta_1 = 2\pi - \phi_2 - \phi_3 - \theta_8, \tag{3.26}$$

$$\theta_2 = \phi_2 + \phi_3 + \theta_8 - \pi, \tag{3.27}$$

$$\theta_7 = \pi - \theta_8, \tag{3.28}$$

$$\theta_3 = \pi - \phi_1 + \phi_4 - \theta_8, \tag{3.29}$$

$$\theta_4 = \phi_1 - \phi_4 + \theta_8, \tag{3.30}$$

$$\theta_5 = 2\phi_4 - \theta_8, \tag{3.31}$$

$$\theta_6 = \pi + \theta_8 - 2\phi_4. \tag{3.32}$$

where θ_8 is treated as the input. Since $\theta_i \in [0,\ \pi](i = 1 \quad 7)$, applying it to Eq. (3.26-3.32) gives

$$\begin{aligned} 0 \le \theta_8 \le \pi, \\ \phi_1 + \phi_4 - \pi \le \theta_8 \le \phi_1 + \phi_4, \\ \phi_4 - \phi_1 \le \theta_8 \le \pi + \phi_4 - \phi_1, \\ 2\phi_4 - \pi \le \theta_8 \le 2\phi_4. \end{aligned} \tag{3.33}$$

Further simplification of the above inequalities yields

$$
\begin{aligned}
0 \le \phi_1 + \phi_4 \le 2\pi, \\
\left|\phi_1 - \phi_4\right| \le \pi, \\
0 \le \phi_4 \le \pi.
\end{aligned}
\tag{3.34}
$$

In order to pack the unit cells compactly with this tiling pattern, there must be $\theta_3 = \pi$, $\theta_5 = \pi$ when $\theta_8 = 0$, which gives

$$
\phi_1 = \phi_4 = \frac{\pi}{2}. \tag{3.35}
$$

Hence, the quadrilateral must have two opposite right internal angles. Figure 3.4(b) shows such an example and Figure 3.4(c) is an assembly made from general quadrilateral unit cells that cannot close pack.

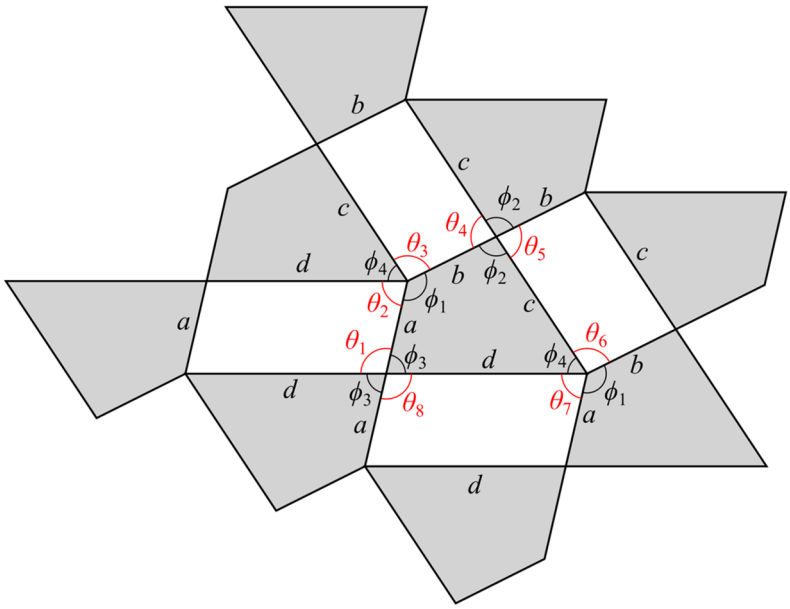

(a) Mathematical model

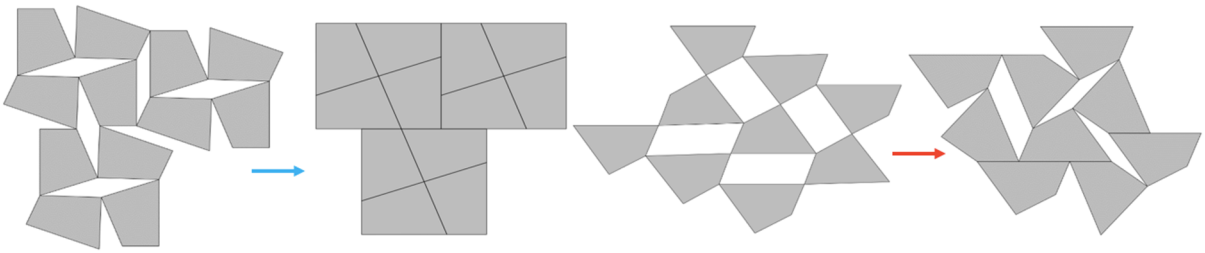

(b) Quadrilateral units with opposite right angles (c) Arbitrary quadrilaterals

Figure 3.4 The third arrangement of identical quadrilateral unit cells.

A total of 56 tiling patterns of quadrilaterals exist (Grünbaum,1986), but most of them are not transformable even if parallelogram voids are introduced. By having parallelogram or rhombic voids, we have found ten arrangements of arbitrary quadrilaterals that are transformable. Let the edge lengths of a quadrilateral be *a*, *b*, *c*, and *d*, we express a rhombic void with edge length of *a* as a^4, and a parallelogram void with lengths of *a* and *b* as a^2b^2. We obtain Table 3.1 that summarises all transformable arrangements. The schematic diagrams of part of the arrangements are also given in the table. Note that Arrangement 1 discussed earlier is a special case of the first transformable type in the table, where the quadrilateral unit cells must be parallelograms, i.e., $a = c$, $b = d$, and the voids parameters become (a^4), (b^4), (a^4) and (b^4). Arrangement 2 is actually type 3 in the table which refers to an arrangement with two squares and two parallelogram voids. Arrangement 3 belongs to type 10 in the table which has four parallelogram voids.

So far, we have found a family of reconfigurable tilings. However, applying the Kutsbach criterion to these assemblies yields no positive number. For instance, for a nine-unit assembly, the mobility *m* is

$$m = 3(n - j - 1) + \sum_{i=1}^{j} f_i = 3(9 - 12 - 1) + 12 = 0 \tag{3.36}$$

where *n*, *j* and f_i are number of unit cells, the number of joints and the degrees of freedom of each joint, respectively. This indicates that the assembly is an overconstrained mechanism, and the existence of mobility in it is due to the special geometry. The entire motion of four interlinked 4R linkages are synchronised to transform with a single degree of freedom.

Table 3.1 Arrangements of arbitrary quadrilaterals that are transformable.

Number and shapes of the voids	Type and parameters of the voids	Schematic diagram of part of the arrangements
4 □	1. (a^4) (b^4) (c^4) (d^4)	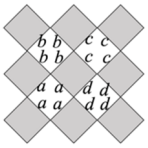
3 □ 1 ▱	2. (a^2c^2) (b^4) (c^4) (d^4)	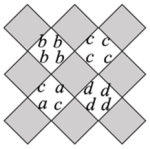
2 □ 2 ▱	3. (a^2c^2) (b^4) (c^2a^2) (d^4) 4. (a^2c^2) (b^2d^2) (c^4) (d^4)	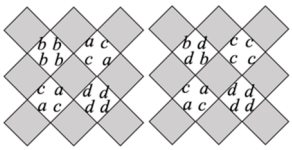
1 □ 3 ▱	5. (a^2c^2) (b^2d^2) (c^2a^2) (d^4)	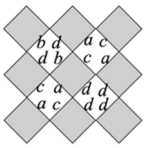
4 ▱	6. (a^2c^2) (b^2d^2) (c^2a^2) (d^2b^2) 7. (a^2b^2) (b^2a^2) (c^2b^2) (d^2a^2) 8. (a^2b^2) (b^2a^2) (c^2b^2) (d^2c^2) 9. (a^2b^2) (b^2a^2) (c^2d^2) (d^2a^2) 10. (a^2b^2) (b^2a^2) (c^2d^2) (d^2c^2)	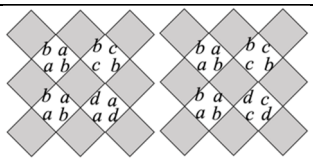 ……

3.3 Analysis of reconfigurable quadrilateral tilings

3.3.1 Alternative shapes of unit cells

The reconfigurable tilings shown so far include only some specific quadrilateral unit cells. One may wonder if they can be replaced by more general shapes, e.g., shapes with curved edges. The answer is positive. The reconfigurable tilings can accommodate such alternative unit cells

if the following two conditions are met. First, the corners of a unit at which the connections to its neighbouring units are located must be identical to those of the original quadrilateral unit arrangements; second, the edges of the alternative unit cells must piece together when they are compacted folded. Two examples that satisfy both conditions are given in Figure 3.5.

To enable an alternative unit to match with its identical neighbours while retracted, its shape should have certain symmetry. If the unit is a mirror symmetry pattern, the assembly can only close in one direction. For instance, the fan shaped unit shown in Figure 3.5(a) has mirror symmetry, the unit cells around the central unit are only capable of rotation anticlockwise about the central unit to 90° at most. At the fully expanded state, the mechanism cannot move any further because the edges of unit cells in the other direction will collide with each other. However, if a unit has rotational symmetry, as demonstrated in Figure 3.5(b), the assembly of the propeller shaped unit cells can transform both ways because the unit has rotational symmetry. These unit cells can transform to 180° and fold completely in both directions.

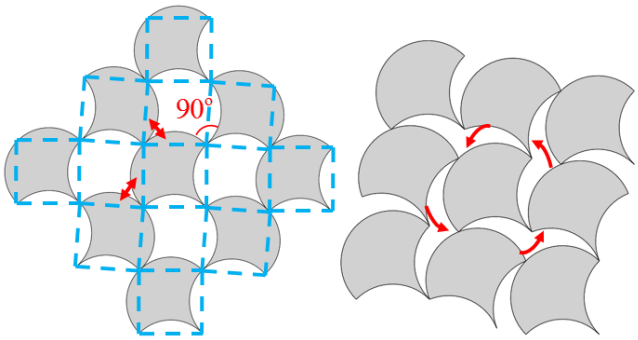

(a) Unit cells with mirror symmetry

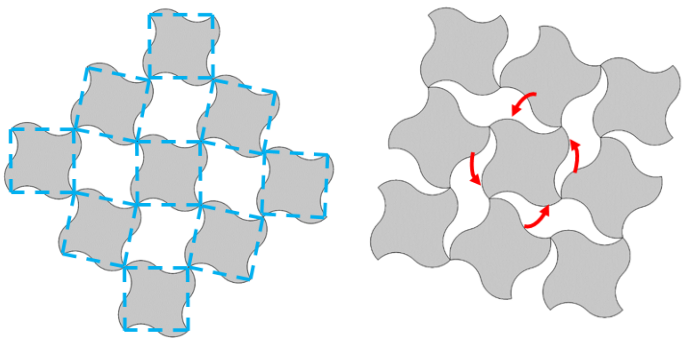

(b) Unit cells with rotational symmetry

Figure 3.5 Reconfigurable tilings made from alternative unit cells.

3.3.2 Orientation and duality

It is interesting to note that the orientations of the unit cells alter when they rotate around each other. To examine it, we mark each unit with an arrow, and make all arrows pointing upwards in the initial state when the structure is close packed. As shown in Figure 3.6, while rotating anticlockwise around the central unit, the directions of the arrows on those units that are not directly connected to the central unit remain unchanged, indicating they translate without any rotation. The rest of the unit cells turn. In the fully opened configuration, the arrows on the translating unit cells remain the same direction whereas the turning unit cells have rotated by 90°. In the final configuration, the unit cells are close packed again. The turning unit cells have now rotated by 180°, whilst the translating unit cells never change their orientations. The orientation variation is a particularly useful feature as it could be used to design programmable acoustic or electromagnetic metamaterials. The switch between geometric states could be used to alter the wave directions.

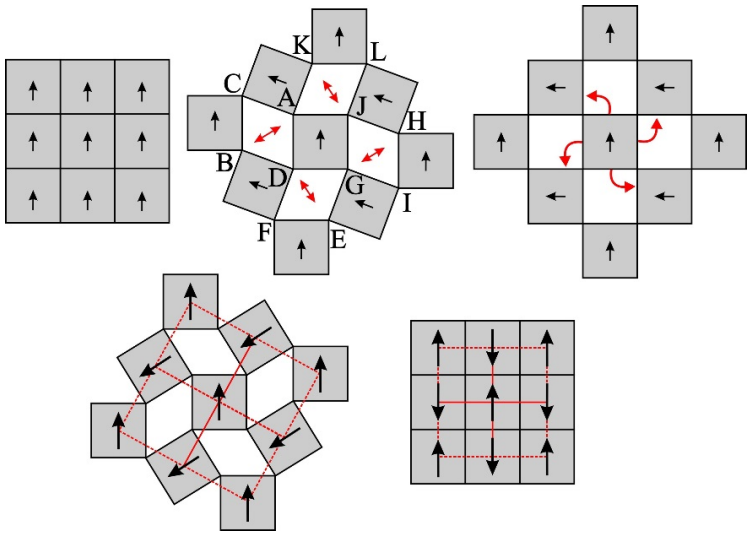

Figure 3.6 Orientation of unit cells in a reconfigurable tiling and its dual.

Whilst the orientation changes with motion, the dual shape of the tiling pattern remains the same no matter how it transforms. Two patterns are called a dual to each other if it is possible to set a one-to-one correspondence between the unit cells, edges and vertices of the first tiling

and those of the second one. The way to draw a dual of an arrangement is to connect the centre of each unit with those of its neighbour's. Take the arrangement given in Figure 3.6 as an example. It can be shown that the dual of this tiling with square unit cells is in the same shape as itself during transformation, and the size of the dual varies to reflect the overall dimension change of tiling patterns. The dual of a transformable tiling is a basic topology feature which can be used to distinguish the tiling from others.

3.3.3 Paired unit cells

Earlier we touched upon the alternative shapes of the unit cells, e.g., those shown in Figure 3.5, and all the unit cells are kept identical. This section discusses the strategy to have paired units which are not necessarily identical to each other.

Figure 3.7 shows two examples of paired unit cells that is based on Arrangement 1 of Table 3.1. Figure 3.7(a) is a jigsaw puzzle tiling where shape A and B are called a pair, and the parameters of Arrangement 1 pattern are given as $a = b = c = d$. We draw dotted straight lines among the connection points of the unit cells, and in such way we can obtain the original square shape pattern again. The motion of the pattern is the same as that of the Arrangement 1. Despite that the two unit cells have different shapes, they bit into each other in the fully compact configuration.

We can also produce reconfigurable tilings with two types of unit cells in different sizes. The example shown in Figure 3.7(b) is a tiling pattern of two types of square tiles: one big and one small. The squares are connected according to Arrangement 1. Because of the different edge length, the voids are parallelograms instead of rhombuses. When the pattern is fully expanded, the parallelogram voids become rectangles instead of squares. Its dual is the same as the Arrangement 1(Figure 3.7(b)), so the motion of this pattern is the same as previously discussed.

The concepts of paired units and units in different sizes can be merged to produce more general assemblies. For instance, if we use a pair of unit cells where one being a four-pointed star and

the other being a square, a tiling pattern shown in Figure 3.8(a) is obtained. The star and square unit cells form a grid once fully open, and the former tightly surround the latter when fully folded. This results in a transformable tiling pattern with an expansion ratio much greater than that of the one made from square unit cells. The expansion ratio is calculated as follows.

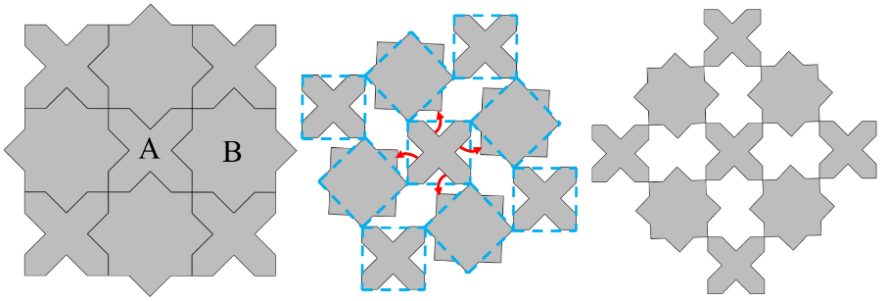

(a) Jigsaw puzzle pair

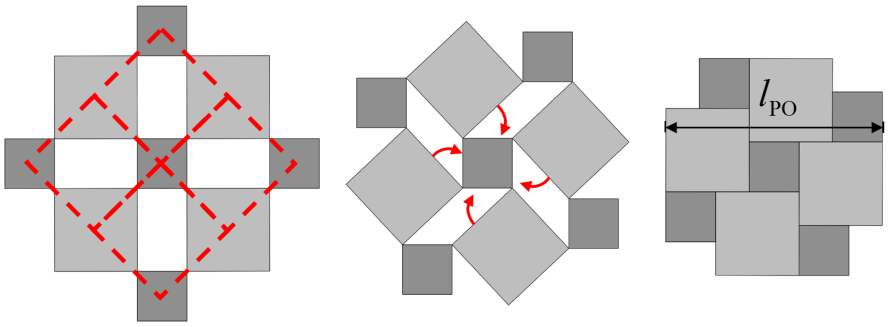

(b) Pair of square unit cells with different sizes

Figure 3.7 Paired unit cells based on the arrangement of Arrangement 1.

The star and square are defined by parameters a and α_s. The fully expanded length l_E can be obtained as

$$l_E = \sqrt{2}a + 4\sqrt{2}a\sin\frac{\alpha_s}{2} \tag{3.37}$$

When the structure is in its packed state, the length l_{PS} becomes

$$l_{PS} = 4a\sin\frac{\alpha_s}{2} + a\sin\frac{\alpha_s}{2}\left(1-\tan\frac{\pi-\alpha_s}{2}\right) \tag{3.38}$$

Thus, the expansion ratio is

$$r = \frac{l_E}{l_{PS}} = \frac{\sqrt{2} + 4\sqrt{2}\sin\frac{\alpha_s}{2}}{4\sin\frac{\alpha_s}{2} + \sin\frac{\alpha_s}{2}(1 - \tan\frac{\pi - \alpha_s}{2})} \tag{3.39}$$

Because $\alpha_s \in [\frac{\pi}{2}, \pi]$, the maximum and minimum values of r are $0.5+\sqrt{2}$ and $\sqrt{2}$, respectively.

If we replace the star unit with a square, as shown previously in Figure 3.7(b), then α_s becomes π (denoted by $\alpha_{s\text{-}o}$) and r is $5\sqrt{2}a$, so the original p ackaged length l_{PO} becomes

$$l_{PO} = 4a\sin\frac{\alpha_{s\text{-}o}}{2} + a\sin\frac{\alpha_{s\text{-}o}}{2}(1 - \tan\frac{\pi - \alpha_{s\text{-}o}}{2}) = 4a + a = 5a\,. \tag{3.40}$$

The expansion ratio r_o is

$$r_o = \sqrt{2}. \tag{3.41}$$

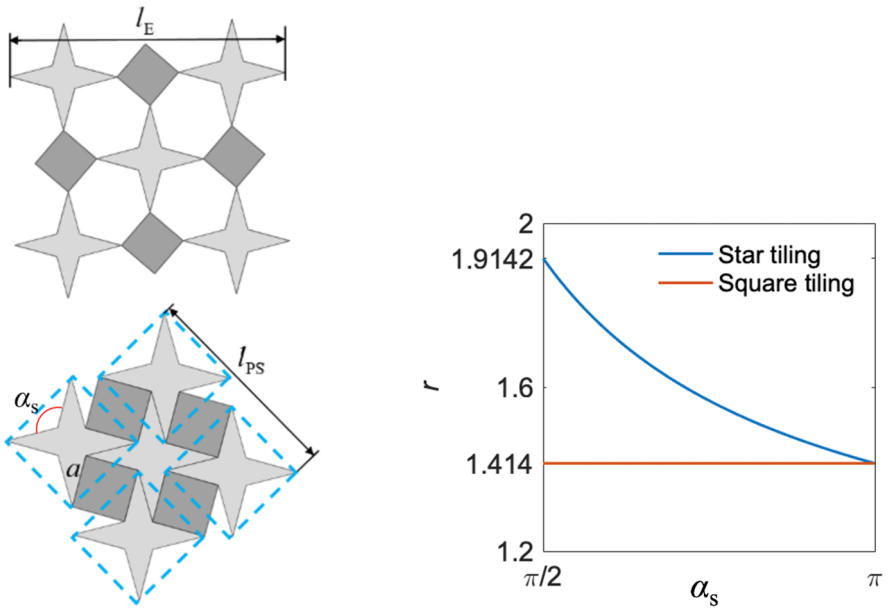

(a) Parameters of two assemblies (b) Expansion ratios of two assemblies

Figure 3.8 Expansion ratios of assemblies with paired unit cells.

Therefore, for the paired square tiling pattern, the expansion ratio is fixed to $\sqrt{2}$, but using the star tiling pattern, the expansion ratio can be tuned by varying the width of the star arm. The value of r in star tiling and paired square tiling is given in Figure 3.8(b). It can be concluded

that, the ‘slimmer’ the star is, the larger the expansion ratio is. This star and square design can be adopted to other types of transformable arrangements.

3.3.4 Fabrication

The reconfigurable tilings are fabricated using two methods. The first one utilises 3D printing to make each tiles, and connects them with tapes. Figure 3.9 shows the corresponding models for the structures in Figure 3.5(a)(b) and Figure 3.8. The advantage of taped samples is that they can transform smoothly as kinematic mechanisms.

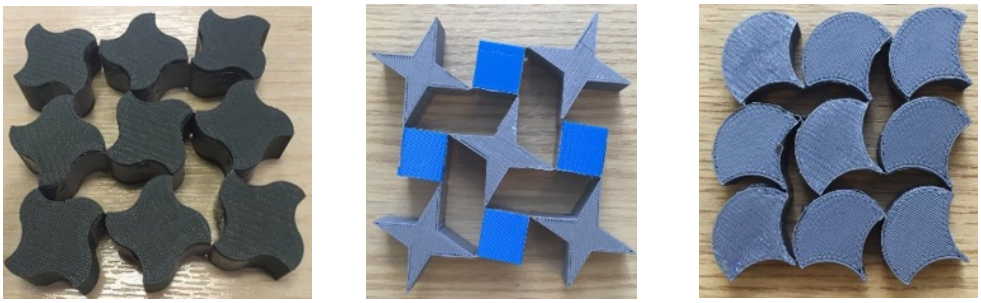

(a) Model in Figure 3.5a (b) Model in Figure 3.8 (c) Model in Figure 3.5b

Figure 3.9 3D printed samples.

While the assembled structures are difficult to make manually when they are scaled down, a second fabrication method is proposed to laser cut the pattern in one piece. A 2.3mm thickness laserable rubber sheet is cut according to the close pack pattern. This process is similar to the way artist make kirigami models. As shown in Figure 3.10, when stretch the cut sheet, the thin ligaments for connection will deform in accordance with the mechanism transformation. It should be noted that if the pattern contains a lot of unit cells, those cells at the boundary will not behave perfectly as those in the middle due to the accumulated error.

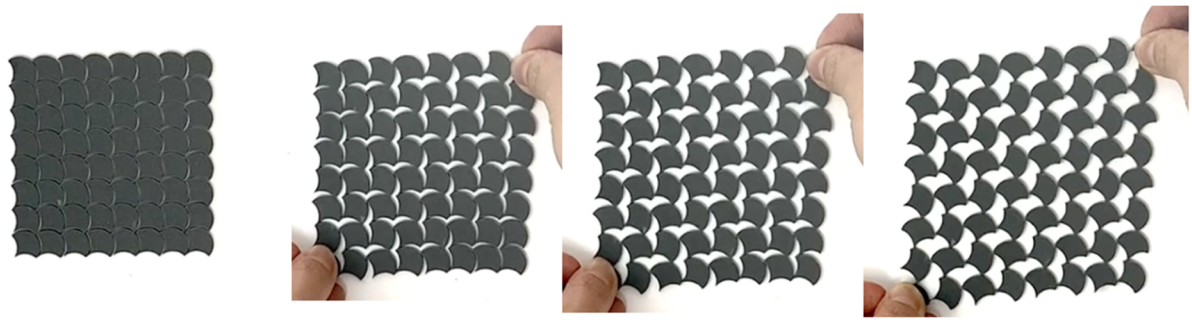

(a) Propeller pattern corrsponding to Figure 3.5a

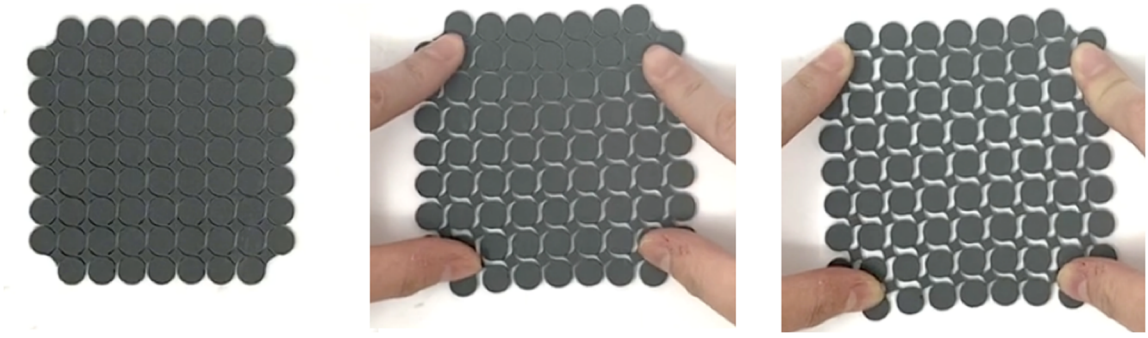

(b) Paired pattern

Figure 3.10 Deformation process of the laser cut samples.

3.4 Other planar reconfigurable tilings

This study so far confines to assemblies made from quadrilateral unit cells and their alternatives, each of which has four connection points. Moreover, there are transformable tilings that are made from shapes other than quadrilaterals. For example, the tiling pattern with hexagon and triangle tiles in Figure 3.11(a) is reconfigurable if it contains rhombus voids. The tiling pattern with triangle, hexagon and trapezium shapes in Figure 3.11(b) is also reconfigurable if it has rhombus voids inside. The key lies in the construction of planar 4*R* linkages for the voids.

If the transformation is the main design objective whereas the number of DOF is less of a concern, other shaped voids could be used. The triangle tiling pattern shown in Figure 3.11(c) has voids which are 6*R* linkages, each of which has 3 DOFs. An assembly based on the tiling pattern shown in Figure 3.11(d) would also have many degrees of freedom because the voids are either 4*R* or 6*R* linkages.

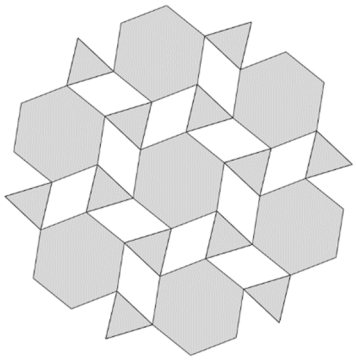

(a) Triangles and hexagons

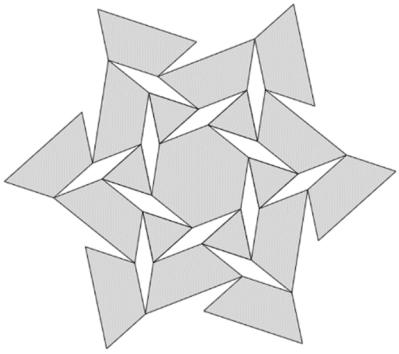

(b)Triangles, trapezium and hexagons

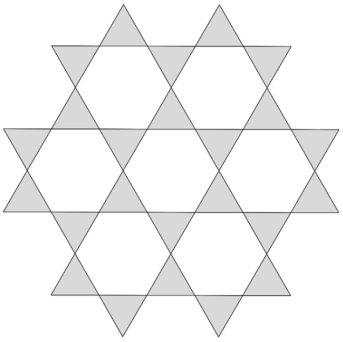

(c) Triangles

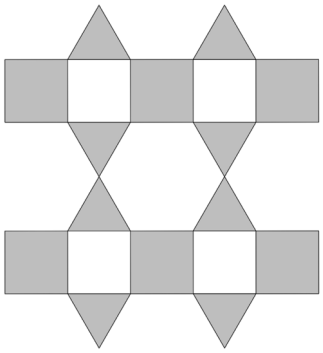

(d) Squares and triangles

Figure 3.11 Other transformable tiling patterns with various polygon tiles.

3.5 Reconfigurable tilted cuboid metamaterial

Most studies on planar reconfigurable metamaterials are based on single layer structures with in-plane deformation capability. 3D structures with multiple layers have rarely been explored. Based on the transformable tilings study in the previous section, a tilted cuboid metamaterial similar to the original modular origami model is proposed: in the folded configuration, the structure is consisted of interlinked polyhedron solids; in the deployed configuration, the slits among the polyhedron solids are transformed into parallelogram voids. Differently from the planar transformable tilings, the polyhedron units that form the cuboid tessellation are neither cubes nor prisms, but they are polyhedrons with sloped surfaces, e.g., rhombohedrons. Consequently, during the transformation the structure folds into a spatial configuration. Designing the tilt directions and angles of the polyhedron can customize the configurations of the structure, making some of them form voids in the final states while others are close packed.

The unit cell of the tilted cuboid structure is first constructed by tilting a prism along the long diagonal line. Figure 3.12 shows the tilting process and the parameters of the rhombohedron unit. The top and the bottom faces are identical parallelograms with side lengths a and b. The shape of the top and bottom faces is defined as the basic shape of the unit. We define the tilt direction along the longer diagonal line of the parallelogram, which is marked by a red arrow. The angle between this diagonal line and the side with length a is γ. Denote by h the distance between two parallel surfaces, which is also known as the unit height, and by α the tilting angle between the inclined edge of the rhombohedron and the longer diagonal line of the bottom. The inclined edge length w is

$$w = \frac{h}{\sin\alpha} \tag{3.42}$$

The corner angle of the side parallelogram plane β is related to other angles by

$$\cos\beta = \cos\alpha \cos\gamma \tag{3.43}$$

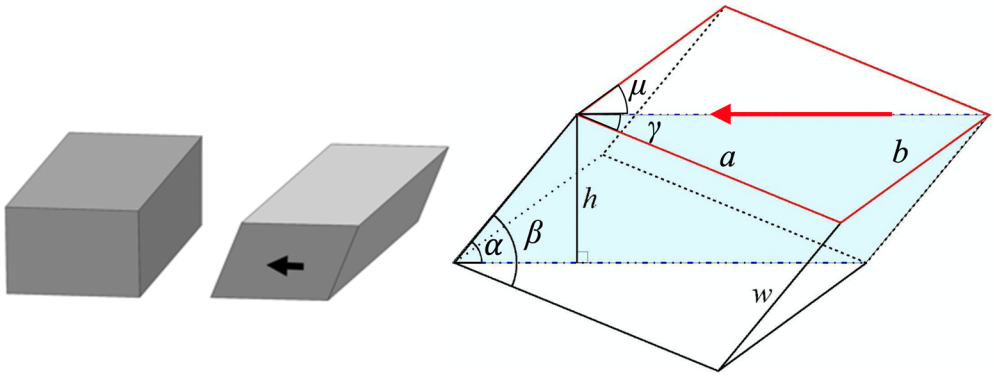

Figure 3.12 The Rhombohedron unit cell from a tilted prism.

Now connecting nine rhombohedron unit edge-by-edge using parallel rotational joints forms a structure shown in Figure 3.13. The configuration of the structure can be uniquely determined by the moving angle θ. Starting from a folded state where $\theta = 0^{o}$, the structure is close packed; then rotate the surrounding units around the central unit by the rotational joints, the structure will open to a deployed state. Finally, when $\theta = 180^{o}$ the side planes of adjacent units contact with each other and the structure locks in a grid pattern as the final configuration.

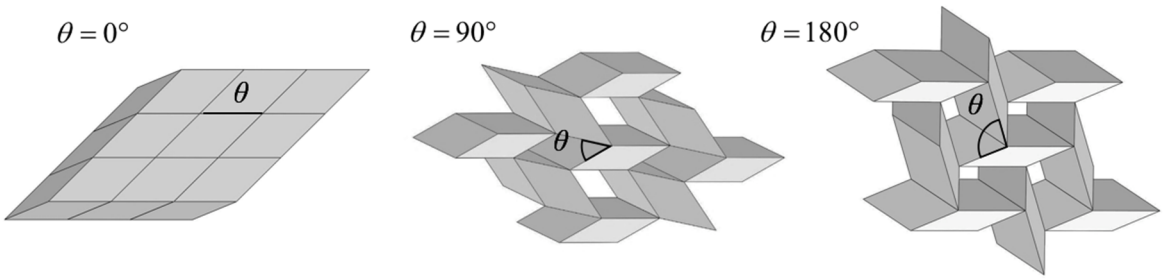

Figure 3.13 Tilted cuboid structure and its configurations during transformation.

When the structure is projected to a plane perpendicular to its joints, a 2D pattern consisted of shaded parallelograms and voids is obtained on plane P (Figure 3.14). This pattern, same as the Arrangement 1 in previous section, has been proved to be transformable with single DOF.

3.6 Configuration analysis of the tilted cuboid metamaterial

In the structure shown in Figure 3.13, each of the rhombohedron unit is determined by edge lengths a and b, angle γ, tilt angle α, unit height h and the tilt direction. These parameters can

be tuned to acquire a series of tilted cuboid metamaterials that deploy to different shapes with various orientations, cover areas and permeability. The features of different models are compared along with their motion.

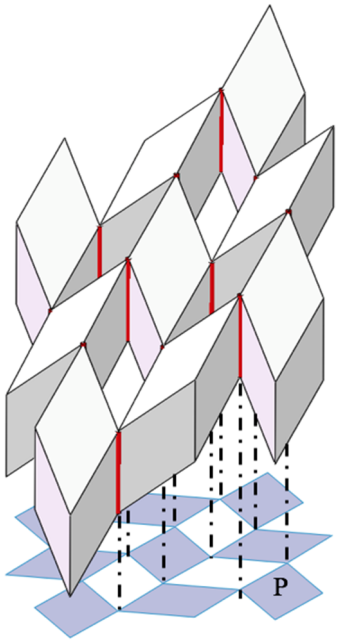

Figure 3.14 Projection of the tilted cuboid structure.

3.6.1 Tilt direction

The rhombohedron unit can be tilted in any directions theoretically. Apart from the tilt direction in Figure 3.13, if the side edges between top and bottom parallelogram faces are tilted along the shorter diagonal line of the parallelogram, the structure shown in Figure 3.15(b) is obtained. Moreover, if the tilt direction is perpendicular to an edge on the top plane, the structure made from such units is shown in Figure 3.15(c), where the angle between edge FG and edge EF is 90º. Let us name the structure in Figure 3.13 as Model 1, and the other newly obtained structures as Model 2 and 3, respectively. All three models have the same parameters $a = b =$ 20mm, h = 10mm and $\gamma = 22.5°$. For the tilting angle, Model 1 has α = 40.62°, Model 2 has α = 51.34°, and Model 3 has α = 26.57°.

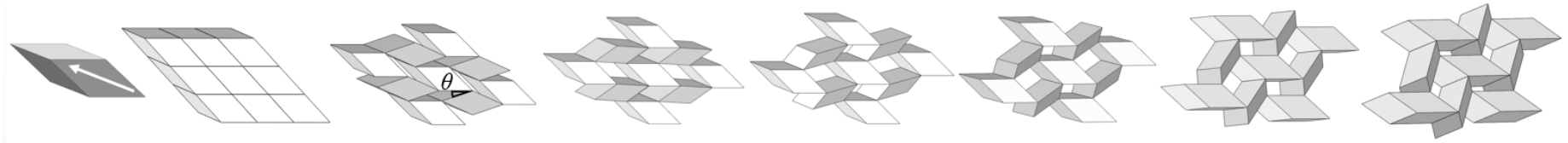

(a) Model 1

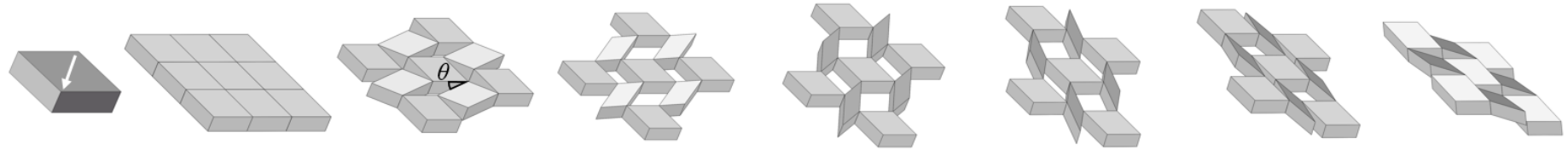

(b) Model 2

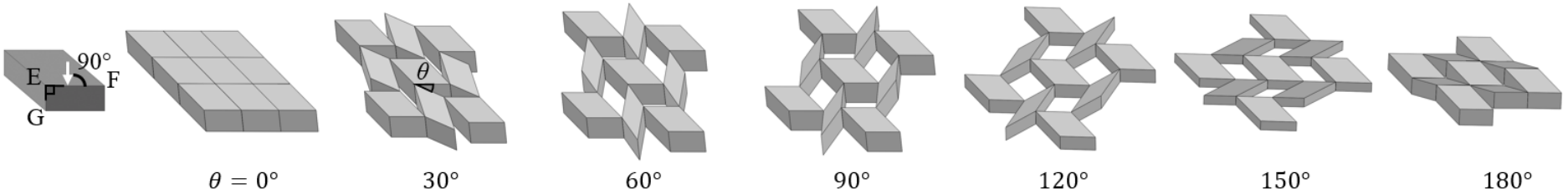

(c) Model 3

Figure 3.15 Transformation processes of models with different tilt directions.

It can be noticed that for different tilt directions, the configurations of the cuboid structures are very different during the transformation. For instance, by fixing the centre unit, Model 1 will rotate around the centre polyhedron and form an oblique square grid in its final configuration in Figure 3.15(a); for Model 2, the structure forms an oblique square grid in the halfway, and the final configuration is a long and narrow parallelogram grid (Figure 3.15(b)).

Denoted by plane P′ (marked in blue in Figure 3.16(a)), the upmost surface of the structure initially contains all the parallelogram planes of the units. During transformation, P′ contains the upper edges of every unit, which are marked in red in Figure 3.16(a). Let δ be the angle between plane P′ and the upper plane of the central unit (marked in orange). During the transformation, δ defines the twist of the structure.

If we connect the centre points N, M, O and P of the four units at the corners, and name the intersection angle between two neighbouring edges of the parallelogram NMOP as η (Figure 3.16(b)), we can use the twist angle δ, intersection angle η and area of NMOP as the indices to describe the spatial configuration. These quantities are plotted in Figure 3.16-3.17.

Consider δ versus θ in Figure 3.16(a). Model 1 has the biggest variation between the original configuration and final configuration, and the slope of δ versus θ remains steady throughout the transformation. Model 2 and 3 have a greater tendency to rotate at the beginning, yet the tendency slows down gradually. The η versus θ relationships are given in Figure 3.16(b). Models 2 and 3 have the largest η of around 90° when $\theta = 90°$ whereas the largest $\eta = 75.6°$ for Model 1 happens at $\theta = 150°$. In other words, models 2 and 3 first transform to a square profile then close to a parallelogram profile, and the fully open states take place when $\theta = 90°$. Model 1 keeps approaching a square shape but cannot fully open to $\eta = 90°$.

Models 2 and 3 have similar plane area variation (Figure 3.17). When $\theta = 90°$, these two models have the longest edge length and the biggest intersection angle, which lead to the largest

cover areas. Model 1 has the longest edge length at θ = 90° as well, but the intersection angle η keeps increasing hereafter, so the largest area is reached when θ = 100°.

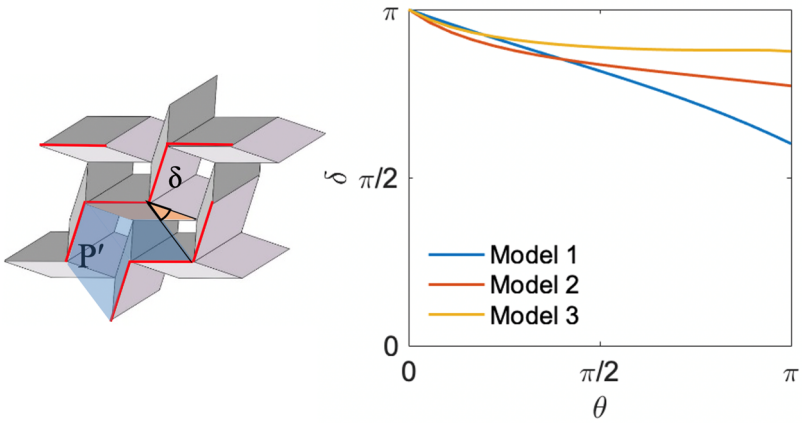

(a) Plane twist angle

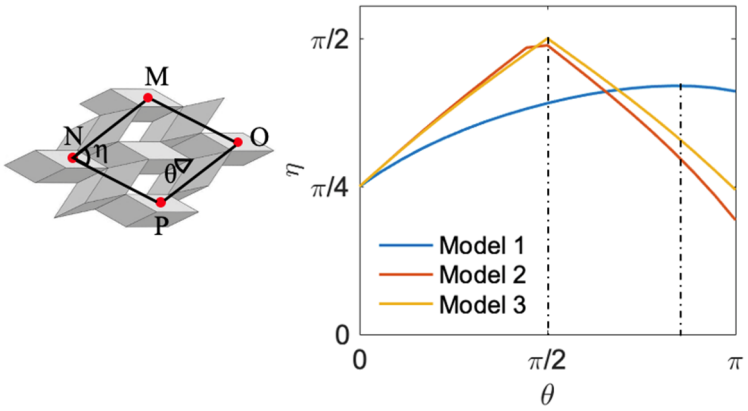

(b) Intersection angle

Figure 3.16 Structure parameters analysis of Model 1-3.

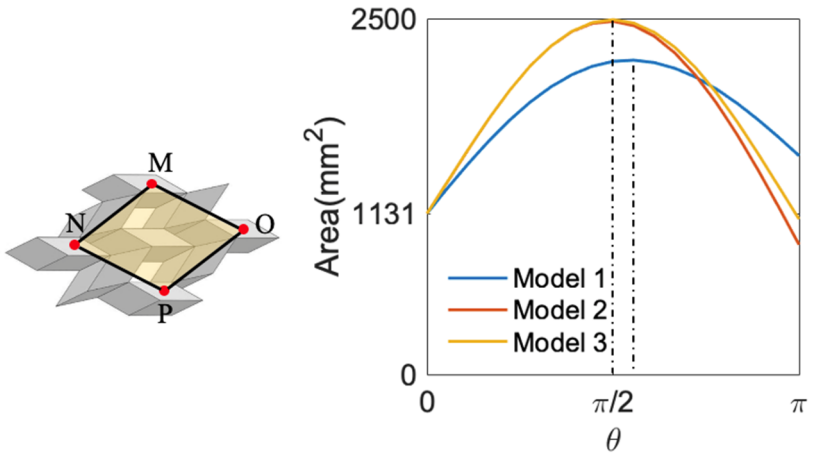

Figure 3.17 Plane area variation of Model 1-3.

3.6.2 Tilt angle and permeability

Next, we consider the influence of tilt angles. Three models are constructed with α = 52.46° for Model 4, α = 40.62° for Model 5 and α = 33.07° for Model 6. Besides the tilt angle α, the units of the models share the same basic pattern where $a = b$ = 20mm and $\gamma = 22.5°$, h = 10mm and their tilt directions are same as Model 1. Figure 3.18 shows δ versus θ and the cover area versus θ. It can be seen that starting from the same value for all three models, the twist angle δ of the final configuration is smaller for Model 6, meaning that the unit with more distortion will twist more during the transformation. In contrast, the cover area is larger with a bigger α, so an obtuse unit will lead to a bigger cover area when fully opened. It can also be observed that α only influences the range of twist angles and structure cover areas without changing the model configurations during the transformation.

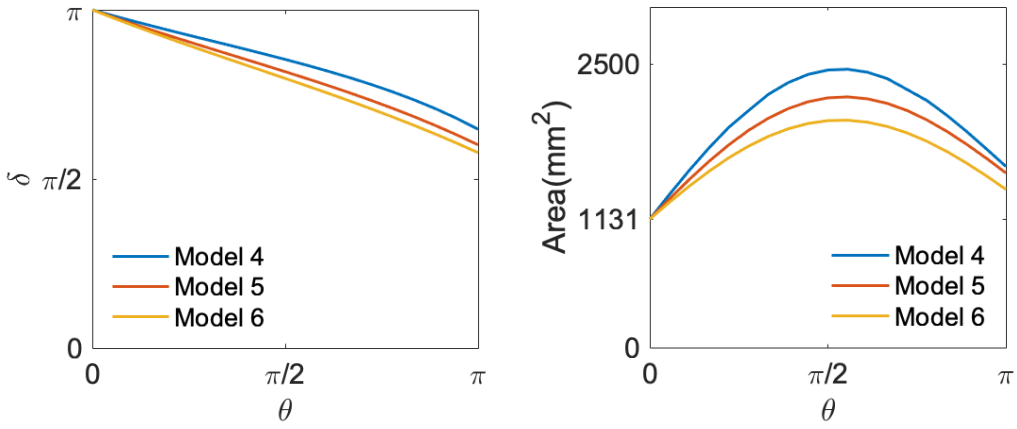

(a) Plane twist angle (b) Plane area

Figure 3.18 Structure parameters analysis of the models with different tilt angles.

Previously we treat the units as rigid bodies and the voids as planar 4*R* linkages. When the cuboid structures are folded into the final configuration where θ = 180°, for some models, every 4*R* linkage has an accessible void in the central. For instance, in Figure 3.19(a), the structure has four voids with two different orientations. These structures are defined as permeable metamaterials. The orientation of the void is regarded as the direction perpendicular

to the voids plane (e.g., plane CDEF in Figure 3.20). Another case is that, half of the 4R linkages have accessible voids while the other half don't. In Figure 3.19(b) the model has two voids with the same orientation, and the other two 4R linkages do not form voids. This is defined as semi-permeable. The last situation is that all of the 4R linkages of the model don't form accessible voids. Then the structure is impermeable. Figure 3.19(c) shows an example where no void exists.

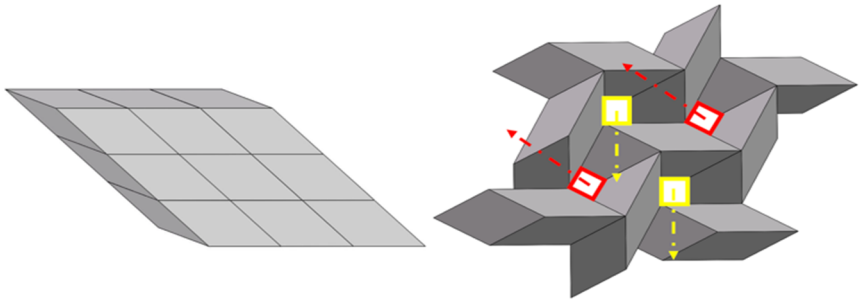

(a) Permeable structure

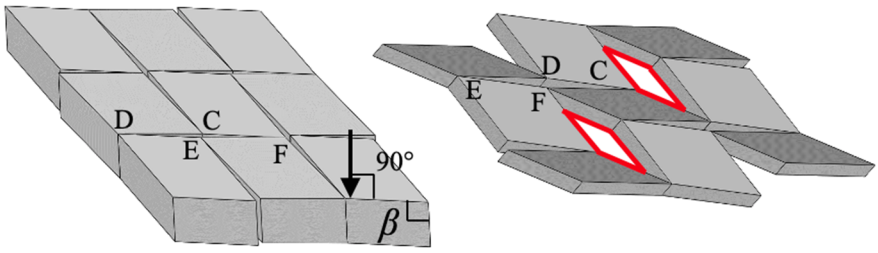

(b) Semi-permeable structure

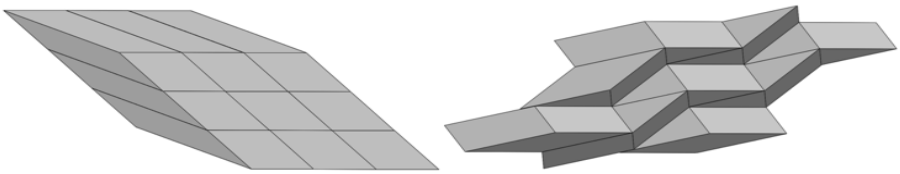

(c) Impermeable structure

Figure 3.19 Permeability of tilted cuboid structures.

The permeability is determined by several geometry parameters of the unit cell. Because of the symmetric nature of the structure, the 4R linkages on each diagonal line are the same, leading to two sets of voids with different orientations. In Figure 3.20, consider one 4R linkage that includes vertices C, D, E, F. In the final configuration where $\theta = 180°$, the side planes of each unit are in contact to its neighbour's. Therefore, edge CD, DE, EF, FC are in the same plane.

If the diagonal DF is longer than the unit side edge GF, the structure will have voids in plane CDEF. Given the parameters of a unit, the side edge length w and angle β can be derived from Eq. (3.41-42).

Since all of the units are the same, there is

$$\overline{CD} = \overline{DE} = \overline{EF} = \overline{FC} = a\,. \tag{3.44}$$

Hence diagonal length can be calculated:

$$l_1 = 2a\cos\beta\,. \tag{3.45}$$

For the other set of 4R linkages, l_2 can be derived as well. The conditions of permeability are: If $l_1 > w \cap l_2 > w$, the structure is permeable; if $l_1 > w \cap l_2 < w$ or $l_1 < w \cap l_2 > w$, the structure is semi-permeable; if $l_1 < w \cap l_2 < w$, the structure is impermeable. The range of β is (0°, 90°).

When the tilt direction is perpendicular to one edge, e.g., in Figure 3.19(b), the tilt direction is perpendicular to edge CF, on the side plane angle β = 90°. In the final configuration, FC is perpendicular to FG and l_1=0. In such case, edge FC will coincide with CD, and EF coincides with DE. This set of voids are fully closed. Note that under the given condition, no matter what basic shape of the units are, tilt angle and unit height are, the permeability of one set of voids is only corresponding to the perpendicular tilt direction.

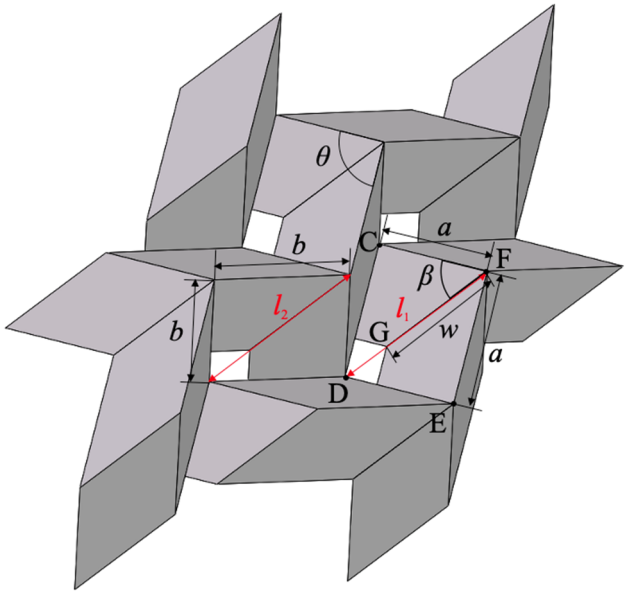

Figure 3.20 Parameters of a tilted cuboid structure.

3.6.3 Basic shapes design

All tilted cuboid structures discussed above use rhombohedron units. Other polyhedron units with various basic shapes can be utilized as long as the projection of the structure, i.e., the projection onto plane P as shown in Figure 3.14, fulfils the geometry conditions in planar transformable quadrilateral tilings. For instance, Figure 3.21(a) shows a structure consisted of polyhedron units with rectangle shape that can close pack uniformly in the final configuration. In Figure 3.21(b) the basic shape of polyhedron units is a pair of squares in different sizes. Figure 3.21(c) shows a curve edge structure in which the basic shape is a propeller. It may have advantages in resisting shear forces. The projections of all three models are shown on the left and they fulfil the geometry conditions for transformable tiling patterns.

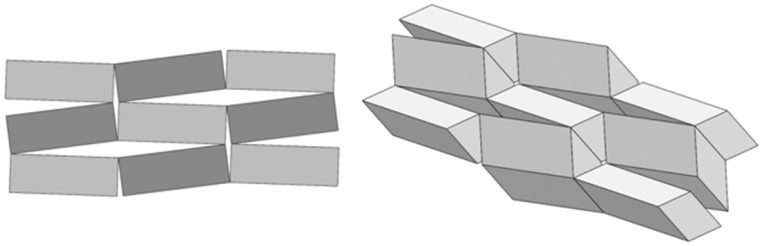

(a) Rectangle shape

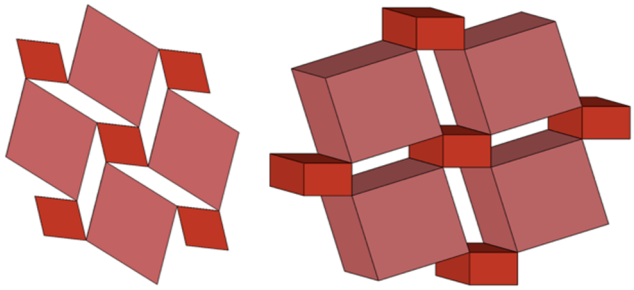

(b) A pair of squares in different sizes

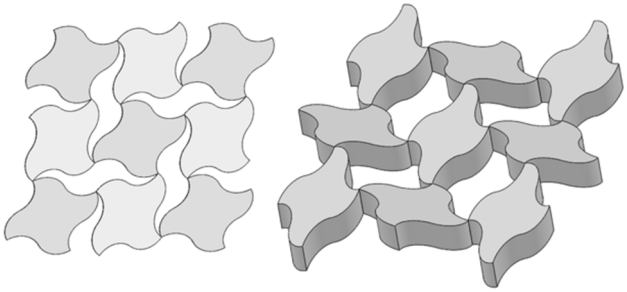

(c) Curved edge propeller shape

Figure 3.21 Tilted cuboid structures with units with other basic shapes.

3D printed samples of Model 1 and a structure with a square basic shape are fabricated (Raise3D N2 printer). Figure 3.22 shows their original configurations, open configurations and close packed configurations. The models are printed in one piece by a flexible filament called Ninjaflex, and they can deform to different configurations with the inbuilt living hinges.

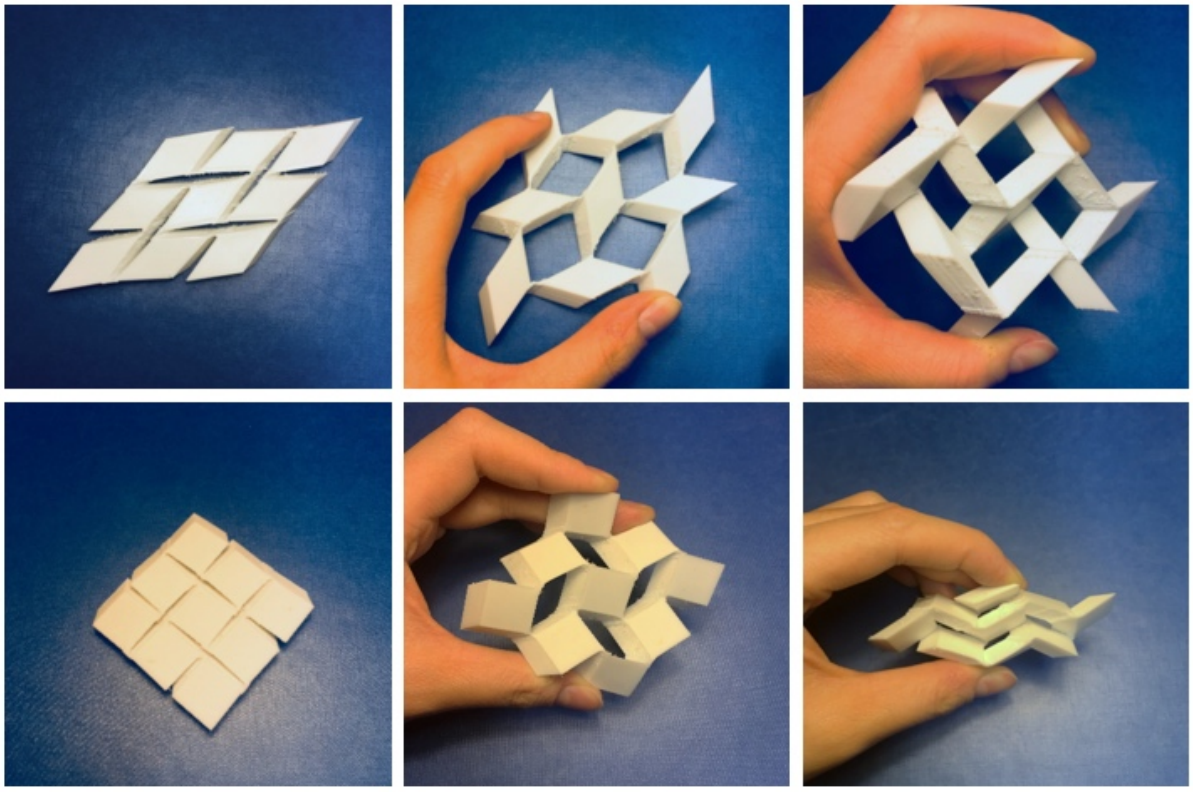

Figure 3.22 3D printed models and their different configurations.

3.7 Multilayer tilted cuboid metamaterials

3.7.1 Stacking method of the tilted cuboid tilings

The tilted cuboid structure can be extended to a larger scale by including more units in a single layer. To extend the structure spatially, a method to stack multiple layers is proposed. In Figure 3.23, a 2×2 cuboid structure with units L_1-L_4 is utilized as the lower layer. Then we duplicate the structure and name the units as U_1-U_4 for the upper layer. As Figure 3.23 shows, when the two layers are opened simultaneously, it can be observed that the edges of the upper layer and

lower layer coincide with each other in a zigzag pattern, as marked in the black lines. We can connect these coincide edges by rotational joints, e.g., the top edge of L_1 is connected with the bottom edge of U_1; L_3 is connected to U_2 and L_4 connects to U_4. During the transformation, the motion of upper layer is synchronized with the lower layer.

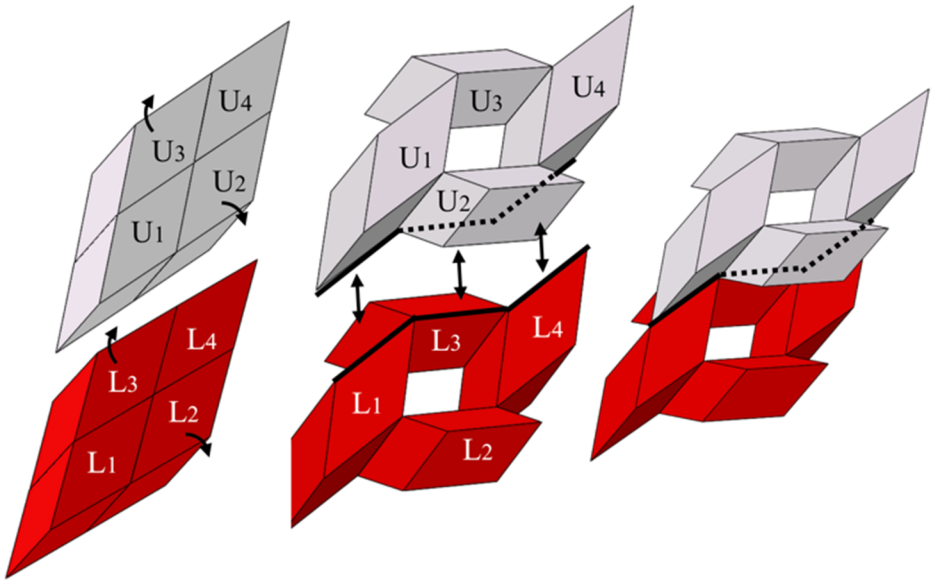

Figure 3.23 Stacking of multiple layers of the tilted cuboid structure.

The same principle applies to other structures with different tilt directions. Figure 3.24(c) shows the double-layer stacking of Model 1-3 which are introduced previously. We define the edges opposite to the tilt direction as the back edges of a unit. The side planes adjacent to these edges cannot be seen from the top view of the unit. Figure 3.24(a) shows the back edges (marked in red) of units in different tilt directions. To stack multiple layers, each unit in the lower-layer is connected to an upper-layer unit along the back edges. The red lines in Figure 3.24(b) indicate the positions of hinges in the lower layer. For different tilt directions, the hinges are always arranged in a repetitive zigzag pattern. In Figure 3.24(c) the hinged edges are marked in black.

Other metamaterials with different basic shapes and tilt angles can be constructed. Figure 3.24(d) shows a piece of metamaterial whose basic shape is a rectangle, the tilt direction is

perpendicular to one edge and other parameters are as follows: a = 20mm, b = 10mm, h = 10mm and $\alpha = \gamma = 45°$. In the initial configuration, it is a tilted cubic solid block. Along with the transformation, the material becomes permeable and fully opens to a multi-layer grid structure with the largest volume. Then it folds in another direction and eventually becomes another solid tilted cuboid with uneven surfaces.

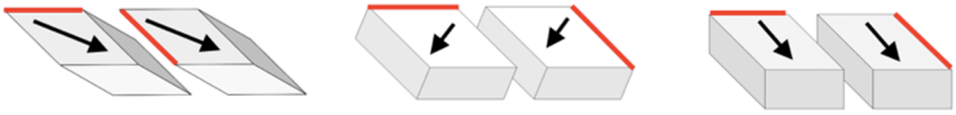

(a) Back edges of unit cells

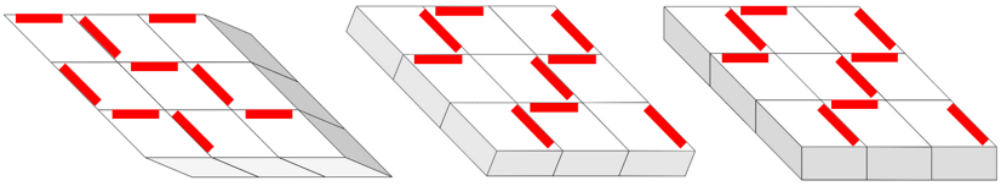

(b) Hinge positions of Model 1-3

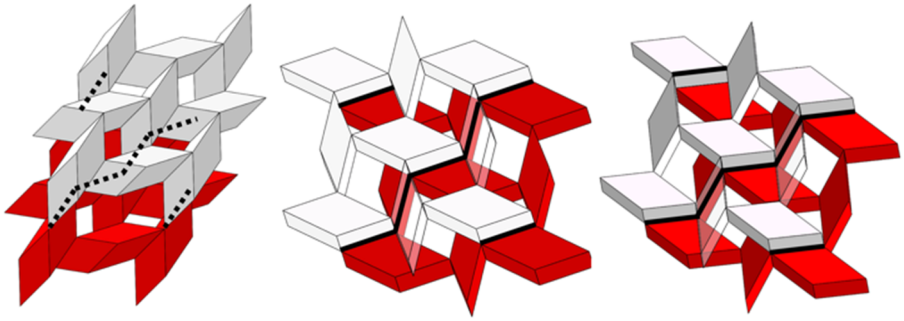

(c) Double-layer metamaterials for Models 1-3

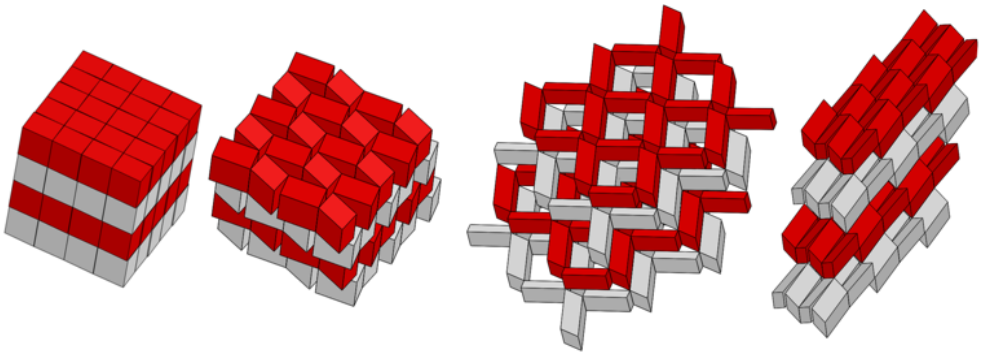

(d) A Rectangular metamaterial

Figure 3.24 Packing method of cuboid structures with different tilt directions and shapes.

3.7.2 Volumetric strain

For a single layer tilted cuboid structure, we use twist angle and planar shape variation to analyse its configuration change. Considering a piece of metamaterial, we adopt the volumetric strain to evaluate its reconfiguration capacity. For the 3×3×3 metamaterial (each layer is a Model 2 structure) in Figure 3.25(a), we connect the centre of each corner unit to form a six-sided chamber, and we define the internal area of the chamber as the volume of the metamaterial. The volume can be calculated by multiplying the area S of NMOP (plotted in Figure 3.17(c)) with the distance h between plane NMOP and N′M′O′P′ (Figure 3.25(c)). The change of distance h is shown in Figure 3.26(a). The volumetric strain can be derived as

$$e = \frac{\Delta V}{V_0} = \frac{hS - h_0 S_0}{h_0 S_0}. \tag{3.46}$$

We compare the height h and volumetric strain of the 3×3×3 metamaterials based on Model 1-3. The units of the structures have the same basic shape and height. The difference of them lies in the tilt direction of the units, as described previously. It can be seen that Model 2 has the biggest height and volumetric strain throughout the transformation process: its largest volume is three times to its original volume. Model 3 has the same tendency. Model 1 has the least height variation and a smaller planar cover area, and the volumetric strain is comparatively the lowest. The biggest volumetric strain happens at θ = 120°, for the biggest cover area is at θ = 100° (Figure 3.17(c)) and biggest height is at θ = 150°. The volumetric change shows that the metamaterial has a large deformation, e.g. the maximum volume of Model 2 can be 4 times of its packed volume. By changing the tilt direction and other parameters, we can program the volume change, which will also lead to the variation in material density.

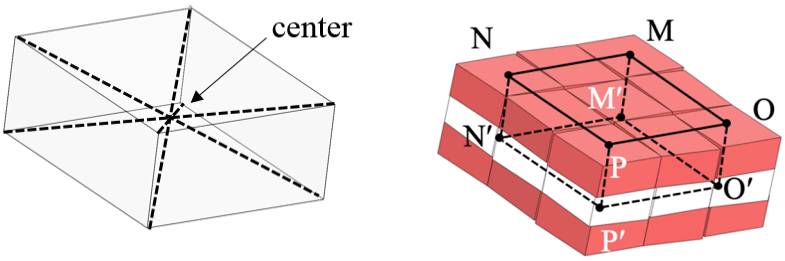

(a) Centre point of the unit and the volume of the metamaterial in its initial configuration

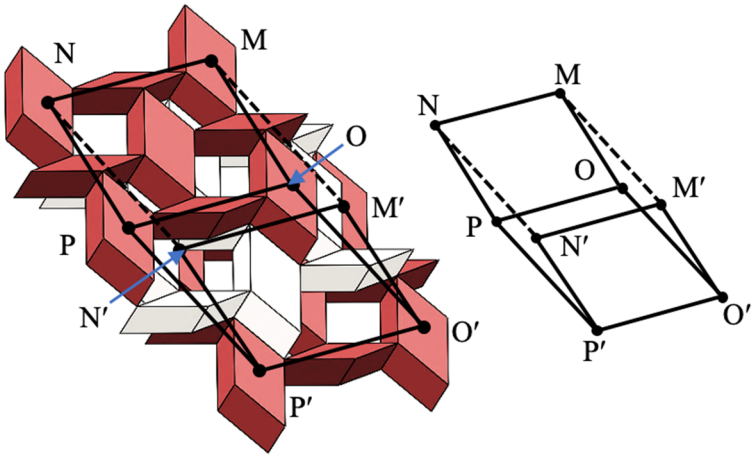

(b) The volume of the metamaterial in its deployed configuration

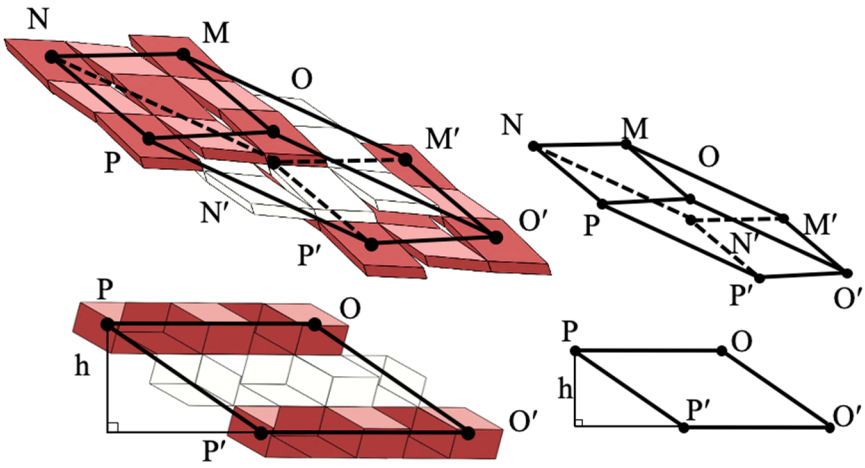

(c) The volume and the height of the metamaterial in its final configuration

Figure 3.25 The volumetric variation of Model 2 in different configurations.

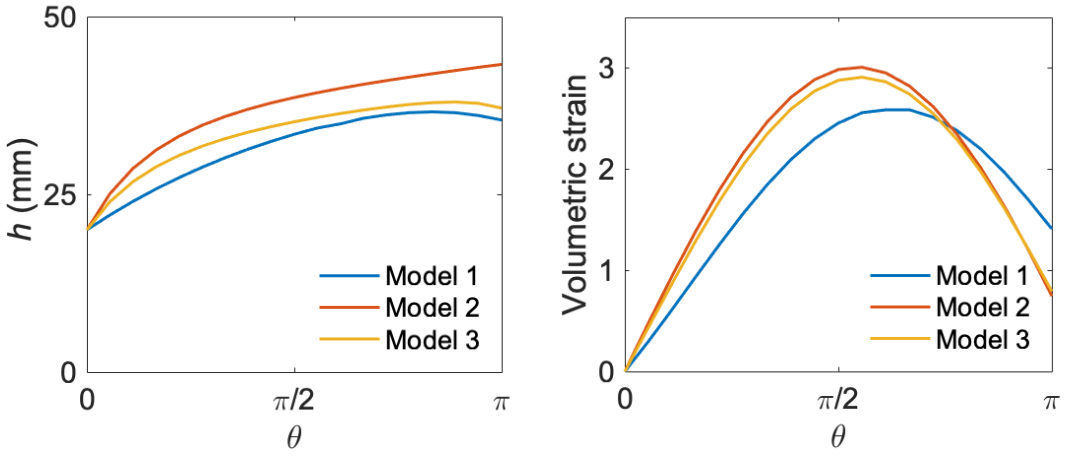

(a) Height of the metamaterial (b) Volumetric strain

Figure 3.26 The height and volumetric strain of models with different tilt directions.

3.8 Conclusion

This chapter has demonstrated a series of reconfigurable metamaterials based on planar mechanisms. In the first part, the kinematic analysis helps to expend the family of transformable tilings. The main findings include:

1) The reconfigurable conditions for quadrilateral tilings (each tile is connected to others by four vertex) is that the shape of the internal voids are all parallelograms.
2) It has been found that during the transformation, the orientation of the tiles will be changed.
3) The identical quadrilateral unit cells could be replaced by alternative or paired unit cells, which maintains the ability of reconfiguration. A special type of star tiling has a tuneable expandable ratio which can be programmed by the shape of stars.
4) Transformable tiling patterns using other polygons are analysed according to the planar linkages inhibited within the patterns.

In the second part, despite that the attention here is paid on 2D patterns, the quadrilateral prisms can be conveniently tilted in one direction to form transformable 3D metamaterials. These tilted cuboid structures can be further stacked to create multi-layer metamaterials. The metamaterial

has a large planar cover area variation and volumetric strain change, making it suitable for the design of large deformation devices and structures. The main achievements include:

1) A numerical parametric study on the tilt direction and tilt angle has been done to achieve the programmability on the plane shape, twist angle and volumetric change.
2) The permeability of the metamaterial can be designed by the tilt direction, tilt angle and the unit height.
3) The paired shape tilings and irregular shape tiles can be adopted in the tilted cuboid metamaterials, similar to the planar transformable tilings.
4) A multi-layer stacking method is provided, along with the analysis on shape transformation and height variation.

For both sections, 3D printed models are designed and manufactured. For planar materials, laser cut samples are also demonstrated. The linkage model of the tilted cuboid structure is similar to the transformable tiling structure. The crucial feature that enables the tilted structure to have spatial transformation is that, the connecting hinges are not perpendicular to the top plane of the structure. Following this inspiration, we can develop other structures whose kinematic models vary largely from their physical models. These structures can transform from planar patterns to complex spatial configurations, and can be used to develop metamaterials, devices or architectures with variable shape, stiffness and volume.

Chapter 4

Spatial Mechanism Based Kinematic Metamaterial

A majority of the current metamaterial research focus on 2D structures. 3D metamaterials with the capacity of large deformation in a predefined path are challenging to design. This chapter proposes a kinematic-based design strategy to create tuneable and programmable 3D mechanical metamaterials. Spatial linkage mechanisms with unique, predefined and reliable deformation paths are entrenched within the units of the metamaterial. Then we connect the kinematic units in a symmetric way using planar mechanisms and tessellate the structure in space to obtain a 3D metamaterial. During the construction, the building block shapes, connection arrangements and entrenched mechanisms can be programmed to provide the metamaterials with various behaviour. Some carefully chosen units have inherent kinematic bifurcations, enabling the metamaterial to switch from one deformation path to another. By utilizing these underlining deformation features, we obtained metamaterials with tuneable multi-channel permeability, tuneable porosity and programmable constant negative Poisson's ratio.

4.1 Introduction

Recent research provokes a new trend on the 3D metamaterial design that incorporates tuneability, an ability for the material's properties to be tuned through deformation, and programmability, where the properties can be adjustable through selection of design parameters. Both properties are mostly studied in 2D metamaterials with single predefined deformation path (Yu et al., 2018; Coulais et al., 2018). Existing examples include auxetic metamaterials demonstrated in previous chapters, cellular materials with re-entrant cells (Lakes, 1987) or porous 2D geometries (Bertoldi et al., 2010), designed using symmetric tessellation (Mitschke, 2013) or topology optimization approach (Schwerdtfeger, 2011). Some of them presents co-existent multiple deformation paths (Overvelde et al., 2017), making the control of deformation rather complex.

3D metamaterials with reliable large deformation are difficult to design. A few 3D metamaterials were reported inspired by origami, kirigami and biological structures. These structures usually exhibit large deformation obtained through the mechanism motion with compliant revolute or pin joints, however, none of them were initially designed from the viewpoint of mechanisms. Hence, a number of problems arose including multiple degrees of freedom (Overvelde et al., 2017), unexpected bifurcations (Gillman et al., 2018), sensitive to the boundary conditions (Javid et al., 2016), and properties coupling with the instantaneous shapes they perform (Silverberg, 2014).

In order to achieve robust programmability and tuneability for various physical properties, a strategy based on constructing mobile assemblies of 3D mechanisms is developed to design kinematic metamaterials with predefined deformation paths in this chapter. To begin with, cubes and prisms building blocks are connected edge by edge, and they are capable of rotation with respect to each other along their connection edges. The mobility of the connected modular

origami structure depends on the condition that, each loop of prisms forms a linkage mechanism which retains mobility. Unlike most of the known metamaterials that employ only the 2D patterns such as the rotating square mechanism (Grima and Evans, 2006) and scissors mechanisms (Ion et al., 2016), in this approach, spatial kinematic mechanisms such as the Sarrus linkage and the Bricard linkage are entrenched within the construction unit of the metamaterial. In addition, some units can deform into various desirable shapes through their inherent kinematic bifurcations. Then these unit cells are subsequently tessellated in three directions to create metamaterials, whose topology is guided by the kinematics so that the tuneability is strictly maintained. Using this approach, we developed a series of 3D kinematic metamaterials whose deformation paths are uniquely defined, enabling them to transform precisely into different shapes under simple stimuli.

This chapter gives three examples of 3D kinematic metamaterials with different properties. In the first example, the metamaterial provides single or multiple open channels in one or more of the orthogonal directions, which can be used to regulate air or fluid flows or to direct sound waves. In the second, we obtain a group of metamaterials that possess negative constant Poisson's ratios in three dimensions, independent of the strains, and are programmable through selecting geometry parameters of the kinematic units. The last family of metamaterials has large tuneable porous architecture. By tuning the pore shapes, sizes and topology during transformation, the elastic and acoustic feature of the metamaterials will be influenced dynamically.

This research paves the way for a new class of 3D kinematic metamaterials that can perform complex reconfiguration with superior physical properties, bringing metamaterials closer to multi-tasks applications.

4.2 Sarrus linkage based kinematic metamaterial

4.2.1 Construction strategy

To begin with, six cubes are connected edge-by-edge to form a close loop, and the cubes are able to rotate with respect to each other along the connected edges. Generally speaking, spatial close loop six-body structures are unable to move because their degrees-of-freedom (DOFs) given by mobility formula is less than one. However, when connected following the arrangement of overconstrained linkages, the structure can have one DOF. To achieve that, the six cubes are constructed to form a Sarrus linkage. The connection edges are divided into two sets facing different directions, and the three edges in each set are parallel to each other. Under such arrangement, the six-cube assembly can perform a rectilinear motion, that is to say, the cube 1 can move vertically up and down relatively to the cube 4, as shown in Figure 4.1(a). This assembly is taken as our kinematic unit. For convenience, let us refer the top and bottom cubes as end blocks, and the blue middle cubes as tie blocks.

The kinematic analysis of the Sarrus linkage has been provided in Chapter 2.2.3. The Sarrus linkage has a single DOF and a bifurcation point leading to two motion paths. For the unit shown in Figure 4.1(a), the dihedral angles θ_x and θ_y can be expressed as $\theta_x = \theta_5 - \pi$, $\theta_y = \theta_2 - \pi$ (θ_2 and θ_5 refer to the angles in Figure 2.17(a) in Chapter 2). Eq. (2.6) and (2.7) then give

$$\theta_x = \theta_y \text{ and } \theta_x = 2\pi - \theta_y, \tag{4.1}$$

respectively. Noting that the motion range for θ_x and θ_y is $[0, \pi]$ when physical interference of the tie blocks is taken into account, we obtain the motion path shown in Fig. 4.2.

A kinematic module is obtained by connecting four such units by joining the parallel edges in the pair of tie blocks with the corresponding edges of those in the adjacent unit. The parallelogram void formed in between two units functions as a planar 4*R* linkage. The module, shown in Figure 4.1(b), always has a square void at its centre. It will have single DOF, because the rectilinear motions of all units are synchronized. Looking from any of the *x*-, *y*- and *z*-

directions, the outline of the module is in a rectangular shape. Therefore, we can tessellate the module in a grid pattern in three directions to construct a 3D kinematic metamaterial. This kinematic metamaterial having a single deformation path as that of its unit. Its volume can increase from the fully close state due to the change in void sizes.

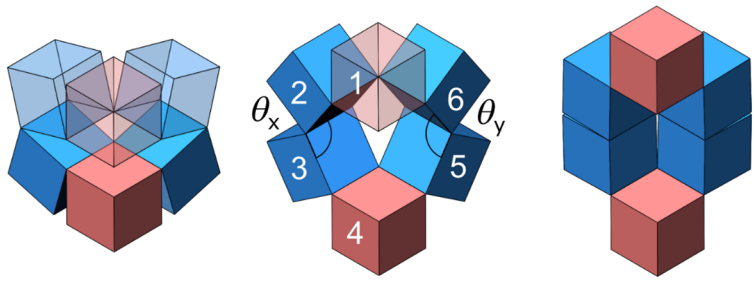

(a) Construction of a kinematic unit following the kinematic criteria of the Sarrus linkage

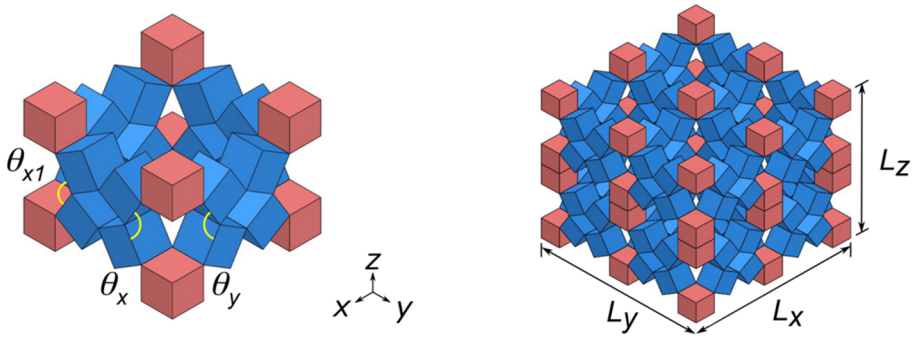

(b) Connecting units to form a kinematic module and tessellate it to create a metamaterial.

Figure 4.1 Construction of Sarrus mechanism-based reconfigurable metamaterials.

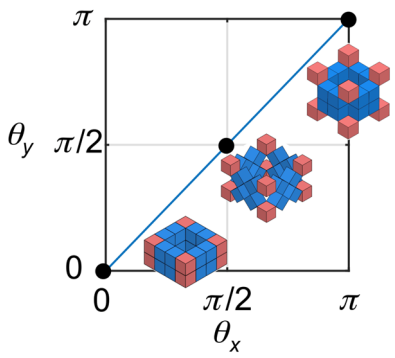

Figure 4.2 The angle relationship of θ_x and θ_y.

4.2.2 Alternative connection method

There is another way to connect the units to construct the module. The adjacent units can share the same tie blocks (Figure 4.3(a)), and there are only two ties between adjacent units. The behaviour of two adjacent units are reversed in this connection method, which is determined by the number of planar 4*R* linkages between two units. Following this rule, the four tie blocks in the first connection method can be replaced by a tessellation of ties which forms a series of planar assemblies of 4*R* linkages. Figure 4.3(b) shows two examples of the kinematic modules where the original planar 4*R* linkage with 2×2 cubes is replaced by assemblies with 3×3 and 4×4 cubes, respectively. It can be seen that when the number of cubes in the planar assembly is even, the motions of neighbouring units are synchronied and the module forms a square tube when closed. If the number of cubes in the planar assembly is odd, the neighbouring units will have reversed motion, and the closed state of the module will have uneven top and bottom surfaces because the end blocks pop up or down symmetrically. By changing the number of columns of planar 4*R* linkages, we can program the behaviour and the size of the modules.

For instance, if the kinematic units are connected following a mixed method, some units will have reversed motion with respect to others, as shown in Figure 4.3(c). Using the combinatorial design of the tie block number, the spatial textile of the metamaterial can be programmed.

4.2.3 Poisson's ratio analysis

Back to the kinematic metamaterial shown in Figure 4.1(b), it has a single mode of reconfiguration: the material generates voids in *x*- and *y*- directions and increases its volume during transformation, indicating it has negative Poisson's ratio. The Poisson's ratio is usually defined as

$$\nu_{xy} = -\frac{\varepsilon_x}{\varepsilon_y} \tag{4.2}$$

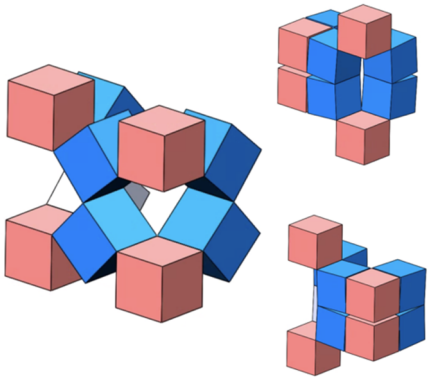

(a) Connection method with reversed motion of adjacent units.

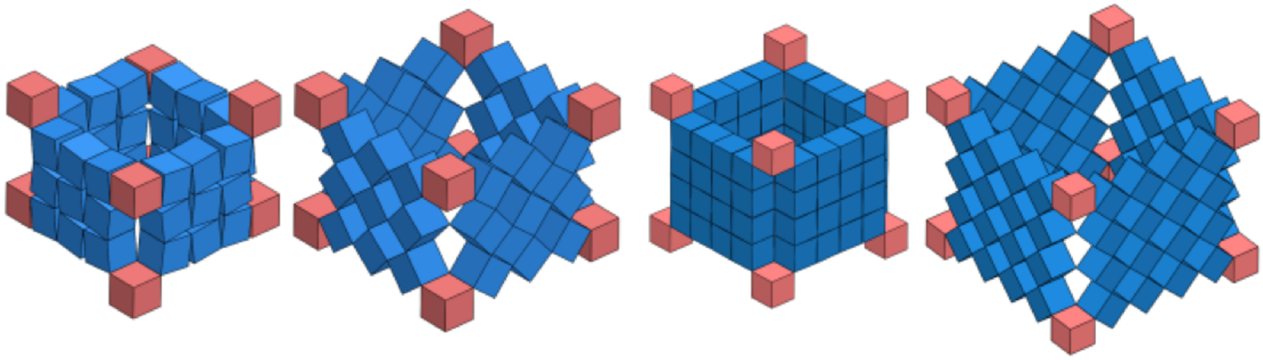

(b) Comparison of odd and even number of tie blocks.

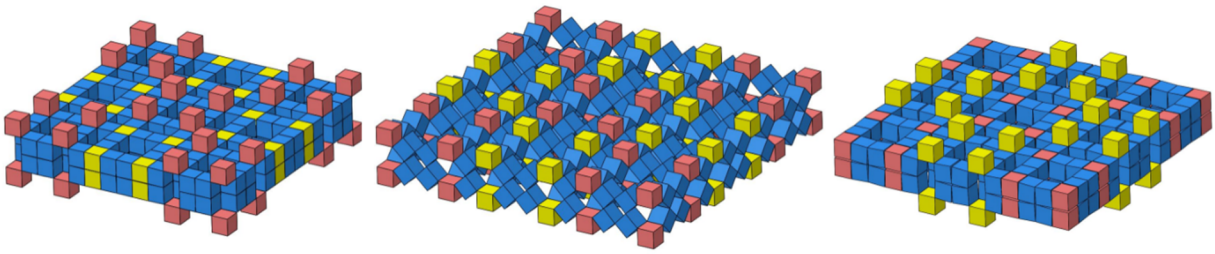

(c) Combinatorial design of the connection methods.

Figure 4.3 Different connection method of units.

where y is the direction of applied force and x is the orthogonal direction, and ε_x and ε_y are strains in x- and y- directions. One can use either the engineering strains e or true strains ε^{log} to calculate the Poisson's ratio. The former is

$$e = \frac{L_i - L_i^0}{L_i^0} \tag{4.3}$$

where L_i is the current length and L_i^0 is the initial length. And the latter is

$$\varepsilon^{\log} = \int_{L_i^0}^{L_i} \frac{\delta L}{L_i} \tag{4.4}$$

If the loading step is small enough, both are equivalent.

These strains are, however, more related to the starting conditions of the measurements and do not reflect the instantaneous conditions. The Poisson's ratio can also be calculated using

$$\varepsilon^{\text{int}} = \frac{\delta L}{L_i} \tag{4.5}$$

which is more appropriate for highly nonlinear material.

The experiment results in this research were obtained by acquiring dimensional variations of the metamaterial prototypes, and then calculating the engineering strains. This has proven to be effective in validating the theoretical expressions of dimensional change during deformation. Once the theoretical expressions were verified, we use them to calculate the instantaneous Poisson's ratios. For the kinematic metamaterial shown in Figure 4.1(b), let the dimension of the cubes be *a*, the number of kinematic modules in each direction be *n*, and the rotational variable θ_x varies between 0 and π. When loading along the *z*- direction, the total length along each direction and their initial lengths can be calculated:

$$L_x = L_y = (n+1)a + 2na(\sin\frac{\theta_x}{2} + \cos\frac{\theta_x}{2}),\ L_z = 2na(1+\sin\frac{\theta_x}{2}) \tag{4.6}$$

If we take the fully compact configuration as the initial state,

$$L_x^0 = L_y^0 = (n+1)a + 2na,\ L_z^0 = 2na \tag{4.7}$$

Hence, the engineering strains and Poisson's ratios are

$$e_x = \frac{\Delta L}{L_i^0} = \frac{L_x - L_x^0}{L_x^0} = \frac{2n}{3n+1}(\sin\frac{\theta_x}{2} + \cos\frac{\theta_x}{2} - 1),\ e_y = e_x,\ e_z = \frac{L_z - L_z^0}{L_z^0} = \sin\frac{\theta_x}{2} \tag{4.8}$$

$$\nu_{xz}^{eng} = -\frac{e_x}{e_z} = -\frac{2n}{3n+1}\frac{\sin\frac{\theta_x}{2}+\cos\frac{\theta_x}{2}-1}{\sin\frac{\theta_x}{2}},\ \nu_{yz}^{eng} = \nu_{xz}^{eng},\ \nu_{xy}^{eng} = -1 \tag{4.9}$$

The instantaneous Poisson's ratio is

$$\nu_{xz}^{\text{int}} = -\frac{\varepsilon_x^{\text{int}}}{\varepsilon_z^{\text{int}}} = -\frac{dL_x/d\theta_x}{dL_z/d\theta_x}\cdot\frac{L_z}{L_x} = -\frac{2(1+\sin\frac{\theta_x}{2})(\cos\frac{\theta_x}{2}-\sin\frac{\theta_x}{2})}{\cos\frac{\theta_x}{2}(1+\frac{a}{n}+2\sin\frac{\theta_x}{2}+2\cos\frac{\theta_x}{2})}, \tag{4.10}$$

$$\nu_{yz}^{\text{int}} = \nu_{xz}^{\text{int}},\ \nu_{xy}^{\text{int}} = -1$$

Both sets of Poisson's ratios are plotted in Figure 4.4. It can be noticed that the trends of engineering Poisson's ratios differ from that of instantaneous Poisson's ratios. However, both engineering and instantaneous Poisson's ratios in *x*- and *y*-directions are −1. They are therefore decoupled with the strains.

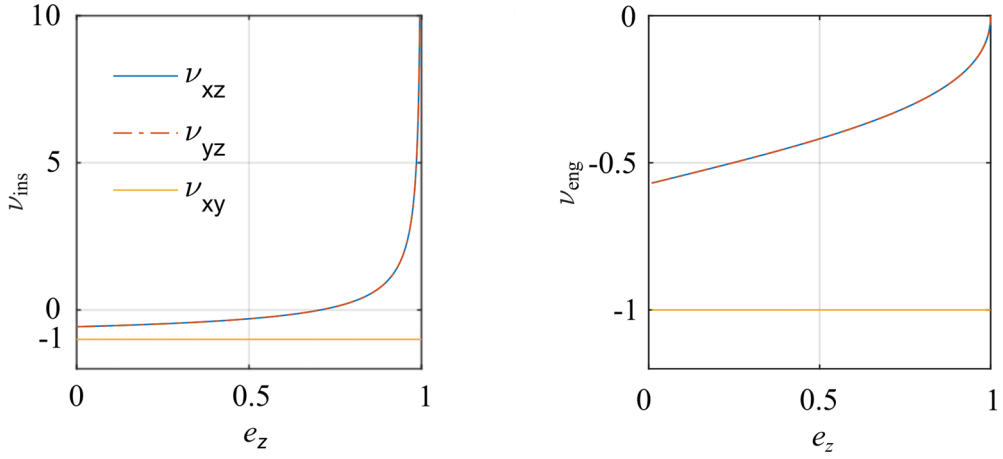

(a) Instantaneous Poisson's ratios (b) Engineering Poisson's ratios

Figure 4.4 Poisson's ratios of the metamaterial in Figure 4.1(b).

In figure 4.5(a), a kinematic metamaterial prototype consisting of 2×2×2 units was fabricated using multi-material additive manufacturing with flexible material for connection hinges (1 mm thickness) and stiffer material for cubes (edge length 8 mm). The details of fabrication process and experiments will be explained in the next section.

It was then mechanically tested under uniaxial compression in *z*-direction using a transparent loading plate. The theoretical and measured results of three Poisson's ratios as a function of the axial engineering strain e_z are given in Figure 4.5(b). The metamaterial has $\nu_{xy} = -1$ due to the symmetry in *x*- and *y*-directions, and $\nu_{yz} = \nu_{xz}$ which varies between – 0.57 and 0. The trends of experimental results correlate well with the theoretical predictions.

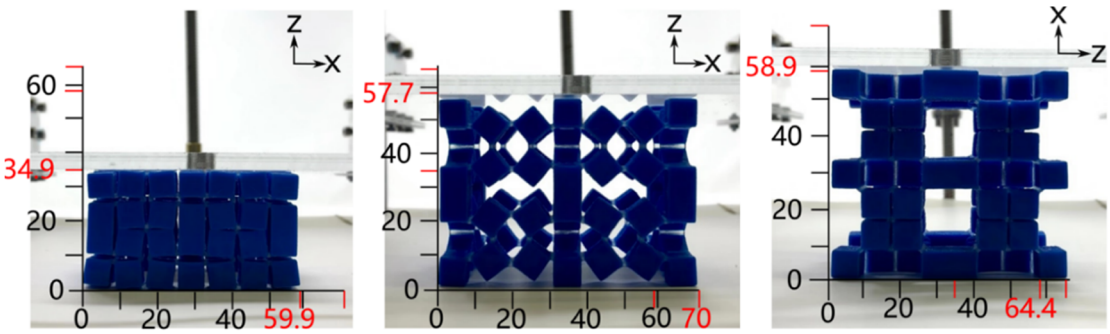

(a) 3D printed sample of the metamaterial.

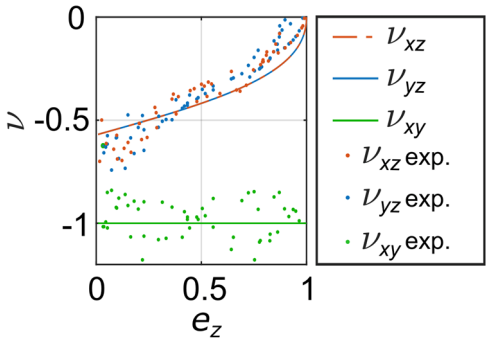

(b) Poisson's ratios of the 3D printed metamaterial.

Figure 4.5 Poisson's ratios of the metamaterial.

4.3 Fabrication and experiments of prototypes

4.3.1 Multi-process technique

Two manufacturing methods are developed for the kinematic metamaterial. The first method is a multi-process technique involves 3D printing and laser cutting. As shown in Figure 4.6(a), we first print each plane of the cube building block with snap-fit clips (two male panels and four female panels), and laser cut 0.05mm mylar sheet into small pieces with holes corresponding to the clip. Then we attach the mylar pieces on the male panels at the edges

where we want to connect with another cube. Next, using the snap-fit clips, we mechanically hold the mylar pieces between two panels. Following this method, the mylar pieces are clamped by two adjacent cubes and work as kinematic hinges. Finally, we clip the cubes one by one to assemble the metamaterial prototype. Using this method, the structure transforms exactly as the kinematic model, because the cube building blocks are rigid and the mylar hinges are thin and strong enough to mimic the perfect revolute joints.

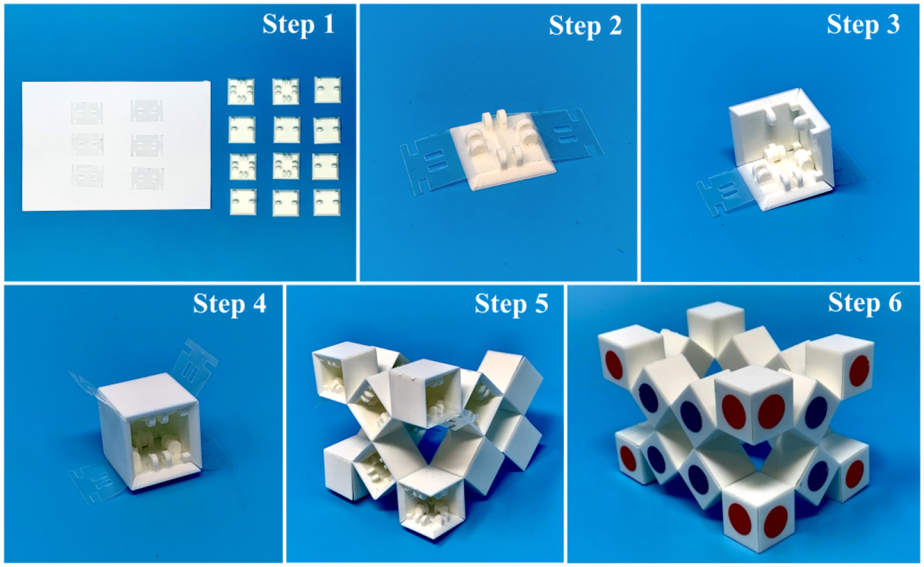

(a) A multi-process technique involves 3D printing and laser cutting.

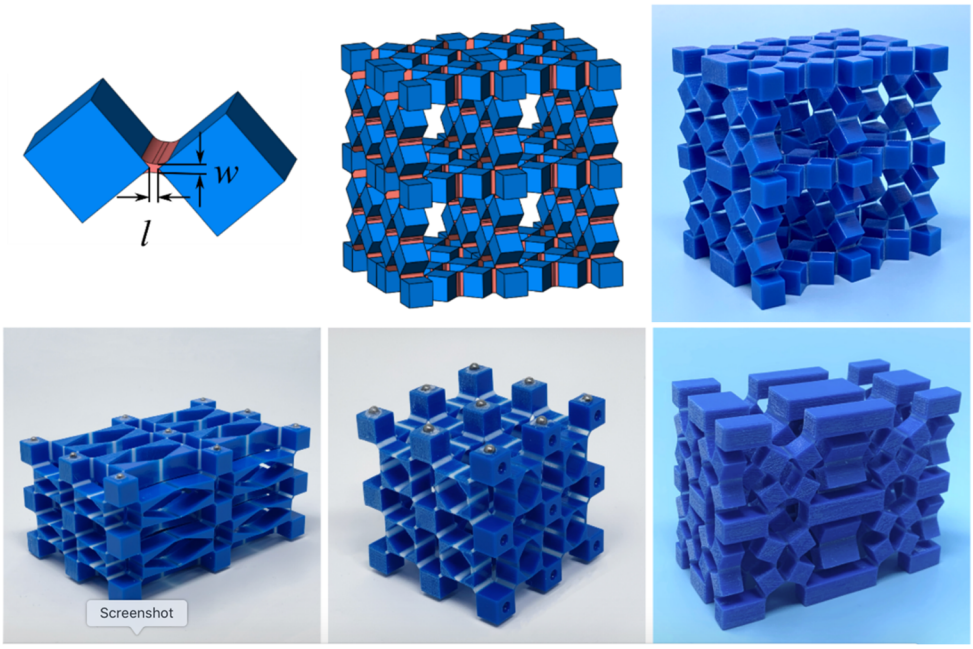

(b) A multi-material printing technique.

Figure 4.6 Two fabrication techniques.

4.3.2 Multi-material additive manufacturing technique

Although matches well with the theoretical model, the first fabrication technique requires manually assembling different parts. To improve this, we utilized an additive manufacturing technique to print the metamaterial. We used a multi-material 3D printer (Stratasys J735) to fabricate the metamaterial in one piece. In Figure 4.6(b), rigid material (Verocyan RGD841, Young's modulus E=2000-3000MPa, Tensile strength 50-65MPa) is used for cube solids (8mm) and flexible but durable material (Agilus30 Clear FLX935, Tensile strength 2.4-3.1MPa) is adopted for the hinges. A parametric study of the hinges has been done and the optimized dimensions of the hinges are w =1mm for thickness and l =1.5mm for length. This method was used to produce all prototypes that are tested for the Poisson's ratio. They were made in the intermediate state with $\theta_x = \pi/2$ to prevent the blocks from sticking together during the -3D printing.

4.3.3 Experiment setup

As shown in Figure 4.7, the metamaterial models are placed between a metal board on the optical table and an acrylic board which can move up and down by the guiding rails. For the assembled models, there is little friction between its top and bottom surfaces and the two plates, so the prototype can shrink or expand freely under compression. For multi-material printed samples, however, the friction could be considerable, which would prevent the prototypes to deform in the predicted manner. To reduce the friction, we embedded a number of 2mm diameter steel balls on the top and bottom surfaces of the end cubes, as shown in Figure 4.7(a).

In our experiments, all of the 3D printed prototypes were placed at their initial printed configurations to start with. The acrylic board was then slowly lowered by compression in z-direction, and the deformation of the metamaterial was recorded by a video camera in x-, y-, z-directions. Each prototype was tested three times. Then the videos were processed as a series

of snapshots, and the length variations in z-direction and x- or y-directions were measured by post-processing the images. Finally, the engineering strains were calculated, which were then used to obtain engineering Poisson's ratios.

Some of the deformation paths required an increase of overall height of the prototypes in z-direction, meaning that stretching of the prototype is required. Since our loading setup does not allow tensile loading, an alternative loading regime, involving compression of the prototype laterally in x- direction, was used. For example, the metamaterial shown in Figure 4.5(a) was tested in two loading regimes: the prototype was compressed from a partially open configuration where $\theta_x = \pi/2$ to fully closed configuration along z-directions, and then the sample was turned by 90° clockwise and compressed to its fully open configuration where $\theta_x = \pi$. This is feasible because, for this material, a decrease in its overall dimension in x-direction is accompanied by an increase in dimension in z- direction. An identical approach was applied to other metamaterial prototypes that have this deformation characteristic.

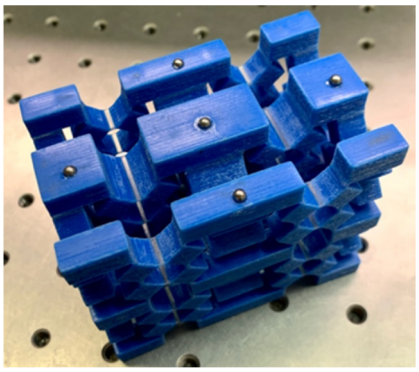

(a) Stainless steel balls were embedded on the surfaces of the material to reduce friction.

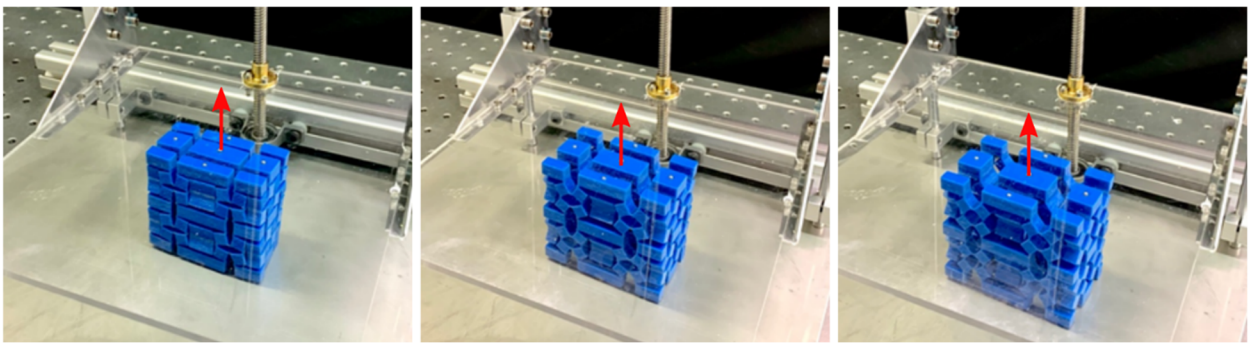

(b) Compression progress of the metamaterial with multi-directional permeability.

Figure 4.7 Experimental setups.

Figure 4.8 shows a comparison of the performances between the assembled prototype and the multi-material printed prototype. It is apparent that the experimental results of assembled prototype match more closely with those of theoretical ones. This is because the hinges in the 3D printed prototype had finite width, whereas the hinge width of the assembled prototype was much narrower (which is the reason why we produced the assembled prototype). Wider width led the hinges to twist slightly during deformation. Moreover, the hinges in 3D printed prototype stored the strain energy when the prototype deformed, whilst the energy stored in mylar sheets of the assembled prototype is almost negligible in comparison.

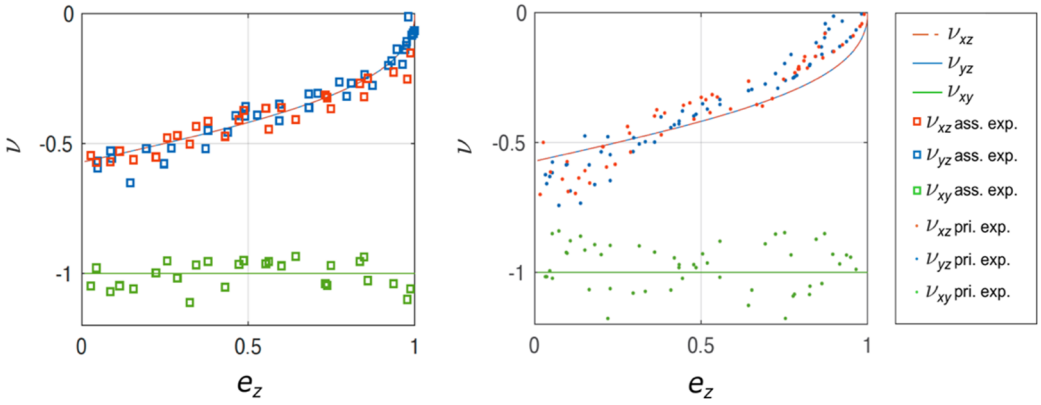

Figure 4.8 Comparison of the assembled model (left) and the multi-material printed model (right) for the Poisson's ratio of the metamaterial in Figure 4.1.

4.4 Metamaterials with multi-path reconfigurability

4.4.1 Construction strategy

The volumetric variation of the metamaterial makes it possible to be used as a tuneable permeable material. However, the directions of the flow channels are coupled, leading to the difficulty of regulating the flow. Next we shall demonstrate an alternative unit which can give rise to a metamaterial with tuneable directional permeability.

In Figure 4.9, we separate the two sets of tie blocks from the end blocks, then in one of the tie blocks, use edge *CC'* instead of *AA'* to reconnect with the edge *OO'* in the end block. To avoid collision of the ties, we use rectangle prisms as the top and bottom blocks of the Sarrus mechanism. In this new unit, the virtual diagonal plane across edge *BB'* and *CC'* forms one equivalent arm of the Sarrus mechanism.

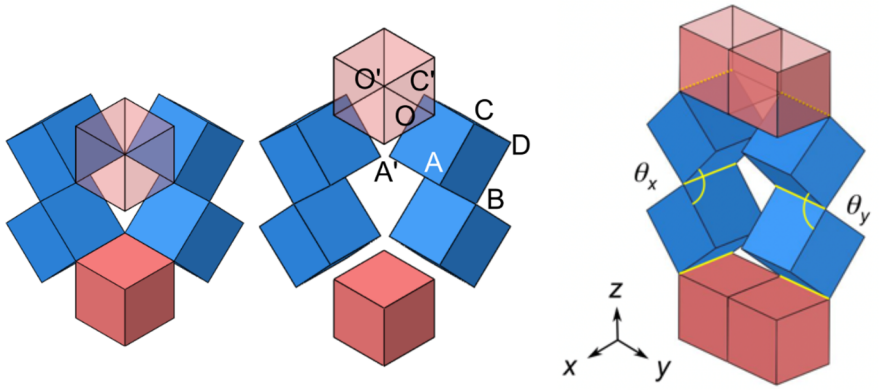

Figure 4.9 Reassembling the unit using different edges of the tie blocks.

Using the same construction method as that for the first unit, we obtain our second module made from four units. The new module and its kinematic deformation paths are displayed in Figure 4.10 together with their corresponding shapes. In general, it has one degree of freedom. However, when the angles between the two adjacent tie blocks, θ_x and θ_y, become $\pi/2$, the two ties are no longer required to swing together, i.e., it is possible for $\theta_x < \pi/2$ whilst $\theta_y > \pi/2$, or vice versa, which leads to two different deformation paths. This particular configuration is a kinematic bifurcation point. A tiny disturbance at the bifurcation point will guide the module to transform into different shapes. Kinematic bifurcation is different from multi-DOF assemblies because the former can only switch its motion paths at the bifurcation point. After a specific path is chosen, the motion can again be fully described by a single input. The first kinematic module in Figure 4.1 does not have this feature.

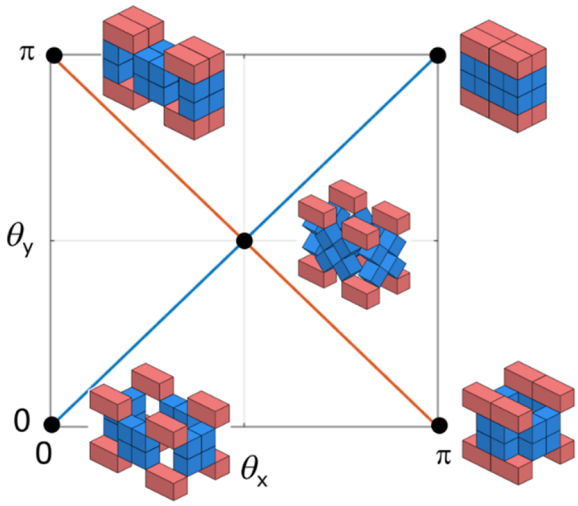

Figure 4.10 Two motion paths of the bifurcated kinematic module.

4.4.2 Multi-path behaviour and related properties

Now tessellate the module in three orthogonal directions without merging the end blocks. Instead, we place them side by side. A periodic metamaterial is obtained. Figure 4.11 shows an example of such metamaterial with 2×2×2 modules. The reason for not merging the end blocks is because the bifurcated kinematic module requires more space to deform without physical collision. The kinematic module has four deformation paths intersecting at one bifurcation point, and the 2×2×2 bifurcated metamaterial has nine deformation paths which are controlled by the θ_x angle in each unit. To show these paths more clearly, we plot them with respect to the engineering strains in two orthogonal directions *x* and *y*. During the deformation, it is observed that in the same row along the *x*-axis of one layer, the width alterations of each module are always the same. Likewise, the width of each module of the same row along *y*-direction is always equal. Therefore, starting from the bifurcation point X, the metamaterial can, for instance, become fully packed without any voids (I), expand only four modules of same column forming two open channels in *x*-direction (II), or expand all eight modules in both columns while keeping *y*-direction firmly shut (III). In total, the metamaterial can realise nine

distinct final states, I – IX, which are displayed in Figure 4.11. To transfer from one final shape to the other, it is necessary to pass through the singular state X of bifurcation.

The final states have the following two distinctive features. First, open channels can be created column by column, which is evident by II and III with channels accessible in *x*-direction only, and IV and VII where channels appear in *y*-direction. This feature can be extended to states where orthogonal channels appear such as in V, VIII, and VI, IX. Secondly, II and III provide open channels in *x*-direction while no voids appear in *y*- and *z*-directions, which indicates that creation of open channels in *x*-directions is completely decoupled with those in *y*- and *z*-directions. However, the appearance of channels in *y*-direction, as shown in IV and VII, is accompanied by channels in *z*-direction, meaning that *y* and *z* are coupled. In the bifurcating state X, there are open channels in all three orthogonal directions.

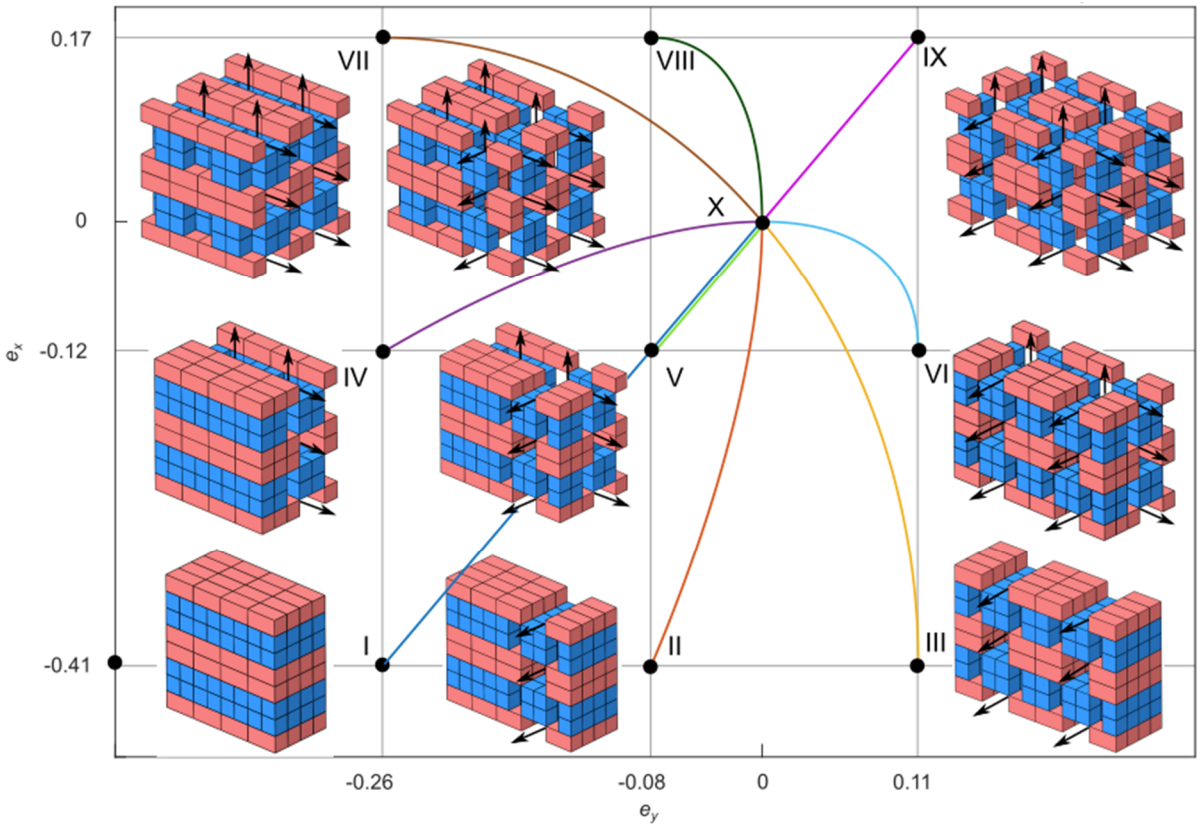

Figure 4.11 The dependence of transverse engineering strain e_x and e_y of the nine motion paths in 2×2×2 bifurcated kinematic metamaterial.

The creation of open channels indicates that this kinematic metamaterial offers multi-directional and controllable permeability through varying the number of open channels and their directions. The switch amongst states can be activated by external stimuli such as global force or triggered by built-in actuations such as shape memory polymers (Felton et al., 2013), heat driven (Breger et al., 2015) or pneumatic hinges (Sun et al., 2015). For instance, if we want to tune the material from state X to IX, we can apply instantaneous tensile force in both *x*- and *y*-directions at configuration X.

The 2×2×2 experimental prototype is fabricated in the bifurcation position using multi-material printing, so we regard X as the initial configuration where $e_x = e_y = 0$. While keeping the state in *y*- direction and changing the unit states in *x*- direction, the relationship between e_y and e_z does not change, so some modes share the same curve respectively. Figure. 4.12(a) shows the experimental results match with our theoretical predictions.

To quantify the permeability of the metamaterial in three orthogonal directions, we also calculate its void fraction f_x, f_y and f_z, the ratio between the cross-sectional areas of the void and the entire metamaterial in *x*-, *y*- and *z*-directions, respectively.

$$f_{ij} = 1 - \frac{A_{s-ij}}{A_{t-ij}} \quad (i, j = x, y, z \text{ and } i \neq j)., \tag{4.11}$$

in which $A_{s\text{-}ij}$ denotes to the surface area of the solid building blocks, and $A_{t\text{-}ij}$ the total surface area of the metamaterial in the *xy*, *zx* or *yz* planes. This term is mainly used in gas-liquid two-phase flow, and here we adopt it to demonstrate the permeability in three orthogonal directions. For an *n*×*n*×*n* module metamaterial, along each path, denote *q* and *p* as the numbers of columns in *x*-direction and *y*-directions that contain open channels, respectively. In *x*-direction, let θ_y be the dihedral angle in *q* columns, and the rest of the columns that are closed will have dihedral angle $\pi - \theta_y$. Similarly, in *y*- direction, let θ_x be the dihedral angle in *p* columns, the rest of the

columns that are closed will have dihedral angle $\pi - \theta_x$. Note that $\theta_x = \theta_y$. The surface area of the solid building blocks can then be calculated as

$$\begin{aligned} A_{s-xz(p,q)} &= 2naL_z + 2(n-q)\tan\frac{\theta_y}{2}a^2 + 2q(2-\tan\frac{\theta_y}{2})a^2, \\ A_{s-yz} &= 2naL_z + 8na^2, \\ A_{s-xy} &= 2naL_x + 2naL_y - 4n^2a^2. \end{aligned} \tag{4.12}$$

The total surface area is simply

$$A_{t-ij} = L_i \cdot L_j (i, j = x, y, z) \tag{4.13}$$

where the dimensions of the metamaterial L_x, L_y, L_z are given by

$$\begin{aligned} L_y &= 4na + p \cdot 2a\sin\frac{\theta_x}{2} + (n-p)\cdot 2a\sin(\frac{\pi-\theta_x}{2}), \\ L_x &= 2na + q \cdot 2a\sin\frac{\theta_y}{2} + (n-q)\cdot 2a\sin(\frac{\pi-\theta_y}{2}), \\ L_z &= 2na + 2na(\sin\frac{\theta_x}{2} + \cos\frac{\theta_x}{2}) \end{aligned} \tag{4.14}$$

Once the surface areas are found, substituting them into Eq. (4.11) gives the void fractions. The results are given in Fig. 4.12(b). As we discussed before, the void fractions at nine terminal states I and IX are most interesting. For example, at state II, $f_x = 0.2$ whereas $f_y = f_z = 0$, indicating that there are only channels in x-direction. At state IV, $f_x = 0$, and $f_y = f_z = 0.18$, which means channels in y- and z-directions co-exist.

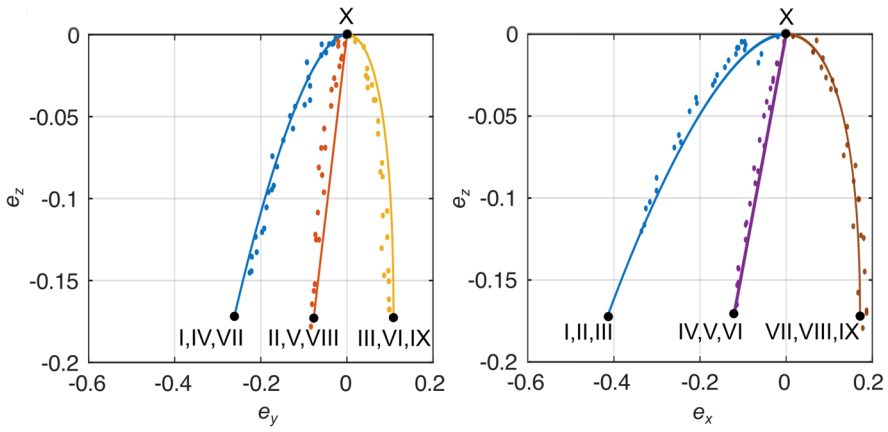

(a) Theoretical engineering strain (solid curves) and experimental validation (dots).

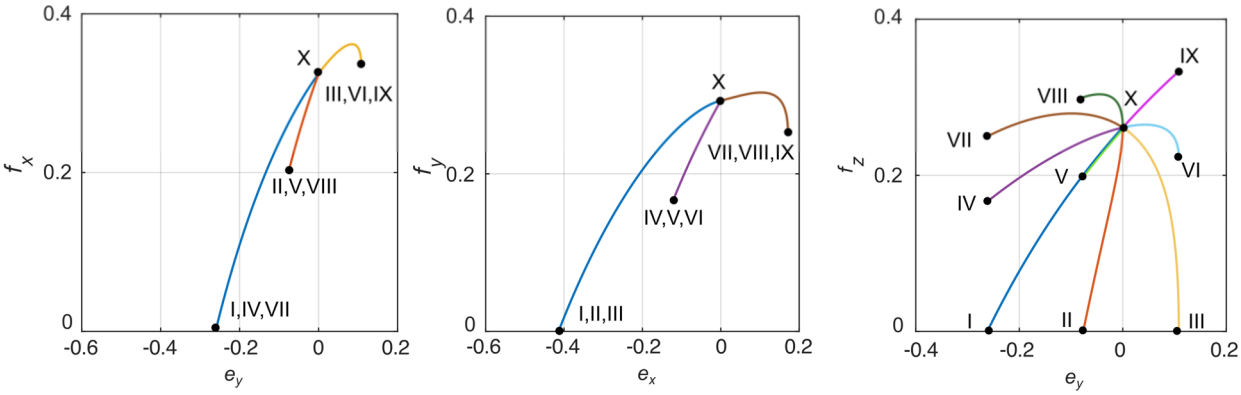

(b) Void fractions in *x*-, *y*- and *z*-directions

Figure 4.12 Evolution of the engineering strain, volumetric strain and void fractions vs. the transverse strains.

Should the number of modules be increased, the number of distinct states will increase, but the fundamental behaviour remains unchanged. For instance, for a metamaterial with $m \times n \times k$ module (in *x*-, *y* and *z*-directions), there will be $(m+1) \times (n+1)$ distinct final states.

4.4.3 Alternative structures

The unit used to create the second kinematic metamaterial is not unique. Other possible unit designs, which can also be used to construct metamaterials with similar features, are introduced as follows. In the kinematic metamaterial in Figure 4.11, the formation of directional channels in *x*- direction is decoupled with those in *y*- and *z*- directions in the nine final states, while those in *y*- and *z*- directions are coupled. The latter indicates that, if the metamaterial deforms into a state with open/close channels in *y*- directions, the channels will open/close in *z*- direction (Figure 4.13(a)).

The coupling or decoupling of formation of directional channels can be tuned by changing the shape of end blocks. For instance, if we adopt the end blocks twice of the size of the current one in Figure 4.13(b), the formation of channels in *z*- direction is coupled with either *x*- or *y*- directions, and those in *x*- and *y*- directions are decoupled. This indicates that the creation of channels in either *x*- or *y*- directions will also lead to channels in *z*- direction. If the units are

arranged in a module by rotational symmetry, Figure 4.13(c), there are always channels in *z*-direction, which is decoupled with the formation of channels in either *x*- or *y*- directions. The formation of channels in *x*- direction is decoupled with that in *y*- direction, and vice versa.

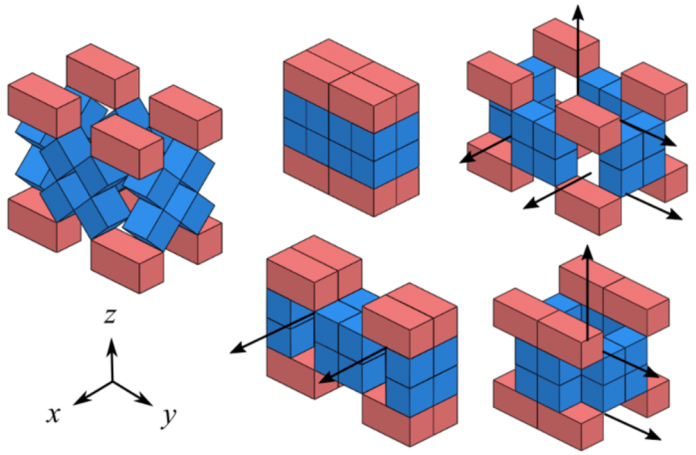

(a) Coupling in *y*- and *z*-directions.

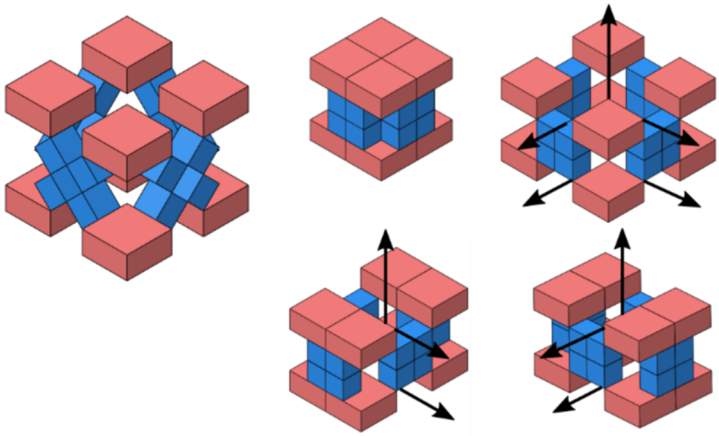

(b) Coupled permeability in *z*- and *x*-, *y*- directions.

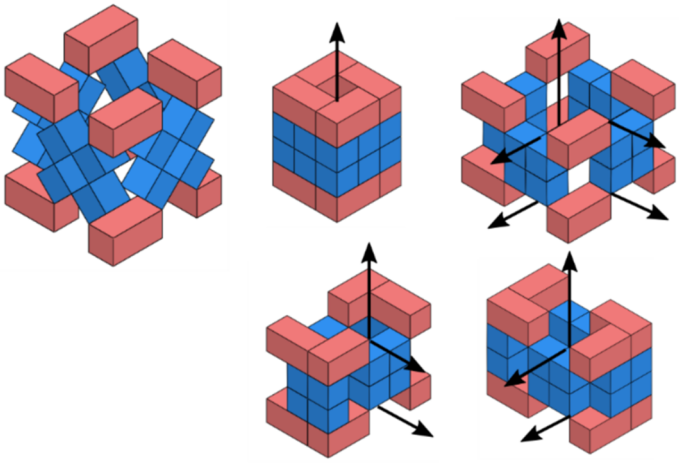

(c) Decoupling in *x*-, *y*- and *z*-directions.

Figure 4.13 Coupling and decoupling of the formation of directional channels.

4.5 Metamaterials with constant negative Poisson's ratio

4.5.1 Construction strategy

The first kinematic metamaterial has already been demonstrated to have constant negative Poisson's ratio, albeit only for $\nu_{xy} = -1$. It is possible to obtain constant negative Poisson's ratio in two or three orthogonal directions with a modified unit after appropriate use of symmetry. To realise such feature, we expand the design space by using other prism shapes as the building block of the kinematic unit. A close examination of the cubic tie blocks of the first metamaterial unit reveals that only three edges on each cube have been used for connection. This makes it possible to remove half of the cube without altering the kinematic behaviour of the unit, which results in the unit shown in Figure 4.14.

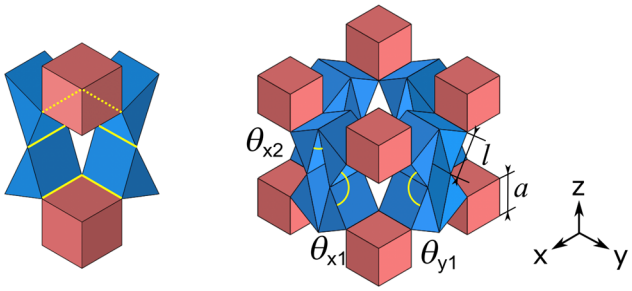

Figure 4.14 Construction of a kinematic module with constant negative Poisson's ratio.

We connect four units to form a module in the same fashion as we did previously (Figure 4.14). The kinematic behaviour of the module can be modelled using three angles: θ_{x1}, θ_{x2} and θ_{y1}. This module has three deformation paths: path 1 is given by $\theta_{y1} = 2\pi - \theta_{x1}$, $\theta_{x2} = \theta_{x1} - \pi/2$, path 2 by $\theta_{y1} = \theta_{x1}$, $\theta_{x2} = \theta_{x1} - \pi/2$, and path 3 with $\theta_{y1} = \theta_{x1}$, $\theta_{x2} = 0$. The paths and the corresponding configurations at the ends of each path are given in Figure 4.15. Noticeably two bifurcation points exist. At (π, $\pi/2$, π) paths 1 and 2 meet, whilst paths 2 and 3 cross over at ($\pi/2$, 0, $\pi/2$). Because the end blocks don't provide enough space for both tie blocks to swing toward each other simultaneously, path 2 is confined between $\theta_{x1} = \pi/2$ and π. Two terminal points of path 2, corresponding to configurations II and VI, are effectively bifurcation points. At

configuration II, the distance between end blocks reaches the maximum, and thus, the unit has the largest volume. At configuration VI, the long edges of two adjacent tie blocks coincide. Along path 3, these pairs of tie blocks remain bonded together and rotate as one. At configurations V and VII, which are two terminal configurations of path 3, the end blocks are not at the same level in *z*-direction.

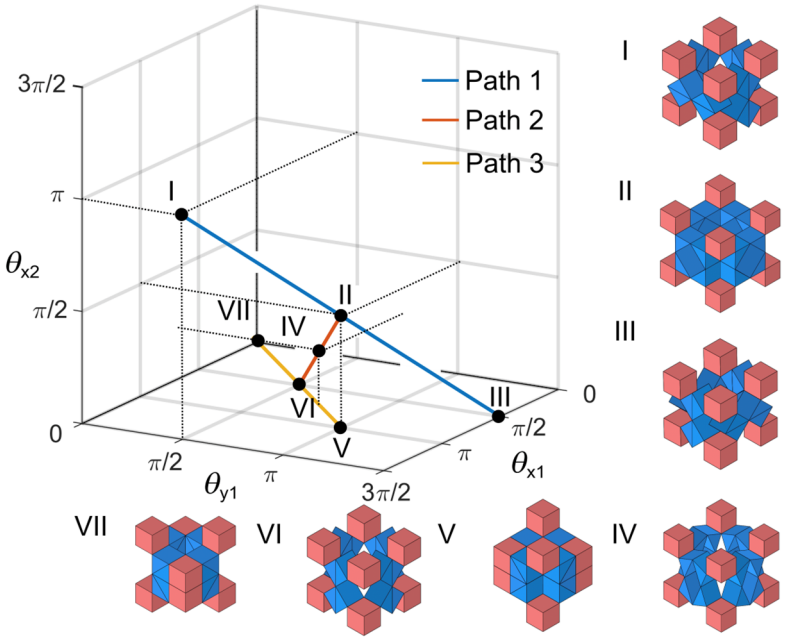

Figure 4.15 The module has two bifurcation points, leading to three transformation modes.

Tessellating the modules and merging the adjacent end blocks results in the third kinematic metamaterial. Without loss of generality, we focus on a 2×2×2 module metamaterial whose various shapes are shown in Figure 4.16. To avoid collision of prisms in adjacent layers, there must be $a \geq 2l\cos(\pi/4)$ where a is the edge length of the end cubes, and l is the length of the shorter edges of the triangular prism. We use configuration II with the maximum height as the initial state. The relation of transverse engineering strain e_x and e_z shows that, when the material is compressed along *z*-direction from the initial state, it can choose either path 1 or path 2 at the beginning since it is a bifurcated configuration. If it follows path 2 to reach configuration VI, which is the other bifurcation point, the metamaterial can then switch to follow path 3 to either reach one of the two final configurations, which have the minimum length in *x*-direction.

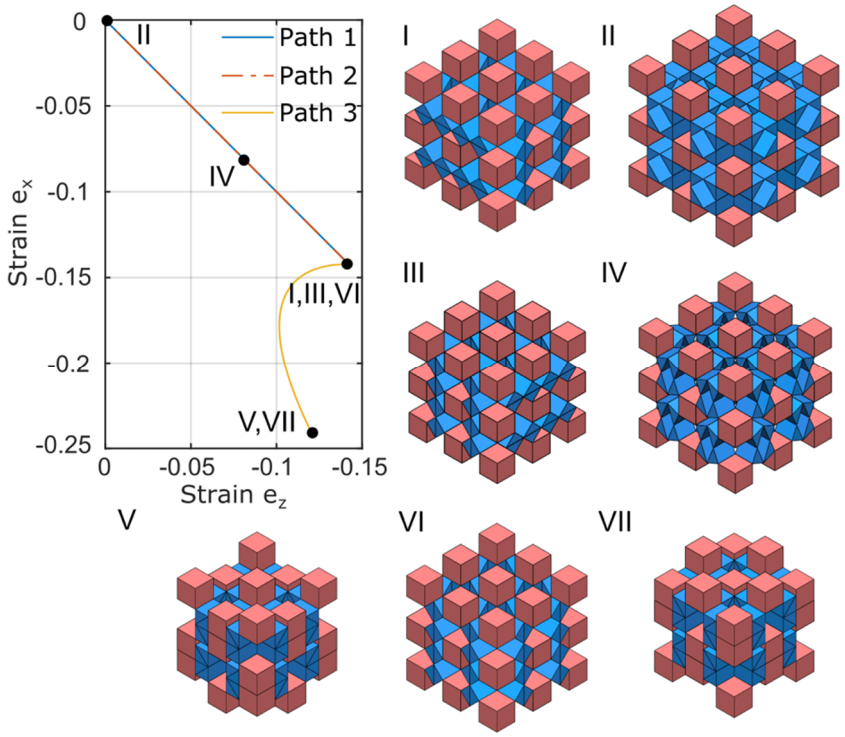

Figure 4.16 Transverse strain in *x*- direction vs. strain in *z*- direction for a 2×2×2 module metamaterial and seven salient states.

4.5.2 Poisson's ratio analysis

For an $n\times n\times n$ unit sample, along paths 1 and 2, the dimensions are (Figure 4.17(a))

$$L_x = L_y = L_z = (n+1)\sqrt{2}a + 2na\sin(\frac{\theta_{x1}}{2}). \tag{4.15}$$

Take state II as the initial state,

$$L_x^0 = L_y^0 = L_x^0 = (n+1)\sqrt{2}a + 2na\ . \tag{4.16}$$

The engineering Poisson's rations are

$$\nu_{xz}^{eng} = \nu_{yz}^{eng} = \nu_{xy}^{eng} = -1 \tag{4.17}$$

Along path 3, taking the longest distance between the top and bottom surfaces as L_z, we have

$$\begin{aligned} L_x &= L_y = (n+1)\sqrt{2}a + na(\sin\frac{\theta_{x1}}{2} + \cos\frac{\theta_{x1}}{2}), \\ L_z &= (n+1)\sqrt{2}a + na(\sin\frac{\theta_{x1}}{2} + \cos\frac{\theta_{x1}}{2}) + \left|a\sin\frac{\theta_{x1}}{2} - a\cos\frac{\theta_{x1}}{2}\right|. \end{aligned} \tag{4.18}$$

The initial state is state II to be in accordance with the first two paths, which gives

$$L_x^0 = L_y^0 = (n+1)\sqrt{2}a + 2na,\ L_z^0 = (n+1)\sqrt{2}a + 2na \tag{4.19}$$

Hence,

$$\nu_{xz}^{eng} = \nu_{yz}^{eng} = -\frac{\sin\frac{\theta_{x1}}{2} + \cos\frac{\theta_{x1}}{2} - 2}{\sin\frac{\theta_{x1}}{2} + \cos\frac{\theta_{x1}}{2} - 2 + \frac{1}{n}\left|\sin\frac{\theta_{x1}}{2} - \cos\frac{\theta_{x1}}{2}\right|}, \nu_{xy}^{eng} = -1 \tag{4.20}$$

The instantaneous Poisson's ratios along paths 1 and 2 are the same as engineering Poisson's ratio. Along path 3, the ν_{xy}^{int} is equivalent to ν_{xy}^{eng}, while those in the other two directions are

$$\nu_{xz}^{\text{int}} = -\left(\frac{\cos\frac{\theta_{x1}}{2} - \sin\frac{\theta_{x1}}{2}}{\cos\frac{\theta_{x1}}{2} - \sin\frac{\theta_{x1}}{2} + \frac{1}{n}\left|\cos\frac{\theta_{x1}}{2} + \sin\frac{\theta_{x1}}{2}\right|}\right)\left(1 + \frac{\left|\sin\frac{\theta_{x1}}{2} - \cos\frac{\theta_{x1}}{2}\right|}{(n+1)\sqrt{2} + n\left(\cos\frac{\theta_{x1}}{2} + \sin\frac{\theta_{x1}}{2}\right)}\right), \tag{4.21}$$

$$\nu_{yz}^{\text{int}} = \nu_{xz}^{\text{int}}.$$

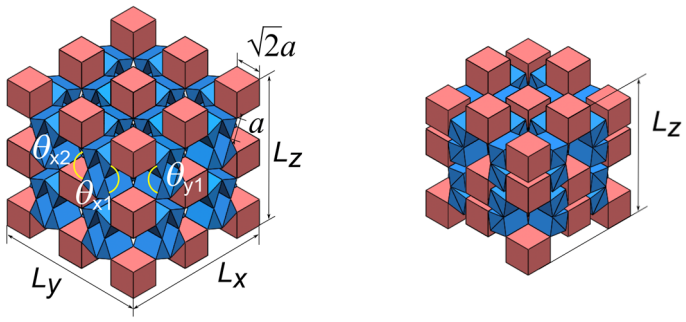

(a) Dimensions of the metamaterial

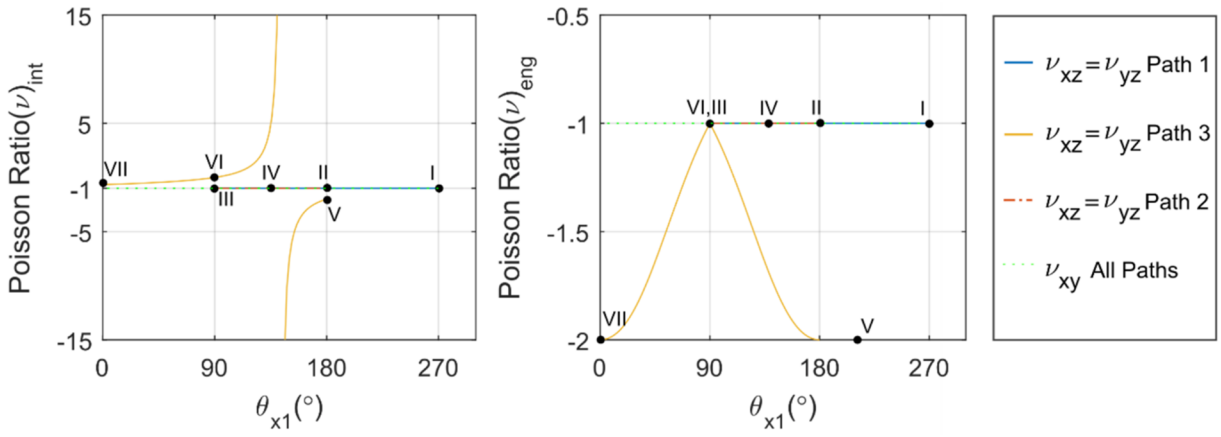

(b) Instantaneous Poisson's ratios (c) Engineering Poisson's ratios

Figure 4.17 Poisson's ratio calculation.

Figure 4.17(b-c) shows the relationship of Poisson's ratio versus rotational variable θ_{x1}. The evaluation of Poisson's ratio as a function of the axial strain e_z is plotted in Figure 4.18. The result indicates that, along deformation paths 1 and 2, the Poisson's ratios, ν_{xz} or ν_{yz}, are always -1 due to the symmetric pattern of the metamaterial. On path 3 the values remain negative, but they are no longer constant and decrease because the transverse strain keeps decreasing while the axial strain recovers. The experimental results and the theoretical curves match well except along path 3. This is due to few reasons. First, along path 3, the pair of tie blocks are bonded together and rotate as one block, which requires larger moment for them because the connection is made of two hinges. Besides, the uneven top and bottom surfaces perpendicular to z-direction, as shown in the shapes of V and VII, make it difficult to compress the material in z-direction. Finally, the test requires both tensile and compression forces since e_z gets smaller and then larger from VI to V or VII, see Figure 4.16. The strength of this structure is that, the increasing of module number doesn't bring more reconfiguration modes, and the metamaterial achieves constant negative Poisson's ratio in two modes. The only deficiency is that mode 3 still have variable Poisson's ratio ν_{xz}, ν_{yz} .

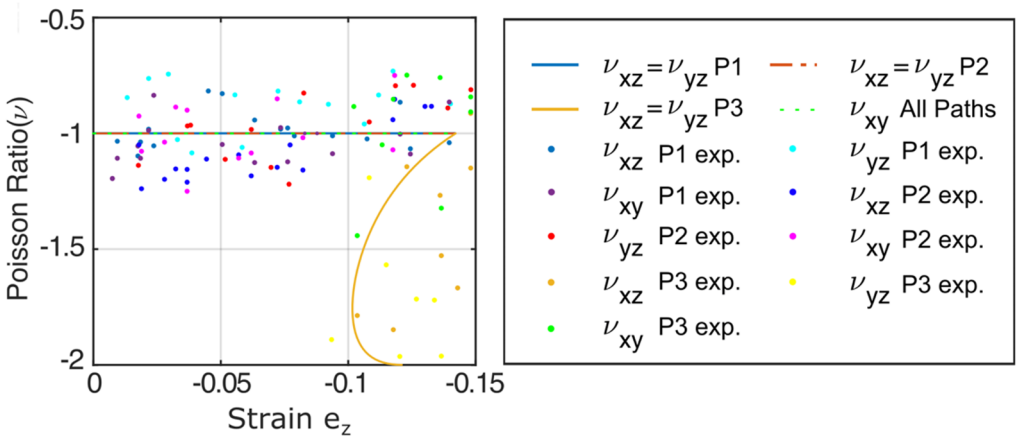

Figure 4.18 Poisson's ratios along three deformation paths.

4.5.3 Optimized design

The metamaterial obtained has only partial constant negative Poisson's ratio along its deformation path. To overcome this shortcoming, we come up with the fourth design by adding tie blocks on top and bottom surfaces of the module shown in Figure 4.14(b). Doing so results in a module that is orthotropic, as shown in Figure 4.19(a). The additional ties remove the bifurcation, making the module has a single deformation path along which it folds and unfolds in a rotational symmetry pattern (Figure 4.20).

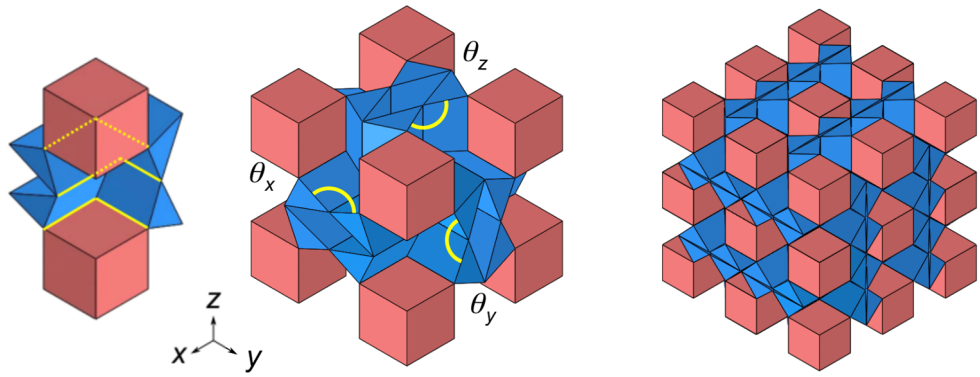

(a) A module with Sarrus linkages in orthogonal directions. (b) The constructed metamaterial.

Figure 4.19 Kinematic metamaterial with constant negative Poisson's ratio.

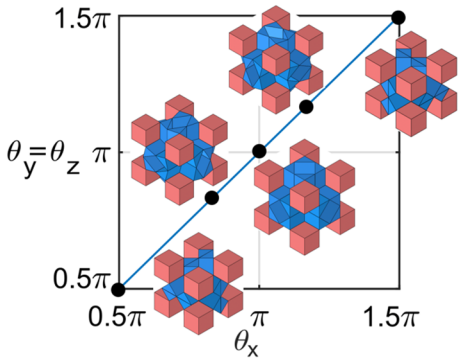

Figure 4.20 The angle relations of the kinematic module.

4.5.4 Programmable constant negative Poisson's ratio

In particular, the expansion ratios of the unit in *x*-, *y*- and *z*-directions always equal to 1 due to the symmetry. Using such modules, the kinematic metamaterial created in the same way as

previous ones will have constant negative Poisson's ratios: $\nu_{xz} = \nu_{yz} = \nu_{xy} = -1$. Hence, the resultant metamaterial is orthotropic (Figure 4.19(b)). As shown in Figure 4.20, the engineering strains and Poisson's ratios of the kinematic metamaterial are calculated:

$$e_i = \frac{2na\sin\frac{\theta_x}{2} - 2na}{(n+1)a + 2na} \quad (i = x,\ y,\ z), \tag{4.22}$$

The initial state is set as the fully open configuration where the dimensions in orthogonal directions are maximum, which happens when θ_x equals to π. Subsequently we have

$$\nu_{ij}^{eng} = -1 \tag{4.23}$$

This indicates that the metamaterial can shrink or expand at the same rate in three orthogonal directions. The experiment measurements in Figure 4.21 achieves good agreement with the theoretical results. The kinematic motion range for the dihedral angle variants is between 0.5π and 1.5π at which the tie blocks start collision, giving an overall maximum strain of 0.15.

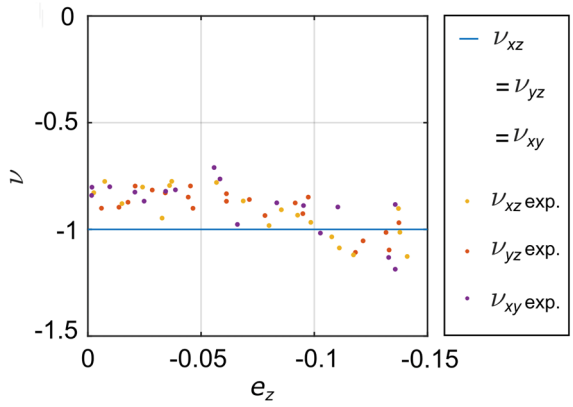

Figure 4.21 The orthotropic metamaterial with a constant negative Poisson's ratio $\nu_{ij} = -1$.

The Poisson's ratio can also be programmed by altering the dimensions of triangular prism tie blocks. Here we denote by a the edge length of the end cubes and by l_x, l_y, and l_z the edge lengths of the tie blocks, as shown in Figure 4.22. Using the dihedral angles of the unit, we have $\theta_y = \theta_2 - \pi, \theta_x = \pi - \theta_5$ (θ_2 and θ_5 are defined in Chapter 2). Although the original Sarrus

linkage has two motion paths, only the path where $\theta_5 = 2\pi - \theta_2$ is possible without physical interference, which results in $\theta_x = \theta_y$. Similarly, we can also show that $\theta_x = \theta_z$. Therefore

$$\theta_x = \theta_y = \theta_z \tag{4.24}$$

This indicates that the module has one DOF. The motion range of θ_x (θ_y or θ_z) is constrained by the interference of triangular prisms. The deformation terminates when middle connections of the tie triangular prisms collide. For the module in Figure 4.19, $0.5\pi \le \theta_y$ (or θ_x, θ_z) $\le 1.5\pi$.

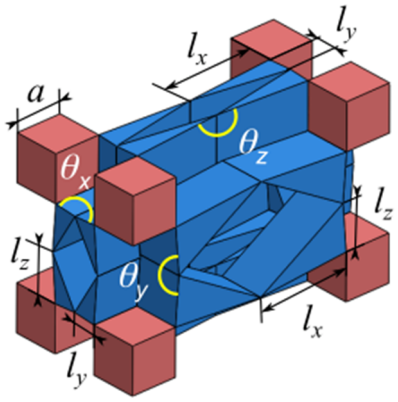

Figure 4.22 Programmable metamaterial with constant negative Poisson's ratio.

For the module of Figure 4.22, assuming that l_y, l_z and l_x are in ascending order,

$$\pi - 2\arctan\left(\frac{l_y}{l_x}\right) \le \theta_x \text{ (or } \theta_y,\ \theta_z) \le 2\pi - \left\{\pi - 2\arctan\left[\min\left(\frac{l_y}{l_z}, \frac{l_z}{l_x}\right)\right]\right\} \tag{4.25}$$

As shown in Figure 4.22, $l_y = 0.5a$, $l_z = a$, $l_x = 2a$, therefore, $0.844\pi \le \theta_x$ (or θ_x, θ_z) $\le 1.295\pi$. Hence, the corresponding strain ranges are $-0.077 \le e_x \le 0$, $-0.042 \le e_y \le 0$ and $-0.058 \le e_z \le 0$ using Eq. (4.26) that appears later. The relations of rotation variables are shown in Figure 4.23. Tessellating $n \times n \times n$ modules as we did previously, a new kinematic metamaterial is obtained. The initial state is taken as the open state when $\theta_x = \pi$. Hence, the engineering strains and Poisson's ratio are

$$e_i = \frac{2nl_i(\sin(\theta_i/2) - 1)}{(n+1)a + 2nl_i},\ (i = x, y, z), \tag{4.26}$$

$$v_{ij} = -\frac{e_i}{e_j} = -\frac{(l_i / a)(n+1+2n(l_j / a))}{(l_j / a)(n+1+2n(l_i / a))} \quad (i, j = x, y, z \text{ and } i \neq j) \tag{4.27}$$

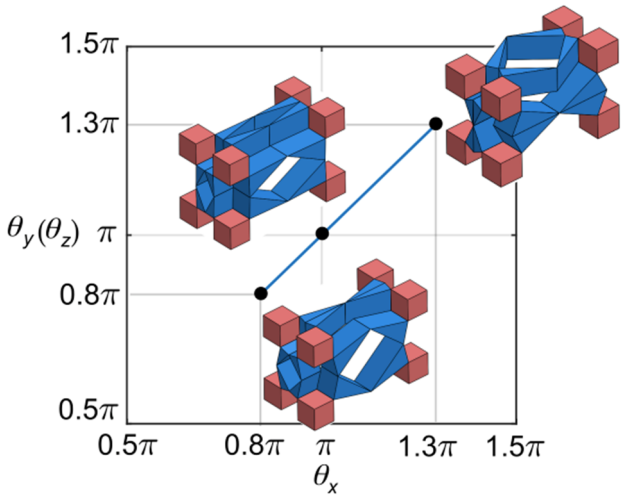

Figure 4.23 The angle relations of a programmable kinematic unit.

It becomes apparent that v_{ij} is independent of the deformation because it does not contain kinematic variable θ_i which defines the motion. v_{ij} is always negative and is predetermined by the ratios amongst edge lengths of end cubes and tie blocks. When n is sufficiently large, v_{ij} converges to l_i/l_j. When n = 2, the Poisson's ratios are v_{xz} = –0.7, v_{yz} = –1.273, v_{xy} = –1.818. The measured results of a 3D printed prototype are shown in Figure 4.24(a), which validates our findings.

We can also calculate the instantaneous Poisson's ratios:

$$v_{ij}^{\text{int}} = -\frac{l_i(1+\frac{1}{n})+2\frac{l_i l_j}{a}\sin\frac{\theta_x}{2}}{l_j(1+\frac{1}{n})+2\frac{l_i l_j}{a}\sin\frac{\theta_x}{2}} \tag{4.28}$$

The two results are compared in Figure 4.24. Although the instantaneous Poisson's ratios are related to the angle θ_x, they remain approximately constant for the entire deformation range (fluctuation range 3.6%). Therefore, we conclude that both engineering and instantaneous Poisson's ratios have the same constant negative values, which can be programmed by changing the dimensions of construction blocks.

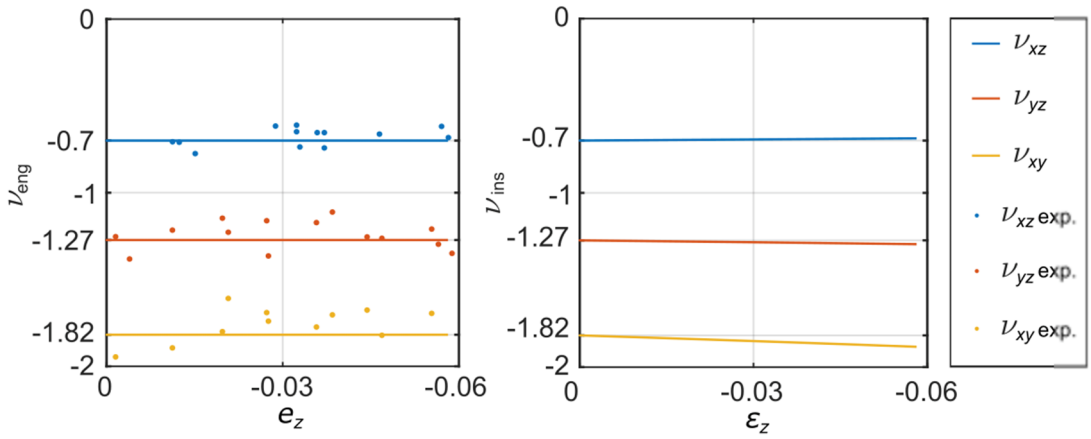

(a) The engineering Poisson's ratio. (b) The instantaneous Poisson's ratio.

Figure 4.24 Constant poisson's ratios of the programmable metamaterial.

The dependence of ν_{ij} on l_i/a and l_j/a when $n = 2$ is given in a contour plot in Figure 4.25, which provides the critical geometrical parameters to tune the value of Poisson's ratios as desired.

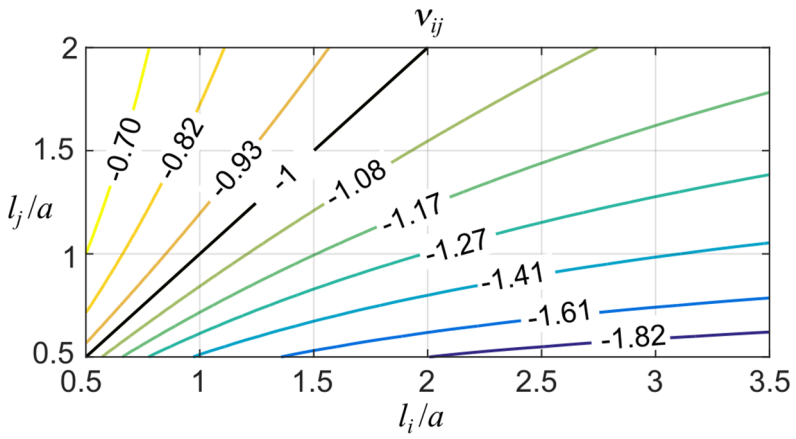

Figure 4.25 The dependence of Poisson's ratio vs. the dimensions of triangular prism tie blocks.

4.6 Metamaterials with tuneable porosity

4.6.1 Construction strategy of Bricard mechanism-based metamaterials

So far, we have demonstrated that, using units formed by kinematic mechanisms, a series of reconfigurable metamaterials with distinctive mechanical features can be obtained. However, the kinematic mechanism used is not confined to Sarrus linkage with rectilinear transformation. Many more elaborate mechanisms can be adopted, which further broaden our design space.

To illustrate this, we introduce another mechanism consisting of six identical equilateral triangular prisms of height *h* and base edge *a*, each of which is connected to its two neighbours via edges to form a three-fold Bricard linkage, as shown in Figure 4.26(b), with three planes of symmetry and a single DOF. Its representation using DH notation is given in Figure 4.26(a). The geometric conditions are

$$\begin{aligned} &a_{12} = a_{23} = a_{34} = a_{45} = a_{56} = a_{61} = h, \\ &\alpha_{12} = \alpha_{34} = \alpha_{56} = \alpha,\ \alpha_{23} = \alpha_{45} = \alpha_{61} = 2\pi - \alpha, \\ &R_i = 0\ \ (i = 1, 2, ..., 6), \end{aligned} \tag{4.29}$$

where *h* and α are known constants. Substituting Eq. (4.29) into Eq. (2.3) in Chapter 2 yields

$$\begin{aligned} \theta_1 &= \theta_3 = \theta_5, \\ \theta_2 &= \theta_4 = \theta_6, \end{aligned} \tag{4.30}$$

and

$$\cos^2\alpha + \sin^2\alpha(\cos\theta_1 + \cos\theta_2) + (1+\cos^2\alpha)\cos\theta_1\cos\theta_2 - 2\cos\alpha\sin\theta_1\sin\theta_2 = 0. \tag{4.31}$$

In the unit shown in Figure 4.26(b), $\alpha = \pi/3$. If we use φ and ψ, the dihedral angles between two neighbouring prisms, to replace kinematic variables, we have $\varphi = \theta_1 - \pi$ and $\psi = \theta_2 - \pi$. Eq. (4.31) then becomes

$$1 - \sqrt{3}(\cos\varphi + \cos\psi) + 5\cos\varphi\cos\psi - 4\sin\varphi\sin\psi = 0 \tag{4.32}$$

which is plotted in Figure 4.26(c). $0 \le \varphi \le \pi/3$ whereas $0 \le \psi \le \pi$ if physical interference between two adjacent prisms during motion is taken into account. No deformation bifurcation is detected within the motion range.

It can be noted that the dimensions *h* and *a* of the prisms do not appear in the relationship, and thus, these parameters can be chosen without altering the kinematic behaviour of the unit.

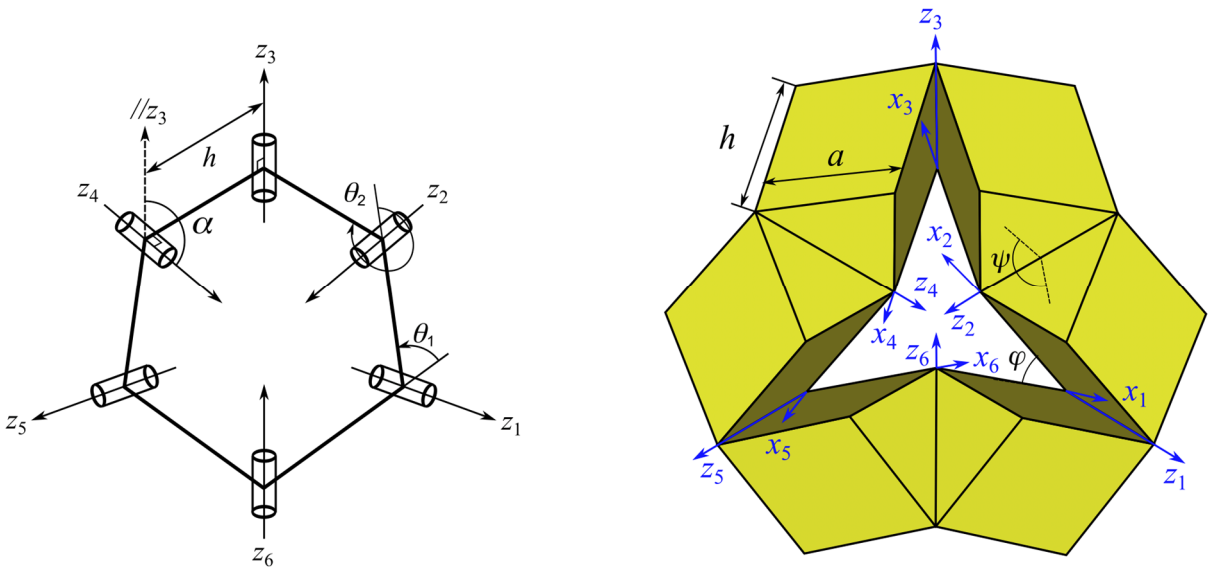

(a) The three-fold symmetric Bricard linkage (b) Coordinate systems under DH notation

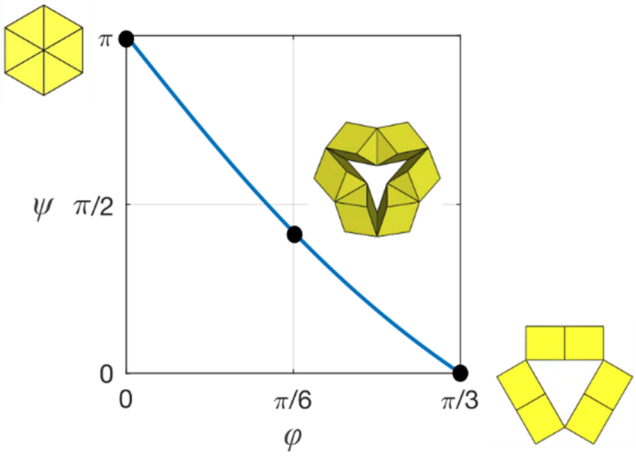

(c) Kinematic relationship between dihedral angles

Figure 4.26 Kinematic analysis of the Bricard linkage-based kinematic unit.

When two units are connected by a pair of edges highlighted in Figure. 4.27(a), these edges, plus the edges between the pairs in each of the units, are always parallel, which then forms a

planar four bar linkage. Hence, the single DOF of the yellow unit is passed on to the red unit. The assembly remains to have mobility one. The same is true when more units are joined in the same way, resulting in the one DOF assemblies shown in the bottom right of Figure 4.27(a). If we have two identical assemblies, they can then be connected via spherical joints at the coplanar vertices of the prisms in these two assemblies, forming a two layered assembly. The top view of the resultant assembly is shown in Figure 4.28(a), with these spherical joints being highlighted. It can be noted that the coplanar spherical joints take a tessellation pattern consisting of a series of hexagons shown in green. Assuming that the single DOF of a unit is frozen, the edge lengths and the shape of the small hexagons will cease to vary. Since the small hexagons are triangulated via the longer edges, these lengths will also cease changing with the frozen DOF. Therefore, we can conclude that the two layered assembly cannot change its shape. In other words, the two layered assembly has only one DOF, the same one as that of the unit. We can extend this approach to indefinite number of layers, leading to a metamaterial that can possess as many units as required whilst maintaining the single DOF.

A variant of this metamaterial can be obtained by modifying the building blocks. Figure 4.27(b) shows units consisting of six truncated equilateral triangular prisms, each of which has one corner sliced off by an equilateral triangle of side length c. The six corner points of the unit, marked by black dots, remain co-planar, but the three pairs of parallel edges, marked by white lines, are, created by the slicing. The remaining construction method is identical to those of the original assembly. The corresponding diagrams are given in Figure 4.27(b) as well as Figure 4.28(b).

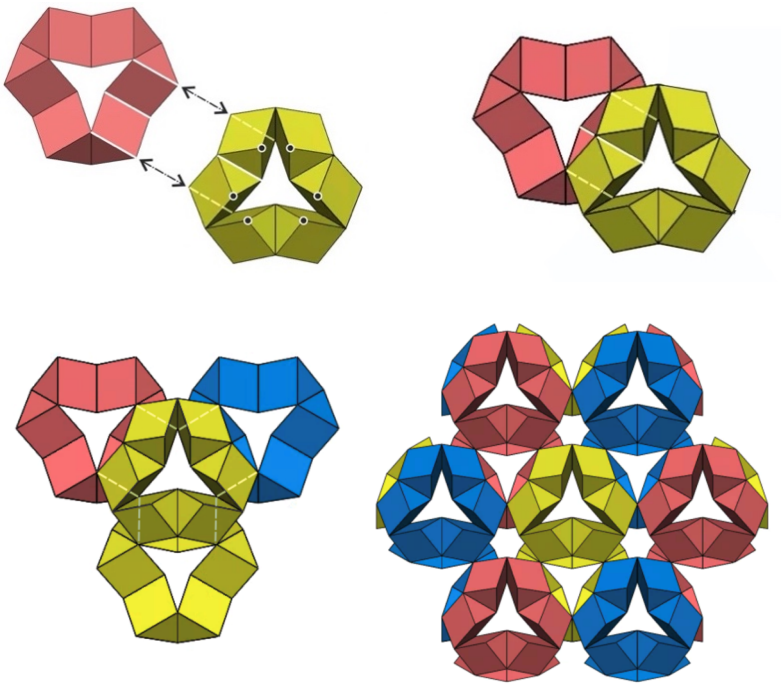

(a) Two units of the original metamaterial connected along two edges.

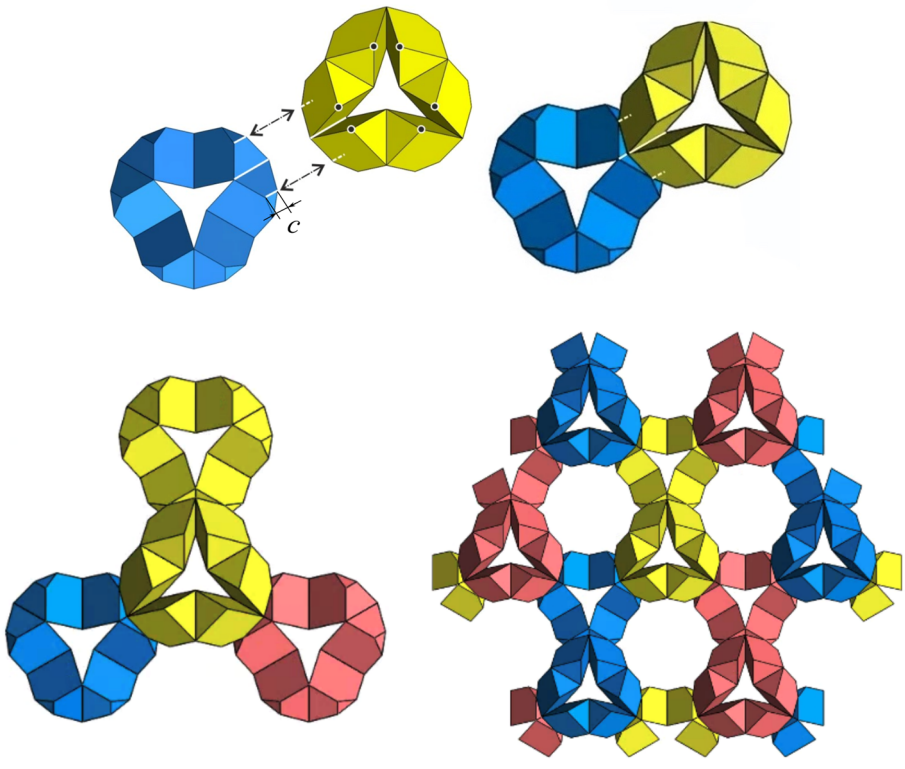

(b) Two units of the variant metamaterial connected along two edges.

Figure 4.27 Connection of multiple units by edges.

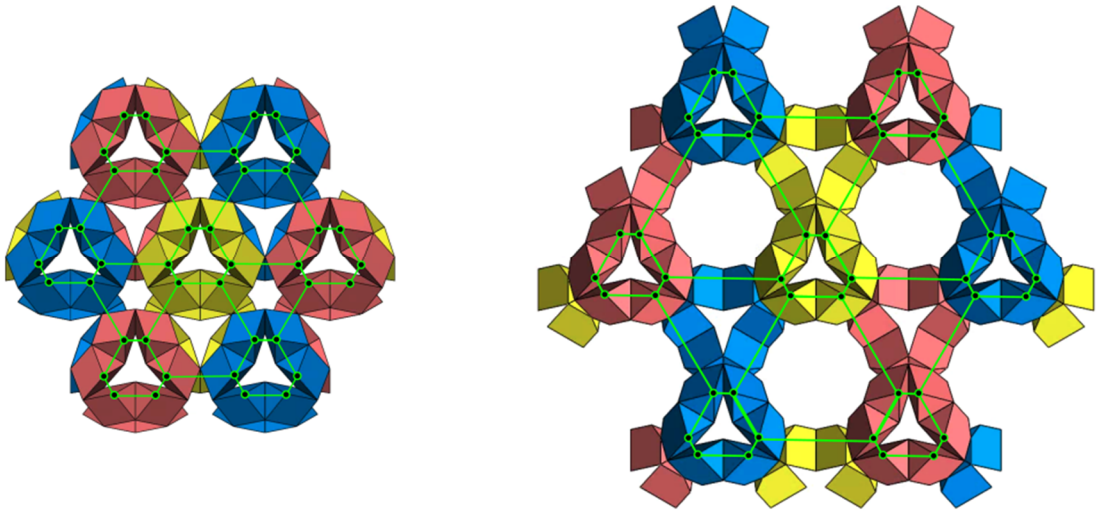

(a) The original metamaterial (b) The variant metamaterial.

Figure 4.28 Connection of multiple units by vertices.

4.6.2 Tuneable porosity of Bricard mechanism-based metamaterials

Both Bricard linkage-based metamaterials have a completely packaged configuration without any voids when $\varphi = 0$. If viewed from top, two types of pores, one with hexagonal and the other with triangular profiles, appear with φ increases (we ignore the little parallelogram shaped voids emerging in the variant metamaterial), as shown in Figure 4.29(a)-(b). Denoting by d_0 and d_1 the diameters of the inscribed circles of pores, and by d_0 and d_2 for those of the variant.

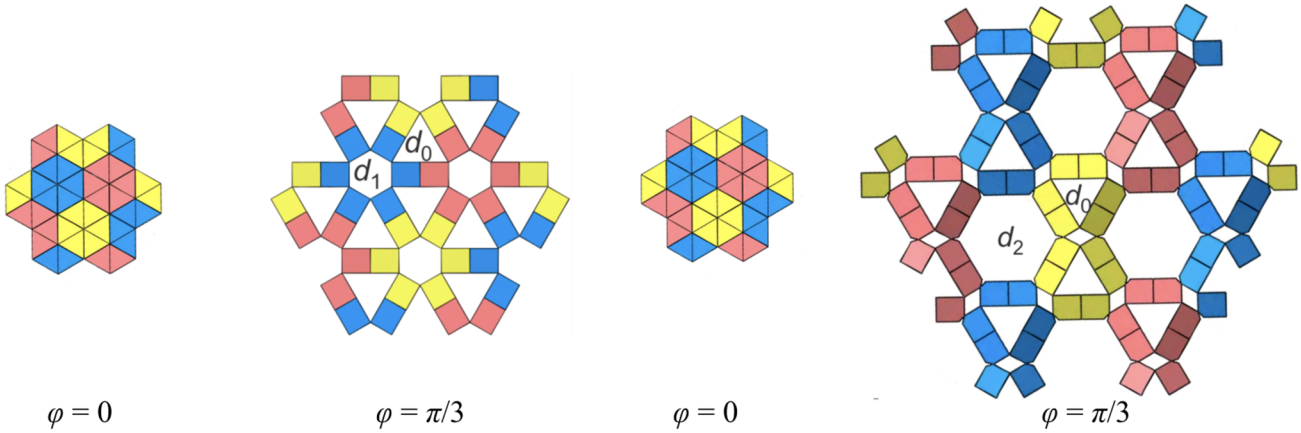

(a) The original metamaterial (b) The variant metamaterial.

Figure 4.29 Pore diameters of the metamaterial.

To calculate the porosity and pore diameter of the original metamaterial and its variant, we first define a representative volume element (RVE) of the metamaterial and then obtain the analytical results geometrically. For the original metamaterial of Figure 4.27(a), we set up a global coordinate system *xyz* whose origin **O** is at the centre of the element shown in Figure 4.30, i.e., the centre of triangle $\mathbf{B}_1\mathbf{MN}$, the *y*-axis is parallel to $\mathbf{A}_7\mathbf{A}_1$, whilst *z*-axis is normal to the plane $\mathbf{B}_1\mathbf{MN}$. When this element appears in the metamaterial assembly, it is shown in Figure 4.31(a). In addition, with the DH notation, we also set up six coordinate systems by placing z_i (i = 1, 2, …, 6) along the axis of each of the joint.

Viewing along *z*-axis, the top area of the RVE is obtained by connecting the centre points of adjacent pores. The height of RVE is defined as the distance between two adjacent planes where spherical joints are. The resultant RVE is an equilateral triangular prism of edge length *L* and height *H*, as shown in Figure 4.31 where the cyan shaded area is the RVE. The porosity can therefore be expressed as

$$P = 1 - \frac{V_0}{V_{\text{RVE}}/2} = 1 - \frac{2V_0}{\frac{\sqrt{3}}{4}L^2 H} \tag{4.33}$$

where V_0 and V_{RVE} are the volumes of a triangular prism building block and a representative volume element, respectively.

L and *H* of the RVE can be derived from the coordinates of the prism corners. In the subsequent derivation, we use the vector form of a point to represent *x*, *y* and *z* coordinate system of that point. For instance, $(\mathbf{A}_1)_2$ is point $\mathbf{A}_1$ in coordinate system 2 (x_2, y_2, z_2), where as $\mathbf{A}_{1,z}$ is *z* coordinate of point $\mathbf{A}_1$ in global coordinate system (*x*, *y*, *z*). Geometrically, we have

$$L = \mathbf{B}_{2,x} + 2[\mathbf{C}_{1,x} - \mathbf{B}_{1,x}],\ H = 2[\mathbf{B}_{2,z} - \mathbf{A}_{1,z}] - [\mathbf{B}_{1,z} - \mathbf{C}_{1,z}],\ V_0 = \frac{\sqrt{3}}{4}a^2 h. \tag{4.34}$$

for the original metamaterial. Therefore, we can calculate the porosity of the material as long as we have the coordinates of $\mathbf{A}_1$, $\mathbf{B}_1$, $\mathbf{C}_1$ and $\mathbf{B}_2$.

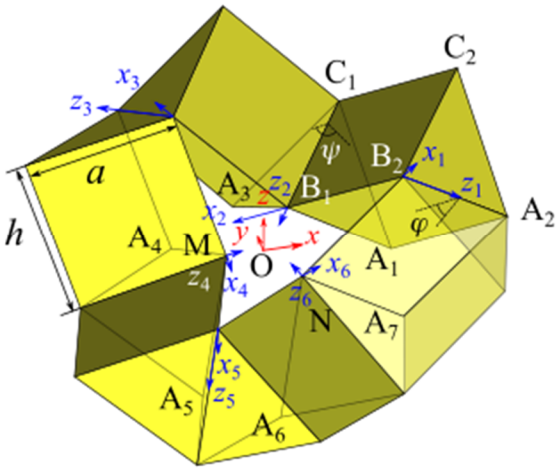

Figure 4.30 Coordinate systems of the kinematic unit using DH notation.

For some prisms, it is relatively straightforward to find the coordinates of some relevant points in particular.

$$(\mathbf{A}_1)_2 = \begin{bmatrix} 0 \\ \frac{\sqrt{3}a}{2} \\ -\frac{a}{2} \end{bmatrix}, (\mathbf{B}_1)_2 = \begin{bmatrix} 0 \\ 0 \\ 0 \end{bmatrix}, (\mathbf{C}_1)_2 = \begin{bmatrix} 0 \\ 0 \\ -a \end{bmatrix}, (\mathbf{B}_2)_2 = \begin{bmatrix} -h \\ 0 \\ 0 \end{bmatrix}, \tag{4.35}$$

$$(\mathbf{M})_4 = \begin{bmatrix} 0 \\ 0 \\ 0 \end{bmatrix}, \ (\mathbf{N})_6 = \begin{bmatrix} 0 \\ 0 \\ 0 \end{bmatrix}, \tag{4.36}$$

$$(\mathbf{A}_3)_3 = \begin{bmatrix} -h \\ 0 \\ a \end{bmatrix}, \ (\mathbf{A}_4)_4 = \begin{bmatrix} 0 \\ \frac{\sqrt{3}a}{2} \\ -\frac{a}{2} \end{bmatrix}, \ (\mathbf{A}_5)_5 = \begin{bmatrix} -h \\ 0 \\ a \end{bmatrix}, \ (\mathbf{A}_6)_6 = \begin{bmatrix} 0 \\ \frac{\sqrt{3}a}{2} \\ -\frac{a}{2} \end{bmatrix}, \ (\mathbf{A}_7)_1 = \begin{bmatrix} -h \\ 0 \\ a \end{bmatrix}. \tag{4.37}$$

The Bricard linkage satisfies the geometrical conditions given in Eq. (4.29). Substituting it the into Eq. (2.4) yields the transformation matrix $\mathbf{T}_{i(i+1)}$ (i = 1, 2, …, 6, and if $i + 1 > 6$, it is replaced by 1), with which we have

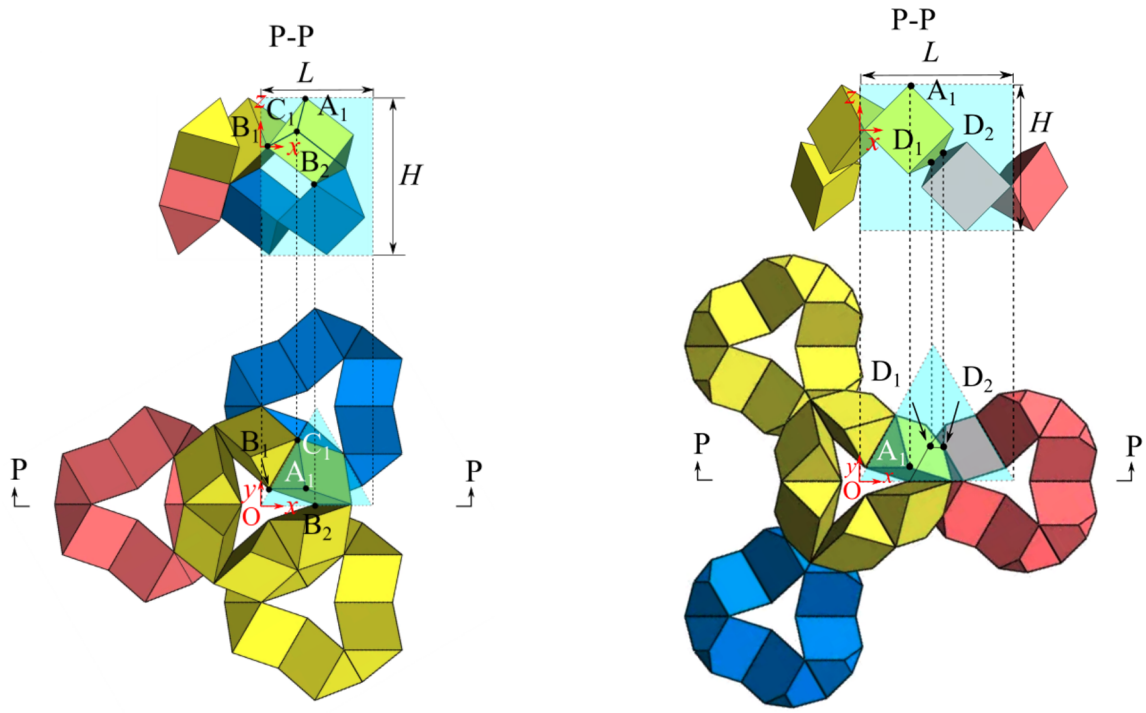

(a) The original metamaterial (b) The variant metamaterial

Figure 4.31 Representative volume elements of the metamaterials.

$$\begin{gathered}(\mathbf{M})_2=\mathbf{T}_{23}^{-1}\mathbf{T}_{34}^{-1}(\mathbf{M})_4,\ (\mathbf{N})_2=\mathbf{T}_{12}\mathbf{T}_{61}(\mathbf{N})_6,\\ (\mathbf{A}_3)_2=\mathbf{T}_{23}^{-1}(\mathbf{A}_3)_3,\ (\mathbf{A}_4)_2=\mathbf{T}_{23}^{-1}\mathbf{T}_{34}^{-1}(\mathbf{A}_4)_4,\ (\mathbf{A}_5)_2=\mathbf{T}_{12}\mathbf{T}_{61}\mathbf{T}_{56}(\mathbf{A}_5)_5,\\ (\mathbf{A}_6)_2=\mathbf{T}_{12}\mathbf{T}_{61}(\mathbf{A}_6)_6,\ (\mathbf{A}_7)_2=\mathbf{T}_{12}(\mathbf{A}_7)_1.\end{gathered} \tag{4.38}$$

For the coordinate system xyz, its origin **O** is at the centre of triangle $\mathbf{B}_1\mathbf{MN}$. Hence,

$$(\mathbf{O})_2=\frac{2}{3}\cdot\frac{(\mathbf{M})_2+(\mathbf{N})_2}{2}+\frac{(\mathbf{B}_1)_2}{3}. \tag{4.39}$$

If we express the unit vector along *x*, *y* and *z* in coordinate system 2, we have

$$\begin{gathered}(\mathbf{e}_x)_2=\frac{(\mathbf{M})_2(\mathbf{O})_2\times(\mathbf{N})_2(\mathbf{O})_2}{\left|(\mathbf{M})_2(\mathbf{O})_2\times(\mathbf{N})_2(\mathbf{O})_2\right|},\\ (\mathbf{e}_y)_2=\frac{(\mathbf{A}_7)_2(\mathbf{A}_1)_2}{\left|(\mathbf{A}_7)_2(\mathbf{A}_1)_2\right|},\\ (\mathbf{e}_z)_2=(\mathbf{e}_y)_2\times(\mathbf{e}_x)_2.\end{gathered} \tag{4.40}$$

Therefore, the transformation matrix from the fixed coordinate system *xyz* to coordinate system 2, $\mathbf{T}_{O2}$, is

$$\mathbf{T}_{O2}=\begin{bmatrix}(\mathbf{e}_{x,x})_2 & (\mathbf{e}_{x,y})_2 & (\mathbf{e}_{x,z})_2 & (\mathbf{O}_x)_2\\ (\mathbf{e}_{y,x})_2 & (\mathbf{e}_{y,y})_2 & (\mathbf{e}_{y,z})_2 & (\mathbf{O}_y)_2\\ (\mathbf{e}_{z,x})_2 & (\mathbf{e}_{z,y})_2 & (\mathbf{e}_{z,z})_2 & (\mathbf{O}_z)_2\\ 0 & 0 & 0 & 1\end{bmatrix}. \tag{4.41}$$

Therefore

$$\mathbf{A}_1=\mathbf{T}_{2O}(\mathbf{A}_1)_2,\ \mathbf{B}_1=\mathbf{T}_{2O}(\mathbf{B}_1)_2,\ \mathbf{C}_1=\mathbf{T}_{2O}(\mathbf{C}_1)_2,\ \mathbf{B}_2=\mathbf{T}_{2O}(\mathbf{B}_2)_2, \tag{4.42}$$

where $\mathbf{T}_{O2}=\mathbf{T}_{2O}^{-1}$. Substitute Eq. (4.42) into Eq. (4.34) and then Eq. (4.33) yields the porosity of the original metamaterial.

For the variant metamaterial, Eq. (4.33) still holds, but now

$$L=\mathbf{D}_{1,x}+\mathbf{D}_{2,x},\ H=\mathbf{D}_{1,z}+\mathbf{D}_{2,z}-2\mathbf{A}_{1,z},\ V_0=\frac{\sqrt{3}}{4}a^2h-\frac{\sqrt{3}}{12}c^3. \tag{4.43}$$

Geometrically,

$$(\mathbf{A}_1)_2=\begin{bmatrix}0\\ \frac{\sqrt{3}a}{2}\\ -\frac{a}{2}\end{bmatrix},\ (\mathbf{D}_1)_2=\begin{bmatrix}-h\\ 0\\ -a\end{bmatrix},\ (\mathbf{D}_2)_2=\begin{bmatrix}-h\\ \frac{\sqrt{3}c}{2}\\ \frac{c}{2}-a\end{bmatrix}. \tag{4.44}$$

The transformation from the fixed coordinate system *xyz* to coordinate system 2 is as same as that given in Eq. (4.41), and thus,

$$\mathbf{A}_1=\mathbf{T}_{2O}(\mathbf{A}_1)_2,\ \mathbf{D}_1=\mathbf{T}_{2O}(\mathbf{D}_1)_2,\ \mathbf{D}_2=\mathbf{T}_{2O}(\mathbf{D}_2)_2. \tag{4.45}$$

Substituting Eq. (4.45) into Eq. (4.43) and then Eq. (4.33) yields the porosity of the variant metamaterial.

The pore diameters can be derived by the coordinates as well. For the original metamaterial

$$d_0=2\sqrt{(\mathbf{B}_{1,x})^2+(\mathbf{B}_{1,y})^2},\ d_1=2(2\mathbf{C}_{1,x}-\mathbf{A}_{1,x}-\mathbf{B}_{1,x}). \tag{4.46}$$

For the variant metamaterial

$$d_0=2\sqrt{(\mathbf{B}_{1,x})^2+(\mathbf{B}_{1,y})^2},\ d_2=2(L-\sqrt{(\mathbf{C}_{1,x})^2+(\mathbf{C}_{1,y})^2}) \tag{4.47}$$

As shown in Figure 4.32, the pore diameters and porosity of the metamaterials are dependent upon the ratio of h to a. The larger h/a is, the bigger the voids. The larger pores of the variant are significantly greater than those of the original. For instance, when c/a = 2/3 and h/a = 2, the maximum d_2/a is 6.229 at $\varphi = \pi / 4$, whist the maximum d_1/a is 1.732 at $\varphi = \pi / 3$. Note that d_0 exceeds d_1 when h/a = 2. Even so, the maximum d_0/a is 2.309, reached at at $\varphi = \pi / 3$.

For both metamaterials, the porosities are higher when h/a is large, and they increase sharply when θ_x changes from 0 to π/6, and then decrease slowly after passing the peaks because the overall height reduction of the material is accompanied by an increase in surface areas. When h/a = 2 the maximum porosities of the original and variant reach 86.29% and 93.90%, respectively, at $\varphi = 0.178\pi$.

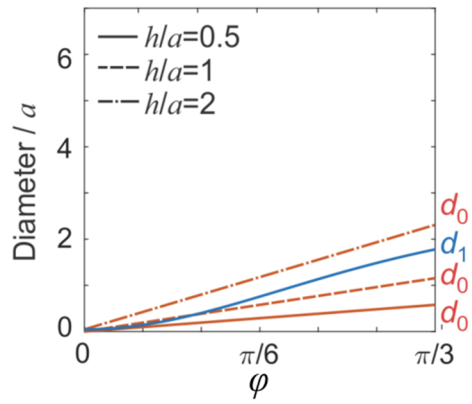

(a)Pore diameter of the original metamaterial

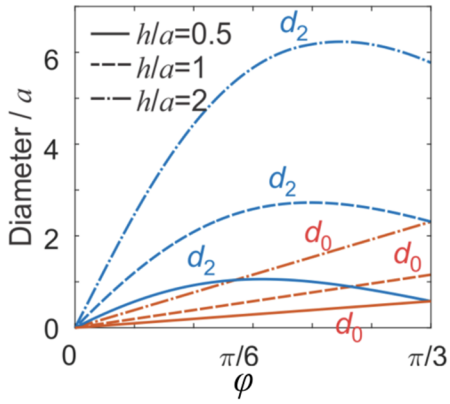

(b)Pore diameter of the variant metamaterial

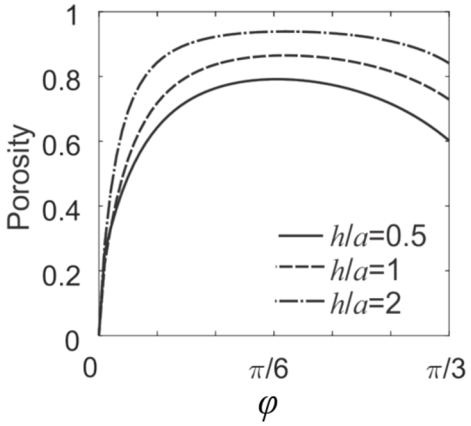

(a) Porosity of the original metamaterial

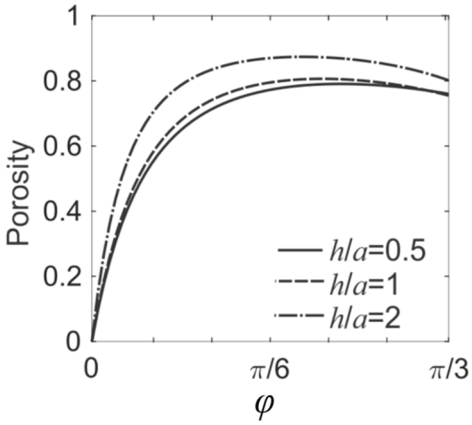

(b) Porosity of the variant metamaterial

Figure 4.32 Pore diameters and porosities of the metamaterials.

4.7 Other spatial mechanism-based metamaterials

The Sarrus linkage and Bricard linkage-based units provide a replicable method to construct 3D mechanical metamaterials. Following this approach, a systematic method can be summarized: first, the kinematic units are designed with entrenched spatial mechanisms. The shape of the prism building blocks can be tuned to fulfil the connection position of spatial mechanisms. For instance, Figure 4.33 shows examples of the Bennett 6*R* linkage-based unit. In Figure 4.33(b), the shape of the cube building block is changed to triangular prisms. Two units are connected by planar 4*R* linkage to form an assembly that can transform from a cube to a rectangular prism. Other units can be constructed using this method, and they can be categorized according to the transformation behaviour such as elongation, expansion, bending and twisting, as shown in Figure 4.34.

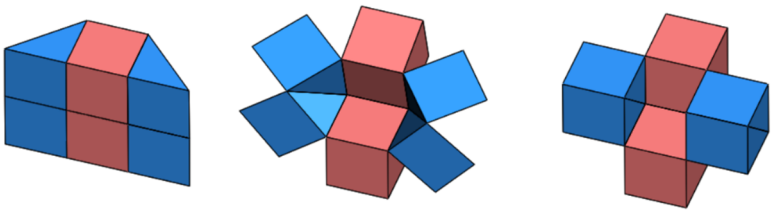

(a) A Bennett 6*R* linkage-based unit

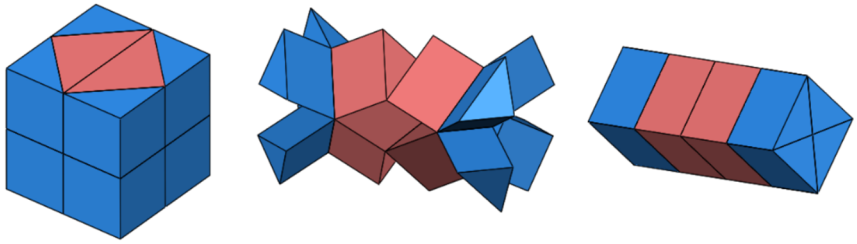

(b) An assembly of the units

Figure 4.33 Bennett 6*R* linkage-based reconfigurable unit.

The second step is to connect the kinematic units with planar 4*R* mechanisms. Designers can program the physical output of the module/assembly by varying the number of prism blocks and the connection position of units. Finally, different modules are connected to form an integrated metamaterial that performs a specific behaviour, such as curling, extension, rotation

or the combination of above. Different unit cells can be placed at various positions in a non-periodic pattern with the consideration of the material functionality.

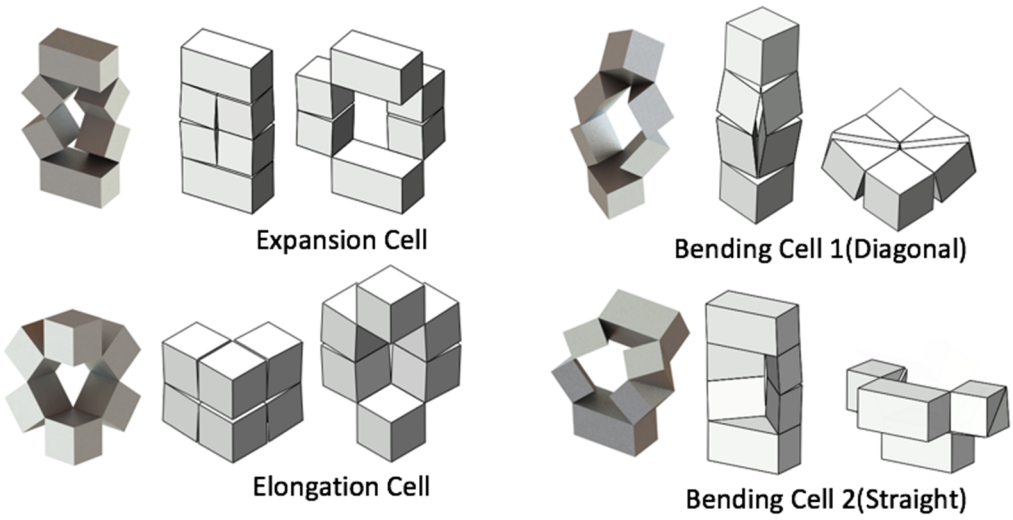

Figure 4.34 Various kinematic unit cells with different transformation behaviours.

One advantage of the kinematic-based metamaterials lies in the rich programmable variables: the selection of unit cells, the number of tie blocks, the tessellation pattern, the shape of building blocks, etc. This family of metamaterials can be applied in future modular robots, foldable furniture and interactive systems with integrated sensors and actuators.

4.8 Conclusion

This chapter mainly focuses on a kinematic-based design strategy to create 3D tuneable and programmable metamaterials. The construction units of our metamaterials are carefully entrenched with spatial mechanisms, and these metamaterials obtained by tessellating the units have predefined and reliable deformation paths inherited within the unit cells. The main findings include:

1) A systematic approach to construct 3D metamaterials using spatial mechanisms: first construct kinematic units embedded with spatial linkage mechanisms; then, connect units using 4*R* mechanisms and tessellate the structure to form metamaterials. The spatial

mechanisms, connection method, and tessellation pattern can be programmed during the design process.

2) Multi-mode reconfigurability through kinematic bifurcation. The bifurcated kinematic unit has a number of deformation paths, arisen exclusively from the underlying topology and geometry, and thus, its deformation along each path can be precisely described mathematically and realized in real prototypes. The deformation paths coincide at a kinematic bifurcation state, enabling the metamaterial to switch from one path to another. These unique properties of the metamaterial are achieved without external synchronization. The only steering required is at the bifurcated state, which can be achieved by external forces, thermal or magnetic-induced actuation. The prototypes fabricated by mechanical assembling and 3D printing with multi-materials have been used to validate our concepts.

3) Metamaterial with programmable constant negative Poisson's ratios in three dimensions, determined solely by geometric dimensions of the prism blocks of the metamaterial. Such metamaterials can be readily utilized in real engineering applications because the constant Poisson's ratios are decoupled from the strains.

4) Metamaterials with large tuneable porous microarchitecture. The pore shapes, sizes and topology of the metamaterial can be programmed by the geometry parameters of the prism blocks. This tunability of pore architecture can influence the elastic and acoustic feature of the metamaterial dynamically.

5) Multi-process and multi-material fabrication method. The motion of multi-process method is in good accordance with the theoretical model. The multi-material printing provides effective proof of concept for evaluation of their mechanical performance.

The kinematic metamaterials are scale and base material independent, and they utilise only flexible rotational connections amongst construction blocks, making it possible to fabricate

them in a wide range of scales and base materials. The stiffness of our materials through the deformation phase is provided by the stiffness of rotational connections. As the deformation of metamaterial follows the kinematic motion path, it offers highly reliable performance with very low sensitivity to both base material and manufacture errors. The proposed design strategy for kinematic metamaterial with entrenched kinematic behaviour that can be turned on/off, or changed by external stimuli can have many applications, ranging from transformable structures in architecture, tuneable acoustic insulation materials, to advanced multi-task applications in soft robotics and wearable devices.

Chapter 5

Functional Kinematic Metamaterial

The final part of this thesis is a study of the electromagnetic application of reconfigurable metamaterial. The rapid development of radio frequency (RF) components requires smart multifunctional materials that can adapt their physical shapes and properties according to the environment. While most current reconfigurable systems provide limited flexibility with high manufacturing cost, this chapter proposes a kirigami-inspired kinematic metamaterial that could deform and lock into different configurations for the purpose of frequency selection. Two types of kirigami patterns are designed and analysed kinematically and dynamically. Due to their multistable properties, the structures could maintain in several configurations with minimum strain energy after the external load is removed. This provides convenient mechanical switching among different passbands. Simplified energy models are built and compared with finite element simulations. The kirigami metamaterials are fabricated by laser engraving and coated by metal paint. The electromagnetic responses of the samples are tested and analysed to validate the application.

5.1 Introduction

To date, the rapid development of electromagnetic metamaterials requires low-cost reconfigurable structures for the design of tuneable antennas, frequency selective surfaces, and other components. Conventional reconfigurable antennas can tune the operational frequency by placements of slots and pins to modify the effective electrical length of the antenna or use the multi-layer structure with specialized mechanical support (Li et al., 2016; Taylor et al., 2011; Ghosh & Srivastava, 2017; Vallecchi et al., 2017), yet in the cases for high-frequency applications, the dielectric loss and resistive losses could largely influence the performance of these devices. In this chapter, mechanical metamaterials with superior flexibility, low electromagnetic loss for millimetre wave and comparatively low fabrication cost are developed to tackle with the issue.

Some attempts of origami-inspired reconfigurable metamaterial (Nauroze et al., 2018; Fuchi et al., 2012) and auxetic structures (Ciobanu, Damian, and Casian-Botez, 2010) have been used for this application. These kinematic mechanisms usually have a continuous motion; therefore, it requires precise control to deploy the structure to a specific configuration to present the given resonance frequency. Achieving a robust and stable switching among several configurations is very challenging, which usually requires a pre-stressed state to be maintained in the structure (Amendola et al., 2018). To solve this problem, we develop a multistable structure that can repeatably lock into several configurations, corresponding to different frequencies. Multistable structures have more advantage over continual motion structures for switchable materials, because they have multiple equilibrium states where the potential energy reaches local minima, and the structure would automatically tend to stay in these configurations.

A general approach for bistable structure construction is to create geometry discrepancy between two stable states to trap strain energy (Rafsanjani and Pasini, 2016; Haghpanah et al.,

2016). To have several switchable configurations, we develop a multistable design inspired by kirigami art. By tuning the cut length and geometry parameters of the patterns, we can program the topologies and shapes of different configurations. The simplified energy model and finite element simulation results are provided to illustrate the influence of critical parameters on the structural bistability. Finally, the electromagnetic experiments are conducted to validate the functionality of proposed kirigami metamaterials.

5.2 Structure design

5.2.1 Triangle model

We create the metamaterials by making cutting pattern on a sheet material, similar to the kirigami art. In the first triangle model shown in Figure 5.1(a), the unit of the cutting pattern is consisted of eight triangles connected to each other at their vertices via thin ligaments. When the unit is stretched horizontally, the thin ligaments act as flexure hinges, and the triangles are capable of rotating about the connection vertices with respect to the adjacent ones. This deployment generates three quadrilateral voids inside the unit cell and six quadrilateral voids between the unit cell and its neighbouring units. When the unit cell is stretched to a specific configuration, it is able to lock in the open state. To recover the unit cell to its original configuration, one needs to compress the unit cell to make it snap-through to the close state. Tessellating the unit cell in two orthogonal directions creates a metasurface, as shown in Figure 5.1(b). The unit cells in the same column will have equivalent motions because their width is constraint by the adjacent top and bottom units; on the other hand, in each row, the unit cell can lock in different configurations. In this way, we can generate metasurface with different topologies by deploying specific columns. Figure 5.1(c) shows a 10×16 metamaterial made by laser engraving.

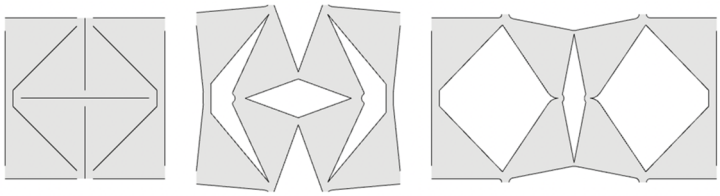

(a) The transformation of a unit cell

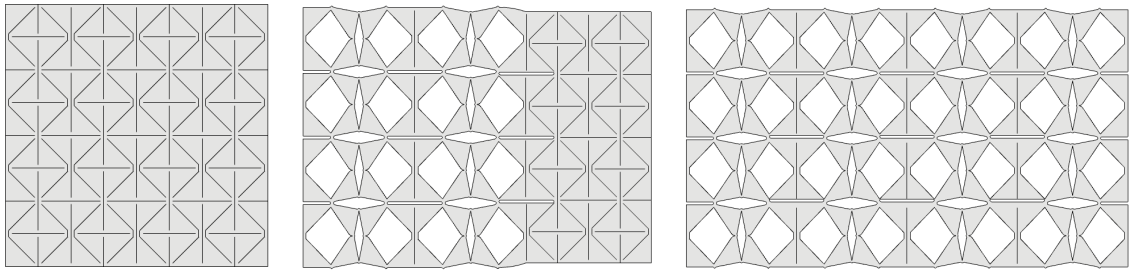

(b) The transformation of the metasurface

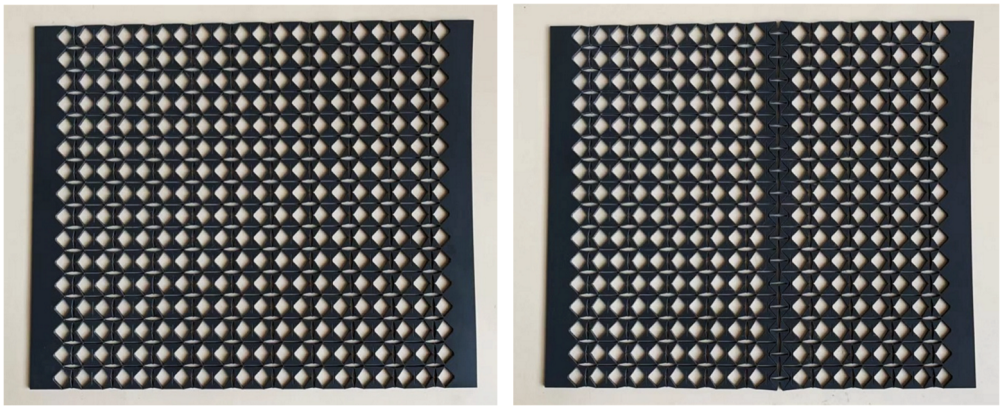

(c) A laser cut sample of the metamaterial

Figure 5.1 Structure design of the triangle model.

The transformation of the metamaterial can be modelled by planar linkage mechanisms. If we assume the thickness of the flexure hinges is zero, in other words, the triangles have an ideal vertex-to-vertex connection, the transformation of the structure can be regarded as a rigid body motion. The mobility of the close chain linkage is given by

$$m = 3(n-1-j) + \sum_{i=1}^{j} f_i = 3(8-1-10) + 10 = 1 \tag{5.1}$$

The motion can be described in three steps, as shown in Figure 5.2:

1) When applying transversal load on the close structure, triangles 1 & 2, 3 & 4, 5 & 6 and 7 & 8 first stick together as squares and move as integrated bodies. The neighbouring squares rotate around the connection vertices with respect to each other and form a planar $4R$ linkage.

2) When the hypotenuses of the triangles in the top and bottom squares become collinear, the structure can choose from two motion paths: either continue the rotation as one part or separate the triangles and form new parallelogram voids within. Because we apply transverse load on the structure, it tends to open up further and separate the triangles. Therefore, two new $4R$ linkages are generated within triangles 1-4 and 5-8. Triangles 1,4,5,8 change their rotation direction from clockwise to anti-clockwise, or vice versa.

3) Finally, the structure reaches the fully open state where its transversal dimension is maximized. The three parallelogram voids morph into two square voids, and triangles 1, 4 contact with 8, 5.

However, in the real material transformation, the structure does not have perfect hinges at the vertex. The flexure hinges will be bent and compressed during the transformation. At a certain point, the energy cost to bend the middle ligaments is higher than the cost to compress them. Therefore, in real structure motion, the model will not reach the configuration where the hypotenuses of the top and bottom triangles become collinear; instead, the pattern will snap from the close to open state and compress the middle ligaments severely because of the geometry discrepancy during transformation, as shown in the second row of Figure 5.2.

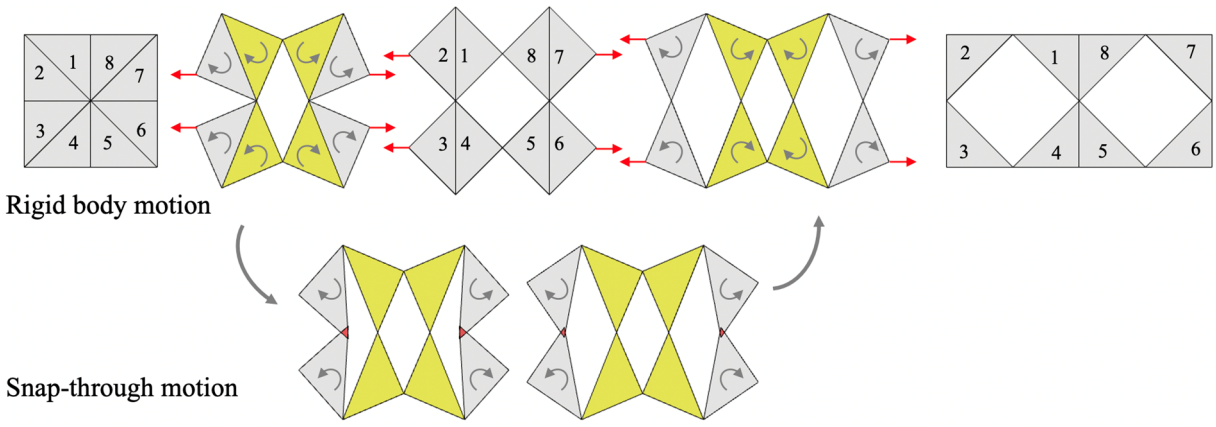

Figure 5.2 Kinematic analysis of the structure

5.2.2 Star model

Another star model is constructed based on similar principles. As shown in Figure 5.3(a), the cut pattern generates eight small triangles connected with a four-pointed star. Kinematically, the structure is not able to deploy. However, if we carefully design the parameters of the thin ligaments, the pattern is transformable through a snap-through process. A quarter of the unit cell is similar to the connection arrangement of the triangle pattern: the two small triangles compress the middle ligament to rotate outwards, and the star restricts the distance between two vertices of these triangles. If the unit is stretched from its four corners, it snaps into an isotropic open pattern. If the unit is stretched along one diagonal line, it will deform into an anisotropic pattern where the pair of triangles along the stretch direction is pulled open, and the other pair keeps undeployed. The structure is only geometrically compatible at the close state, open state and semi-open state, as shown in Figure 5.3(b). During the deformation, the ligaments between two triangles are severely compressed until the structure reaches one of the stable states. When tessellated in the plane, the geometry of the unit is coupled with its neighbours, therefore, the metamaterial has four stable states regardless of the number of units.

5.3 Simplified elastic energy model for bistability analysis

5.3.1 Energy model of the triangle pattern

Why is the total energy cost to bend the middle ligaments higher than the snap-through behaviour? This bistable phenomenon can be explained by a simplified elastic energy model of the structure. The total potential energy Π, is the sum of the elastic strain energy U stored in the deformed body and the potential energy of the applied load V associated with the applied forces. The system is in equilibrium if an infinitesimal change of the position does not change the total potential energy:

$$\delta\Pi = \delta(U + V) = 0 \tag{5.2}$$

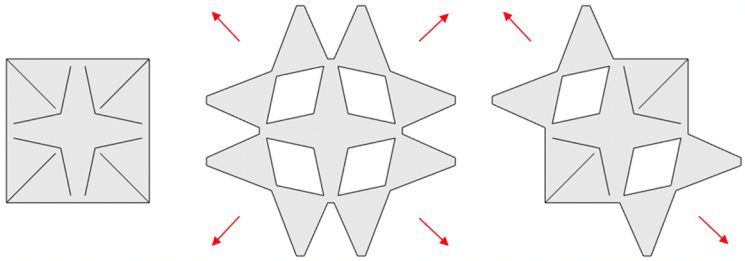

(a) The transformation of a unit cell

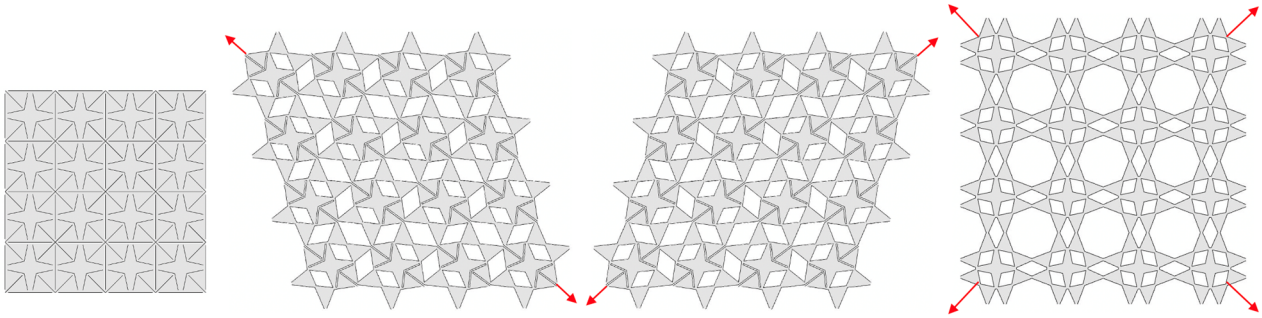

(b) The transformation of a metasurface

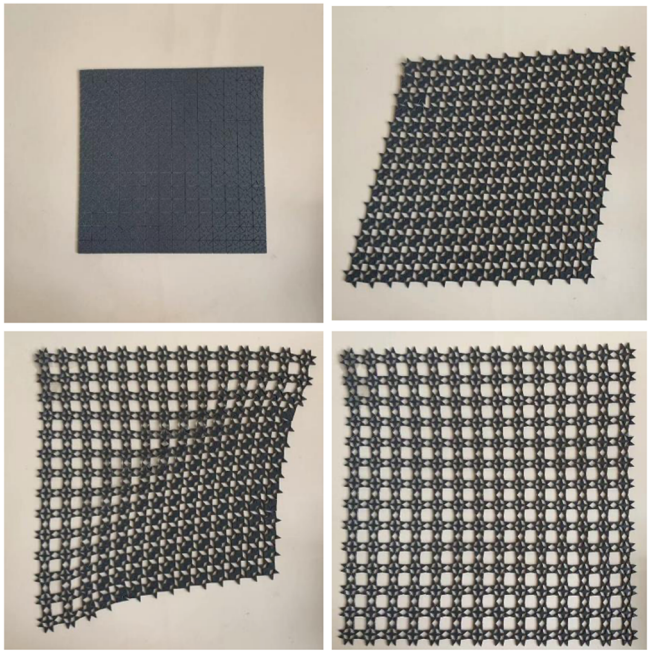

(c) A laser cut sample of the metamaterial

Figure 5.3 Structure design of the star model.

To be able to free stand at the stable states, the potential energy of the applied load at the stable state is zero. Therefore, the derivative of strain energy U is also zero to make the system in equilibrium. This indicates that the stable states happen when the strain energy reaches local

minima. In the triangle model, the elastic strain energy U is mainly consisted of the energy in the bending ligaments by pure moment

$$U = \int_0^L \frac{M^2}{2EI} dx = \frac{EI}{2L} d\theta^2 \tag{5.3}$$

Where the area moment of inertia I can be derived as

$$I = \frac{bt^3}{12} \tag{5.4}$$

For each unit, the strain energy of the bending hinges can be calculated as

$$U_B = \sum_i^6 \frac{EI_i}{2a_i} d\theta_i^2 = \sum_i^6 \frac{1}{2} k_i d\theta_i^2 \tag{5.5}$$

$$k_i = \frac{Eb_i t_i^3}{12a_i} \tag{5.6}$$

k_i can be seen as the equivalent stiffness of the flexure hinge, and it is determined by the geometry of the hinge according to Eq. (5.6). As shown in Figure 5.4, b_i denotes to the thickness of the sheet material, t_i is the width of the hinge i, a_i is the length of the hinge. The length of hinge a_i is hard to define; here we use an approximate value measured from real sample behaviour. E is the modulus of elasticity. The dimension of the unit is l and one acute angle of the right triangle is α. Here we use isosceles right triangles so $\alpha = \pi/4$.

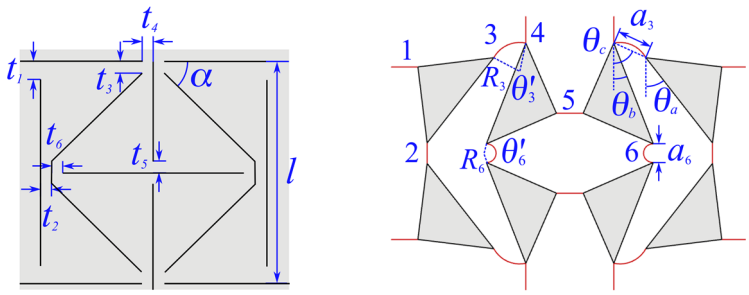

Figure 5.4 The parameters of triangle model unit cell.

We assume the bending arc of each flexure hinge is tangent to the adjacent triangle edges. Therefore, the bending angle of the hinge is equal to the intersection angle of two adjacent triangle edges on the same side. Especially, hinge 3 and 6 are compressed severely during the

snap through, so they tend to have bigger curvatures. Their bending angle is calculated by adding the intersection angle and a local rotational angle θ_i'.

$$R_i\theta_i^{'} = a_i^0, i = 3,6 \tag{5.7}$$

$$2R_i \sin\frac{\theta_i^{'}}{2} = a_i \tag{5.8}$$

Therefore

$$2\frac{a_i^0}{\theta_i^{'}}\sin\frac{\theta_i^{'}}{2} = a_i \tag{5.9}$$

Here, a_i^0 is the original length of the thin ligament and a_i is the distance at the vertex between two triangles connected by hinge *i*. R_i is the radius of the local arc corresponding to θ_i'.

The void inside the hinge 2,3,6 needs to fulfil the physical constraint:

$$\frac{a_2}{2} + \sqrt{2}l\cos\theta_a + a_3\cos\theta_c = \sqrt{2}l\cos\theta_b + \frac{a_6}{2}, \theta_c \in (0, \frac{\pi}{2}) \tag{5.10}$$

According to Figure 5.4, we can list the bending angle of each hinge:

$$d\theta_1 = d\theta_2 = d\theta_4 = 2(\theta_a - \alpha) \tag{5.11}$$

$$d\theta_5 = 2(\theta_b - \alpha) \tag{5.12}$$

$$d\theta_3 = \theta_a - \theta_b + \theta_3^{'} \tag{5.13}$$

$$d\theta_6 = 2(\theta_b - \alpha) + \theta_6^{'} \tag{5.14}$$

$$\theta_a \in (0, \alpha), \theta_b \in (-\alpha, \alpha) \tag{5.15}$$

Sum up the bending energy of each hinge we have the following equation:

$$U = \sum_i^6 n_i \frac{1}{2}k_i d\theta_i^2 = 2\times\frac{1}{2}(k_2 d\theta_1^2 + k_5 d\theta_2^2 + k_6 d\theta_6^2) + 4\times\frac{1}{2}k_3 d\theta_3^2 + \frac{4}{2}\times\frac{1}{2}(k_1 d\theta_4^2 + k_4 d\theta_5^2) \tag{5.16}$$

n_i is the number of identical hinges in a single unit. By scanning the whole parameter space of $\theta_a, \theta_b, \theta_3', \theta_6'$, we can plot the minimum energy of each corresponding θ_b in Figure 5.5.

During the deformation, θ_a will first decrease from α to a certain angle, then recover to α in the end; θ_b will decrease all along until the limit. Therefore, the energy in hinge 1,2 and 4 will increase in the beginning to reach local maxima and decrease afterwards, while the energy in other hinges will keep increasing during the motion. The energy variation in hinge 1,2,4 raises the bistability, so we can tune the property by changing the stiffness of these hinges. According to Eq. (5.5)-(5.6), k_i can be seen as the equivalent stiffness of the flexure hinge. For hinge 1,4,5 the hinge length can be seen as the cut width $a_i = t_c \approx 0.3$mm, $i = 1,4,5$; for hinge 2,3,6, the length is much bigger than cut width, which is approximately $a_2 = 5t_c$, $a_3 = a_6 = 3t_c$. The dimension of the unit cell is $l = 12$mm to ensure that the resonance frequency of the metasurface is within our measurement range. The maximum length for t_1 and t_4 is 6mm, which is half the size of a unit cell. Under such cases, there will be not cut between the adjacent unit cells. When increasing t_2, we keep α unchanged. This influences the dimension of the structure and result in a wider unit. There is no maximum length for t_2. The limits of hinge widths are summarized

$$\begin{aligned} t_i &= 0.8\text{mm}(i = 3,5,6), \\ t_c &\approx 0.3\text{mm}, \\ t_1, t_4 &\in [0.5\text{mm}, 6\text{mm}], \end{aligned} \tag{5.17}$$

$$k_i \propto \frac{t_i^3}{a_i}. \tag{5.18}$$

5.3.2 Parametric analysis of the triangle pattern

It can be noticed that the width of the hinge largely influences the hinge stiffness. Therefore, we use the width of hinge 1,2 and 4 to tune the elastic energy. The initial setting for other hinge widths is $t_i = 0.8$mm. Figure 5.5 plots the influence of these parameters on the strain energy. Figure 5.5(a) shows that the width of hinge 1 influences the strain energy the most. When t_1 reaches the maximum, the cuts at the two sides of the unit cell disappear. This design directly constrains the deformation of the four triangles at the corner and make θ_a a constant value of

π/4. Therefore, the bistability of the pattern reaches the extremum. Hinge 4 has the same effect as hinge 1(Figure 5.5(c)).

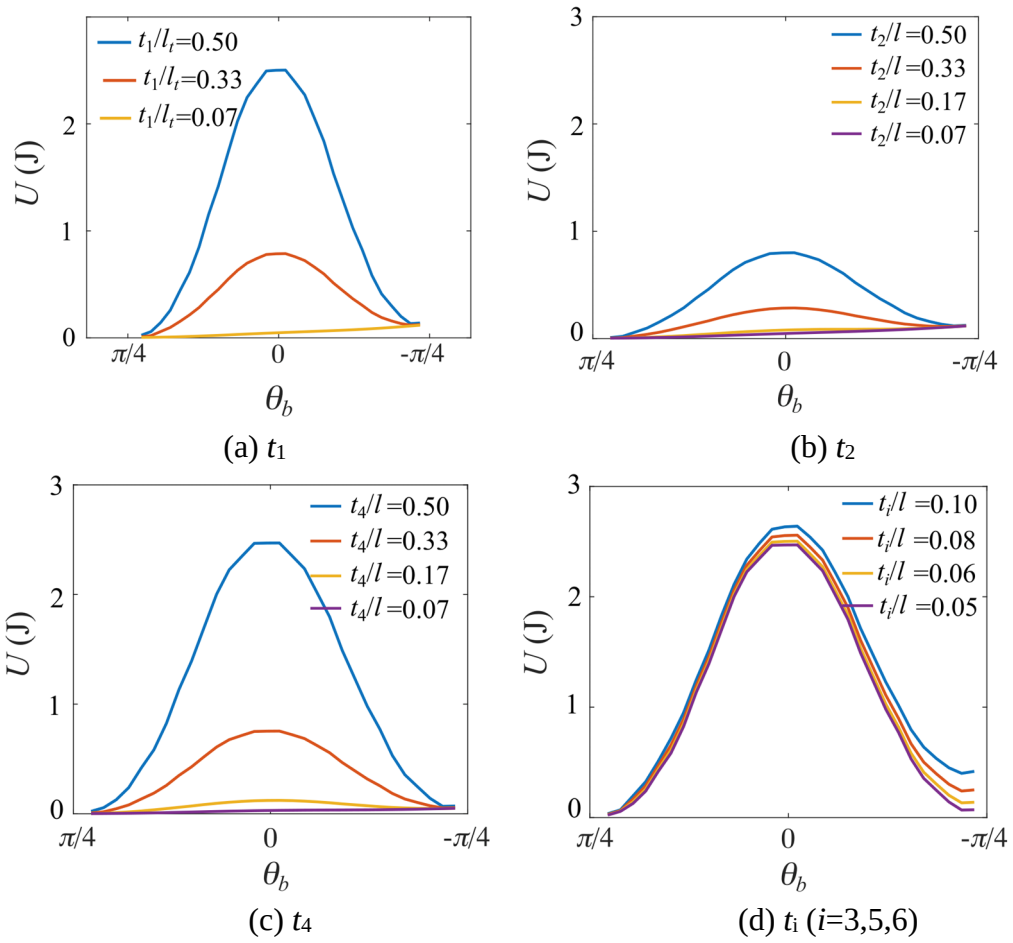

Figure 5.5 The elastic energy as a function of the rotational angle θ_b with different hinge parameters. The initial values of these parameters are: t_i =0.8 (i=1,2,3,4,5,6).

Hinge 2 can tune the stability as well, but not as effective as hinge 1 and 4 works. Although the stiffness of hinge 2 is largely increased, the geometry discrepancy is not very obvious and the triangles are free to transform. Thus, we did not choose this parameter to tune the bistability. The evolution of strain energy versus t_i shows that the thickness of other hinges has limited influence on the bistability. From another hand, t_i tunes the minimum energy of the second stable state. The thicker the hinges are designed, the harder the structure can stay stably at the open state. This does not indicate a thinner hinge will give better bistable performance because

they are more likely to break after repetitive deployment. We found that when t_i = 0.8mm, the pattern achieves a good balance between the stability and strength of the thin ligament.

5.3.3 Energy model of the star pattern

For the star pattern, the elastic strain energy U, consisted of the energy in the bending ligaments, can also be calculated using Eq. (5.5). It should be noted that hinge 2 in Figure 5.6 undergoes severe deformation during the snap-through. We calculate the bending angle of hinge 2 using the method adopted for hinge 3 and 6 in the triangle structure.

$$2\frac{a_2^0}{\theta_2^{'}}\sin\frac{\theta_2^{'}}{2}=a_2 \tag{5.19}$$

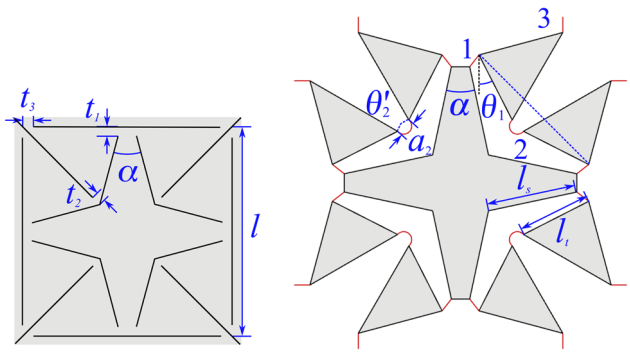

Figure 5.6 The parameters of star model unit cell.

The bending angle θ_2' is related to the distance a_2 between two neighbouring triangles. a_2^0 is the original length of hinge 2. Assuming the edge length of the star arm is l_s, the length of the triangle edge which is adjacent to the star is l_t, the star pattern should fulfil the following relation during transformation:

$$l_s=\frac{\frac{l}{2\sqrt{2}}}{\cos(\frac{\pi}{4}-\frac{\alpha}{2})} \tag{5.20}$$

$$l_t=l_s-\frac{\frac{a_2}{2}}{\cos(\frac{\pi}{4}-\frac{\alpha}{2})} \tag{5.21}$$

$$a_2 = 2(\frac{l}{2\sqrt{2}} - l_t \cos\left|\theta_1 - \frac{\pi}{4} + \frac{\alpha}{2}\right|) \tag{5.22}$$

α denotes to the angle of the star arm, l denotes to the dimension of the unit, and θ_1 refers to the rotating angle of hinge 1. We can list the bending angle of each hinge in Figure 5.6:

$$d\theta_3 = 2(d\theta_1) \tag{5.23}$$

$$d\theta_2 = 2(d\theta_1) + \theta_2^{'} \tag{5.24}$$

$$d\theta_3 = 2(d\theta_1) \tag{5.25}$$

$$\theta_1 \in (0, \frac{\pi}{2} - \alpha) \tag{5.26}$$

Sum up the bending energy of each hinge we have the following equation:

$$U = \sum_i^6 n_i \frac{1}{2} k_i d\theta_i^2 = 8 \times \frac{1}{2} k_1 d\theta_1^2 + 4 \times \frac{1}{2} k_2 d\theta_2^2 + \frac{8}{2} \times \frac{1}{2} k_3 d\theta_3^2 \tag{5.27}$$

n_i is the number of the identical i hinges in a single unit. By scanning the parameter space of θ_1, we can plot the minimum energy of the structure during transformation.

5.3.4 Parametric analysis of the star pattern

Among the three hinges, hinge 2 has the biggest deformation and contributes the most to the bistability behaviour. When θ_1 equals to $\alpha/2$ or $\pi/2$-$\alpha/2$, the length of a_2 will return to its original length a, which means the deformation of hinge 2 reaches the smallest, leading to the reduction of elastic energy. Again, we can tune the strain energy landscape by changing the stiffness of the hinges through varying their width. Figure 5.7 shows the influence of t_1, t_2 and star angle α.

As expected, t_2 determines the bistability of the pattern, while t_1 has rather small influence in the performance. t_3 have similar performance as t_1, so we did not plot the figure here. It is worth noting that the increase of t_2 will raise the overall strain energy of the open stable state. If the energy is too high, the structure will tend to snap back to the original close configuration. Hence,

the pattern does not become more bistable with the increase of t_2 after certain value. We found that when t_2 = 0.7mm, the pattern can free stand at the stable states.

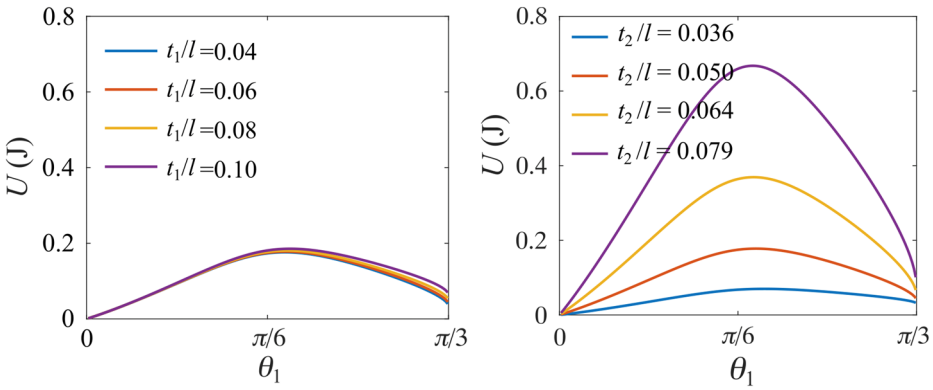

(a) t_1 (b) t_2

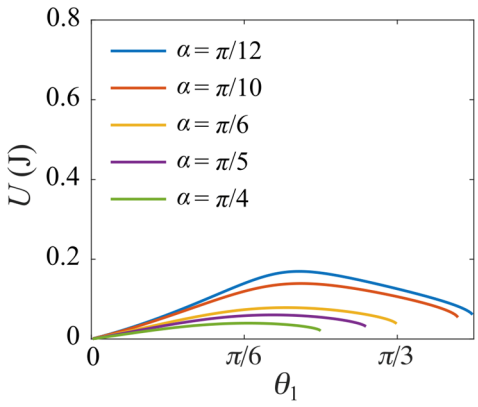

(c) Angle α

Figure 5.7 The elastic energy as a function of the rotational angle θ_1 with different hinge and angle parameters. The initial values of these parameters are: t_i =0.7mm (i=1,2,3), α = π/6.

Another parameter that has influence on the bistability is the star arm angle α. The smaller α is, the distance between the star arms is shorter, indicating the deformation of hinge 2 becomes larger. Figure 5.7(c) shows the comparison of the elastic energy of patterns with different star arm angles. Its tuning capability is more moderate than the hinge width t_2. The smaller α is, the more bistable the pattern becomes. This angle will also constrain the working space of θ_1 according to Eq (5.26).

5.4 Finite element simulation

5.4.1 Triangle model

A nonlinear FE analysis was conducted to explore the bistability of the structure. The simulation was performed with ABAQUS Standard Implicit Dynamics solver with moderate dissipation which improves convergence when self-contact is present (Figure 5.8). We use the Neo-Hooke method for the hyperelastic feature of rubber sheets, and the geometric nonlinearities were taken into account. The models were discretized with CPS8R and CPS6. For single unit cell models, periodic boundary conditions were applied. A simplified contact law was assigned to the model with hard contact for normal behaviour. A parametric model is created using the Python scripting interface of ABAQUS to further investigate the role of different geometrical parameters on the response of the designed mechanical metamaterials. The size of the unit cell is l = 12mm, and the thickness of the cut is 0.3mm.

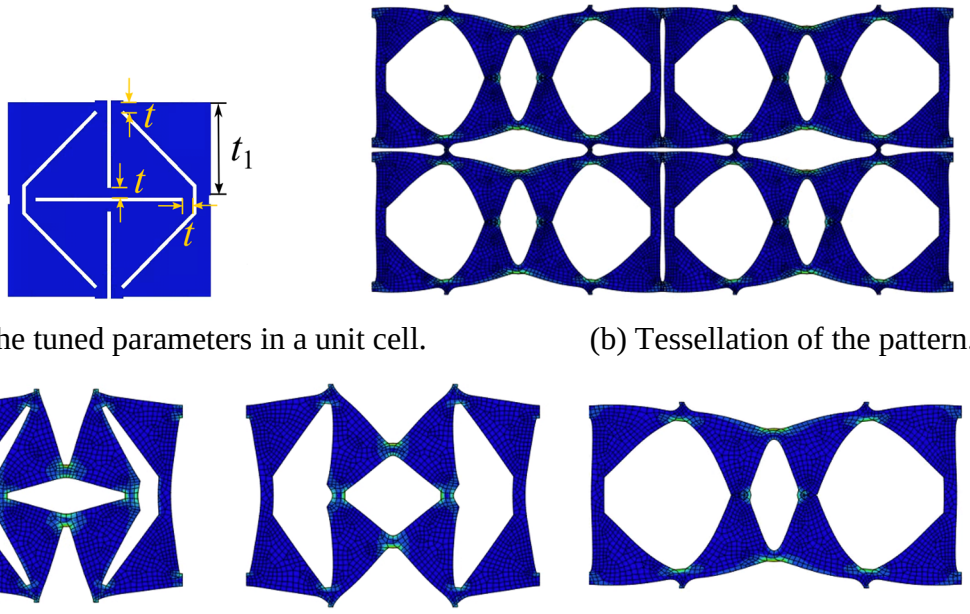

(a) The tuned parameters in a unit cell. (b) Tessellation of the pattern.

(c) Deformation process of the structure.

Figure 5.8 Finite element simulation of the triangle model.

As shown in Figure 5.8, the deformation process of the FE analysis is in accordance with the theoretical results and the real deformation. Here we mainly analysis the influence of hinge

thickness t_1, which is proved to be the driven parameter of the structural bistability, and the thickness t of other hinges. The initial setting of these two parameters are: t_1 = 6mm (there is no vertical cut between two adjacent unit cells), t = 0.8mm.

The results are plotted in Figure 5.9. First, t_1 largely defines the bistability of the structure. If the ligament is very long, the pattern will perform very snappy behaviour; if the hinge is as short as t, the structure will not have a second stable state. On the other hand, even with the bistable design where t_1 reaches the maxima, the increasing thickness of t will lead to more elastic energy of the structure, which may eventually eliminate the bistability. Therefore, a balance in choosing t_1 and t is important to realize the structural bistability.

Moreover, in a multi-column structure, we can tune t_1 to control the open sequence and topology of the pattern. For instance, each column can have a different t_1 value. The smaller t_1 is, the earlier that corresponding column will open when applied force. If we don't want to deploy certain column, it can be realized by eliminating the bistability in the column – the pattern will open up when applied force, yet when released, that column cannot free stand in the second stable state.

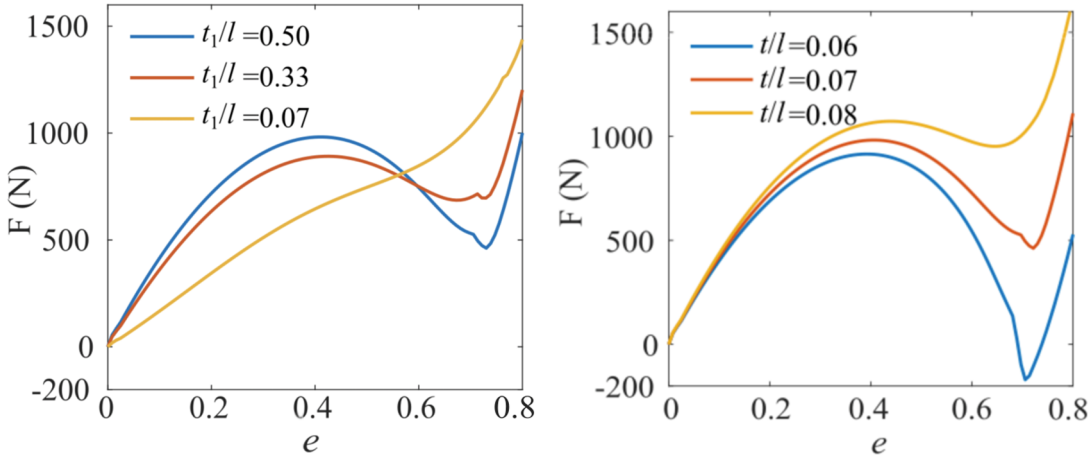

(a) t_1 (b) t

Figure 5.9 Bistable behaviour of the unit cells obtained from FE simulations.

5.4.2 Star model

The star model is simulated using the same approach. We apply horizontal and vertical load at four corners of the unit cell. Figure 5.10(a) shows the main control variables t_2 and α. The initial settings of the parameters are: the size of the unit cell is l = 12mm; the thickness of the cut is 0.3mm; t_2 = 0.7mm and α =24°. Figure 5.10(c) shows the deformation process of the star model. As observed in reality, the pattern will open symmetrically at the beginning, then two pairs of the triangles along the diagonal line tend to open further while the other two pairs collapse to the original close state. When the first two pairs of triangles reach the open state, the other two pairs of triangles begin to deploy again, and eventually, every pair is fully open. The FE results are plotted in Figure 5.11. In accordance with the theoretical results, the thickness of hinge 2 has a great influence on the bistability of the structure: the thinner hinge 2 is, the lower elastic energy the structure has at the second stable state, indicating it's more likely to have bistable behaviour. However, we cannot make the hinge too thin because the connection will be too fragile after several rounds of deployment. The minimum thickness of the hinge is 0.5mm using the laser cutter. The structure will have an extra stable state at the semi-open configuration in Figure 5.10(c), because the model is also geometrically compatible at this configuration, as we illustrated earlier in Figure 5.3. This is evident when t_2 = 0.5 ~ 0.7mm, and the semi-open state happens around 30% of strain. For samples with a thicker hinge 2 width, the elastic energy is too high at the deployed configurations to make the structure free stand at these states. Therefore, for t_2 = 1.1mm, neither of these bistable states exist.

The angle of the star arm α is tuned and the results are plotted in Figure 5.11(b). The angle does not influence the elastic energy at the second stable state; instead, it determines the energy difference of the highest elastic energy and the energy at the stable state. A smaller α leads to a bigger difference, indicating the structure is snappier. Moreover, α determines the strain when

the bistability takes space. The smaller α is, the bigger the strain is, and the structure can deploy to a greater extent.

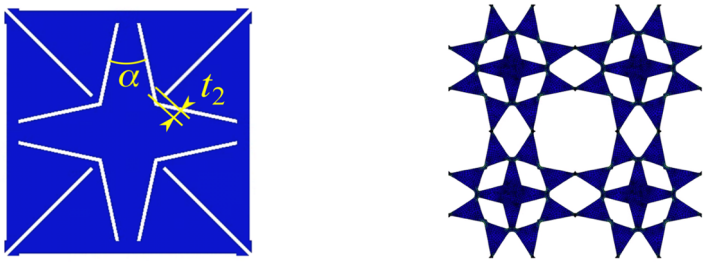

(a) The tuned parameters in a unit cell. (b) Tessellation of the pattern.

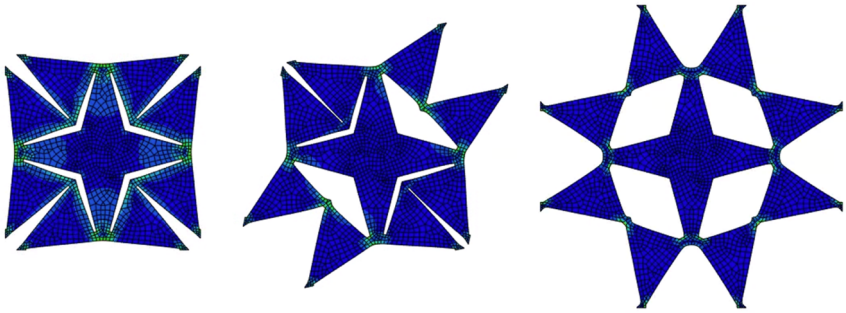

(c) Deformation process of the structure.

Figure 5.10 Finite element simulation of the star model.

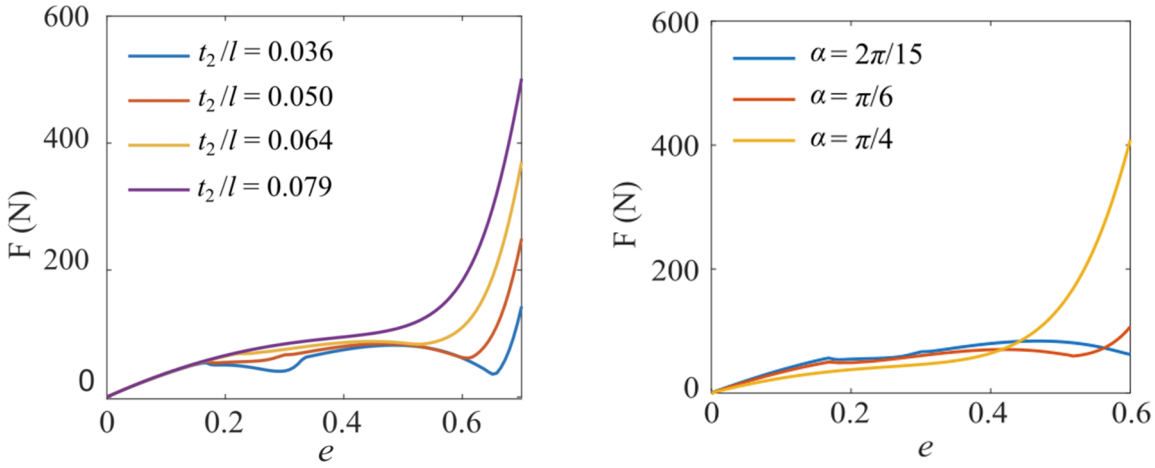

(a) t_2 (b) α

Figure 5.11 Bistability behaviour of unit cells obtained from FE simulations. Resistance force versus strain for different (a) t_2 and (b) α.

5.5 Fabrication

5.5.1 Conductive paint coating method

The samples are fabricated by perforating the designed patterns into low odour laserable rubber sheet (A4 size, 2.3mm thick, shown in Figure 5.12(a)) using a laser cutter. The cut width is around 0.2-0.4mm. We tested that the sufficient thickness for the hinge to be fabricated and bearable under repeat loading is 0.5mm. For the triangle model, the size of the unit cell is 12×12mm, which brings the resonance of the metasurface around 10-12GHz (the measurement range is about 8-14 GHz). The angle α is $\pi/4$. The ligament width for the hinges is $t_i = 0.8$mm (i = 2-6). To achieve strong bistability, we make $t_1 = 6$mm, meaning there is no cut between two neighbouring units in one row. The metamaterial is composed of 17 units in each direction, and the total dimension of the sample is 204×228mm. For the star pattern, the size of the unit cell is 14×14mm and the star angle α is 24°. To make the structure have robust bistability, we design the hinge width to be $t_i = 0.7$mm (i = 1,2,3). The metamaterial is composed of 15 units in each direction with a dimension of 210×210mm.

To coat the sample with metal, we pre-processed the rubber sheets before laser cutting. First, we clean and polish the rubber surface thoroughly and brush metal paint (Copper conductive paint, Caswell) on it. The paint is coated three times to make sure the conductivity on the rubber sheet is good. Then the coated sheet is cut with the designed pattern. After this, the cut sheet is cleaned and painted again for two times to keep the conductivity at thin ligaments. Finally, we tested the surface resistivity of the copper paint coating by using the four-probe method and a source meter (Keithley 2400). The conductivity of the applied copper paint was measured to be a factor 10^4 smaller than that of pure copper. If the sample has no defect, it is ready to be measured as a Frequency Selective Surface. The whole fabrication process and the fabricated samples are shown in Figure 5.12.

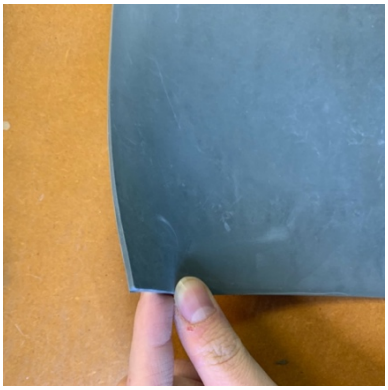

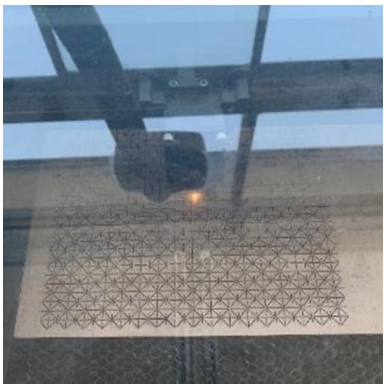

(a) The laserable rubber sheet (b) Sheet coated by metal paint (c) Engraving the rubber sheet

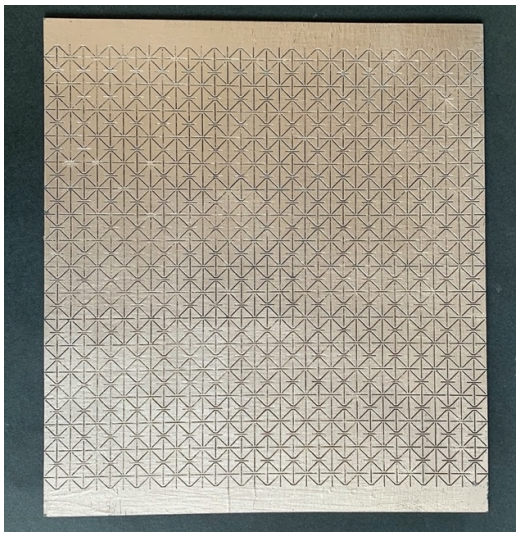
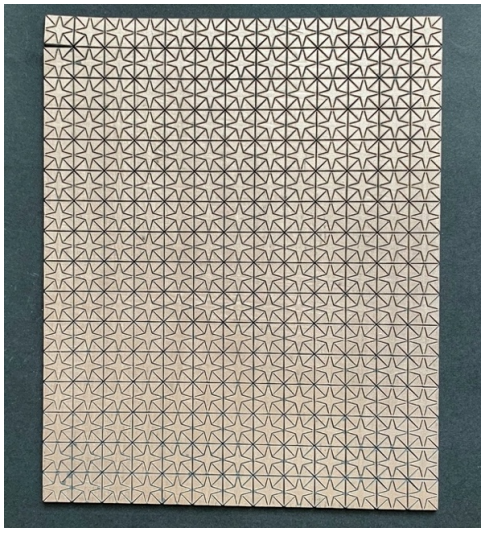

(d) The fabricated samples of the triangle and star models.

Figure 5.12 Fabrication process of the Frequency selective surface.

5.5.2 Other metalizing method

Although the conductivity of the metal paint coating is sufficient for measurement, it may not be ideal for a commercialized device. To improve this, we also tried other metal coating method. The first one, known as the thin-film metal coating, is carried out by physical vapour deposition. The principle is that the coating metal is heated and evaporated in a vacuum, which will condense the base material mounted at the top of the process chamber. The coating metal layer is around 0.1μm. The fabricated sample shown in Figure 5.13(a) has a smooth finish, however, the conductivity is worse than the metal paint. A possible reason could be that the thin ligaments are not coated densely, and some part of the hinges lose continuity of the

conductivity after deformation. The second method we tried is to fabricate a flexible printed circuit board, laser cut the Kapton substrates then glue the PCB on rubber sheet (Figure 5.13(b)). This method achieves good measurement results. The weaknesses lie in the difficulty to glue the PCB smoothly on the rubber sheet, and the problem of structure reconfiguration. The copper hinges are much stiffer than rubber ligaments, so they tend to have wrinkles or out-of-plane twist during the transformation, which will largely influence the functionality. Finally, we decided to adopt the metal paint approach to fabricate the reconfigurable metamaterial as a proof of concept and produce rigid PCB boards engraved with different stable configurations to validate the response.

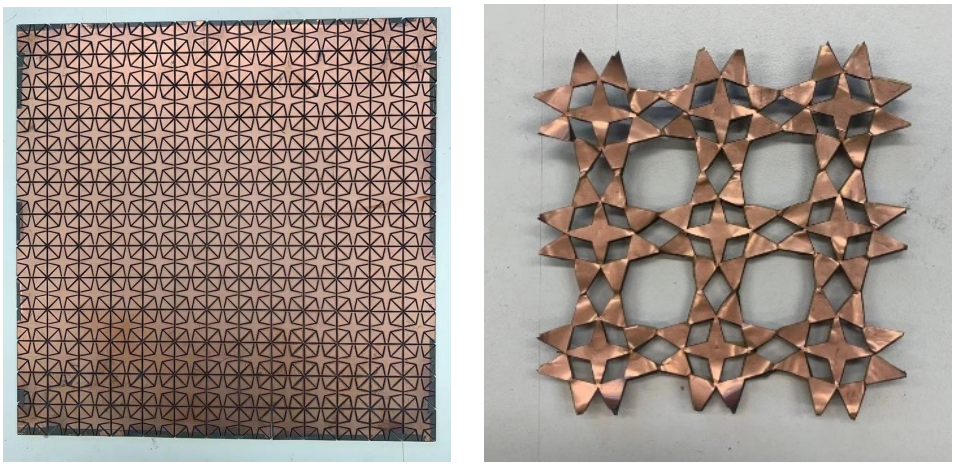

(a) Thin film metal coating (b) Attach a flexible PCB layer on the rubber sheet

Figure 5.13 Other fabrication methods.

5.6 Tensile test

5.6.1 Tensile test setup

We fabricated the triangle model specimens with 2×2 unit cells. The unit cell has a dimension of 14mm and there are 8mm of extra rubber at both ends of the specimen so as to be fixed on the frame(Figure 5.14). The force was measured during loading with a displacement speed of 1 mm/min. We tune the value of t_1 and t to observe the bistability of the structure. The results are shown in Figure 5.15.

5.6.2 Mechanical response of the triangle model

From Figure 5.15, we can note when t_1 is 3.5mm and 7mm, the structure reaches negative force at the second stable states; when t_1 is 0.8mm the force is always positive. The influence of t is very obvious in changing the strain energy of the structure. Eventually, the structure will not be bistable because it cost too much energy to stay in the second stable state.

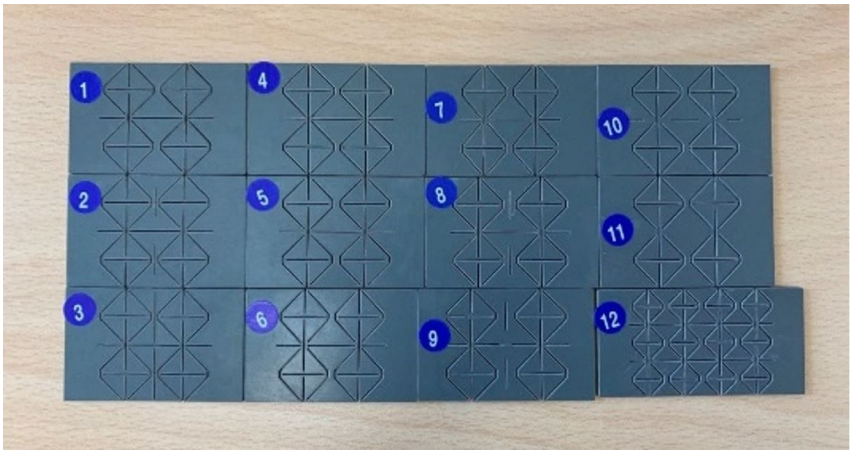

Figure 5.14 Tensile test specimens

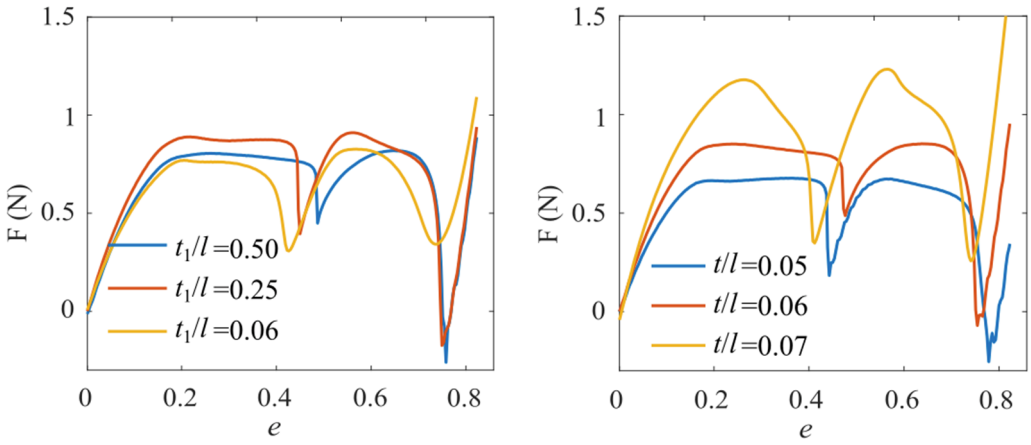

(a) t_1 (b) t

Figure 5.15 Mechanical response of triangle pattern specimens with different parameters.

Because of the gravity, the top column will deploy first and generate the first local minima of force. The results will also be influenced by out-of-plane deformation: it has been observed that the more out-of-plane deformation happens, the more difference will there be between the two local minima. The out-of-plane behaviour is undesirable because it causes more

deformation in the hinges, which accelerate the speed to failure. We can optimize the experiment set up by adding an acrylic board for guiding lateral expansion. In conclusion, the tensile test results generally agree with the FE simulations and the simplified energy model.

5.7 Electromagnetic response of the Metamaterial

5.7.1 Triangular metamaterial

The designed kinematic metamaterials could be used as Frequency Selective Surfaces (FSS). The electromagnetic (EM) response of the FSSs in the closed and open triangle kirigami structures have been simulated with CST Microwave Studio (MWS) using a single unit cell of the kirigami pattern with doubly periodic boundary conditions. We initially aimed at using standard low cost printed circuit technology to validate simulations, so the conducting layer is assumed to be formed by a 0.035mm-thick sheet of pure copper ($\sigma_{Cu} = 5.96\times10^7$ S/m) placed on top of an RF laminate with $\varepsilon_r = 4.3$ and $\tan\delta = 0.025$ (glass-reinforced epoxy, FR4). The metasurface with multiple columns of unit cells can be stretched horizontally and deploy any number of columns. Here, we only focus on its closed and fully open states because the semi-open ones do not provide any interesting functionality. The simulated reflection and transmission coefficients of the open and closed triangle FSSs at normal plane wave incidence are shown in Figure 5.18.

The printed circuit FSS prototypes displayed in Figure 5.16 have been manufactured by Copper Clad FR4 Laminates in static versions of the closed and open kirigami configurations. The specimens are experimentally characterized by measuring their transmission coefficient. The measurements were conducted in an anechoic chamber with the setup shown in Figure 5.17. The FSS circuits were fitted in a metallic frame placed between two standard pyramidal horns, connected to a vector network analyser (VNA). The diffraction by the frame window was calibrated out first by characterizing the fixture without samples.

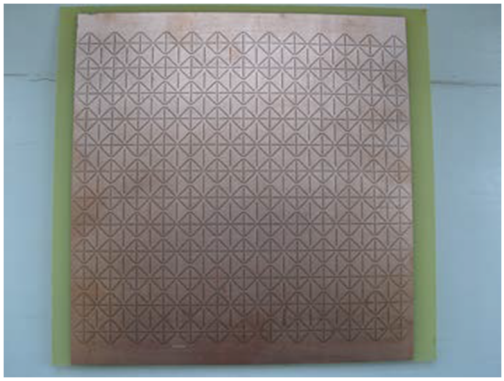

(a)Close state triangle pattern

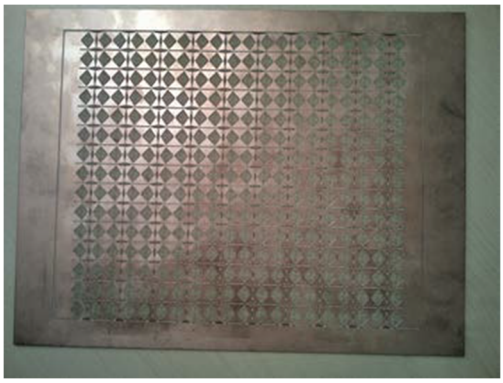

(b) Open state triangle pattern

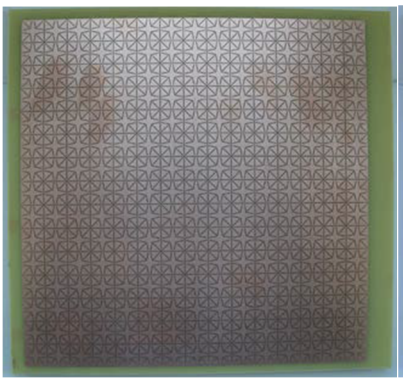

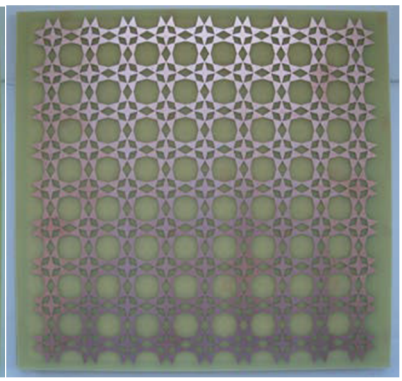

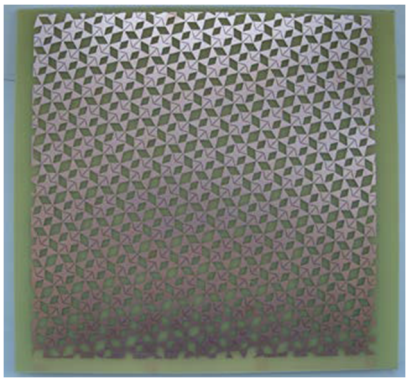

(c) Close state star pattern (d) Open state star pattern (e) Semi-open state star pattern

Figure 5.16 FSS prototypes printed on FR4 laminates to reproduce the different states of triangular and star kirigami models.

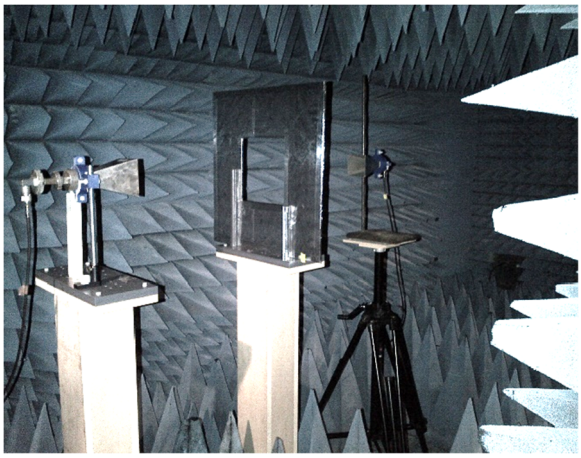

Figure 5.17 Experimental setup in an anechoic chamber.

The measured transmittances for different polarizations are superimposed with the corresponding simulation results in Figure 5.18. It can be observed that the agreement between measurements and simulations is good, especially around the FSS fundamental resonance. In

the simulation results, it is interesting to note that for the horizontal polarization, the FSS in the open state is substantially opaque to the incident field at the frequency around 7.9 GHz at which the closed FSS exhibits its fundamental passband resonance; while for the vertical polarization, there is a similar situation but with roles reversed (i.e., at the fundamental resonance of the FSS in its open state (around 7.8GHz), the closed FSS is screening most of the incoming radiation) Therefore, this structure enables the realization of bistate anisotropic FSS, whose response can be switched on/off by mechanical transformation of the pattern. Overall, these measurements of actual finite-size FSS samples confirm predictions based on the simulation of the corresponding ideal infinite periodic structures and prove that transformable kirigami patterns hold the potential to enable a new class of reconfigurable FSSs not relying on any electronic components for their operation. However, an actual implementation of this concept requires the metallization to be applied directly on top of the laserable rubber sheets from which the kirigami are fabricated by using a laser cutter and that the deformability of the structure is preserved in the process.

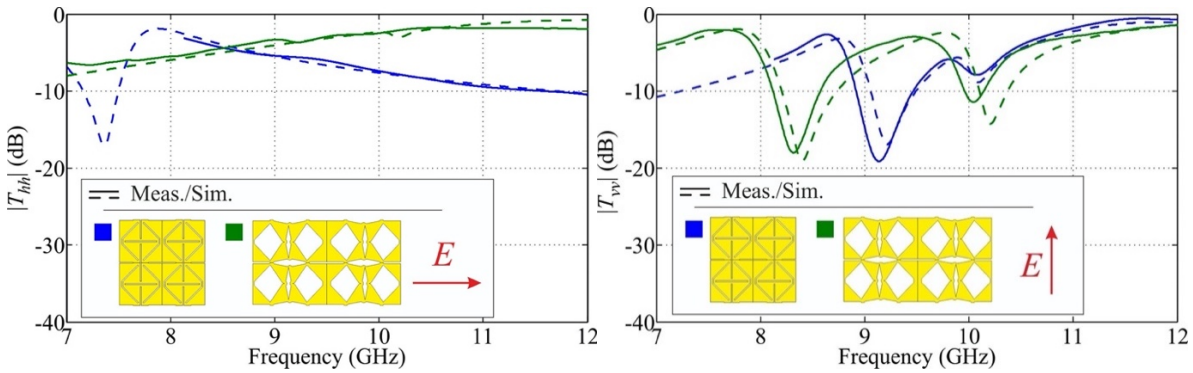

(a) Close state (b) Open state

Figure 5.18 Simulated and measured responses of the PCB triangular kirigami FSS.

Therefore, another triangular kirigami FSS prototype was realized by coating the rubber sheets with copper paint. The transmittance of these FSS prototypes was measured by the same method used for the PCB samples. In Figure 5.19, the measurements and simulation results are obtained by assuming the copper paint layer has a conductivity around $\sigma = \sigma_{Cu} / 5 \times 10^7 = 10^3$

S/m. We also include the simulation results of the case assuming the rubber sheets are coated with pure copper for a reference. The agreement between simulations and measurements is satisfactory when the FSS is in the open state. However, the transmission at the fundamental passband resonance of the FSS in the close state undergoes significant attenuation (-6 dB) due to the poor conductivity of the copper paint. For the FSS in the closed state, measured transmittance differs significantly from the corresponding simulated data. This is attributed to the conductive paint penetrating the slots of the kirigami pattern and covering their internal walls; as a result, when the FSS is closed, the slots are partially obstructed and short-circuited by these amounts of copper paint, which leads to increased reflection as well as larger attenuation, and thus lower transmission, across the entire frequency range than that predicted by simulations. As a result, in the closed state the triangular kirigami FSS tends to behave as a uniform lossy conductor screen.

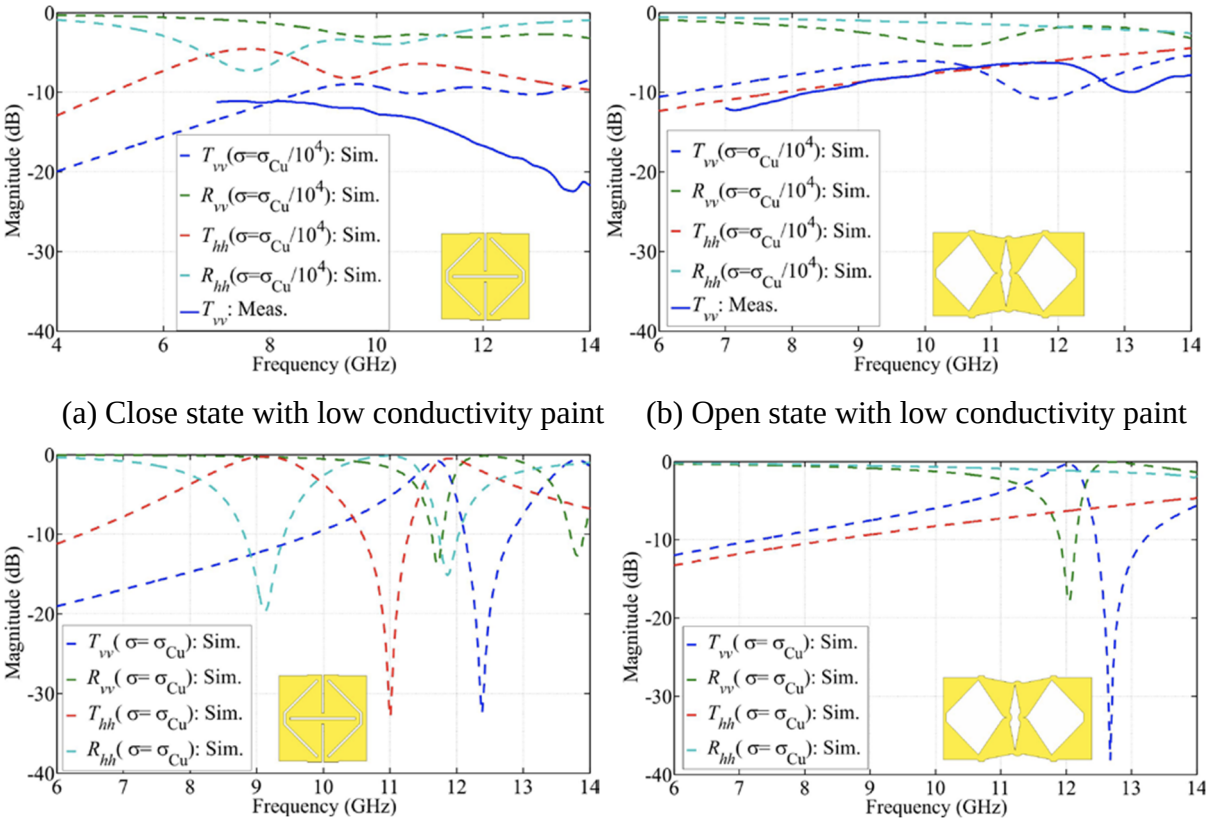

(a) Close state with low conductivity paint (b) Open state with low conductivity paint

(c) Close state with pure copper (d) Open state with pure copper

Figure 5.19 Simulation of the triangular kirigami FSSs made by coating the rubber sheet.

5.7.2 Star kirigami FSS

The star kirigami FSS are simulated, fabricated and measured using the same method. The simulated transmission and reflectance coefficients of the three different configurations at normal plane wave incidence are shown in Figure 5.20. The measured transmission coefficients of the printed circuit FSS prototypes are superimposed with the corresponding simulation results. The responses of the closed and fully open patterns are substantially isotropic due to the four-fold rotational symmetry of their unit cells. Therefore, only the transmittance at one incident polarization are presented in Figure 5.20 (a) and (b). When the kirigami unit cells are closed, the FSS exhibits its fundamental passband resonance at about 6.7 GHz, whereas for the open pattern the resonance occurs at 7.8 GHz. In other words, in principle, a 15% shift in frequency of the FSS fundamental passband response can be obtained by mechanically transforming the kirigami structure, although the change of state does not result in a substantial attenuation of transmission at the frequencies of each FSS passband.

The FSS corresponding to the semi-open state of the star kirigami pattern features an anisotropic response. Its transmittance and reflectance at normal incidence of both horizontally and vertically polarized plane waves are displayed in Figure 5.20 (c) and (d), respectively. The fundamental resonance occurs at about 5.5 GHz for this configuration, and since the principal axes of anisotropy are rotated 35° with respect to the axes of the four-point star at the centre of the unit cell, for the considered incident polarizations, cross-polarized components are nonnegligible.

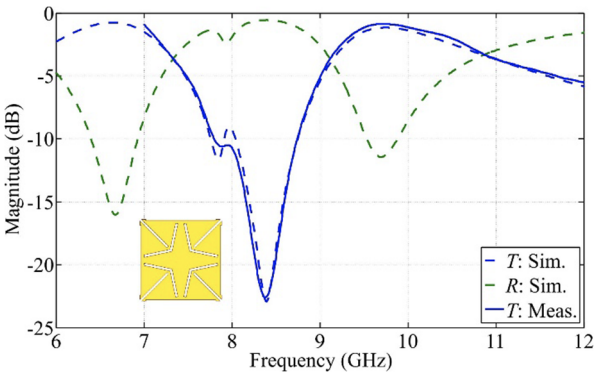

(a) Close state

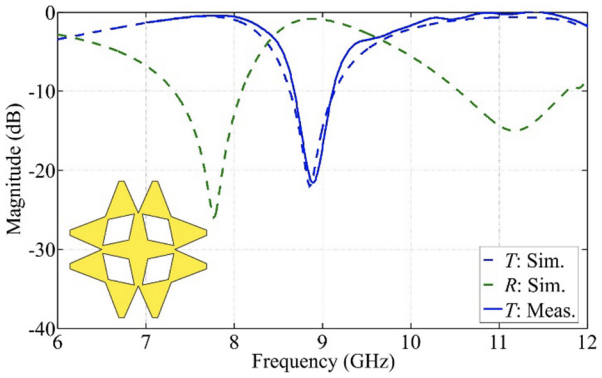

(b) Open state

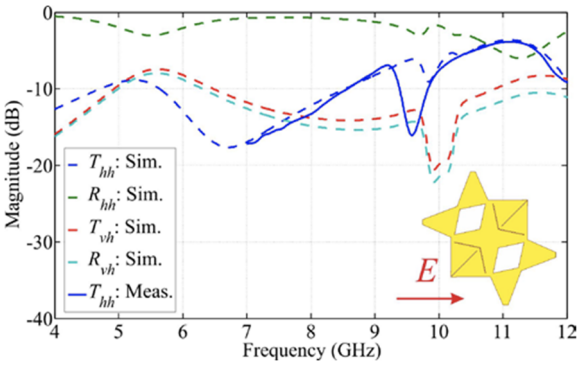

(c) Semi-open state in horizontally polarized wave

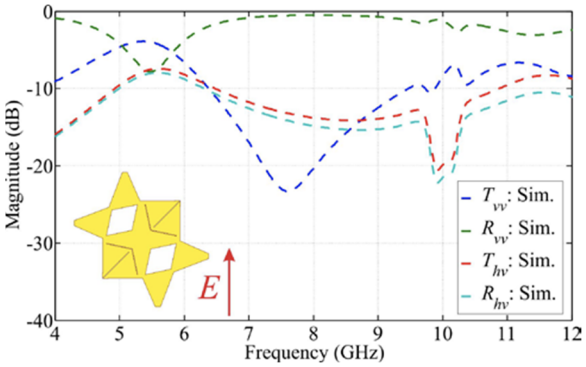

(d) Semi-open state in vertically polarized plane wave

Figure 5.20 Simulated reflectance and transmittance of the star kirigami FSSs at normal plane wave incidence in its three stable states.

We manufactured the second set of FSS by coating the rubber sheets with copper paint. As shown in Figure 5.21, the results of the measurements and simulations with a conductivity of copper paint around $\sigma = \sigma_{Cu} / 5 \times 10^7 = 10^3$ S/m are presented, together with the reference of pure copper.

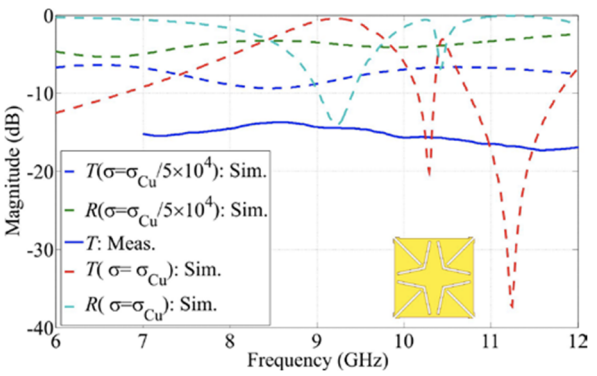

(a) Close state

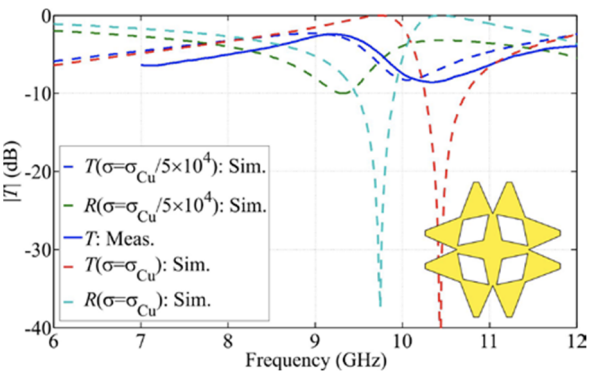

(b) Open state

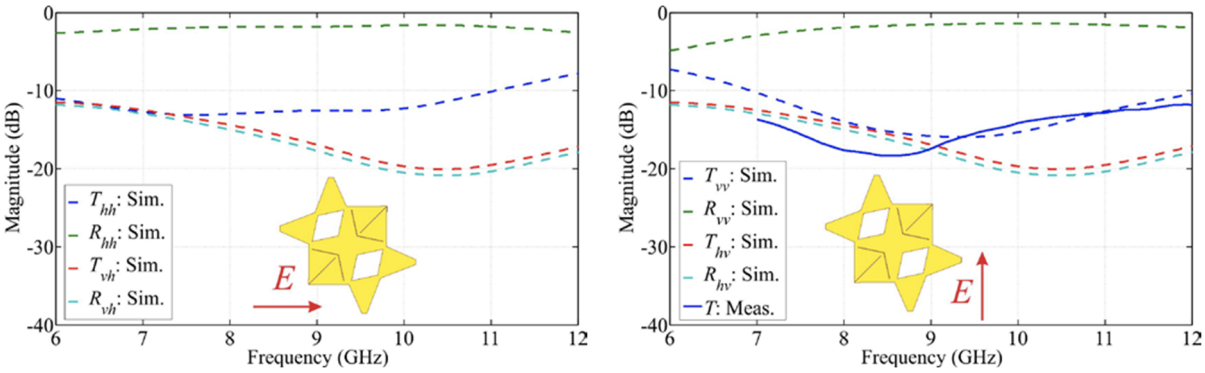

(c) Semi-open state in horizontally polarized wave

(d) Semi-open state in vertically polarized plane wave

Figure 5.21 Simulated reflectance and transmittance of the star kirigami FSSs made by coating rubber sheets with copper paint.

The agreement between simulations and measurements is satisfactory when the FSSs is in the open and semi-open states. For the closed state, measured transmittance differs significantly from the corresponding simulated data, attributed to the conductive paint penetrating the slots of the kirigami pattern and covering their internal walls. To highlight the effect of the short-circuits formed by extra copper paint, the modified closed star unit cell is displayed in Figure 5.22(a), which includes a distribution of little metallic notches along the edges of the pattern. This model is simulated assuming the metal layer on top of the rubber sheet to be pure copper. In the closed state, these notches short-circuit the slots, while in the open pattern, it is not significantly modified by their presence. As shown in Figure 5.22(b), the effect of these short-circuits is to shift upwards in frequency the fundamental resonance associated with the slot pattern in the closed state, reducing the level of transmittance in the frequency range. This approach could indeed be used to realize a bistate mechanically switchable FSS, with the FSS being practically opaque to the incident field in the closed state at the frequencies where the open pattern exhibits its passband resonance.

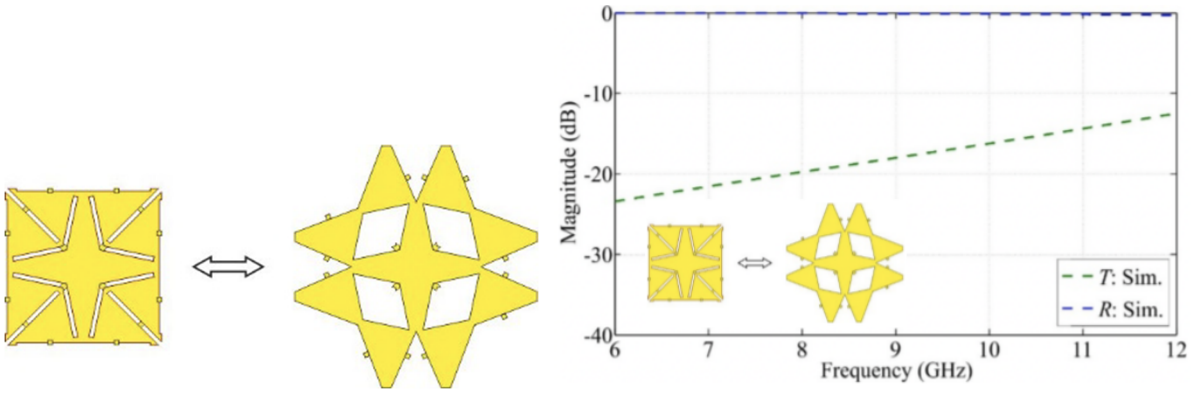

(a) Modified star unit cell (b) Response of the FSS with modified unit in the close state.

Figure 5.22 Modified star unit cell which illustrate the short-circuits effect of the copper paint.

5.8 Conclusion

This chapter demonstrated the electromagnetic application of the kirigami kinematic metamaterial. A triangle and a star bistable structures are designed to lock the metamaterial at several designed patterns. The electromagnetic responses are simulated and measured to validate the idea. The main findings include:

1) The bistability property of the structure can be designed and tuned by incorporating the geometry discrepancy into the mechanisms. By changing the connection thickness of the kirigami patterns, we constrain the distance between two vertices of the triangles, therefore generating the bistability. The snap-through behaviour can be programmed by the connection hinge thickness.
2) The kirigami metamaterials are utilized as frequency selective surfaces. Simulations and measurements have been conducted on both patterns to show that, when the structures are closed, the FSS could be opaque to the incident field (with the short-circuit effect) or exhibit a fundamental passband resonance; when the structures are open, the FSS exhibit another passband resonance. This frequency shift is obtained by mechanically tuning the structure without any loss from the dc control circuits, which usually happens in traditional tuneable FSS.
3) A preliminary manufacturing technique has been developed by coating the laser cut rubber sheet with metal paint. Although the conductivity of the samples is measured to be a factor 10^4 smaller than that of pure copper, the agreement between the simulations and measurements is satisfactory.

In conclusion, the presented application shows a proof of concept of the unite of mechanical and electromagnetic metamaterials. The large topology change in reconfigurable metamaterials provides a big tuning range for the dielectric properties and EM responses of tuneable antennas,

filters and other components. This project could be extended to more electromagnetic applications in the future using continuous-changing structures or three-dimensional kinematic metamaterials.

Chapter 6

Conclusion

6.1 Summary of achievements

This thesis is mainly concerned with the development of mechanical metamaterials using kinematic principles, including findings in 2D and 3D metamaterials. The major achievements are summarized in three aspects, followed by an attempt to identify necessary future work.

6.1.1 Design strategy of mechanical metamaterials using kinematic mechanisms

The main effort of this research is to build the bridge among mechanisms networks, modular origami structures and mechanical metamaterial. Researchers have tried to analyse and construct reconfigurable metamaterials using basic planar mechanisms previously, yet it has never been systematically studied to construct metamaterials using spatial mechanism networks with a synchronized motion. This was achieved step-by-step in this thesis. Chapter 3 presented designs and optimization of a series of 2D metamaterials modelled by planar 4*R* linkages and proposed a tilted method to construct 3D metamaterials that constructed by planar linkages. Based on this, Chapter 4 further proposed to use spatial linkages to construct kinematic units and utilized planar mechanisms to connect the units into a kinematic module. Tessellating the kinematic module in three directions leads to 3D metamaterials whose topology is guided by the entrenched spatial mechanisms, so that the tunability of the unit cell

is strictly maintained. By programming the connection of units and network topology, the mechanical metamaterials can achieve complex transformation without frustration. This kinematic-induced construction method provides several novel properties:

1) A systematic way to construct 3D mechanical metamaterials

While most current mechanical metamaterial research focus on 2D patterns, 3D reconfigurable metamaterials are more difficult to design due to their structural complexity. This thesis provides two methods to build 3D material network. The first one described in Chapter 3 programs the shape of building blocks to generate spatial configurations of the metamaterial. The second method in Chapter 4 claims to entrench spatial mechanisms into the unit of metamaterials and tessellate the kinematic units in three directions. Both methods can be universally adopted while constructing a 3D network of kinematic metamaterial. Following this path, a great number of 3D metamaterials are remained to be explored.

2) Programmable kinematic metamaterials with large optimization space

The programmability of a metamaterial requires the behaviour of materials to be adjustable through the selection of design parameters. This can be conveniently achieved in kinematic induced metamaterials. The motion of a kinematic chain is largely defined by the position and orientation of the kinematic joints. As long as the linkage joints are determined, the geometry of the rigid bodies can be tuned into random shapes without influencing the transformation behaviour. The shape of the building blocks determines the working space of the mechanisms and sometimes generates kinematic bifurcations. The kinematic metamaterials designed in this research inherited this property. As Chapter 3-5 shows, by combining different kinematic units, one can program the output behaviour of the metamaterial; by tuning the geometry of building blocks, one can program the shape, working space of the metamaterial. Therefore, the kinematic metamaterials provide a large optimization space for varies mechanical properties.

3) Metamaterials with multiple reconfiguration modes

Most mechanical metamaterial systems have only one mode of reconfiguring, meaning it can only deform along a predefined path between two final configurations. This research proposed a series of metamaterials with built-in kinematic bifurcations which enables the material to switch from one deformation path to another (Chapter 4). The designed structure has a particular bifurcation point where it can be guided by global forces to choose from different transformation paths. Once it left the bifurcation point, its motion is uniquely defined by the chosen path. In such a way, a mechanical metamaterial can perform various responses adaptive to external stimuli, leading to an exciting avenue towards responsive smart material with multiple functionalities.

6.1.2 Development of electromagnetic functionality of mechanical metamaterials

To date, the design of reconfigurable metamaterials for tuneable functionalities remains challenging, and many designs rely on luck and intuition. In this thesis, an application of kinematic metamaterials on frequency selective surfaces is introduced in Chapter 5. The proposed kirigami patterns are designed to be bistable to lock in several configurations corresponding to specific passband. The metamaterials are manufactured and tested to validate the simulations. The cases shown in this thesis proved that the proposed kinematic metamaterials have great potentials in other multi-functional applications.

6.1.3 Advanced fabrication strategy of mechanical metamaterials

Advanced manufacturing techniques have played a crucial role in developing mechanical metamaterials. Sometimes, the complexity of the porous structure and mechanical requirements of connection joints make it difficult to fabricate prototypes using a single manufacturing technique. Chapter 4 described two methods to fabricate the metamaterials and compared their strengths and weaknesses. The combinatorial strategy that uses strong materials

for hinges and rigid materials for building blocks leads to good performance of the proposed metamaterial. Chapter 5 introduced a method to fabricate metal-coated kirigami metamaterials using laser engraving and metal paint coating, which demands low fabrication cost and time requirement. These methods provide rich experiences for the manufacturing of functional metamaterials in the future.

6.2 Future works

This dissertation has established preliminary results for kinematic mechanism induced metamaterials, which opens up a multitude of potential research paths.

Firstly, from the design aspect, more work is needed to flesh out the notions of mechanism-based aperiodic material and bifurcation-induced multi-path properties into a coherent theory. Preliminary results in Chapter 4 showed that these intuitive attempts could be realized, yet many questions still remain open. For aperiodic structures, the difficulty lies in the design of transition mechanisms. It is not clear how to generalize the rule to design materials that can morph into several predefined random 3D shapes. For multi-path metamaterials, the arisen of bifurcation paths is highly related to the symmetric shape of the unit cell. How to generate a bifurcation path in more generalized shapes is yet to be explored.

Secondly, new applications will arise in smaller and larger scales of current designs. Although in mechanism theories the transformations are essentially homogeneous and scale-free, there still remains large correlation between structure dimensions and the reliability of their functions. For instance, in smaller scales (mm size), the rigidity of building blocks is hard to improve, and in larger scales (m size), the difficulty lies in the reduction of the accumulative error from network connections. To what extent do defects change the properties of multiscale kinematic metamaterials requires further exploration.

Thirdly, the fabrication of ideal reconfigurable metamaterials is still very challenging. Many current techniques including 3D printing, lithography and lamination need further optimization to produce reliable motion structures. For each technique, the applicable base materials are different. While kinematic-induced metamaterials have different preference of materials for different parts, how to allocate these materials in preferable location is a big challenge. The study of combinatorial strategy is in demand to improve the performance of mechanical metamaterial.

Finally, the actuation of kinematic metamaterials is rarely explored. Current metamaterials require passive activation from external compression or stretching. Future metamaterial can be used for robotics or drug delivery applications if it can be activated by external fields, temperature or motors. Moreover, the corresponding behaviour of the material can transmit the environmental information. The integration of sensing with actuation will open the door to truly responsive smart metamaterials.

References

An, S., Zheng, B., Tang, H., Shalaginov, M. Y., Zhou, L., Li, H., ... & Zhang, H. (2019). Generative multi-functional meta-atom and metasurface design networks. *arXiv preprint arXiv:1908.04851*.

Ambati, M., Fang, N., Sun, C., & Zhang, X. (2007). Surface resonant states and superlensing in acoustic metamaterials. *Physical Review B*, *75*(19), 195447.

Amendola, A., Krushynska, A., Daraio, C., Pugno, N. M., & Fraternali, F. (2018). Tuning frequency band gaps of tensegrity mass-spring chains with local and global prestress. *International Journal of Solids and Structures*, 155, 47-56.

Aukes, D. M., Goldberg, B., Cutkosky, M. R., & Wood, R. J. (2014). An analytic framework for developing inherently-manufacturable pop-up laminate devices. *Smart Materials and Structures*, *23*(9), 094013.

Babaee, S., Shim, J., Weaver, J. C., Chen, E. R., Patel, N., & Bertoldi, K. (2013). 3D soft metamaterials with negative Poisson's ratio. *Advanced Materials*, *25*(36), 5044-5049.

Babaee, S., Overvelde, J. T., Chen, E. R., Tournat, V., & Bertoldi, K. (2016). Reconfigurable origami-inspired acoustic waveguides. *Science Advances*, *2*(11), e1601019.

Badagavi, P., Pai, V., & Chinta, A. (2017, May). Use of origami in space science and various other fields of science. In *2017 2nd IEEE International Conference on Recent Trends in Electronics, Information & Communication Technology (RTEICT)* (pp. 628-632). IEEE.

Bauer, J., Hengsbach, S., Tesari, I., Schwaiger, R., & Kraft, O. (2014). High-strength cellular ceramic composites with 3D microarchitecture. *Proceedings of the National Academy of Sciences*, *111*(7), 2453-2458.

Bauer, J., Meza, L. R., Schaedler, T. A., Schwaiger, R., Zheng, X., & Valdevit, L. (2017). Nanolattices: an emerging class of mechanical metamaterials. *Advanced Materials*, *29*(40), 1701850.

Beggs, J. S. (1966). *Advanced mechanism*. Macmillan.

Bennett, G. T. (1903). A new mechanism. *Engineering*, *76*, 777.

Benouhiba, A., Rabenorosoa, K., Ouisse, M., & Andreff, N. (2017). An Origami-Based Tuneable Helmholtz Resonator for Noise Control: Introduction of the Concept and Preliminary Results. In *ASME 2017 Conference on Smart Materials, Adaptive Structures and Intelligent Systems*. American Society of Mechanical Engineers Digital Collection.

Bertoldi, K., & Boyce, M. C. (2008). Mechanically triggered transformations of phononic band gaps in periodic elastomeric structures. *Physical Review B*, *77*(5), 052105.

Bertoldi, K., Reis, P. M., Willshaw, S., & Mullin, T. (2010). Negative Poisson's ratio behaviour induced by an elastic instability. *Advanced materials*, *22*(3), 361-366.

Bertoldi, K., Vitelli, V., Christensen, J., & van Hecke, M. (2017). Flexible mechanical metamaterials. *Nature Reviews Materials*, *2*(11), 1-11.

Blees, M. K., Barnard, A. W., Rose, P. A., Roberts, S. P., McGill, K. L., Huang, P. Y., ... & McEuen, P. L. (2015). Graphene kirigami. *Nature*, *524*(7564), 204-207.

Boatti, E., Vasios, N., & Bertoldi, K. (2017). Origami metamaterials for tuneable thermal expansion. *Advanced Materials*, *29*(26), 1700360.

Borcea, C. S., & Streinu, I. (2014). Frameworks with crystallographic symmetry. *Philosophical Transactions of the Royal Society A: Mathematical, Physical and Engineering Sciences*, *372*(2008), 20120143.

Breger, J. C., Yoon, C., Xiao, R., Kwag, H. R., Wang, M. O., Fisher, J. P., ... & Gracias, D. H. (2015). Self-folding thermo-magnetically responsive soft microgrippers. *ACS applied materials & interfaces*, *7*(5), 3398-3405.

Bricard, R. (1897). Mémoire sur la théorie de l'octaèdre articulé. *Journal de Mathématiques pures et appliquées*, *3*, 113-148.

Bricard, R., & de Cinématique, L. (1927). Tome II. *Gauthier-Villars, Pairs*, 203-204.

Bückmann, T., Kadic, M., Schittny, R., & Wegener, M. (2015). Mechanical cloak design by direct lattice transformation. *Proceedings of the National Academy of Sciences*, *112*(16), 4930-4934.

Castles, F., Isakov, D., Lui, A., Lei, Q., Dancer, C. E. J., Wang, Y., ... & Grant, P. S. (2016). Microwave dielectric characterisation of 3D-printed BaTiO 3/ABS polymer composites. *Scientific reports*, *6*, 22714.

Celli, P., McMahan, C., Ramirez, B., Bauhofer, A., Naify, C., Hofmann, D., ... & Daraio, C. (2018). Shape-morphing architected sheets with non-periodic cut patterns. *Soft matter*, *14*(48), 9744-9749.

Chen, D., & Zheng, X. (2018). Multi-material additive manufacturing of metamaterials with giant, tailorable negative Poisson's ratios. *Scientific reports*, *8*(1), 1-8.

Chen, H., & Chan, C. T. (2007). Acoustic cloaking in three dimensions using acoustic metamaterials. *Applied physics letters*, *91*(18), 183518.

Chen, Y., Feng, H., Ma, J., Peng, R., & You, Z. (2016). Symmetric waterbomb origami. *Proceedings of the Royal Society A: Mathematical, Physical and Engineering Sciences*, *472*(2190), 20150846.

Cheng, H., Zhang, Y., Hwang, K. C., Rogers, J. A., & Huang, Y. (2014). Buckling of a stiff thin film on a pre-strained bi-layer substrate. *International Journal of Solids and Structures*, *51*(18), 3113-3118.

Chen, Y., Peng, R., & You, Z. (2015). Origami of thick panels. *Science*, *349*(6246), 396-400.

Chen, Y., & You, Z. (2005). Mobile assemblies based on the Bennett linkage. *Proceedings of the Royal Society A: Mathematical, Physical and Engineering Sciences*, *461*(2056), 1229-1245.

Chen, Y., You, Z., & Tarnai, T. (2005). Threefold-symmetric Bricard linkages for deployable structures. *International journal of solids and structures*, *42*(8), 2287-2301.

Cheng, Y., Yang, F., Xu, J. Y., & Liu, X. J. (2008). A multilayer structured acoustic cloak with homogeneous isotropic materials. *Applied Physics Letters*, *92*(15), 151913.

Cheung, K. C., Tachi, T., Calisch, S., & Miura, K. (2014). Origami interleaved tube cellular materials. *Smart Materials and Structures*, *23*(9), 094012

Ciobanu, R., Damian, R., & Casian-Botez, I. (2010). Electromagnetic characterization of chiral auxetic metamaterials for EMC applications. *Computer Standards & Interfaces*, *32*(3), 101-109.

Conway, J. H., Friedrichs, O. D., Huson, D. H., & Thurston, W. P. (2001). On three-dimensional space groups. *Contributions to Algebra and Geometry*, *42*(2), 475-507.

Coulais, C., Overvelde, J. T., Lubbers, L. A., Bertoldi, K., & van Hecke, M. (2015). Discontinuous buckling of wide beams and metabeams. *Physical review letters*, *115*(4), 044301.

Coulais, C., Sabbadini, A., Vink, F., & van Hecke, M. (2018). Multi-step self-guided pathways for shape-changing metamaterials. *Nature*, *561*(7724), 512-515.

Coulais, C., Sounas, D., & Alù, A. (2017). Static non-reciprocity in mechanical metamaterials. *Nature*, *542*(7642), 461-464.

Coulais, C., Teomy, E., De Reus, K., Shokef, Y., & Van Hecke, M. (2016). Combinatorial design of textured mechanical metamaterials. *Nature*, *535*(7613), 529-532.

Dudte, L. H., Vouga, E., Tachi, T., & Mahadevan, L. (2016). Programming curvature using origami tessellations. *Nature materials*, *15*(5), 583-588.

Edmondson, B. J., Lang, R. J., Magleby, S. P., & Howell, L. L. (2014). An offset panel technique for thick rigidily foldable origami. In *ASME 2014 International Design Engineering Technical Conferences and Computers and Information in Engineering Conference*. American Society of Mechanical Engineers Digital Collection.

Eidini, M., & Paulino, G. H. (2015). Unraveling metamaterial properties in zigzag-base folded sheets. *Science advances*, *1*(8), e1500224.

Evans, K. E., & Alderson, A. (2000). Auxetic materials: functional materials and structures from lateral thinking!. *Advanced materials*, *12*(9), 617-628.

Evans, K. E., Nkansah, M. A., & Hutchinson, I. J. (1994). Auxetic foams: modelling negative Poisson's ratios. *Acta metallurgica et materialia*, *42*(4), 1289-1294.

Fargette, A., Neukirch, S., & Antkowiak, A. (2014). Elastocapillary snapping: Capillarity induces snap-through instabilities in small elastic beams. *Physical review letters*, *112*(13), 137802.

Felton, S. M., Tolley, M. T., Shin, B., Onal, C. D., Demaine, E. D., Rus, D., & Wood, R. J. (2013). Self-folding with shape memory composites. *Soft Matter*, *9*(32), 7688-7694.

Filipov, E. T., Tachi, T., & Paulino, G. H. (2015). Origami tubes assembled into stiff, yet reconfigurable structures and metamaterials. *Proceedings of the National Academy of Sciences*, *112*(40), 12321-12326.

Frenzel, T., Kadic, M., & Wegener, M. (2017). Three-dimensional mechanical metamaterials with a twist. *Science*, *358*(6366), 1072-1074.

Fuchi, K., Tang, J., Crowgey, B., Diaz, A. R., Rothwell, E. J., & Ouedraogo, R. O. (2012). Origami tuneable frequency selective surfaces. *IEEE antennas and wireless propagation letters*, *11*, 473-475.

Gansel, J. K., Thiel, M., Rill, M. S., Decker, M., Bade, K., Saile, V., ... & Wegener, M. (2009). Gold helix photonic metamaterial as broadband circular polarizer. *Science*, *325*(5947), 1513-1515.

Gatt, R., Mizzi, L., Azzopardi, J. I., Azzopardi, K. M., Attard, D., Casha, A., ... & Grima, J. N. (2015). Hierarchical auxetic mechanical metamaterials. *Scientific reports*, *5*, 8395.

Ge, Q., Sakhaei, A. H., Lee, H., Dunn, C. K., Fang, N. X., & Dunn, M. L. (2016). Multimaterial 4D printing with tailorable shape memory polymers. *Scientific reports*, *6*, 31110.

Ghosh, S., & Srivastava, K. V. (2017). Broadband polarization-insensitive tuneable frequency selective surface for wideband shielding. *IEEE Transactions on Electromagnetic Compatibility*, 60(1), 166-172.

Gibson, L. J. (2005). Biomechanics of cellular solids. *Journal of biomechanics*, *38*(3), 377-399.

Gillman, A., Fuchi, K., & Buskohl, P. R. (2018). Truss-based nonlinear mechanical analysis for origami structures exhibiting bifurcation and limit point instabilities. International Journal of Solids and Structures, 147, 80-93.

Grima, J. N., & Evans, K. E. (2006). Auxetic behaviour from rotating triangles. *Journal of materials science*, *41*(10), 3193-3196.

Grünbaum, B. (1977). Regular polyhedra—old and new. *aequationes mathematicae*, *16*(1-2), 1-20.

Grünbaum, B., & Shephard, G. C. (1986). *Tilings and patterns*. WH Freeman & Co..

Haghpanah, B., Salari-Sharif, L., Pourrajab, P., Hopkins, J., & Valdevit, L. (2016). Multistable shape-reconfigurable architected materials. *Advanced Materials*, *28*(36), 7915-7920.

Hawkes, E., An, B., Benbernou, N. M., Tanaka, H., Kim, S., Demaine, E. D., ... & Wood, R. J. (2010). Programmable matter by folding. *Proceedings of the National Academy of Sciences*, *107*(28), 12441-12445.

Hoberman, C. (2010). *U.S. Patent No. 7,794,019*. Washington, DC: U.S. Patent and Trademark Office.

Hunt, K. H. (1978). *Kinematic geometry of mechanisms* (Vol. 7). Oxford University Press, USA.

Ion, A., Frohnhofen, J., Wall, L., Kovacs, R., Alistar, M., Lindsay, J., ... & Baudisch, P. (2016, October). Metamaterial mechanisms. In *Proceedings of the 29th Annual Symposium on User Interface Software and Technology* (pp. 529-539).

Ion, A., Wall, L., Kovacs, R., & Baudisch, P. (2017, May). Digital mechanical metamaterials. In *Proceedings of the 2017 CHI Conference on Human Factors in Computing Systems* (pp. 977-988).

Jang, D., Meza, L. R., Greer, F., & Greer, J. R. (2013). Fabrication and deformation of three-dimensional hollow ceramic nanostructures. *Nature materials*, *12*(10), 893-898.

Javid, F., Liu, J., Shim, J., Weaver, J. C., Shanian, A., & Bertoldi, K. (2016). Mechanics of instability-induced pattern transformations in elastomeric porous cylinders. Journal of the Mechanics and Physics of Solids, 96, 1-17.

Jiang, Y., & Li, Y. (2018). 3D printed auxetic mechanical metamaterial with chiral cells and re-entrant cores. *Scientific reports*, *8*(1), 1-11.

Kadic, M., Milton, G. W., van Hecke, M., & Wegener, M. (2019). 3D metamaterials. *Nature Reviews Physics*, *1*(3), 198-210.

Kang, S. H., Shan, S., Noorduin, W. L., Khan, M., Aizenberg, J., & Bertoldi, K. (2013). Buckling-induced reversible symmetry breaking and amplification of chirality using supported cellular structures. *Advanced materials*, *25*(24), 3380-3385.

Kim, D. H., Lu, N., Ma, R., Kim, Y. S., Kim, R. H., Wang, S., ... & Yu, K. J. (2011). Epidermal electronics. *science*, *333*(6044), 838-843.

Kokkinis, D., Schaffner, M., & Studart, A. R. (2015). Multimaterial magnetically assisted 3D printing of composite materials. *Nature communications*, *6*(1), 1-10.

Kolken, H. M., Janbaz, S., Leeflang, S. M., Lietaert, K., Weinans, H. H., & Zadpoor, A. A. (2018). Rationally designed meta-implants: a combination of auxetic and conventional meta-biomaterials. *Materials Horizons*, *5*(1), 28-35.

Konaković-Luković, M., Panetta, J., Crane, K., & Pauly, M. (2018). Rapid deployment of curved surfaces via programmable auxetics. *ACM Transactions on Graphics (TOG)*, *37*(4), 1-13.

Kuribayashi, K., Tsuchiya, K., You, Z., Tomus, D., Umemoto, M., Ito, T., & Sasaki, M. (2006). Self-deployable origami stent grafts as a biomedical application of Ni-rich TiNi shape memory alloy foil. *Materials Science and Engineering: A*, *419*(1-2), 131-137.

Lakes, R. (1987). Foam structures with a negative Poisson's ratio. *Science, 235*, 1038-1041.

Li, L., Wang, J., Wang, J., Ma, H., Du, H., Zhang, J., ... & Xu, Z. (2016). Reconfigurable all-dielectric metamaterial frequency selective surface based on high-permittivity ceramics. Scientific reports, 6, 24178.

Liu, J., Gu, T., Shan, S., Kang, S. H., Weaver, J. C., & Bertoldi, K. (2016). Harnessing buckling to design architected materials that exhibit effective negative swelling. *Advanced Materials*, *28*(31), 6619-6624.

Lee, K., Chien, C. W., Lee, B., Lamoureux, A., Shlian, M., Shtein, M., ... & Forrest, S. (2016). Origami solar-tracking concentrator array for planar photovoltaics. *ACS Photonics*, *3*(11), 2134-2140.

Lee, S., Kim, S., Kim, T. T., Kim, Y., Choi, M., Lee, S. H., ... & Min, B. (2012). Reversibly stretchable and tuneable terahertz metamaterials with wrinkled layouts. *Advanced Materials*, *24*(26), 3491-3497.

Li, J., Shim, J., Deng, J., Overvelde, J. T., Zhu, X., Bertoldi, K., & Yang, S. (2012). Switching periodic membranes via pattern transformation and shape memory effect. *Soft Matter*, *8*(40), 10322-10328.

Liu, Z., Du, H., Li, J., Lu, L., Li, Z. Y., & Fang, N. X. (2018). Nano-kirigami with giant optical chirality. *Science advances*, *4*(7), eaat4436

Lv, C., Krishnaraju, D., Konjevod, G., Yu, H., & Jiang, H. (2014). Origami based mechanical metamaterials. *Scientific reports*, *4*, 5979.

Maloney, K. J., Roper, C. S., Jacobsen, A. J., Carter, W. B., Valdevit, L., & Schaedler, T. A. (2013). Microlattices as architected thin films: Analysis of mechanical properties and high strain elastic recovery. *APL Materials*, *1*(2), 022106.

Miura, K. (1985). Method of packaging and deployment of large membranes in space. *Title The Institute of Space and Astronautical Science Report*, *618*, 1.

Mitschke, H., Robins, V., Mecke, K., & Schröder-Turk, G. E. (2013). Finite auxetic deformations of plane tessellations. *Proceedings of the Royal Society A: Mathematical, Physical and Engineering Sciences*, *469*(2149), 20120465.

Mitschke, H., Schröder-Turk, G. E., Mecke, K., Fowler, P. W., & Guest, S. D. (2013). Symmetry detection of auxetic behaviour in 2D frameworks. *EPL (Europhysics Letters)*, *102*(6), 66005.

Morgan, M. R., Lang, R. J., Magleby, S. P., & Howell, L. L. (2016). Towards developing product applications of thick origami using the offset panel technique. *Mechanical Sciences*, 7(1), 69-69.

Morin, S. A., Shepherd, R. F., Kwok, S. W., Stokes, A. A., Nemiroski, A., & Whitesides, G. M. (2012). Camouflage and display for soft machines. *Science*, *337*(6096), 828-832.

Mukerji, M. (2007). *Marvelous modular origami*. AK Peters/CRC Press.

Mullin, T., Deschanel, S., Bertoldi, K., & Boyce, M. C. (2007). Pattern transformation triggered by deformation. *Physical review letters*, *99*(8), 084301.

Nauroze, S. A., Novelino, L. S., Tentzeris, M. M., & Paulino, G. H. (2018). Continuous-range tuneable multilayer frequency-selective surfaces using origami and inkjet printing. *Proceedings of the National Academy of Sciences*, *115*(52), 13210-13215.

Neville, R. M., Scarpa, F., & Pirrera, A. (2016). Shape morphing Kirigami mechanical metamaterials. *Scientific reports*, *6*, 31067.

Ou, J., Ma, Z., Peters, J., Dai, S., Vlavianos, N., & Ishii, H. (2018). KinetiX-designing auxetic-inspired deformable material structures. *Computers & Graphics*, *75*, 72-81.

Overvelde, J. T., De Jong, T. A., Shevchenko, Y., Becerra, S. A., Whitesides, G. M., Weaver, J. C., ... & Bertoldi, K. (2016). A three-dimensional actuated origami-inspired transformable metamaterial with multiple degrees of freedom. *Nature communications*, *7*(1), 1-8.

Overvelde, J. T., Weaver, J. C., Hoberman, C., & Bertoldi, K. (2017). Rational design of reconfigurable prismatic architected materials. *Nature*, *541*(7637), 347-352.

Overvelde, J. T., Shan, S., & Bertoldi, K. (2012). Compaction through buckling in 2D periodic, soft and porous structures: effect of pore shape. *Advanced Materials*, *24*(17), 2337-2342.

Pandey, A., Moulton, D. E., Vella, D., & Holmes, D. P. (2014). Dynamics of snapping beams and jumping poppers. *EPL (Europhysics Letters)*, *105*(2), 24001.

Panetta, J., Zhou, Q., Malomo, L., Pietroni, N., Cignoni, P., & Zorin, D. (2015). Elastic textures for additive fabrication. *ACM Transactions on Graphics (TOG)*, *34*(4), 1-12.

Pei, E., Melenka, G. W., Schofield, J. S., Dawson, M. R., & Carey, J. P. (2015). Evaluation of dimensional accuracy and material properties of the MakerBot 3D desktop printer. *Rapid Prototyping Journal*.

Pendry, J. B. (2000). Negative refraction makes a perfect lens. *Physical review letters*, *85*(18), 3966.

Pouya, C., Overvelde, J. T., Kolle, M., Aizenberg, J., Bertoldi, K., Weaver, J. C., & Vukusic, P. (2016). Characterization of a mechanically tuneable gyroid photonic crystal inspired by the butterfly parides sesostris. *Advanced Optical Materials*, *4*(1), 99-105.

Qi, X., Huang, H., Miao, Z., Li, B., & Deng, Z. (2017). Design and mobility analysis of large deployable mechanisms based on plane-symmetric Bricard linkage. *Journal of Mechanical Design*, *139*(2).

Radkovskaya, A., Kiriushechkina, S., Vakulenko, A., Petrov, P., Solymar, L., Li, L., ... & Shamonina, E. (2018). Superdirectivity from arrays of strongly coupled meta-atoms. *Journal of Applied Physics*, *124*(10), 104901.

Rafsanjani, A., & Bertoldi, K. (2017). Buckling-induced kirigami. *Physical review letters*, *118*(8), 084301.

Rafsanjani, A., & Pasini, D. (2016). Bistable auxetic mechanical metamaterials inspired by ancient geometric motifs. *Extreme Mechanics Letters*, *9*, 291-296.

Rafsanjani, A., Zhang, Y., Liu, B., Rubinstein, S. M., & Bertoldi, K. (2018). Kirigami skins make a simple soft actuator crawl. *Science Robotics*, *3*(15), eaar7555.

Resch, R. D. (1977). *U.S. Patent No. 4,059,932*. Washington, DC: U.S. Patent and Trademark Office.

Restrepo, D., Mankame, N. D., & Zavattieri, P. D. (2016). Programmable materials based on periodic cellular solids. Part I: Experiments. *International Journal of Solids and Structures*, *100*, 485-504.

Saito, K., Fujimoto, A., & Okabe, Y. (2016). Design of a 3d wing honeycomb core based on origami techniques. In *ASME 2016 International Design Engineering Technical Conferences and Computers and Information in Engineering Conference*. American Society of Mechanical Engineers Digital Collection.

Sarrus, P. T. (1853). Note Sur la Transformation des Mouvements Rectilignes Alternatifs, en Mouvements Circulaires, et Reciproquement, Comptes. Rendus. *Acad. Sci., Paris*, *36*, 1036.

Schaedler, T. A., Jacobsen, A. J., Torrents, A., Sorensen, A. E., Lian, J., Greer, J. R., ... & Carter, W. B. (2011). Ultralight metallic microlattices. *Science*, *334*(6058), 962-965.

Schaedler, T. A., Ro, C. J., Sorensen, A. E., Eckel, Z., Yang, S. S., Carter, W. B., & Jacobsen, A. J. (2014). Designing metallic microlattices for energy absorber applications. *Advanced Engineering Materials*, *16*(3), 276-283.

Schattschneider, D., & Walker, W. (1977). *MC Escher kaleidocycles* (No. 76Escher). Ballantine Books.

Schenk, M., & Guest, S. D. (2013). Geometry of Miura-folded metamaterials. *Proceedings of the National Academy of Sciences*, *110*(9), 3276-3281.

Schurig, D., Mock, J. J., Justice, B. J., Cummer, S. A., Pendry, J. B., Starr, A. F., & Smith, D. R. (2006). Metamaterial electromagnetic cloak at microwave frequencies. *Science*, *314*(5801), 977-980.

Schwerdtfeger, J., Wein, F., Leugering, G., Singer, R. F., Körner, C., Stingl, M., & Schury, F. (2011). Design of auxetic structures via mathematical optimization. *Advanced materials*, *23*(22-23), 2650-2654.

Shan, S., Kang, S. H., Raney, J. R., Wang, P., Fang, L., Candido, F., ... & Bertoldi, K. (2015). Multistable architected materials for trapping elastic strain energy. *Advanced Materials*, *27*(29), 4296-4301.

Shaw, L. A., Chizari, S., Dotson, M., Song, Y., & Hopkins, J. B. (2018). Compliant rolling-contact architected materials for shape reconfigurability. *Nature communications*, *9*(1), 1-12.

Silverberg, J. L., Evans, A. A., McLeod, L., Hayward, R. C., Hull, T., Santangelo, C. D., & Cohen, I. (2014). Using origami design principles to fold reprogrammable mechanical metamaterials. *science*, *345*(6197), 647-650.

Silverberg, J. L., Na, J. H., Evans, A. A., Liu, B., Hull, T. C., Santangelo, C. D., ... & Cohen, I. (2015). Origami structures with a critical transition to bistability arising from hidden degrees of freedom. *Nature materials*, *14*(4), 389-393.

Simon, L., Arnstein, B., & Gurkewitz, R. (2012). *Modular Origami Polyhedra: Revised and Enlarged Edition*. Courier Corporation.

Song, Z., Ma, T., Tang, R., Cheng, Q., Wang, X., Krishnaraju, D., ... & Jiang, H. (2014). Origami lithium-ion batteries. *Nature communications*, *5*(1), 1-6.

Song, Z., Wang, X., Lv, C., An, Y., Liang, M., Ma, T., ... & Jiang, H. (2015). Kirigami-based stretchable lithium-ion batteries. *Scientific reports*, *5*(1), 1-9.

Stevens, C. J. (2014). Magnetoinductive waves and wireless power transfer. *IEEE Transactions on Power Electronics*, *30*(11), 6182-6190.

Sun, C., Fang, N., Wu, D. M., & Zhang, X. (2005). Projection micro-stereolithography using digital micro-mirror dynamic mask. *Sensors and Actuators A: Physical*, *121*(1), 113-120.

Sun, Y., Choi, W. M., Jiang, H., Huang, Y. Y., & Rogers, J. A. (2006). Controlled buckling of semiconductor nanoribbons for stretchable electronics. *Nature nanotechnology*, *1*(3), 201.

Sun, X., Felton, S. M., Niiyama, R., Wood, R. J., & Kim, S. (2015, May). Self-folding and self-actuating robots: a pneumatic approach. In *2015 IEEE International Conference on Robotics and Automation (ICRA)* (pp. 3160-3165). IEEE.

Sussman, D. M., Cho, Y., Castle, T., Gong, X., Jung, E., Yang, S., & Kamien, R. D. (2015). Algorithmic lattice kirigami: A route to pluripotent materials. *Proceedings of the National Academy of Sciences*, *112*(24), 7449-7453.

Tachi, T. (2011). Rigid-foldable thick origami. *Origami*, *5*, 253-264.

Tachi, T., & Miura, K. (2012). Rigid-foldable cylinders and cells. *Journal of the international association for shell and spatial structures*, *53*(4), 217-226.

Taylor, P. S., Parker, E. A., & Batchelor, J. C. (2011). An active annular ring frequency selective surface. *IEEE Transactions on antennas and propagation*, 59(9), 3265-3271.

Tang, Y., Lin, G., Han, L., Qiu, S., Yang, S., & Yin, J. (2015). Design of hierarchically cut hinges for highly stretchable and reconfigurable metamaterials with enhanced strength. *Advanced materials*, *27*(44), 7181-7190.

Tang, Y., Lin, G., Yang, S., Yi, Y. K., Kamien, R. D., & Yin, J. (2017). Programmable Kiri-Kirigami Metamaterials. *Advanced Materials*, *29*(10), 1604262.

Tang, Y., & Yin, J. (2017). Design of cut unit geometry in hierarchical kirigami-based auxetic metamaterials for high stretchability and compressibility. *Extreme Mechanics Letters*, *12*, 77-85.

Tao, H., Strikwerda, A. C., Fan, K., Padilla, W. J., Zhang, X., & Averitt, R. D. (2009). Reconfigurable terahertz metamaterials. *Physical review letters*, *103*(14), 147401.

Tarnai, T., Kovács, F., Fowler, P. W., & Guest, S. D. (2012). Wrapping the cube and other polyhedra. *Proceedings of the Royal Society A: Mathematical, Physical and Engineering Sciences*, *468*(2145), 2652-2666.

Tibbits, S. (2014). 4D printing: multi-material shape change. *Architectural Design*, *84*(1), 116-121.

Valdevit, L., Jacobsen, A. J., Greer, J. R., & Carter, W. B. (2011). Protocols for the optimal design of multi-functional cellular structures: from hypersonics to micro-architected materials. *Journal of the American Ceramic Society*, *94*, s15-s34.

Vallecchi, A., Langley, R. J., & Schuchinsky, A. G. (2017). Bistate frequency selective surfaces made of intertwined slot arrays. *IEEE Transactions on Antennas and Propagation*, 65(6), 3093-3101.

Wadley, H. N. (2002). Cellular metals manufacturing. *Advanced engineering materials*, *4*(10), 726-733.

Wadley, H. N., Fleck, N. A., & Evans, A. G. (2003). Fabrication and structural performance of periodic cellular metal sandwich structures. *Composites science and technology*, *63*(16), 2331-2343.

Wang, P., Casadei, F., Shan, S., Weaver, J. C., & Bertoldi, K. (2014). Harnessing buckling to design tuneable locally resonant acoustic metamaterials. *Physical review letters*, *113*(1), 014301.

Wei, Z. Y., Guo, Z. V., Dudte, L., Liang, H. Y., & Mahadevan, L. (2013). Geometric mechanics of periodic pleated origami. *Physical review letters*, *110*(21), 215501.

Wilt, J. K., Yang, C. X., & Gu, G. X. Accelerating Auxetic Metamaterial Design with Deep Learning. *Advanced Engineering Materials*.

WOOD-SKIN - Redefining Material Properties. (2017). Accessed August 11. https://wood-skin.com/.

Xie, R., Chen, Y., & Gattas, J. M. (2015). Parametrisation and application of cube and eggbox-type folded geometries. *International Journal of Space Structures*, *30*(2), 99-110.

Xu, S., Yan, Z., Jang, K. I., Huang, W., Fu, H., Kim, J., ... & Badea, A. (2015). Assembly of micro/nanomaterials into complex, three-dimensional architectures by compressive buckling. *Science*, *347*(6218), 154-159.

Yang, N., & Silverberg, J. L. (2017). Decoupling local mechanics from large-scale structure in modular metamaterials. *Proceedings of the National Academy of Sciences*, *114*(14), 3590-3595.

Yang, S., Choi, I. S., & Kamien, R. D. (2016). Design of super-conformable, foldable materials via fractal cuts and lattice kirigami. *MRS Bulletin*, *41*(2), 130-138.

Yang, W., Li, Z. M., Shi, W., Xie, B. H., & Yang, M. B. (2004). Review on auxetic materials. *Journal of materials science*, *39*(10), 3269-3279.

Yang, Y., & You, Z. (2018). Geometry of transformable metamaterials inspired by modular origami. *Journal of Mechanisms and Robotics*, *10*(2).

Yoon, C., Xiao, R., Park, J., Cha, J., Nguyen, T. D., & Gracias, D. H. (2014). Functional stimuli responsive hydrogel devices by self-folding. *Smart Materials and Structures*, *23*(9), 094008.

You, Z., & Chen, Y. (2011). *Motion structures: deployable structural assemblies of mechanisms*. Crc Press.

Yu, X., Zhou, J., Liang, H., Jiang, Z., & Wu, L. (2018). Mechanical metamaterials associated with stiffness, rigidity and compressibility: A brief review. *Progress in Materials Science*, *94*, 114-173.

Zadpoor, A. A. (2016). Mechanical meta-materials. *Materials Horizons*, *3*(5), 371-381.

Zárate, Y., Babaee, S., Kang, S. H., Neshev, D. N., Shadrivov, I. V., Bertoldi, K., & Powell, D. A. (2016). Elastic metamaterials for tuning circular polarization of electromagnetic waves. *Scientific reports*, *6*(1), 1-8.

Zhang, X., Zhang, J., Liu, H., Su, X., & Wang, L. (2014). Soft plasmons with stretchable spectroscopic response based on thermally patterned gold nanoparticles. *Scientific reports*, *4*, 4182.

Zhang, Y., Matsumoto, E. A., Peter, A., Lin, P. C., Kamien, R. D., & Yang, S. (2008). One-step nanoscale assembly of complex structures via harnessing of an elastic instability. *Nano letters*, *8*(4), 1192-1196.

Zhang, Y., Yan, Z., Nan, K., Xiao, D., Liu, Y., Luan, H., ... & Ren, W. (2015). A mechanically driven form of Kirigami as a route to 3D mesostructures in micro/nanomembranes. *Proceedings of the National Academy of Sciences*, *112*(38), 11757-11764.

Zhao, Z., Wu, J., Mu, X., Chen, H., Qi, H. J., & Fang, D. (2017). Origami by frontal photopolymerization. *Science advances*, *3*(4), e1602326.

Zheng, X., Deotte, J., Alonso, M. P., Farquar, G. R., Weisgraber, T. H., Gemberling, S., ... & Spadaccini, C. M. (2012). Design and optimization of a light-emitting diode projection micro-stereolithography three-dimensional manufacturing system. *Review of Scientific Instruments*, *83*(12), 125001.

Zheng, X., Lee, H., Weisgraber, T. H., Shusteff, M., DeOtte, J., Duoss, E. B., ... & Kucheyev, S. O. (2014). Ultralight, ultrastiff mechanical metamaterials. *Science*, *344*(6190), 1373-1377.

Zhu, J., Dexheimer, M., & Cheng, H. (2017). Reconfigurable systems for multifunctional electronics. *npj Flexible Electronics*, *1*(1), 1-13.